ABSTRACT

Title of dissertation: Correlation-based Transition Modeling for External Aerodynamic Flows

Shivaji Medida, Doctor of Philosophy, 2014

Dissertation directed by: Dr. James D. Baeder
Department of Aerospace Engineering

Conventional turbulence models calibrated for fully turbulent boundary layers often over-predict drag and heat transfer on aerodynamic surfaces with partially laminar boundary layers. A robust correlation-based model is developed for use in Reynolds-Averaged Navier-Stokes simulations to predict laminar-to-turbulent transition onset of boundary layers on external aerodynamic surfaces. The new model is derived from an existing transition model for the two-equation k-ω Shear Stress Transport (SST) turbulence model, and is coupled with the one-equation Spalart-Allmaras (SA) turbulence model. The transition model solves two transport equations for intermittency and transition momentum thickness Reynolds number. Experimental correlations and local mean flow quantities are used in the model to account for effects of freestream turbulence level and pressure gradients on transition onset location. Transition onset is triggered by activating intermittency production using a vorticity Reynolds number criterion.

In the new model, production and destruction terms of the intermittency equation are modified to improve consistency in the fully turbulent boundary layer post-

transition onset, as well as ensure insensitivity to freestream eddy viscosity value specified in the SA model. In the original model, intermittency was used to control production and destruction of turbulent kinetic energy. Whereas, in the new model, only the production of eddy viscosity in SA model is controlled, and the destruction term is not altered. Unlike the original model, the new model does not use an additional correction to intermittency for separation-induced transition. Accuracy of drag predictions are improved significantly with the use of the transition model for several two-dimensional single- and multi-element airfoil cases over a wide range of Reynolds numbers. The new model is able to predict the formation of stable and long laminar separation bubbles on low-Reynolds number airfoils that is not captured with conventional turbulence models.

The validated transition model is successfully applied to rotating blade configurations in axial flow conditions to study the effects of transitional boundary layers on rotor thrust and torque. In helicopter rotors, inclusion of transition effects increased thrust prediction by 2% and decreased torque by as much as 8% at lower collective angles, due to reduced airfoil profile drag. In wind turbine rotors, transition model predicted a 7%–70% increase in generated shaft torque at lower wind speeds, due to lower viscous drag. This has important implications for CFD analysis of small wind turbines operating at low values of rated power. Transition onset locations along upper and lower surfaces of rotor blades are analyzed in detail.

A new crossflow transition onset criterion is developed to account for crossflow instability effects in three-dimensional boundary layers. Preliminary results for swept wing and rotating blade flows demonstrate the need to account for crossflow

transition in three-dimensional simulations of wings, rotating blades, and airframes. Inclusion of crossflow effects resulted in accelerated transition in the presence of favorable pressure gradients and yawed flow. Finally, a new correction to the wall damping function in the Spalart-Allmaras turbulence model is proposed to improve sensitivity of the model to strong adverse pressure gradients (APG). The correction reduces turbulence production in the boundary layer when the ratio of magnitudes of local turbulent stress to the wall shear stress exceeds a threshold value, therefore enabling earlier separation of boundary layer. Improved prediction of static and dynamic stall on two-dimensional airfoils is demonstrated with the APG correction.

Correlation-based Transition Modeling for External Aerodynamic Flows

by

Shivaji Medida

Dissertation submitted to the Faculty of the Graduate School of the
University of Maryland, College Park in partial fulfillment
of the requirements for the degree of
Doctor of Philosophy
2014

Advisory Committee:
Dr. James D. Baeder, Chair/Advisor
Dr. Inderjit Chopra
Dr. Christopher Cadou
Dr. Johan Larsson
Dr. Kenneth Kiger, Dean's Representative

Dedication

This dissertation is dedicated to my mother, Subhashini Medida, and my wife, Ramya Alexander, for their immense love and support.

Acknowledgments

I would like to express my sincere gratitude to my advisor, Dr. James Baeder, for giving me the opportunity to pursue doctoral research at the University of Maryland. His guidance, support, encouragement, and immense patience throughout my doctoral research has made this dissertation possible. I have learned a great deal from my discussions with him on various research problems, and his insights into research problems has always amazed me. The freedom and flexibility that Dr. Baeder has provided me to explore new research topics has played a crucial role in forming my current research interests and approach to problem solving.

I would also like to thank my dissertation committee members: Dr. Inderjit Chopra, Dr. Christopher Cadou, Dr. Kenneth Kiger, and Dr. Johan Larsson, for their insightful feedback as well as constructive criticism on my research work, and for their time to serve on my committee. I would like to acknowledge the financial support provided for this research work under the Alfred Gessow Vertical Lift Rotorcraft Center of Excellence (VLRCOE) research program.

I would like to thank all my friends and colleagues with whom I shared wonderful times during my stay in graduate school. I cannot forget the role of my good friends Ravikanth and Rajesh who supported me in my decision to pursue Aerospace Engineering almost 12 years ago. Finally, I am deeply indebted to my wife, Ramya Alexander, who has been my strongest support and encouragement throughout my graduate research.

Table of Contents

List of Tables vii

List of Figures viii

1 **Introduction** 1
- 1.1 Motivation . . . 1
- 1.2 Physical Problem . . . 3
- 1.3 Brief History of Transition Studies . . . 5
- 1.4 Physics of Boundary Layer Transition . . . 7
  - 1.4.1 Natural Transition . . . 9
  - 1.4.2 Bypass Transition . . . 10
  - 1.4.3 Intermediate Mechanisms . . . 10
  - 1.4.4 Modern Perspective on Transition Mechanisms . . . 11
  - 1.4.5 Factors Affecting Transition . . . 14
- 1.5 Challenges in Laminar-Turbulent Transition Modeling . . . 22
- 1.6 Objectives . . . 24
- 1.7 Contributions of Thesis . . . 25
- 1.8 Scope and Organization of Thesis . . . 25

2 **Progress in Transition Modeling** 28
- 2.1 Transition Prediction in Modern CFD Solvers . . . 28
- 2.2 Direct Numerical Simulation (DNS) and Large Eddy Simulation (LES) 30
- 2.3 Models based on Hydrodynamic Stability Theory . . . 39
- 2.4 Correlation-based Models . . . 41
  - 2.4.1 Transition Onset Prediction Models . . . 41
  - 2.4.2 Transition Extent Prediction Models . . . 43
  - 2.4.3 Transition Onset and Extent Prediction Models . . . 45
- 2.5 Summary . . . 50

3 **Transition Model Development** 52
3.1 Summary of $\gamma - Re_\theta$ Transition Model . . . 53
3.2 Formulation of the $\gamma - Re_\theta -$ SA Transition Model . . . 57
3.2.1 Modified Experimental Correlations for $\mathrm{Re}_{\theta t}$ . . . 58
3.2.2 Intermittency Production and Destruction . . . 62
3.3 Model Calibration and Verification . . . 65
3.4 Final Form of $\gamma - Re_\theta -$ SA Transition Model . . . 75
3.5 Computational Cost . . . 78
3.6 Summary . . . 79

4 **Numerical Methodology** 80
4.1 Governing Equations . . . 80
4.2 Rotating Reference Frame . . . 84
4.3 Non-dimensional Form of Equations . . . 86
4.4 Reynolds-Averaged Navier-Stokes Equations . . . 87
4.5 Curvilinear Coordinate Transformation . . . 90
4.6 Mesh Topology . . . 91
4.7 Overset Mesh Methodology . . . 95
4.8 Parallelization . . . 98
4.9 Numerical Algorithms in OverTURNS . . . 99
4.9.1 Inviscid Fluxes . . . 100
4.9.2 Viscous Fluxes . . . 101
4.9.3 Turbulence Modeling . . . 102
4.9.4 Time Integration . . . 104
4.9.5 Convergence Acceleration for Low-Speed Flows . . . 107
4.9.6 Initial Conditions . . . 107
4.9.7 Boundary Conditions . . . 108
4.10 Summary . . . 113

5 **Two-dimensional Airfoil Simulations** 114
5.1 Computational Grids . . . 114
5.2 Aerospatiale–A Airfoil . . . 118
5.3 VA-2 Supercritical Airfoil . . . 121
5.4 S809 Airfoil . . . 124
5.5 Eppler 387 Airfoil . . . 128
5.6 NACA 64_2(A)015 Airfoil . . . 133
5.7 MD 30P–30N Multi-element Airfoil . . . 135
5.8 SC2110 w/ Leading-edge Slat . . . 138
5.9 Summary . . . 142

6 **Three-dimensional Rotor Simulations** 144
6.1 Computational Grids . . . 145
6.2 Rotorcraft Flows . . . 146
6.2.1 BO 105 Rigid Rotor . . . 149
6.2.2 UH60-A Rigid Rotor . . . 157

6.3 Wind Turbine Flows . . . 167
6.3.1 Previous CFD Studies of NREL Phase VI Rotor . . . 168
6.3.2 NREL Phase VI Rotor Simulations . . . 170
6.4 Summary . . . 194

7 **Conclusions** 195
7.1 Summary . . . 195
7.2 Key Observations . . . 197
7.2.1 Two-Dimensional Airfoil Simulations . . . 197
7.2.2 Three-dimensional Rotor Simulations . . . 199
7.3 Recommendations for Future Work . . . 203

A Crossflow Transition Onset Correlation 206
A.1 Introduction . . . 206
A.2 Crossflow Transition Physics and Modeling . . . 207
A.3 New Crossflow Transition Onset Criterion - Modified Crossflow Reynolds Number . . . 210
A.4 Preliminary Results . . . 215
A.5 Summary . . . 217

B Strong Adverse Pressure Gradient Correction 222
B.1 Introduction . . . 222
B.2 Spalart-Allmaras Turbulence Model . . . 224
B.3 APG Modification to S-A Model . . . 226
B.4 Preliminary Results . . . 229
B.5 Summary . . . 239

Bibliography 241

List of Tables

3.1 Piecewise linear correlations between $\mathrm{Re}_{\theta t}$ and Tu 61

5.1 Two-dimensional airfoil test cases 115
5.2 Lift and drag coefficient predictions for VA-2 supercritical airfoil . . 124
5.3 Transition onset locations (x/c_{main}) for MD–30P–30N multi-element airfoil configuration (error reported as a % of main element chord length, c_{main}) 138

6.1 Effect of transition model on performance predictions for BO 105 rotor 152
6.2 Comparison of thrust predictions for NREL Phase VI rotor (thrust in Newtons) 172
6.3 Comparison of shaft torque predictions for NREL Phase VI rotor (torque in Newton-meter) 173

A.1 NLF(2)-0415 Infinite Swept Wing - Comparison of CFD ($\mathrm{Re}_{\mathrm{MCF}_2}$) and Experimental [130] Transition Onset Locations 214

B.1 Flow conditions for 2-D dynamic stall test case of SC1095 airfoil (sinusoidal pitching motion - $\alpha(t) = \alpha_o + \alpha_s \sin(\omega t)$) 233

List of Figures

1.1 Boundary layer transition on a flat plate 3
1.2 Boundary layer profiles showing laminar-to-turbulent transition on a flat plate at zero pressure gradient (reproduced from [1]) 4
1.3 Paths to Boundary Layer Turbulence (reproduced from [13]) 8
1.4 Instantaneous and time-averaged skin friction profiles showing transition onset due to introduction of one penetrating and one non-penetrating modes in the freestream (reproduced from [24]) 12
1.5 Visualization of boundary layer evolution with introduction of penetrating and non-penetrating modes in the freestream (reproduced from [24]) 13
1.6 Variation of momentum thickness Reynolds number with freestream turbulence intensity, at start and end of transition on a flat plate at zero pressure gradient (reproduced from [1]) 15
1.7 Effect of pressure gradient on transition onset on a flat plate (reproduced from [1]) 16
1.8 Laminar separation bubble formation due to strong adverse pressure gradient (reproduced from [6]) 18
1.9 Crossflow transition on swept wings (reproduced from [27]) 20

2.1 (a) u-component and (b) v-component of fluctuations showing streaks, spots, and transition of boundary layer beneath freestream turbulence(reproduced from DNS study [39]) 34
2.2 Instantaneous and mean skin friction predictions from DNS studies showing elevated levels inside a turbulent spot (reproduced from [39,40]) 35
2.3 Iso-surfaces of second invariant of velocity gradient tensor colored by local values of u showing hairpin structures; (a) to (f) are different streamwise zones (reproduced from DNS study of [40]) 36
2.4 Snapshot of iso-surface of spanwise vorticity (= -150) identifying impinging wake and boundary layer separation (reproduced from DNS study of [41]) 37
2.5 Stages of natural transition in plane channel flow (reproduced from LES study of [42]) 37

2.6 Time-averaged skin friction on the suction side of a low-pressure turbine blade subject to periodic impinging wakes (reproduced from LES study of [43]) . . . 38
2.7 Skin friction predictions on MD 30P/30N multi-element airfoil; dashed lines indicate beginning and end of transition region from experimental data (reproduced from WMSLES study of [44]) . . . 38
2.8 Schematic of scaled vorticity Reynolds number profile in a laminar boundary layer (reproduced from [6]) . . . 49

3.1 Cartesian mesh and boundary conditions used for zero-pressure gradient flat plate simulations . . . 59
3.2 Evaluation of new correlations between $\mathrm{Re}_{\theta t}$ and Tu based on T3-series flat plate data and Vorticity Reynolds number criterion . . . 60
3.3 Comparison of present transition onset correlations with previous correlations . . . 62
3.4 Flat plate intermittency contours – improved intermittency recovery in turbulent boundary layer . . . 63
3.5 Transition model sensitivity to critical Reynolds number and intermittency production term strength . . . 66
3.6 Transition model sensitivity to variation in freestream Eddy viscosity 67
3.7 Skin friction prediction on a flat plate at zero pressure gradient using $\gamma - Re_\theta -$ SA transition model . . . 68
3.8 Solution of $\overline{Re_{\theta t}}$ transport equation for flow past an S809 airfoil section at 0^o AoA . . . 69
3.9 Near-wall solution of $\overline{Re_{\theta t}}$ for flow past an S809 airfoil section at 0^o AoA (not to scale) . . . 70
3.10 Production of Eddy viscosity downstream of transition onset location for flow past an S809 airfoil section at 0^o AoA (not to scale) . . . 71
3.11 Surface pressure, skin friction, and intermittency profiles for flow past an S809 airfoil section at 0^o AoA . . . 71
3.12 Grid convergence study for flow past an S809 airfoil section at 0^o AoA 72
3.13 Demonstration of hysteresis-free and relaminarization properties of $\gamma - Re_\theta -$ SA transition model by simulating a sinusoidally pitching S809 airfoil section . . . 73

4.1 Curvilinear mapping of physical space onto computational space (reproduced from [85]) . . . 91
4.2 Structured, C-topology, 2-D mesh around an airfoil section . . . 92
4.3 Structured, C-O topology, 3-D mesh on a rotor blade . . . 93
4.4 Overset mesh system for rotor blades. Green – C-O topology blade mesh, Red – Cylindrical background mesh for wake capture . . . 94
4.5 Schematic of Chimera hole-cutting technique. Red circles: Hole points, Blue circles: Hole fringe points, Black circles: Chimera boundary points. (reproduced from [86]) . . . 95

4.6 Hole-cutting for a multi-element airfoil in a background wind-tunnel mesh. Red: Leading-edge slat mesh, Green: Main element, Blue: Wind tunnel mesh . . . 96
4.7 Schematic of a computational cell on a structured mesh. (reproduced from [86]) . . . 97
4.8 Spanwise domain decomposition of a C-O topology rotor blade mesh. Each color represents a sub-domain that is solved on a separate processor. . . . 98
4.9 Boundary conditions on a structured C-topology mesh (reproduced from [86]) . . . 109
4.10 Schematic of point-sink boundary condition for downstream boundary of rotor wake mesh (reproduced from [86]) . . . 110

5.1 Computational meshes for single-element airfoil simulations . . . 116
5.2 Computational meshes used for multi-element airfoil simulations . . . 117
5.3 Pressure and skin friction profiles for Aerospatiale-A airfoil (Experiment [100]) . . . 118
5.4 Intermittency and Eddy viscosity production for Aerospatiale-A airfoil (not to scale) . . . 119
5.5 Eddy viscosity contours for flow past Aerospatiale-A airfoil . . . 120
5.6 Skin friction profiles for VA-2 supercritical airfoil (Experiment [102]) . 122
5.7 Presurre coefficient profiles for VA-2 supercritical airfoil . . . 123
5.8 Transition Model predictions for S809 airfoil section (Experiment [104]) 125
5.9 Streamlines colored by velocity magnitude showing separation at high AoA on S809 airfoil section . . . 126
5.10 Comparison of pressure profiles for S809 airfoil section (Experiment [104]) . . . 127
5.11 Comparison of skin friction profiles for S809 airfoil section . . . 128
5.12 Lift and drag variation for E387 airfoil section (Experiment [105]) . . 129
5.13 Laminar separation and turbulent reattachment predictions for E387 airfoil section (Experiment [105]) . . . 130
5.14 Pressure and skin friction profiles on S809 airfoil section showing presence of laminar separation bubbles . . . 131
5.15 Visualization of laminar separation bubble for E387 airfoil at AoA = 0° and Re = 200,000 . . . 132
5.16 Transition onset and Eddy viscosity production for E387 airfoil at AoA = 0° and Re = 200,000 . . . 133
5.17 High Reynolds number transition onset location predictions for NACA 64_2(A)015 airfoil section (Experiment [106]) . . . 134
5.18 Pressure coefficient prediction on MD 30P–30N airfoil configuration - Effect of wall distance function evaluation (Experiment [108]) . . . 135
5.19 Intermittency contours showing transition onset on MD 30P-30N multi-element airfoil configuration: Blue - Laminar, Red - Turbulent (Experiment [108]) . . . 137

5.20 Lift and drag predictions for SC2110 w/ Slat multi-element airfoil (Experiment [110]) . . . 139
5.21 Lift-to-Drag ratio for SC2110 w/ Slat multi-element airfoil (Experiment [110]) . . . 140
5.22 Comparison of surface pressure and skin friction profiles for SC2110 w/ Slat multi-element airfoil . . . 141
5.23 Comparison of Eddy viscosity contours for SC2110 w/ Slat multi-element airfoil . . . 142

6.1 Visualization of transitional boundary layer on BO 105 rotor blades using Acenaphthene coating: Light regions – Laminar, Dark regions – Turbulent (figure reprocued from [114], Experiment [115]) . . . 148
6.2 Overset mesh system used for BO 105 rotor blade simulations: Green – blade mesh, Red – background mesh for wake capture . . . 150
6.3 Transition onset prediction on BO 105 rigid rotor with three wrap-around grid resolutions. N_{wall} – number of grid points on blade surface in wrap-around direction (Experiment [115]) . . . 153
6.4 Intermittency contours on BO 105 rotor blade surface: Blue – laminar, Red – turbulent. . . . 154
6.5 Spanwise vorticity contours on BO 105 rotor blade surface . . . 154
6.6 Chordwise distribution of spanwise-vorticity profiles at six spanwise stations on the BO 105 rotor blade – sudden jump in vorticity indicates transition to turbulence . . . 155
6.7 Tip-vortex and wake visualization for BO 105 rotor blade . . . 156
6.8 Overset mesh system used for UH60-A rotor blade simulations: Green – blade mesh, Red – background mesh for wake capture . . . 159
6.9 Blade surface intermittency contours on UH60A rotor at collective pitch angles (in degrees): 0, 4, 8, 12, 15. Blue: Laminar, Red: Turbulent 160
6.10 Variation of transition onset location with collective pitch angle on UH60-A rigid rotor . . . 161
6.11 Effect of transition model on rotor thrust and torque for UH60-A rigid rotor . . . 162
6.12 Effect of transition model on rotor thrust and torque for UH60-A rigid rotor (positive % change represents increase from fully turbulent value, and vice versa) . . . 163
6.13 Effect of transition model on rotor figure of merit for UH60-A rigid rotor . . . 164
6.14 Tip-vortex and wake visualization on UH60-A rotor blade at 10° collective pitch angle . . . 165
6.15 Tip-vortex roll-up for UH60-A rotor blade at 10° collective pitch angle 166
6.16 Overset mesh system used for NREL Phase VI rotor blade simulations: Green – blade mesh, Red – background mesh for wake capture 171
6.17 NREL Phase VI rotor thrust and torque predictions with $\gamma - Re_\theta -$SA transition model (Experiment from [103]) . . . 174

6.18 NREL Phase VI rotor spanwise thrust and torque distribution profiles at wind speeds of 3.5 m/s and 5.0 m/s. Data is plotted for one rotor revolution. Red: SA–Turbulent, Green: SA–Transition 175
6.19 NREL Phase VI rotor spanwise thrust and torque distribution profiles at wind speeds of 7 m/s and 10 m/s. Data is plotted for one rotor revolution. Red: SA–Turbulent, Green: SA–Transition 176
6.20 NREL Phase VI rotor spanwise thrust and torque distribution profiles at a wind speed of 15 m/s. Data is plotted for one rotor revolution. Red: SA–Turbulent, Green: SA–Transition 177
6.21 Chordwise blade surface pressure distribution profiles at four spanwise stations for wind speed of 7 m/s on the NREL Phase VI rotor blade (Experiment from [103]) 179
6.22 Chordwise blade surface pressure distribution profiles at four spanwise stations for wind speed of 10 m/s on the NREL Phase VI rotor blade (Experiment from [103]) 180
6.23 Chordwise blade surface pressure distribution profiles at four spanwise stations for wind speed of 15 m/s on the NREL Phase VI rotor blade (Experiment from [103]) 181
6.24 Chordwise blade surface pressure distribution profiles at four spanwise stations for wind speed of 20 m/s on the NREL Phase VI rotor blade (Experiment from [103]) 182
6.25 Chordwise blade surface pressure distribution profiles at four spanwise stations for wind speed of 25 m/s on the NREL Phase VI rotor blade (Experiment from [103]) 183
6.26 Blade surface streamlines on NREL Phase VI rotor at wind speeds of 3.5 m/s and 5 m/s. SA: SA–Turbulent, SAT: SA–Transition 186
6.27 Blade surface streamlines on NREL Phase VI rotor at wind speeds of 7 m/s and 10 m/s. SA: SA–Turbulent, SAT: SA–Transition 187
6.28 Blade surface streamlines on NREL Phase VI rotor at wind speeds of 15 m/s and 20 m/s. SA: SA–Turbulent, SAT: SA–Transition 188
6.29 Blade surface intermittency contours on NREL Phase VI rotor for wind speed range 3.5–25 m/s. Blue: Laminar, Red: Turbulent 189
6.30 Spanwise variation of Eddy viscosity contours at V = 10 m/s showing increased unsteady separated flow with transition model (red indicates separated flow regions) 190
6.31 Iso-surfaces of vorticity magnitude showing tip vortices for the NREL Phase VI rotor blade 192
6.32 Vorticity magnitude contours in one azimuthal cross-section of rotor wake flow field, showing root and tip vortices for the NREL Phase VI rotor blade 193

A.1 Crossflow transition on swept wings [27] 207
A.2 Modified Crossflow Reynolds Number Profiles for Laminar Boundary Layer at Re = 3.73×10^6 on NLF(2)-0415 infinite swept-wing 212

A.3 Modified Crossflow Reynolds Number Profiles for Boundary Layer Tripped at 25% of chord, Re = 3.73 × 10^6 on NLF(2)-0415 infinite swept-wing . . . 213
A.4 Improved transition onset prediction with new crossflow transition criterion: ONERA M6 Wing . . . 219
A.5 UH60-A rotor system with offset blades to create outboard yawed flow (blades rotate counter-clockwise) . . . 220
A.6 Intermittency contours for UH60-A rotor in hover without offset (Blue - Laminar, Red - Turbulent, L - Lower Surface, U - Upper Surface) . 221

B.1 Effect of adverse pressure gradient on the defect layer (NACA 0012 airfoil, Re = 6×10^6) . . . 224
B.2 δ profiles on a zero pressure gradient flat plate . . . 228
B.3 δ criterion indicating strong adverse pressure gradient region on the upper surface of NACA 0012 airfoil at 10° AoA, Re = 6 × 10^6 . . . 229
B.4 Improved static stall prediction with SA-APG model (Expt [137]: NACA 0012 airfoil, Re = 6 × 10^6, M = 0.15) . . . 230
B.5 δ criterion indicating strong adverse pressure gradient region on the upper surface of NACA 0012 airfoil at 10° AoA, Re = 6 × 10^6 . . . 231
B.6 Upper surface mean velocity profiles at 10° AoA on NACA 0012 airfoil, Re = 6 × 10^6 . . . 233
B.7 Upper surface mean velocity profiles at 10° AoA on NACA 0012 airfoil, Re = 6 × 10^6 . . . 234
B.8 δ criterion indicating strong adverse pressure gradient region on the upper surface of NACA 0012 airfoil at 15° AoA, Re = 6 × 10^6 . . . 234
B.9 Upper surface mean velocity profiles at 15° AoA on NACA 0012 airfoil, Re = 6 × 10^6 . . . 235
B.10 Upper surface mean velocity profiles at 15° AoA on NACA 0012 airfoil, Re = 6 × 10^6 . . . 236
B.11 Upper surface Eddy viscosity profiles at 15° AoA on NACA 0012 airfoil, Re = 6 × 10^6 . . . 237
B.12 Upper surface Eddy viscosity profiles at 15° AoA on NACA 0012 airfoil, Re = 6 × 10^6 . . . 238
B.13 Improved dynamic stall predictions with SA-APG model (Expt [138]: SC1095 airfoil) . . . 238
B.14 Improved shock location prediction with SA-APG model (NACA 0012 airfoil, Expt [139]: Re = 9 × 10^6, M = 0.799, AoA = 2.26°) . . . 240

Nomenclature

a	Speed of sound $= \sqrt{\gamma RT}$
C_d	Sectional drag coefficient $= \dfrac{D}{\frac{1}{2}\rho_\infty U_\infty^2 c}$
C_f	Skin friction coefficient $= \dfrac{\tau_w}{\frac{1}{2}\rho_\infty U_\infty^2}$
C_l	Sectional lift coefficient $= \dfrac{L}{\frac{1}{2}\rho_\infty U_\infty^2 c}$
C_p	Pressure coefficient $= \dfrac{p - p_\infty}{\frac{1}{2}\rho_\infty U_\infty^2}$
C_Q	Rotor torque coefficient $= \dfrac{Q}{\rho_\infty \pi R^3 V_{tip}^2}$
$C_{Q_{\text{ideal}}}$	Ideal torque coefficient $= \dfrac{C_T^{3/2}}{\sqrt{2}}$
C_T	Rotor thrust coefficient $= \dfrac{T}{\rho_\infty \pi R^2 V_{tip}^2}$
d	Nearest wall distance
D	Drag force
e	Internal energy
FM	Figure of Merit $= \dfrac{C_{Q_{\text{ideal}}}}{C_Q}$
H	Shape factor $= \dfrac{\delta^*}{\theta}$
k	Turbulent kinetic energy $= \dfrac{1}{2}\left[\overline{(u')^2} + \overline{(v')^2} + \overline{(w')^2}\right]$
L	Reference length / Lift force
M	Mach number
p	Static pressure
Pr	Prandtl number
Q	Roror torque
r	Distance along rotor blade non-dimensionalized by rotor radius
R	Roror radius
Re	Reynolds number $= \dfrac{\rho_\infty U_\infty L}{\mu_\infty}$
Re_θ	Reynolds number based on momentum thickness $= \dfrac{\rho_\infty U_\infty \theta}{\mu_\infty}$
$Re_{\theta t}$	Re_θ at transition onset location
$\overline{Re_{\theta t}}$	Transport variable for $Re_{\theta t}$
Re_v	Vorticity Reynolds number $= \dfrac{\rho d^2 \Omega}{\mu}$
S	Strain rate magnitude
t	Time
T	Roror thrust

Tu_∞	Freestream turbulence intensity = $\frac{\sqrt{2k/3}}{U_\infty}$
u, v, w	Flow velocity components along Cartesian coordinate directions
u', v', w'	Turbulent fluctuation velocities along Cartesian coordinate directions
$\overline{u_i' u_j'}$	Time-average of Reynolds stress tensor components
U_∞	Total freestream velocity magnitude
U_e	Boundary layer edge velocity magnitude
V_{tip}	Rotor blade tip speed in azimuthal direction
x,y,z	Cartesian coordinate directions

Symbols

δ	Boundary layer thickness
δ^*	Displacement thickness
γ	Ratio of specific heats / Intermittency
λ	Pressure gradient parameter = $\frac{\rho\theta^2}{\mu}\frac{dU}{ds}$
μ	Molecular viscosity
μ_t	Turbulent/Eddy viscosity
ν	Kinematic viscosity = $\frac{\mu}{\rho}$
ω	Specific dissipation rate
Ω	Vorticity magnitude
ρ	Density
τ_w	Wall shear stress
θ	Momentum thickness

Subscripts

e	Boundary layer edge
s	Streamline direction
v	Viscous quantities
∞	Freestream flow variables

Abbreviations

DES	Detached Eddy Simulation
DNS	Direct Numerical Simulation
LES	Large Eddy Simulation
MUSCL	Monotone Upstream-centered Schemes for Conservation Laws
NREL	National Renewable Energy Laboratory
OverTURNS	Overset Transonic Unsteady Rotor Navier-Stokes
RANS	Reynolds-Averaged Navier-Stokes

1 Introduction

1.1 Motivation

Laminar-turbulent transition of boundary layers affects viscous drag, heat transfer, and onset of separation in aerodynamic flows. Therefore, transition to turbulence plays an important role in the design and performance of many internal and external flow applications. For example, turbine blades in a gas turbine engine operate in the unsteady, turbulent wake of upstream blade rows at very high temperatures (around 2500° F) and experience increased heat transfer to the blade surface if the boundary layer becomes turbulent. In combination with the high centrifugal forces, this additional heat transfer can make the blades more susceptible to structural failure. In subsonic and transonic fixed wing aircraft, significant fuel savings can be obtained if the overall drag can be reduced by maintaining a laminar boundary layer on the wings and the airframe. Transition also plays an important role in determining the power requirements of rotorcraft as well as the generated power of wind turbines. Due to the spanwise variation of local Reynolds number in rotating blades, large regions of laminar are likely to be present in the inboard regions. In the design of hypersonic vehicles and their heat shields, high-

speed transition plays a critical role in determining surface heating during certain phases of the flight such as re-entry. In low-Reynolds number applications such as Unmanned Aerial Vehicles (UAVs), small wind turbines, and under-water vehicles, large regions of laminar flow are often present on the aerodynamic surface and therefore transition prediction is essential for accurate estimation of drag and stall onset. Numerical simulations at low Reynolds numbers (under 1 million) show that drag can be significantly over-predicted (as high as twice its actual value) if the boundary layer is treated as fully turbulent. One of the primary goals of transition research is to develop flow control techniques that will delay or accelerate transition, depending on the specific application. This provides a strong incentive to further our understanding of transition and relaminarization physics, as well as to develop capabilities to predict their occurrence in boundary layers.

Conventional turbulence models are not equipped to handle transitional boundary layers since they were developed and calibrated for fully turbulent flows at high Reynolds numbers. It is easy to verify that most of the turbulence models predict transition almost immediately downstream of the stagnation point and generate excessive turbulence resulting in over-prediction of viscous drag and heat transfer. Accurate numerical prediction of transitional boundary layers through Direct Numerical Simulations (DNS) for high-Reynolds number flows and complex configurations is beyond the reach of current computational resources. In addition, a quick and reasonable estimate of quantities such as drag and heat transfer is invaluable to the design process in several applications. This provides a strong motivation to develop *low-fidelity* transition prediction methods that can be a good substitute for

expensive and time-consuming experiments or DNS computations. The scope of the present work is limited to developing and validating an empirical correlation-based transition prediction methodology for subsonic, external flow applications.

1.2 Physical Problem

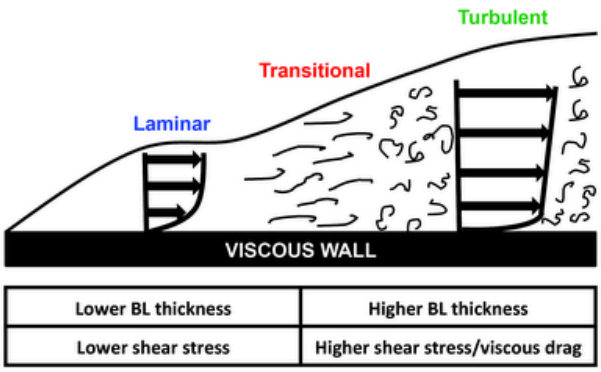

Figure 1.1: Boundary layer transition on a flat plate

Fluid flow past a solid surface can be divided into two distinct regions: (1) a thin region adjacent to the wall, where viscous flow effects are dominant, and (2) a largely inviscid outer flow region above the viscous layer in the wall normal direction. The presence of such a viscous region, commonly known as the *boundary layer*, was first discovered by Ludwig Prandtl in 1904. Figure 1.1 shows a schematic of a boundary layer developing on a flat plate. The boundary layer begins at the stagnation point formed at the leading-edge of the flat plate. Initially, it is in a laminar state, where the adjacent fluid layers tend to flow parallel to each other without significant mixing. Due to various external factors such as freestream turbulence, adverse pressure gradients, surface curvature, roughness, and vibrations,

instabilities often develop in a laminar boundary layer, causing it to transition to a turbulent state. This process is known as *laminar-to-turbulent* transition, and the opposite is called relaminarization or reverse transition. The mixing nature of turbulence enhances momentum and energy transport from the outer flow towards the near-wall region of the boundary layer. This manifests as increased skin friction / viscous drag on and heat transfer to the surface. In addition, the near-wall momentum deficit governs the point of flow reversal and boundary layer separation.

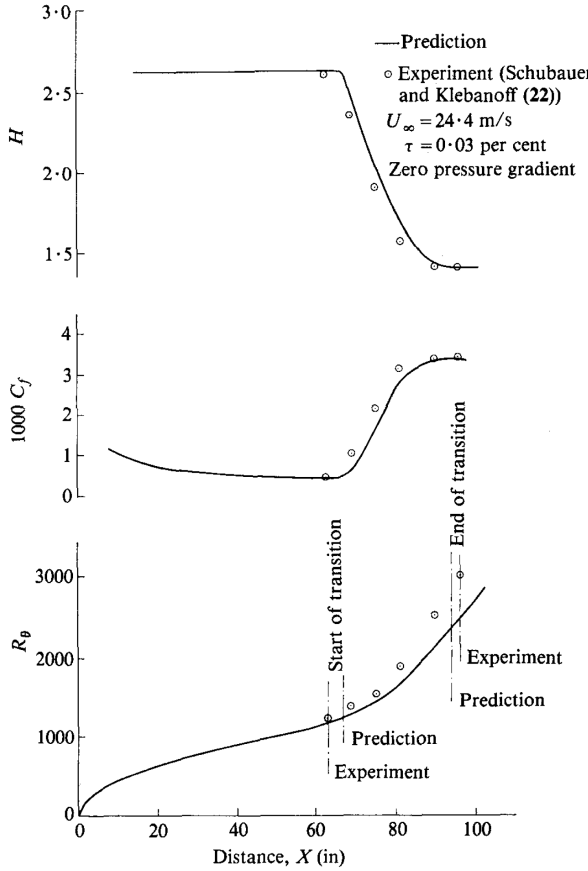

Figure 1.2: Boundary layer profiles showing laminar-to-turbulent transition on a flat plate at zero pressure gradient (reproduced from [1])

Figure 1.2 shows the streamwise profiles of shape factor (H), skin friction coefficient (C_f), and momentum thickness Reynolds number (Re_θ) of a transitional boundary layer on a flat plate at zero pressure gradient. The point of minimum skin friction is typically considered the start of transition. The transition process is considered complete when skin friction reaches its fully turbulent value. The region between the start and the end of transition is known as the *transition extent*. Across the transition zone, the shape factor decreases from its laminar value of 2.59 to a turbulent value of 1.3. Correspondingly, the momentum thickness Reynolds number and the skin friction coefficient increase.

1.3 Brief History of Transition Studies

The process of boundary layer transition from a stable laminar state to a fully turbulent state is one of the most widely studied phenomena in fundamental fluid mechanics. Over the years, comprehensive review articles were published in the open literature, summarizing the current understanding and outstanding issues of transition research [2–6]. Reshotko [7] provides an excellent historical survey of the progress, accomplishments, and issues in transition theory, experiments, prediction and control methods. Historically, boundary layer stability and transition have been studied under the area of *Hydrodynamic Stability*, whose focus was to explain why a laminar boundary layer cannot continue to stay laminar indefinitely. Osborne Reynolds (circa 1883) conducted one of the earliest controlled scientific experiments and identified a critical non-dimensional parameter, called the *Reynolds number*

(Eq.1.1), at which stable laminar flow in a pipe becomes turbulent.

$$Re = \frac{\rho U L}{\mu} \tag{1.1}$$

Theoretical studies began with Lord Rayleigh's inviscid inflection point criterion (1887) that relates the existence of an unstable mode to the presence of an inflection point in the mean velocity profile. William Orr (1907) and Arnold Sommerfeld (1908) used linear stability theory to develop a hydrodynamic stability criterion for the Navier-Stokes equations governing a parallel, laminar flow. After Prandtl's observation that viscosity can destabilize a boundary layer (1921), rigorous theoretical work by Walter Tollmien (1929) and Hermann Schlichting (1935) identified the presence of the Tollmien-Schlichting steamwise instability waves that can trigger the onset of turbulence in a laminar boundary layer. On the experimental side, the work of Schubauer and Skramstad (1947) is one of the earliest to demonstrate the presence of Tollmien-Schlichting waves in a laminar boundary layer on a flat plate at very low freestream turbulence levels. The experiments of Schubauer and Klebanoff (1955) revealed the presence of turbulent spots and the intermittent nature of turbulence during the transitional phase of a boundary layer. In the 1940s and 1950s, several NACA wartime reports document wind tunnel experiments and flight tests performed to study the effects of transition on aircraft performance, motivated by the need to develop low-drag airfoils. Starting in the late 1950s, theoretical studies were devoted to obtaining the exact numerical solutions to the linearized disturbance equations of Orr and Sommerfeld, which resulted in reliable transition prediction methods such as the e^N method. In addition, the wealth of high qual-

ity experimental data generated for transitional boundary layers has enabled the development of several correlation-based transition prediction models. With the advent of computers, many of these analytical and correlation-based models continue to be verified and validated through multi-fidelity numerical simulations of boundary layer flows in industrial applications. Increased availability of high performance computing resources has made *Direct Numerical Simulations* (DNS) and *Large Eddy Simulations* (LES) of canonical flow problems feasible, to investigate and uncover the rich features of transitional boundary layers.

1.4 Physics of Boundary Layer Transition

Current understanding of boundary layer transition comes from a rich history of experimental, theoretical, and high-fidelity computational studies. Notable researchers such as Morkoivn, Reshotko, and Saric have contributed significantly to the advancement of the field of transition and helped uncover the various complex mechanisms involved [8–12]. Transition of a stable laminar boundary layer to a turbulent state can be viewed as the non-linear response of a very complicated oscillator to a random forcing function, of infinitesimal amplitude relative to the appropriate laminar-flow quantities [3]. The schematic in Fig.1.3 outlines five different paths to breakdown of laminar flow and onset of turbulence in the boundary layer, in response to external forcing [13]. In this schematic, the forcing amplitude increases from left to right. Instabilities can be triggered due to the exposure of the boundary layer to a multitude of external disturbances such as freestream turbulence, surface rough-

ness, and vibrations. The concept of *Receptivity* was introduced by Morkovin [8] to describe the manner in which a particular external disturbance enters the boundary layer and the nature of its signature in the perturbed flow. Receptivity concerns the generation of instability waves, rather than their evolution. It determines the initial conditions of the transition process including the amplitude, frequency, and phase of the forcing function. Saric et al. [13] review the current understanding of boundary layer receptivity to external acoustic and vortical disturbances. Depending on

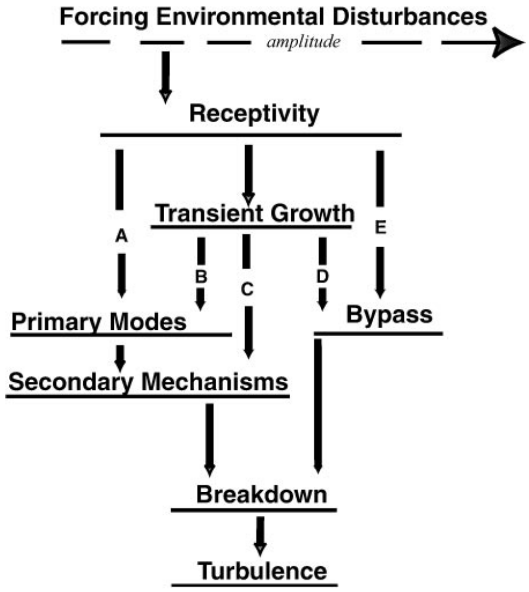

Figure 1.3: Paths to Boundary Layer Turbulence (reproduced from [13])

a number of factors such as Reynolds number, pressure gradients, wall curvature, and surface roughness, various primary instability mechanisms can develop independently or together. As the response amplitude grows, nonlinear interactions can occur in the form of secondary instabilities before reaching the breakdown phase. The breakdown phase is a 3-D phenomenon in an otherwise 2-D flow, and is char-

acterized by the formation of intermittent turbulent spots that grow at a constant rate and independently of each other [14]. Experiments [15] confirmed the existence of such turbulent spots and suggested that a turbulent spot is initiated when the maximum velocity fluctuation in the streamwise direction exceeds about one-fifth of the freestream velocity, almost independently of the Reynolds number [16]. The *intermittency* factor was introduced [17] to quantify the rate of turbulent spot production, and a relation between the transition Reynolds number and the intermittency factor was deduced. Once initiated, these intermittent turbulent spots grow in size as they travel downstream, until they merge into a fully turbulent boundary layer, thus completing the transition process.

1.4.1 Natural Transition

Path *A* is traditionally known as *natural transition*, and is the most common onset mechanism on transport aircraft in flight. Natural transition is well described by linear stability theory and the Orr-Sommerfeld equations [18–20]. Transition onset follows this path in weak disturbance environments, where the transient growth is insignificant and breakdown is reached through linear processes such as Tollmien-Schlichting, Gortler, or crossflow instabilities. The existence of two-dimensional Tollmien-Schlichting waves was first confirmed in the flat plate experiments of Schubauer and Skramstad [21] conducted at very low freestream turbulence levels (0.03%). In three-dimensional boundary layers, Gortler instability occurs due to concave surface curvature, and crossflow instability is caused due to a combination

of pressure gradients and sweep.

1.4.2 Bypass Transition

In scenarios where the initial disturbance amplitude is sufficiently high (caused by surface roughness or high freestream turbulence levels), the growth of linear disturbances is *bypassed* [8] and turbulent spots could form very quickly, as depicted in path E of the schematic. Although bypass transition has been observed in experiments with high freestream turbulence levels and surface roughness [10, 22], it has not been very well understood or described theoretically. Due to the highly non-linear nature of the disturbance growth, linear stability theory is not applicable in this mechanism. Bypass transition is the primary mechanism in turbomachinery due to the high freestream turbulence levels of the wake from upstream blade rows and the blade surface roughness.

1.4.3 Intermediate Mechanisms

Although natural and bypass transition have been considered the two primary paths to turbulence, recent work in the area of transient growth has revealed additional intermediate mechanisms [13]. Transient growth occurs when two, non-orthogonal, stable models interact, undergo algebraic growth, and then decay exponentially. Streamwise and wall-normal vorticity are considered important in transient growth. Depending on the amplitude, transient growth can lead to spanwise modulations of two-dimensional waves (path B), direct distortion of the basic state

that leads to secondary or subcritical instabilities (path C), or direct bypass (path D). Paths B and C are seen in external flows, whereas path D is more common in internal flows.

1.4.4 Modern Perspective on Transition Mechanisms

Recent theoretical and numerical studies by Durbin et al. [23, 24] introduce a new perspective on transition mechanisms that questions the conventional classification into natural and bypass transition. Since bypass transition is defined by what does not occur – Tollmien-Schlichting waves are *bypassed* – it allows for much ambiguity in describing the exact processes involved. Instead, they propose discrete modes (T-S waves) and continuous modes as the two possible transition mechanisms. In discrete mode transition, the imaginary part of the eigenvalue (frequency) determines the disturbance growth rate. In continuous mode transition, the starting point is the mode shape. They conducted Direct Numerical Simulations simulations to look at the evolution of continuous modes by prescribing one, two, or a few modes at the inlet. Simulations with single mode at the inlet produced an evolution that agreed with linear stability theory. Single mode perturbation was found to decay by viscous action. When two high-frequency (non-penetrating) modes were introduced, they decayed with little effect on the boundary layer. Introduction of two low-frequency modes was found to generate boundary layer disturbances that decayed by the end of the domain.

However, when one penetrating (low-frequency), and one non-penetrating (high-

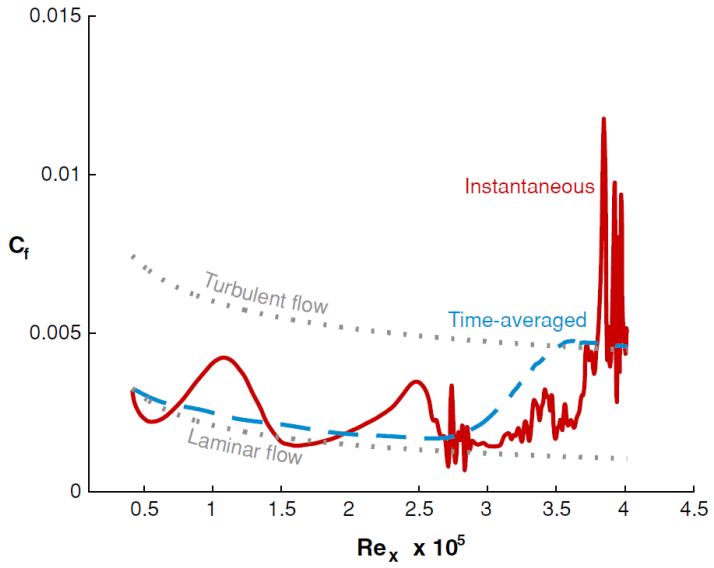

Figure 1.4: Instantaneous and time-averaged skin friction profiles showing transition onset due to introduction of one penetrating and one non-penetrating modes in the freestream (reproduced from [24])

frequency) mode were introduced, only the lower frequency mode was seen inside the boundary layer. This was caused due to the filtering of the high frequency mode by the shear layer, termed as, shear filtering. The penetrating mode generated perturbation jets, which seemed to begin decaying, but a patch of turbulence suddenly appeared in the middle of the domain resembling a turbulent spot (but unlike the classic Emmons spot). This resulted in a sudden turbulent burst in skin friction as shown in Fig. 1.4, which is a characteristic of bypass transition. Figure 1.5 visualizes the boundary layer evolution when one mode and two modes are introduced in the freestream.

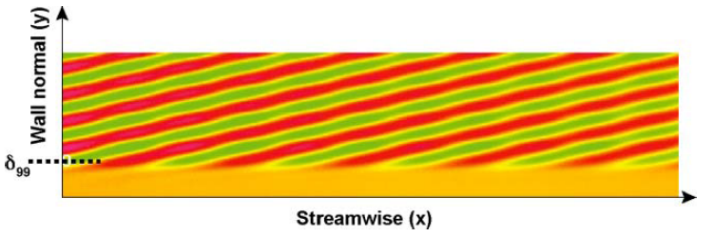

One nonpenetrating mode in the freestream. Contours of perturbation velocity.

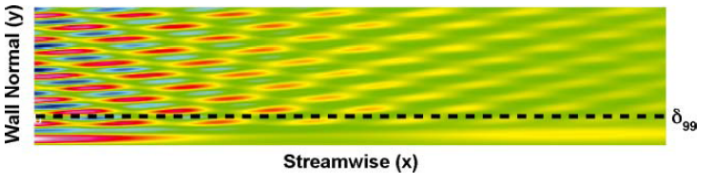

Two modes in the freestream; only the low frequency penetrates the boundary layer.

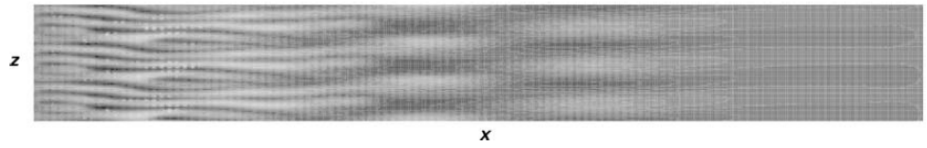

Instantaneous u contours. The plane is at $y/\delta = 0.8$. The spanwise coordinate is enlarged by a factor of three. The boundary layer is perturbed by two low-frequency modes.

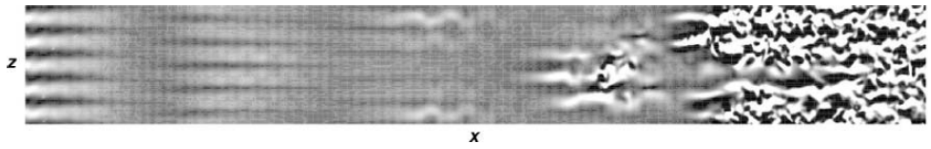

Instantaneous v contours at $y/\delta = 0.5$. The boundary layer is perturbed by a high- and a low-frequency mode.

Figure 1.5: Visualization of boundary layer evolution with introduction of penetrating and non-penetrating modes in the freestream (reproduced from [24])

1.4.5 Factors Affecting Transition

Transition onset mechanisms are strongly influenced by factors such as freestream turbulence, pressure gradients, surface curvature, surface roughness, sweep, and compressibility. Each of these factors can accelerate or delay transition onset depending on whether they stabilize of destabilize a particular mode. Therefore, understanding their role is essential to developing numerical prediction methods and feasible flow control techniques. This section summarizes the effect of some of the parameters on transition onset.

Freestream Turbulence

Increase in freestream turbulence intensity (Tu), causes earlier transition onset and shrinks the size of transition zone. This trend is documented in several experimental studies of flow past a flat plate at zero pressure gradient, for turbulence intensity values ranging from 0.03% to 10%. Natural transition occurs at Tu values below 1.0%, and bypass transition is triggered at larger Tu values. Figure 1.6 shows the variation of momentum thickness Reynolds number at the start and the end of transition zone, with freestream turbulence intensity, obtained from multiple experimental sources. All the data sets show that the transition onset location is relatively insensitive to freestream turbulence intensity greater than 4%. Abu-Ghannam and Shaw [1], and a few others developed correlations between transition momentum thickness Reynolds number ($Re_{\theta t}$), and freestream turbulence intensity (Tu). The popular correlations of Abu-Ghannam and Shaw (AGS) [1], and Mayle [25] are given

in Eq. 1.2 and Eq. 1.3 respectively.

$$Re_{\theta t,\mathrm{AGS}} = 163.0 + \exp(6.91 - Tu) \tag{1.2}$$

$$Re_{\theta t,\mathrm{Mayle}} = 400.0\, Tu^{-5/8} \tag{1.3}$$

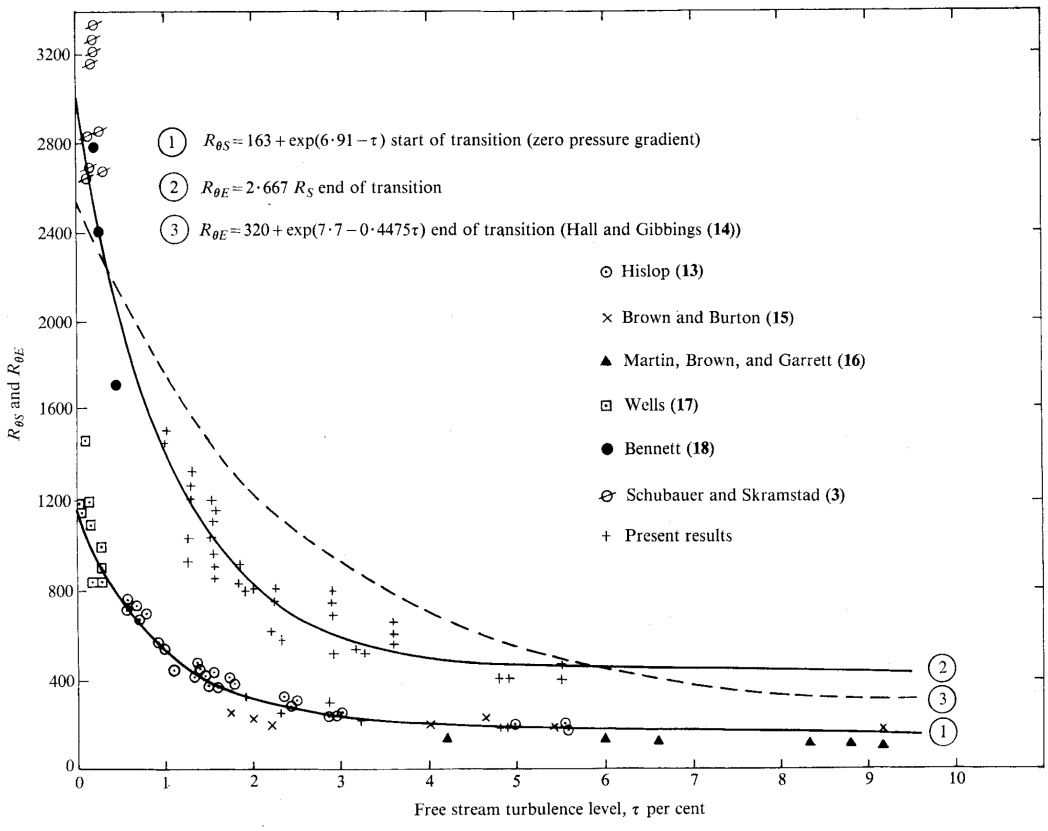

Figure 1.6: Variation of momentum thickness Reynolds number with freestream turbulence intensity, at start and end of transition on a flat plate at zero pressure gradient (reproduced from [1])

Streamwise Pressure Gradient

An adverse pressure gradient ($dP/dx > 0$) in the streamwise direction creates an inflection point in boundary layer profiles. Based on linear stability theory, this is a destabilizing effect and therefore, causes the transition onset location to move upstream. Conversely, a favorable pressure gradient ($dP/dx < 0$) has a stabilizing effect and delays transition onset. This trend is shown in Fig. 1.7, through the dependence of $Re_{\theta t}$ on a pressure gradient parameter, λ_θ, defined by Eq. 1.4

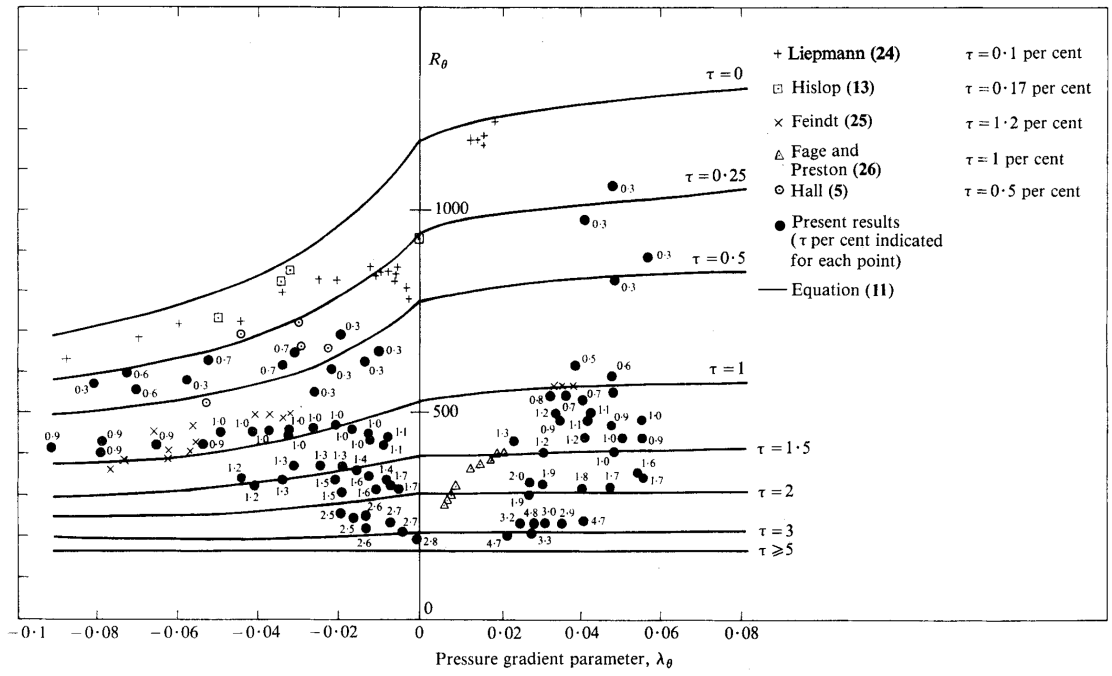

Figure 1.7: Effect of pressure gradient on transition onset on a flat plate (reproduced from [1])

$$\lambda_\theta = \frac{\theta^2}{\nu}\frac{dU_\infty}{dx} \tag{1.4}$$

A negative value of λ_θ is indicative of a boundary layer experiencing an adverse pressure gradient, and vice versa. The Abu-Ghannam and Shaw correlation [1] for $Re_{\theta t}$ at the start of transition, as a combined function of local pressure gradient parameter and freestream turbulence intensity, is given by Eq. 3.30–1.7.

$$Re_{\theta t} = 163.0 + \exp\left\{F(\lambda_\theta) - \frac{F(\lambda_\theta)}{6.91}Tu\right\} \tag{1.5}$$

$$F(\lambda_\theta) = 6.91 + 12.75\lambda_\theta + 63.64(\lambda_\theta)^2) \text{ for } \lambda_\theta < 0 \tag{1.6}$$

$$F(\lambda_\theta) = 6.91 + 2.48\lambda_\theta - 12.27(\lambda_\theta)^2) \text{ for } \lambda_\theta > 0 \tag{1.7}$$

Experimental data in Fig. 1.7 indicate that the effect of adverse pressure gradient on accelerating transition process is stronger than the effect of favorable pressure gradient on delaying it. In addition, the effect of pressure gradient decreases with increasing freestream turbulence intensity, as transition is dominated by bypass mechanisms at higher turbulence levels. The data in Fig. 1.7 corresponds to a constant pressure gradient value along the flat plate. However, in practical scenarios such as flow past an airfoil, pressure gradient is often varying along the streamwise direction and the pressure gradient history becomes an important factor. Flat plate experiments with decreasing streamwise adverse and favorable pressure gradients [1] showed that the transition onset location is significantly altered compared to a constant pressure gradient value. Therefore, it is important to account for history effects of pressure gradient in numerical transition onset prediction.

Separation-induced Transition

When a laminar boundary layer experiences a strong adverse pressure gradient, it often separates and may reattach as a turbulent boundary layer due to enhanced mixing in the separation bubble (Fig. 1.8). This process is called separation-induced transition, and is often seen downstream of the suction peak on airfoils. Pressure and streamwise velocity remain constant over the length of the bubble. At low Reynolds numbers on airfoils, laminar-separation bubbles can form over a large portion of the chord (up to 50%), and result in significantly increased viscous drag. If the adverse pressure gradient is too strong, the bubble may not reattach, and this phenomenon is called bubble-bursting.

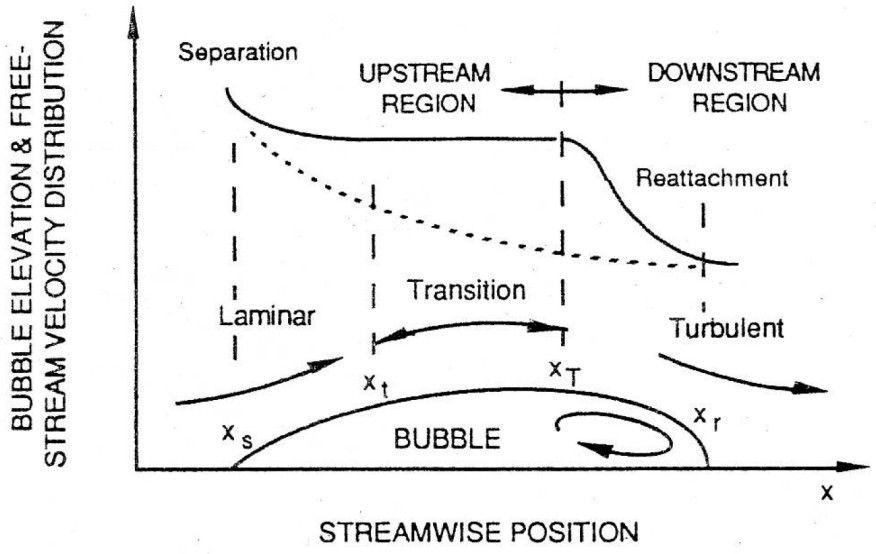

Figure 1.8: Laminar separation bubble formation due to strong adverse pressure gradient (reproduced from [6])

Streamwise Surface Curvature

A boundary layer on a surface with streamwise concave curvature experiences an instability due to centrifugal pressure gradient, producing a three-dimensional system of alternating streamwise vortices. This instability was studied by Gortler [26] and is defined by a critical value of a non-dimensional parameter known as the Gortler number, given by Eq. 1.8

$$G = \frac{U_e \theta}{\nu} \left(\frac{\theta}{R} \right)^{1/2} \tag{1.8}$$

where, U_e is the boundary layer edge velocity, R is the radius of curvature of the wall, ν is the dynamic viscosity, and θ is the momentum thickness. Gortler vortices appear when the value of G exceeds 1.2, and are amplified with increasing downstream distance [2].

Leading-edge Sweep

On swept surfaces or rotating discs, a three-dimensional crossflow instability occurs in regions of non-zero pressure gradient and results in transition to turbulence [27]. Crossflow transition can occur rapidly on swept wings even before the streamwise Tollmien-Schlichting waves are amplified and cause breakdown. Figure 1.9 shows a schematic of streamlines and velocity profiles in a typical 3-D boundary layer on a swept wing. Inside the boundary layer, the streamwise velocity is reduced, but the pressure gradient is unchanged. Thus, the balance between centripetal acceleration and pressure gradient does not exist. This imbalance results

in a secondary flow in the boundary layer, called crossflow, that is perpendicular to the direction of the inviscid streamline. Because the crossflow velocity must vanish at the wall and at the edge of the boundary layer, an inflection point exists and provides a source of an inviscid instability. The instability appears as co-rotating vortices whose axes are aligned to within a few degrees of the local inviscid streamlines. At low freestream turbulence levels, the dominant crossflow wave is stationary while moderate to high turbulence levels initiate dominant traveling waves [28].

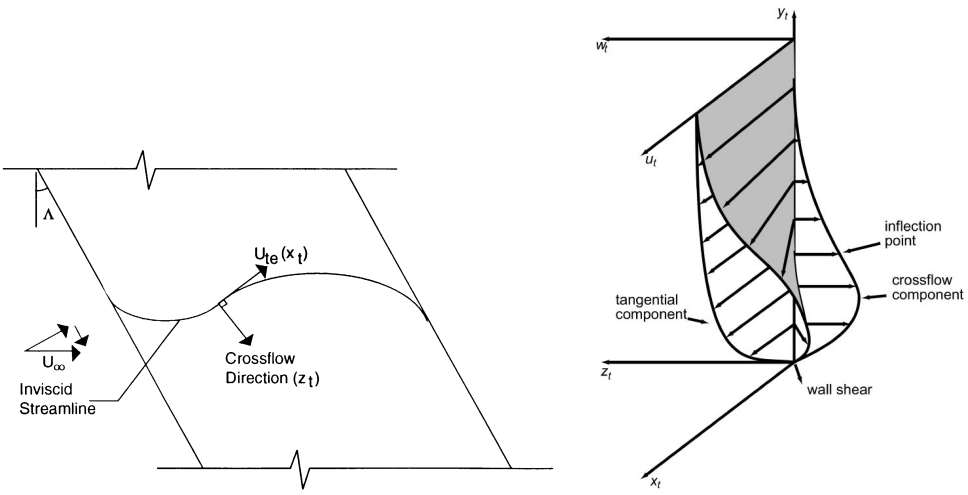

(a) Curved inviscid streamlines on a swept wing (b) Crossflow velocity profile

Figure 1.9: Crossflow transition on swept wings (reproduced from [27])

Surface Roughness

The presence of two-dimensional roughness, such as a trip wire placed normal to the freestream, accelerates transition onset due to the disturbances in the separated flow behind the roughness element. Upstream movement of transition onset location due to 2-D roughness is *gradual*. However, the effect of three-dimensional

roughness elements such as a sphere, on transition onset, is quite complex [4]. Transition location movement is more abrupt in the presence of 3-D roughness. Experimental studies [29, 30] have also shown that discrete 3-D roughness elements can be used to delay crossflow transition. In this approach, a stationary crossflow disturbance is forced with subcritical roughness spacing, that is, the spacing between roughness elements is less than the wavelength of the unstable mode [28]. Under these conditions, the rapid growth of the forced mode completely suppresses the linearly most unstable mode, thereby delaying transition beyond its *natural* location (i.e. where transition occurs in the absence of artificial roughness). These data demonstrate that surface roughness can be used to control the stationary crossflow disturbance wavenumber spectrum in order to delay transition on swept wings.

Compressibility and High Speed Transition

Increased aerodynamic heating and drag due to high-speed transition are critically important to design and operation of supersonic and hypersonic vehicle. The transition process is further complicated at supersonic and hypersonic Mach numbers due to the presence of shock waves, surface irregularities, and chemical nonequilibrium effects [31]. Attempts have been made to study stability and transition of compressible boundary layers through linear stability analysis [32].

1.5 Challenges in Laminar-Turbulent Transition Modeling

The primary goal of transition modeling research is to predict transition onset and relaminarization in boundary layers using inexpensive numerical models based on theory, experiments, and empiricism. Despite the tremendous progress made in theory and experiments, the richness and complexity of transition-related phenomena present several challenges to translating that knowledge into prediction capability. Progress of transition modeling also suffers from the lack of high quality DNS and experimental studies that are carefully planned to provide modelers with flow field information required to come up with new correlations. Consequently, much of the success in transition modeling has come through a combination of theory and empiricism. Since it may not be feasible to develop a universal transition model that predicts all possible transition mechanisms, the traditional approach to transition modeling has been to develop models that can predict individual transition mechanisms as a function of the various influencing factors such as freestream turbulence, pressure gradients, sweep angle, surface curvature, and roughness.

Reliable methods such as the e^N model based on linear stability theory, and the correlation-based transport equation approach have been developed to predict certain types of transition, and are being successfully used in industrial CFD simulations. However, many of the existing transition models are unsuitable for use in industrial applications with complex geometries due to their dependence on boundary layer quantities such as edge velocity, momentum thickness, streamline distance from stagnation point, etc. Evaluation of these parameters involves non-local opera-

tions such as integration or searching along streamlines and wall-normal directions. These operations may not be suitable for unstructured or mixed-element grids that are commonplace in industrial CFD simulations. There are two primary reasons for the dependence of early transition prediction methods on boundary layer quantities: (1) lack of sophisticated experimental methods to measure flow quantities inside the boundary layer, and (2) use of boundary layer codes that solve parabolized Navier-Stokes equations. Parameters such as displacement thickness or shape factor are readily available in boundary layer codes. Langtry [6] summarizes the requirements of transition modeling tools to handle the complex geometries and unsteady flow scenarios often encountered in industrial applications. Some of the requirements for a good transition model include: 1) ability to predict multiple modes of 2-D and 3-D transition, 2) computational affordability and 3) compatibility with both structured and unstructured Navier-Stokes CFD codes by avoiding search and integration operations. Langtry and Menter [33] developed a correlation-based transport model for the two-equation k-ω Shear Stress Transport (SST) turbulence model [34], called the $\gamma - Re_\theta$ transition model, with the aim of addressing many of the current issues. With modern experimental and numerical methods, extraction of high-resolution flow field data is being made possible and transitional boundary layers are being characterized more accurately. It is expected that these technological advances will lead to improved transition modeling methods that satisfy the requirements of industrial CFD simulations.

1.6 Objectives

The discussion in this chapter highlights the need for transition onset prediction and outlines the challenges of developing a prediction tool with the desired capabilities. In particular, methods applicable to structured and unstructured grid topologies that are readily compatible with current Navier-Stokes solvers are few in number. The $\gamma - Re_\theta$ transition model of Langtry and Menter [33] is currently the most successful approach due to its careful and elegant formulation that avoids non-local operations and predicts multiple modes of transition through simple correlations. Due to the robustness and reliability of the one-equation Spalart-Allmaras (SA) turbulence model for external flow applications [35], its lower computational cost compared to the k-ω SST model, and its Delayed-Detached Eddy Simulation (DDES) extension for massively separated flow simulations, it is highly desirable to have a similarly capable transition model that is compatible with the SA model. The primary objective of this thesis is to reformulate the $\gamma - Re_\theta$ model and integrate it with the SA model to investigate the effect of transition modeling on performance of rotorcraft and wind turbine applications. To achieve this, the original transition model equations are reformulated with modified source terms to improve robustness and accuracy. The modified model is validated against experimental data for several two-dimensional airfoil flows. The validated model is then used to study the effect of transition on rotating blade flows in axial flow conditions. The new transition model coupled with the SA model is named the $\gamma - Re_\theta -$ SA model.

1.7 Contributions of Thesis

Key contributions of this research are listed below:

1. Demonstrated inability of the one-equation Spalart-Allmaras turbulence model to accurately predict drag in partially laminar boundary layers

2. Developed a robust correlation-based laminar-turbulent transition prediction model for the Spalart-Allmaras turbulence model. The transition model is also formulated to be independent of the choice of the turbulence model.

3. Improved prediction of skin friction drag on external flows past lifting surfaces using the $\gamma - Re_\theta -$ SA transition model

4. Improved the understanding of transition onset phenomenon on rotating blades in axial flow conditions, and quantified the effects of transition on rotorcraft and wind turbine performance

5. Developed preliminary crossflow transition onset criterion for swept wings

6. Improved stall onset prediction by improving sensitivity of the Spalart-Allmaras turbulence model to strong adverse pressure gradients

1.8 Scope and Organization of Thesis

The present work is concerned with the prediction of laminar-turbulent transition of boundary layers on external aerodynamic surfaces. The newly developed transition model is capable of predicting two-dimensional transition due to non-zero

pressure gradients in low freestream turbulence environments. This thesis details the motivation for this research, previous efforts, overall approach, and application of the new model to various two-dimensional and three-dimensional flows. The rest of the thesis is organized as follows:

1. Chapter 2 presents a selective literature review of various transition prediction methods. Benefits and drawbacks of each transition model are highlighted.

2. Chapter 3 presents the formulation, calibration, and verification of the $\gamma - Re_\theta - \text{SA}$ transition model. Integration of the transition model with the underlying turbulence model is also discussed.

3. Chapter 4 provides details of the RANS-based computational methodology used in this work. Details of the various aspects of the methodology are presented, including governing equations, spatial and temporal discretization methods, grid topologies, boundary conditions, and overset mesh algorithms.

4. Chapter 5 presents results of several two-dimensional airfoil simulations with and without the transition model. This chapter demonstrates the accuracy of the new model as well as highlights the need to include transition effects in partially laminar boundary layers.

5. In Chapter 6, the $\gamma - Re_\theta - \text{SA}$ model is applied to three-dimensional rotorcraft and wind turbine configurations. Results and analysis include predicted transition onset locations on rotor blades under various flow conditions, and

comparison of rotor thrust and torque obtained with and without the transition model.

6. Chapter 7 summarizes key results and conclusions from this work, and provides recommendations for future work.

7. Appendix A presents the details of a new crossflow transition onset criterion with some preliminary results for a swept wing and a helicopter rotor in hover.

8. Appendix B presents the details of an empirical correction to the Spalart-Allmaras turbulence model for strong adverse pressure gradient flows to improve stall prediction on airfoils.

2 Progress in Transition Modeling

A complete transition model needs to predict the following two parameters in a boundary layer: (1) onset location of transition and relaminarization, and (2) extent of transition zone. Transition prediction methods can be categorized into groups based on various attributes: (1) models based on hydrodynamic stability theory versus models based on empirical correlations, (2) models that can predict onset versus models that can prediction extent versus models that can do both, (3) algebraic models versus linear-combination models versus transport-equation based models. Many transition models have one or more of these attributes. Recent articles by Pasquale [36] and Sveningsson [37] provide a comprehensive review of various transition modeling methods for practical applications.

2.1 Transition Prediction in Modern CFD Solvers

There are many ways in which various transition models can be integrated into a full Navier-Stokes (N-S) solver. Some of them are summarized below [38]:

1. Direct coupling of a N-S solver with a stability code – laminar mean flow profiles are obtained from a highly resolved flow field from a N-S solver. The

stability code computes exact growth rates using mean flow profiles. Mean flow resolution and exact stability computations can be quite expensive.

2. Coupling of a N-S solver with a boundary layer code and a database for growth rates – the boundary layer code computes the mean flow profiles on a high-resolution grid. Disturbance growth rates are obtained from a look-up database or analytical relationships based on exact stability computations for self-similar mean velocity profiles in non-zero pressure gradients (Falkner-Skan profiles in 2-D incompressible flows).

3. Direct implementation of simple algebraic transition onset criteria into baseline turbulence models.

4. Multiplying eddy viscosity obtained from baseline turbulence models with an intermittency function obtained using empirical correlations with or without solving additional transport equations.

5. Multiplying source terms of baseline turbulence models with an intermittency function that is obtained from solving additional transport equations.

Besides the use of database look-up in methods such as e^N, many transition models rely upon quantities such as boundary layer edge velocity, boundary layer thickness, displacement thickness, momentum thickness, and inviscid streamline radius of curvature. These quantities involve non-local operations such as integration and searching along streamlines or wall-normal direction. Most of these methods are suitable for implementation into boundary layer codes, since these quantities are

readily available when solving the boundary layer equations. However, automatic transition prediction using modern RANS/LES-based flow solvers is extremely desirable in the aerospace industry. Non-local operations and database look-up methods are not suitable and efficient, and sometimes impossible to use in massively parallel unstructured CFD codes and complex geometries such as turbomachinery. Requirements for a transition model that is fully compatible with modern CFD codes are summarized by Langtry [6]:

1. Allow calibrated prediction of transition onset and length
2. Predict various 2-D and 3-D transition mechanisms
3. Transition criteria based only on local flow field variables (without integration or searching), and applicable to structured and unstructured grid topologies
4. Retain behavior of baseline turbulence model in fully turbulent regions
5. Robust numerical convergence properties similar to underlying turbulence model, and allowing integration down to the wall boundary.

2.2 Direct Numerical Simulation (DNS) and Large Eddy Simulation (LES)

Although DNS and LES methods are currently impractical for routine use in industrial applications due to large computational times, they play a crucial role in uncovering transition mechanisms that can be used to develop lower-fidelity transition prediction methods. Besides the computational expense, these simulations also

need to address the issue of inflow turbulence content specification. DNS simulations are performed by solving the full unsteady Navier-Stokes equations without any filtering or Reynolds-averaging operations with the objective of resolving the full range of length and time scales using an extremely fine computational grid. DNS simulations of bypass transition by Jacobs and Durbin [39] obtained new perspectives from numerical flow fields. It was the first approach to construct turbulent inflow from Orr-Sommerfeld continuous modes. Approximately 70 million grids points were used in this DNS study. Simulations showed that transition precursors consist of long backward jets contained in the fluctuating u-velocity field, i.e. they flow backwards relative to the local mean velocity. These jets extend into the outer portion of the boundary layer and interact with freestream eddies, resulting in turbulent spot formation. The turbulent spots spread longitudinally and laterally and ultimately merge into the downstream turbulent boundary layer. Formation of streaks, spots, and transition to turbulence phenomenon is visualized by u- and v-component fluctuations in Fig. 2.1. Wu and Moin [40] performed DNS on a zero pressure gradient flat plate for a momentum thickness Reynolds number (Re_θ) range of 80 to 940. Grid sizes of 100 million and 200 million points were used in this study. Transition was completed at approximately $\mathrm{Re}_\theta = 750$ due to intermittent localized disturbances arising from patches of isotropic turbulence introduced periodically from the freestream at $\mathrm{Re}_\theta = 80$. This study showed the first direct evidence of the dominance of hairpin vortices in a spatially developing flat plate boundary layer shown in Fig. 2.3 (in the form of a *solution* to the Navier-Stokes equations, obeying the statistical measurements, as opposed to synthetic superposition of the structures).

DNS predictions of instantaneous and mean skin friction profiles on a transitional flat plate boundary layer shown in Fig. 2.2 indicate elevated levels of skin friction in the turbulent spot region [39, 40]. Wissink [41] performed DNS of separation-induced transition on a flat plate with adverse pressure gradient at Re = 60,000. These simulations used grids ranging from 30 million to 500 million points. Numerical round-off errors were found to be responsible for triggering Kelvin-Helmholtz instability leading to the roll-up of the separated boundary layer, followed by rapid transition to turbulence. Addition of uniform external disturbances was found to reduce the size of the separation bubble. When the uniform external disturbances were replaced by fluctuations of a periodically passing wake, the location of transition was found to move upstream and downstream alternately. Figure 2.4 shows a snapshot of boundary layer separation due to impinging wakes in this DNS study.

The Large Eddy Simulation (LES) approach solves filtered Navier-Stokes equations to resolve large scale eddies and uses a sub-grid scale eddy viscosity model to account for energy in smaller scales [45]. Applicability of LES models for transition prediction was recently studied by Schlatter [46]. Their simulations investigated how well sub-grid scale (SGS) models on coarse grids are able to predict the various physical mechanisms of transition such as Λ-vortices, roll-up of shear layers, and hairpin vortices using coarse grids. It was found that the dynamic Smagorisnky model [47] when used on coarse grids, does not capture the initial stages of breakdown such as the formation of hairpin vortices. Flow visualization of natural transition in a plane channel flow obtained from LES simulations of Schlatter [42] is shown in Fig.

2.5. The various stages of natural transition are clearly seen in this figure: 2-D T-S waves, spanwise vorticity, 3-D breakdown, turbulent spots, and fully turbulent flow. In early LES simulations of transitional boundary layers, transition onset location is sensitive to the choice of Smagorinsky constant of the SGS model [6]. Michelassi [43] performed LES simulations of a low-pressure turbine blade with periodically impinging wakes. Although good qualitative agreement of skin friction profile was seen between LES and DNS predictions, the LES transition onset location was predicted about 10% of chord length downstream of the DNS prediction, as seen in Fig. 2.6.

More recently, Bodart and Larsson [44] developed a robust sensor-based transition prediction technique using wall-modeled LES (WMSLES). The sensor is defined for arbitrary geometries and is based on spatially local turbulent kinetic energy. It is used to activate the wall-model only when the boundary layer is detected to be turbulent. This approach was successfully used to predict transition in boundary layers on a flat plate as well as a multi-element MD 30P/30N airfoil. The multi-element airfoil case was simulated at a Reynolds number of 9 million and used a grid with 74 million control volumes. Figure 2.7 shows skin friction prediction obtained using WMSLES from this study. The difference between the predicted and the experimental data does not exceed 2% and remains within experimental uncertainty. This approach brings high-fidelity methods such as WMLES closer to transition prediction in practical applications.

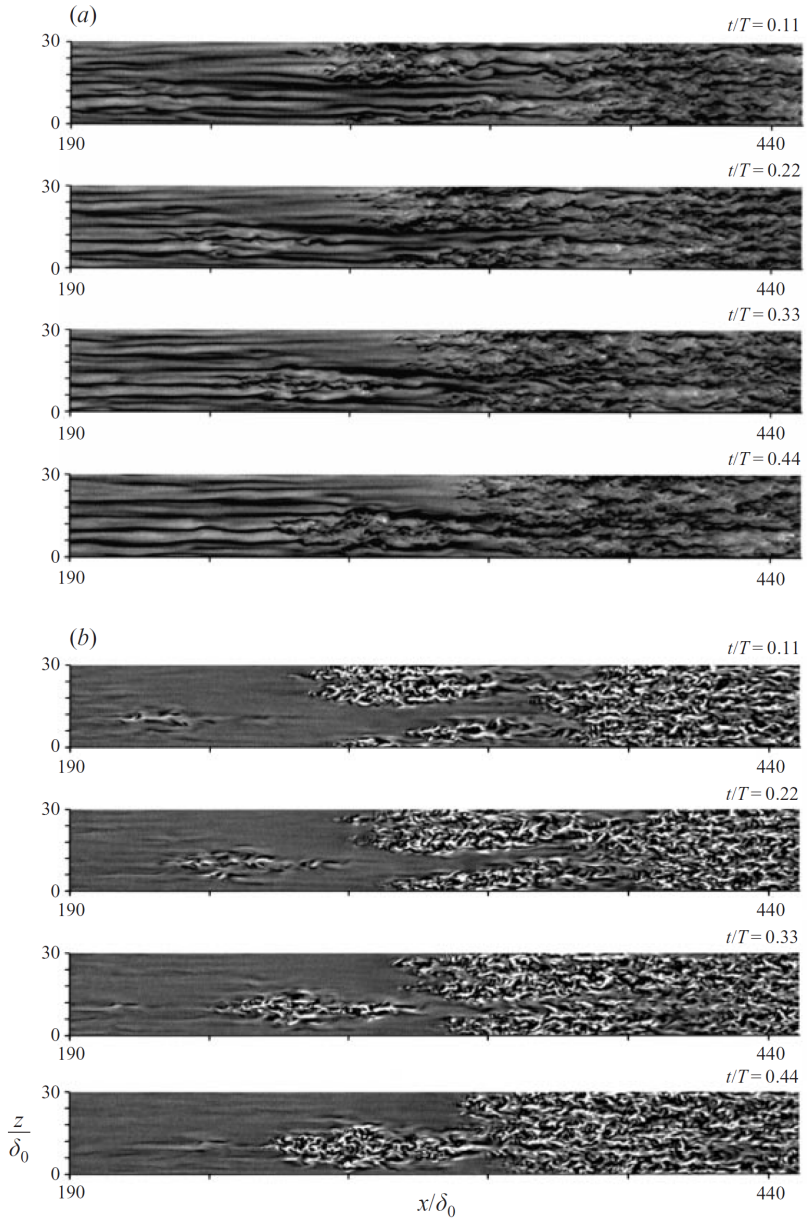

Figure 2.1: (a) u-component and (b) v-component of fluctuations showing streaks, spots, and transition of boundary layer beneath freestream turbulence(reproduced from DNS study [39])

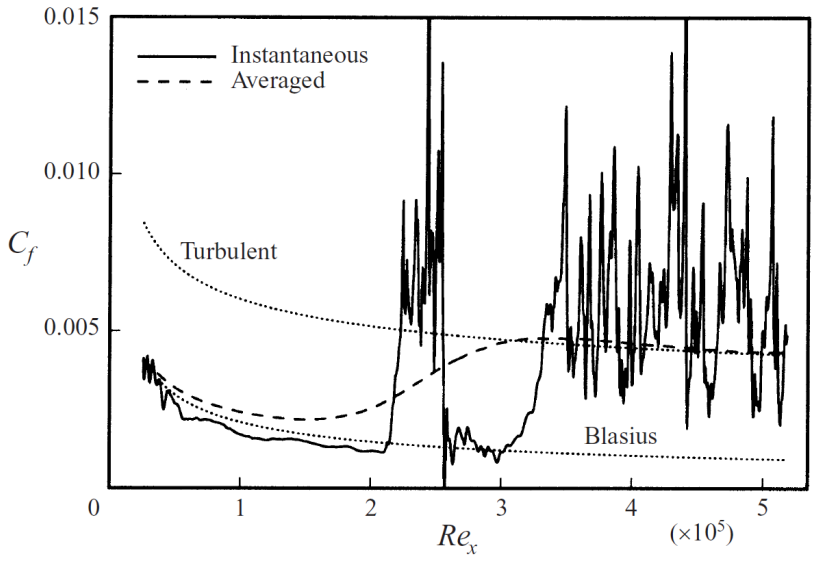

(a) DNS study of Jacobs and Durbin [39]

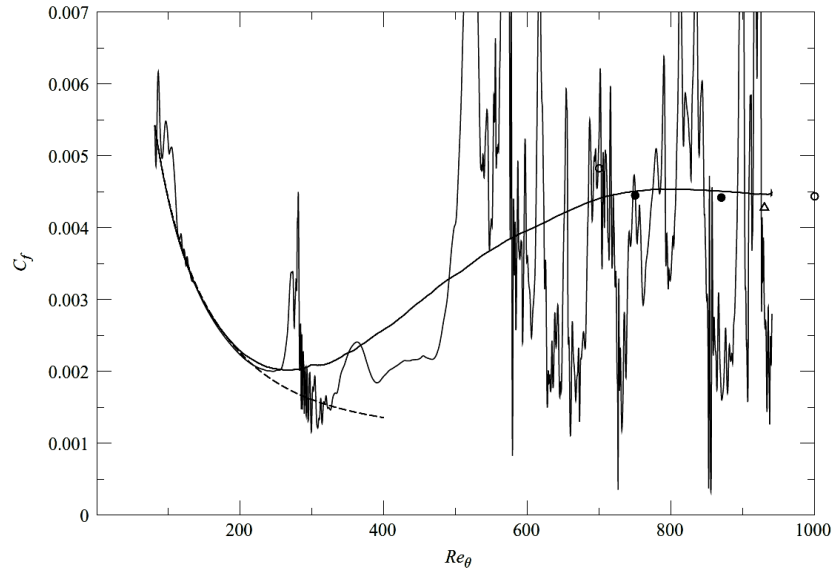

(b) DNS study of Wu and Moin (light solid line - instantaneous, Dark solid line - mean) [40]

Figure 2.2: Instantaneous and mean skin friction predictions from DNS studies showing elevated levels inside a turbulent spot (reproduced from [39, 40])

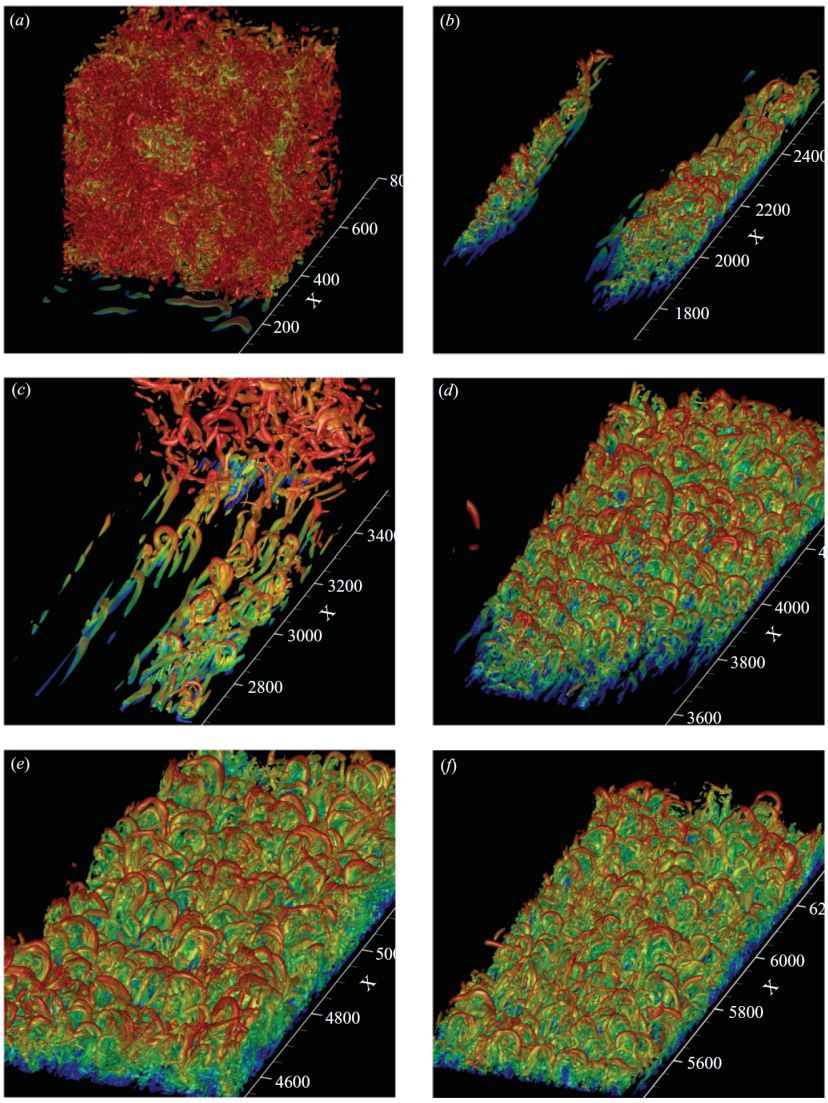

Figure 2.3: Iso-surfaces of second invariant of velocity gradient tensor colored by local values of u showing hairpin structures; (a) to (f) are different streamwise zones (reproduced from DNS study of [40])

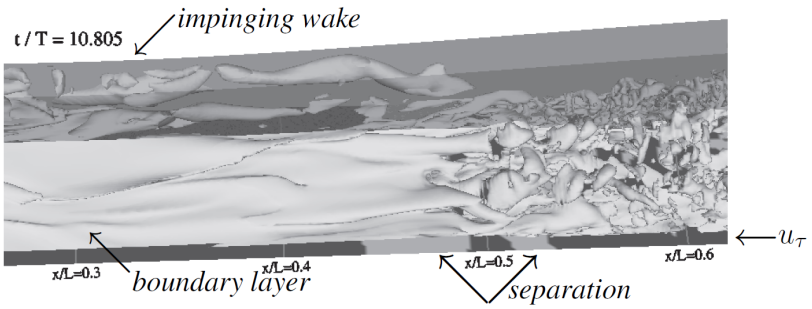

Figure 2.4: Snapshot of iso-surface of spanwise vorticity (= -150) identifying impinging wake and boundary layer separation (reproduced from DNS study of [41])

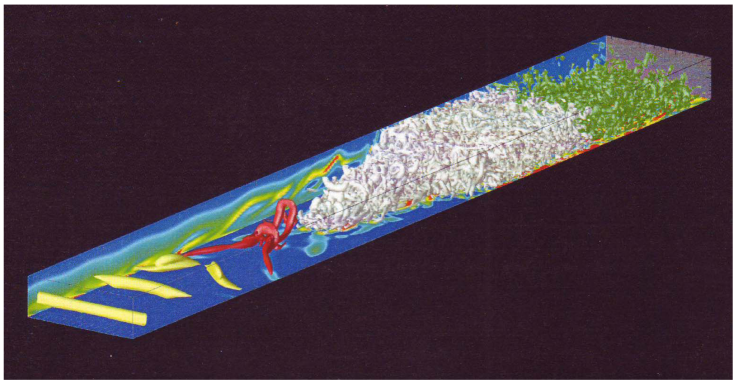

Figure 2.5: Stages of natural transition in plane channel flow (reproduced from LES study of [42])

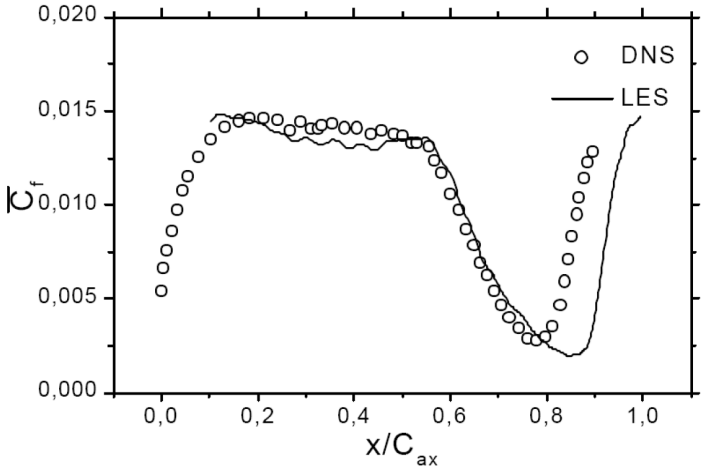

Figure 2.6: Time-averaged skin friction on the suction side of a low-pressure turbine blade subject to periodic impinging wakes (reproduced from LES study of [43])

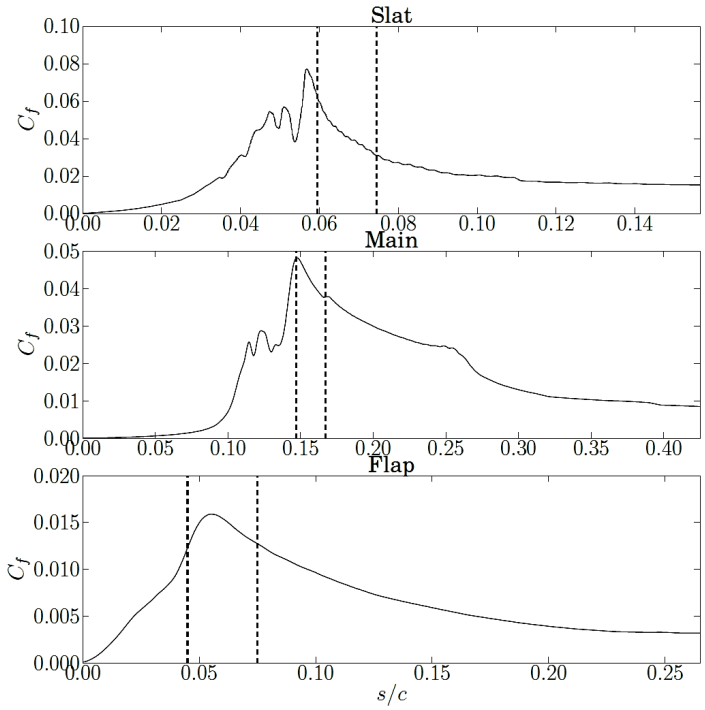

Figure 2.7: Skin friction predictions on MD 30P/30N multi-element airfoil; dashed lines indicate beginning and end of transition region from experimental data (reproduced from WMSLES study of [44])

2.3 Models based on Hydrodynamic Stability Theory

Reed and Saric [48] review linear stability theory applied to boundary layer transition prediction. The basic idea behind linear stability theory is to superpose small disturbances onto the local, undisturbed boundary-layer state (termed as the "basic state") and determine whether these perturbations grow or decay. The boundary layer is considered stable if all perturbations decay. Linear stability analysis is performed by locally linearizing the complete unsteady Navier-Stokes equations about the basic flow state which is assumed to be locally parallel to the wall surface. The Orr-Sommerfeld stability equations are obtained by substituting stream function representation of a two-dimensional, single frequency disturbance as given below:

$$\psi(x, y, t) = \phi(y) e^{i(\alpha x - \omega t)} \tag{2.1}$$

where, $\phi(y)$ is an amplitude function, y is normal to the wall, α is a complex wavenumber in the x-direction, and ω is real and represents the wave frequency. If the disturbance amplitude grows spatially, then the boundary layer is unstable and transition to turbulence occurs. This happens when the sign of the imaginary part of α is negative.

The e^N method based on linear stability theory is one of the most widely used methods to predict natural transition in boundary layers at relatively low freestream turbulence levels. It was independently and simultaneously proposed by Smith and Gamberoni, and Van Ingen [49, 50]. A recent article by Van Ingen [51] presents a historical review of the e^N method and its variations during the past 50

years. It is applicable to both 2-D and 3-D boundary layers with non-zero pressure gradients and laminar separation bubbles. This makes it suitable for transition prediction on isolated airfoils. Variations of the method are also capable of predicting crossflow transition onset in 3-D boundary layers. Design and analysis codes such as XFOIL [52], MISES [53], and XFLR5 [54] use the e^N method for transition prediction on airfoils and model aircraft wings. The e^N method is based on an eigenvalue analysis of the Orr-Sommerfeld equations for viscous parallel flow, which is not the case in realistic boundary layers. The linear Parabolized Stability Equations (PSE) method [55] was developed to address the non-parallel effects neglected in linear stability theory. Since the baseline e^N method is based on a small disturbance assumption, it cannot be used to predict non-linear mechanisms such as bypass transition and roughness-induced transition. The non-linear PSE method further extends the linear PSE method by including non-linear growth effects.

Implementation of stability theory based methods involves three steps: (1) compute laminar velocity and temperature profiles at different streamwise stations, (2) compute local amplification rates of the most unstable waves for each profile by solving local linear stability equations or the Parabolized Stability Equations (PSE), and (3) integrate local amplification rates along each streamline to obtain the N factor. Transition is considered to occur when the value of N crosses a threshold, which is a function of freestream turbulence intensity. Typical values of N vary between 7 and 9. In its original form, the e^N method needs integration of flow quantities along streamlines, making it unsuitable for complex three-dimensional flow configurations often encountered in industrial applications. However, recent work of

Krumbein [56, 57] developed a hybrid framework that couples a RANS solver, a boundary-layer code, and a fully automated local, linear stability code that is capable of predicting transition due to Tollmien-Schlichting and crossflow instabilities on complex aircraft configurations. Two separate N-factors are computed, one for Tollmien-Schlichting disturbances (N_{TS}) and one for crossflow disturbances (N_{CF}). It uses a database look-up approach to estimate growth rates for different velocity profiles computed in advance using exact solutions to the linearized equations.

2.4 Correlation-based Models

Correlation-based models discussed below are divided into three groups based on whether they can predict transition onset or transition extent or both.

2.4.1 Transition Onset Prediction Models

Since transition onset can be triggered due to a multitude of factors and mechanisms, the most practical means of transition prediction is to employ separate empirical correlations (based on theory and experiment) for each mode of transition. Transition onset location is typically specified in terms of the local momentum thickness Reynolds number ($Re_{\theta t}$) as a function various flow parameters such as freestream turbulence level, pressure gradient or acceleration parameter, surface curvature, displacement thickness, etc. Some of the popular correlations for 2-D and 3-D transition onset are listed below.

Abu Ghannam and Shaw Correlation [**1**]: Streamwise transition onset as

a function of freestream turbulence intensity (Tu) and pressure gradient parameter (λ_θ, also known as the Pohlhausen parameter).

$$Re_{\theta t} = 163.0 + \exp\left\{F(\lambda_\theta) - \frac{F(\lambda_\theta)}{6.91}Tu\right\} \tag{2.2}$$

$$F(\lambda_\theta) = \begin{cases} 6.91 + 12.75\lambda_\theta + 63.64(\lambda_\theta)^2, & \lambda_\theta \leq 0 \\ 6.91 + 2.48\lambda_\theta - 12.27(\lambda_\theta)^2, & \lambda_\theta > 0 \end{cases} \tag{2.3}$$

$$\lambda_\theta = \frac{\rho\theta^2}{\mu}\frac{dU_e}{ds} \tag{2.4}$$

Mayle's Correlation [25]: Streamwise transition onset as a function of freestream turbulence intensity (Tu)

$$Re_{\theta t,\text{Mayle}} = 400.0\ Tu^{-5/8} \tag{2.5}$$

AHD Criterion [58]: Streamwise transition onset for freestream turbulence intensity (Tu) $< 0.1\%$.

$$Re_{\theta CR} = \exp\left[\frac{E}{H_i} - F\right] \tag{2.6}$$

where, H_i is the incompressible shape factor. The distance from stagnation point to the first point where $Re_\theta = Re_{\theta CR}$ is s_{CR}.

$$\overline{\lambda_\theta} = \frac{1}{s - s_{CR}}\int_{s_{CR}}^{s} \lambda_\theta ds \tag{2.7}$$

$$Re_{\theta TR} = Re_{\theta CR} + \text{A.exp}(B\overline{\lambda_\theta})\left[\ln(C.Tu) - D.\overline{\lambda_\theta}\right] \tag{2.8}$$

The coefficients A–F are functions of freestream Mach number given below [58]:

A = 98.64 M_e^3 - 356.44 M_e^2 + 117.13M_e - 236.69

B = -13.04 M_e^4 + 38.5 M_e^3 - 30.07 M_e^2 + 10.89 M_e + 22.7

C = 0.21 M_e^3 + 4.79 M_e^2 - 1.76 M_e + 22.56

D = -3.84 M_e^4 + 6.26 M_e^3 - 3.45 M_e^2 + 0.23 M_e + 12.0

E = 0.6711 M_e^3 - 0.7379 M_e^2 + 0.167 M_e + 51.904

F = 0.3016 M_e^5 - 0.7061 M_e^4 + 0.3232 M_e^3 + 0.0083 M_e^2 - 0.1745 M_e + 14.6

C1 Criterion [59]: Crossflow transition onset in terms of critical crossflow displacement thickness Reynolds number ($Re_{\delta 2t}$).

$$Re_{\delta 2t} = 150.0, \quad \text{if } H_i < 2.3 \quad \text{and} \tag{2.9}$$

$$Re_{\delta 2t} = \frac{300}{\pi}\arctan\left[\frac{0.106}{(H_i - 2.3)^2 .05}\right], \quad \text{if } 2.3 \leq H_i \leq 2.7 \tag{2.10}$$

where, δ_2 is the boundary layer displacement thickness.

$$Re_{\delta_2} = \frac{U_e \delta_2}{\nu\,(1 + 0.2M_e^2)}; \qquad \delta_2 = -\int_0^\delta \frac{w}{U_e} dy \tag{2.11}$$

Kohama Parameter [60]: Crossflow transition onset as a function of momentum thickness (θ), and inviscid streamline radius of curvature parallel to wall (R).

$$C_k = \frac{U_e \theta}{\nu}\sqrt{\frac{\theta}{R}} \tag{2.12}$$

Critical value of C_k for a rotating disk is 5.0 and a yawed cylinder is 2.8.

2.4.2 Transition Extent Prediction Models

Most of the transition length prediction models use the concept of intermittency (γ) to control the value of eddy viscosity (μ_t) in the flow field. In such models, total viscosity is defined as the sum of the molecular viscosity (μ) and the intermittency-weighted eddy viscosity as given below:

$$\mu_{\text{total}} = \mu + \gamma \mu_t \tag{2.13}$$

Dhawan and Narasimha [17]: Dhawan and Narasimha observed that the scalar intermittency function (γ) provides a measure of progression towards a fully turbulent boundary layer. Based on measured streamwise intermittency distributions on flat plate boundary layers, they proposed the following expression for streamwise intermittency profile:

$$\gamma = \begin{cases} 0, & x < x_t \\ 1.0 - \exp\left[-\dfrac{(x-x_t)^2 n\sigma}{U}\right] = 1.0 - \exp(-0.41\xi^2), & x_t \geq x \end{cases} \tag{2.14}$$

where, x_t is the transition onset location, n is the spot formation rate (per unit time, per unit distance in the spanwise direction), σ is a spot propagation parameter (= 0.25), U is the freestream velocity, and

$$\xi = \frac{x - x_t}{\lambda} \tag{2.15}$$

is a non-dimensional variable using the distance λ between the stations where γ = 0.25 and 0.75 to characterize the extent of the transition zone.

Dey and Narasimha Model [61]: This model was developed based on the concept that a transitional boundary layer is a linear combination of laminar and turbulent flow fields weighted by the intermittency function of Dhawan and Narasimha (Eq. 2.14). In this approach, a complete laminar flow solution is obtained first, followed by a turbulent solution. In the fully turbulent simulation, the turbulence model is activated at the transition specified transition onset location. The two solutions are then linearly combined in the ratio of (1-γ) to γ. The mean velocity (U) and skin friction (C_f) profiles are computed as shown below:

$$U = (1-\gamma)U_L + \gamma U_T \tag{2.16}$$

$$C_f = (1-\gamma)C_{fL} + \gamma C_{fT} \tag{2.17}$$

The subscripts L and T represent laminar and turbulent solutions respectively. Using this approach, the transition extent was typically under-predicted and heat transfer at the end of transition region was over-predicted.

Cho and Chung Model [62]: Cho and Chung developed a k–ϵ–γ turbulence model for free shear flows. Intermittency was computed using a transport equation and eddy viscosity was represented as a function of k, ϵ, and γ. The model was tested for a plane jet, a round jet, a plane far wake, and a mixing layer.

Steelant and Dick Model [63]: Steelant and Dick proposed a transport equation for intermittency in which the source term of the equation is designed to reproduce the γ distribution of Dhawan and Narasimha [17]. The intermittency transport equation was derived by differentiating the intermittency distribution of Dhawan and Narasimha along the streamline direction s, and was solved in conjunction with conditioned Navier-Stokes equations. The production term of the intermittency equation used a variation of the spot formation rate term from Dhawan and Narasimha's correlation (Eq. 2.14).

2.4.3 Transition Onset and Extent Prediction Models

Low Reynolds Number Models: Most of the low Reynolds number models [64,65] rely on the ability of wall damping functions to capture transition effects. In order to predict transition onset, they depend on the diffusion of turbulence from freestream into the boundary layer and its interaction with the turbulence model

source terms [6]. Therefore, they are more suited for bypass transition prediction [66]. However, their performance has been unreliable and unsatisfactory, and their limited success is coincidental due to the similarity between a developing laminar boundary layer and a viscous sublayer. They do not have proper sensitivity to strong adverse pressure gradients and separated shear layers. In addition, they suffer from convergence issues for separation-induced transition cases [6].

Warren and Hassan Model [67]: Warren and Hassan developed one of the first unified models to determine both transition onset and extent in a single formulation. It is capable of predicting both streamwise and crossflow transition mechanisms in 2-D and 3-D boundary layers. The model is based on the concept of non-turbulent fluctuations in a manner similar to that used in describing turbulence. The effective eddy viscosity (μ_e) is an intermittency-weighted sum of two contributions as shown below:

$$\mu_e = (1-\gamma)\mu_{nt} + \gamma\mu_t \tag{2.18}$$

where, γ is the intermittency function of Dhawan and Narasimha, μ_{nt} is the eddy viscosity due to non-turbulent fluctuations and μ_t is the eddy viscosity due to turbulent fluctuations. Non-turbulent fluctuation contribution can be computed using:

$$\mu_{nt} = 0.09\rho k\tau_{nt} \tag{2.19}$$

where, τ_{nt} is a non-turbulent time scale that is a function of the frequency of the first mode disturbance with the maximum amplification rate. To predict crossflow transition, a crossflow viscosity time scale that is a function of the wavelength of crossflow disturbances is used. This model was coupled to the two-equation k-ζ

turbulence model [68] and the one-equation Spalart-Allmaras turbulence model [35]. It was validated against experimental data for flat plates, airfoils, and infinite swept wings. It is not a fully local formulation due to its dependence on integral boundary layer quantities such as the boundary layer thickness and the displacement thickness.

Suzen and Huang Model [69]: Suzen and Huang developed an intermittency transport equation by blending the production terms of two previous transition models [62, 63]. Intermittency production was triggered at the point of transition onset which was determined using experimental correlations. The model successfully reproduces experimentally observed streamwise intermittency profiles and realistic cross-stream intermittency profiles in the transition zone. The intermittency factor thus obtained was used to scale the eddy viscosity field computed from the SST k-ω turbulence model. This model was successfully validated against several low-pressure turbine experiments. However, this model is not a fully local formulation since it uses freestream turbulence intensity, and therefore requires the boundary layer edge velocity.

Walters and Leylek Model [70, 71]: This model predicts natural and by-pass transition by solving a transport equation for "laminar kinetic energy". It is based on the understanding that high-amplitude streamwise fluctuations in the pre-transitional boundary layer are caused due to freestream turbulence and these fluctuations are very different from traditional turbulence fluctuations [25]. They are identified as "laminar kinetic energy" (k_L). Growth of k_L correlates with low-frequency wall-normal fluctuations of the freestream turbulence. The total kinetic energy is assumed to be the sum of the small-scale kinetic energy that contributes to

traditional turbulence production, and large-scale energy that contributes to laminar kinetic energy production. The transport equation for laminar kinetic energy (k_L) is solved in conjunction with equations for turbulent kinetic energy (k_T) and specific dissipation rate ($\omega = \epsilon/k_T$). This model uses a fully local formulation without needing integration or searching operations. It has been successfully validated for flat plates, airfoils, and turbine cascade flows. This approach is more promising compared to the other methods discussed above, and should be validated on a wider range of flow problems by more researchers.

Langtry and Menter Model [33]: The correlation-based $\gamma - Re_\theta$ model of Langtry and Menter is currently one of the most widely used transition models in industrial CFD applications. It was developed with the objective of satisfying all the criteria for a Navier-Stokes solver compatible model, listed at the beginning of this chapter. The model solves two additional transport equations for intermittency (γ) and transition momentum thickness Reynolds number ($Re_{\theta t}$), coupled with the SST k-ω turbulence model [34]. The primary reasons for the success of this model are its fully local formulation and its ability to predict natural, bypass, and separation-induced transition mechanisms using experimental correlations. It is applicable to both unstructured and structured grid topologies. It has been successfully applied to several internal and external flow applications including 2-D airfoils, 3-D fixed wings, airframes, rotor blades, and turbomachinery. Recently, Coder [72] replaced the equation for Re_θ with an equation for the amplification factor N from the e^N model using additional correlations.

In this model, transition onset and extent are predicted using a combination of

experimental and numerical correlations. Transition onset is triggered based on the *Vorticity Reynolds Number* criterion of Van Driest and Blumer [73] as given below:

$$Re_{\theta t} = \frac{\max(Re_v)}{2.193} \tag{2.20}$$

This equation states that transition onset occurs when the local momentum thickness Reynolds number (Re_θ) in a laminar boundary layer exceeds the maximum value of scaled vorticity Reynolds number (Re_v) profile at a given streamwise station. Vorticity Reynolds number is given by:

$$Re_v = \frac{\rho d^2 \Omega}{\mu} \tag{2.21}$$

where, ρ is the density, d is the nearest wall distance, Ω is the vorticity magnitude,

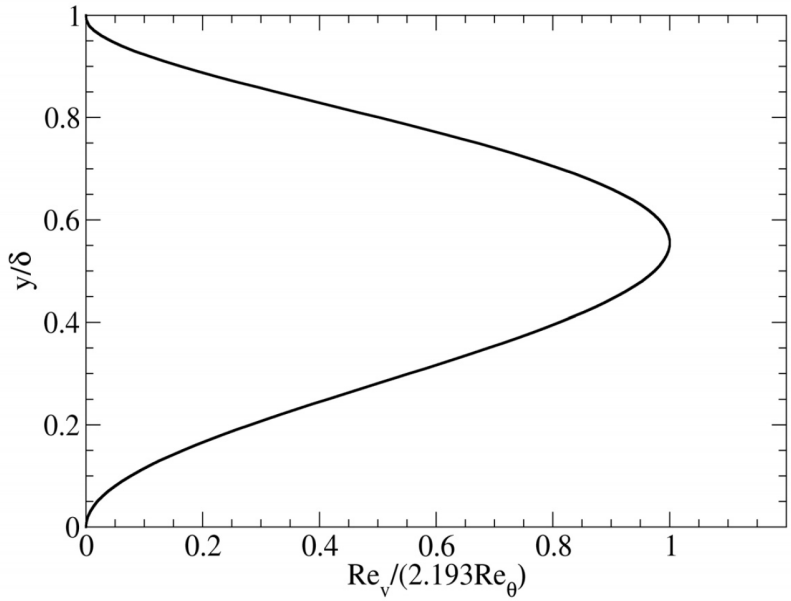

Figure 2.8: Schematic of scaled vorticity Reynolds number profile in a laminar boundary layer (reproduced from [6])

and μ is the laminar viscosity. All these quantities are readily available at every

grid point in most structured and unstructured CFD codes. The vorticity Reynolds number profile in a laminar boundary layer attains its maximum value at around 60% of the boundary layer thickness, as shown in Fig. 2.8. The critical value of Re_θ is obtained by solving a transport equation that uses experimental correlations for $\mathrm{Re}_{\theta t}$ as a function of freestream turbulence intensity and a local pressure gradient parameter. Solving a transport equation and using experimental correlations to obtain critical $\mathrm{Re}_{\theta t}$ avoids the need for the exact computation of local momentum thickness Reynolds number through numerical integration along the wall-normal direction. A second transport equation is solved for intermittency, whose production is controlled by the vorticity Reynolds number criterion. The intermittency field thus obtained is multiplied with the production and dissipation terms of the two-equation k-ω SST turbulence model [34].

Although complete details of the $\gamma - Re_\theta$ model are now available in the open literature [33], certain numerical correlations were not published in the original version of the model [6]. Therefore several follow-up efforts were focused on model calibration and validation [74–78]. Since the $\gamma - Re_\theta$ model is also the focus of the present work, a more detailed discussion of this model will be presented in Chapter 3 of this thesis.

2.5 Summary

This chapter summarized the history and state-of-the-art of laminar-turbulent transition modeling methods. The role of high-fidelity DNS and LES simulations to

further the understanding of transition mechanisms and aiding development of new low-fidelity models was discussed. The discussion included encouraging recent work in wall-modeled LES for transition modeling on multi-element airfoils. Difficulties in developing a comprehensive transition model that is compatible with modern CFD codes have been discussed. The correlation-based $\gamma - Re_\theta$ transition model of Langtry and Menter has been introduced and its benefits over the other models have been highlighted. The next chapter presents development of a modified version of the $\gamma - Re_\theta$ model that is compatible with the one-equation Spalart-Allmaras turbulence model.

3 Transition Model Development

This chapter details the formulation and calibration of a modified version of the $\gamma - Re_\theta$ transition model, and its integration with the one-equation Spalart-Allmaras turbulence model. The original $\gamma - Re_\theta$ transition model was developed for the two-equation k-ω SST turbulence model. It is currently the most widely used transition model in industrial applications due to its compatibility with both structured and unstructured RANS flow solvers. Due to the robustness and reliability of S-A model for external flow applications, its lower computational cost compared to the k-ω model, and its Delayed-Detached Eddy Simulation (DDES) extension for massively separated flow simulations, it is highly desirable to have a similarly capable transition model based on correlation-based transport equations. Therefore, in this work, the $\gamma - Re_\theta$ transition model is modified, re-calibrated, and integrated with the S-A model. Since the original $\gamma - Re_\theta$ model depends entirely on mean flow quantities in a laminar boundary layer that are readily available in any CFD simulations, it can be readily coupled with any choice of turbulence model. Summary of the original $\gamma - Re_\theta$ model is presented first, followed by a detailed development of the $\gamma - Re_\theta -$ SA model.

3.1 Summary of $\gamma - Re_\theta$ Transition Model

The $\gamma - Re_\theta$ transition model uses the concept of intermittency (γ), in order to trigger transition locally, by controlling the production of turbulent kinetic energy. In this context, intermittency is a scalar transport variable that varies between 0 (always laminar) and 1 (always turbulent). The local intermittency value is used to turn on production of turbulent kinetic energy (TKE) in the k-equation of the SST $k - \omega$ turbulence model as follows:

$$\frac{D(\rho k)}{Dt} = \tilde{P}_k - \tilde{D}_k + \frac{\partial}{\partial x_j}[(\mu + \sigma_k \mu_t)\frac{\partial k}{\partial x_j}] \tag{3.1}$$

where, the production and destruction terms of the original k-equation from SST $k-\omega$ turbulence model (P_k and D_k), are modified using the local intermittency value as shown in Eq. 3.2. The governing equation for the specific turbulence dissipation rate, ω, is not modified in this formulation.

$$\tilde{P}_k = \gamma_{\text{eff}} P_k; \quad \tilde{D}_k = \min(\max(\gamma_{\text{eff}}, 0.1), 1.0) D_k \tag{3.2}$$

A transport equation based only on the local flow field variables and gradients, along with the nearest wall distance, is solved to obtain the intermittency field. The intermittency transport equation as proposed by Langtry [6] is given below:

$$\frac{D(\rho\gamma)}{Dt} = P_\gamma - D_\gamma + \frac{\partial}{\partial x_j}\left[(\mu + \frac{\mu_t}{\sigma_f})\frac{\partial \gamma}{\partial x_j}\right] \tag{3.3}$$

Intermittency production and destruction terms are given by Eqs. 3.4–3.11.

$$P_\gamma = F_{\text{length}} c_{a1} \rho S [\gamma F_{\text{onset}}]^{0.5} (1.0 - c_{e1}\gamma) \tag{3.4}$$

$$D_\gamma = c_{a2}\rho\Omega\gamma F_{\text{turb}}(c_{e2}\gamma - 1.0) \tag{3.5}$$

$$F_{\text{onset}} = \max\left(F_{\text{onset2}} - F_{\text{onset3}}, 0\right) \tag{3.6}$$

$$F_{\text{onset1}} = \frac{Re_v}{2.193.Re_{\theta c}} \tag{3.7}$$

$$F_{\text{onset2}} = \min\left(\max\left(F_{\text{onset1}}, F_{\text{onset1}}^4\right), 2.0\right) \tag{3.8}$$

$$F_{\text{onset3}} = \max\left(1 - \left(\frac{R_T}{2.5}\right)^3, 0\right) \tag{3.9}$$

$$F_{\text{turb}} = e^{\left(-\frac{R_T}{4}\right)^4} \tag{3.10}$$

$$Re_v = \frac{\rho d^2 S}{\mu}, \quad R_T = \frac{\rho k}{\mu\omega} \tag{3.11}$$

Transition onset occurs when the ratio of the local vorticity Reynolds number and the critical Reynolds number exceeds a value of 2.193, as shown in Eq. 3.7. The intermittency production term depends on two parameters: (1) Critical Reynolds number $Re_{\theta c}$, and (2) Transition length function F_{length}. The critical Reynolds number determines the transition onset location, and is defined as the point at which intermittency first starts to grow in a laminar boundary layer. This occurs slightly upstream of the transition momentum thickness Reynolds number, $Re_{\theta t}$. The F_{onset} function uses $Re_{\theta c}$ and is designed to rapidly switch from 0 in a laminar boundary layer to 1 in a turbulent boundary layer. The F_{length} function determines the length of the transition regime, during which the boundary layer becomes fully turbulent. These two parameters are calculated based on correlations that are functions of the local transition momentum thickness Reynolds number $\overline{Re_{\theta t}}$. These correlations can be developed based on a few benchmark cases of transitional flow past a flat plate

and are given in [33]. Intermittency is set to 1.0 in the freestream and a zero-gradient condition is specified at a solid wall boundary.

A second equation governs the transport of $\overline{Re_{\theta t}}$ as follows:

$$\frac{D(\rho\overline{Re_{\theta t}})}{Dt} = P_{\theta t} + \frac{\partial}{\partial x_j}\left[\sigma_{\theta t}(\mu + \mu_t)\frac{\partial\overline{Re_{\theta t}}}{\partial x_j}\right] \tag{3.12}$$

The source term for $\overline{Re_{\theta t}}$ is defined as:

$$P_{\theta t} = c_{\theta t}\frac{\rho}{t}(Re_{\theta t} - \overline{Re_{\theta t}})(1.0 - F_{\theta t}), \tag{3.13}$$

$$F_{\theta t} = \min\left(\max\left(F_{\text{wake}}.e^{-\left(\frac{d}{\delta}\right)^4}, 1.0 - \left(\frac{\gamma - 1/c_{e2}}{1.0 - 1/c_{e2}}\right)^2\right), 1.0\right) \tag{3.14}$$

$$\theta_{\text{BL}} = \frac{\overline{Re_{\theta t}}\mu}{\rho U}; \quad \delta_{\text{BL}} = 7.5\theta_{\text{BL}}; \quad \delta = \frac{50\Omega d}{U}.\delta_{\text{BL}} \tag{3.15}$$

$$F_{\text{wake}} = e^{\left(\frac{Re_\omega}{1E+5}\right)^2}; \quad Re_\omega = \frac{\rho\omega d^2}{\mu} \tag{3.16}$$

where t is a timescale present for dimensional reasons, and $F_{\theta t}$ is a blending function that turns off the source terms inside a boundary layer. The source term ($P_{\theta t}$) is designed to maintain the freestream value of $Re_{\theta t}$ outside the boundary layer ($\overline{Re_{\theta t}} = Re_{\theta t\infty}$), and is turned off inside the boundary layer allowing for the convection and diffusion of the conserved quantity.

The motivation behind solving a transport equation for $\overline{Re_{\theta t}}$ rather than directly using algebraic experimental correlations is that, since the turbulence intensity can strongly vary in internal flow applications such as turbomachinery, it is not appropriate to use the freestream value of $Re_{\theta t}$ to determine transition onset and extent. Instead, the freestream turbulence effects need to be transported into the boundary layer. Additionally, it was shown by Langtry [6] that this governing equation

accounts for history effects of pressure gradient on the onset of transition, since transition onset is influenced not just by the local value of the pressure gradient, but also by its variation upstream of the point of transition.

The local value of $Re_{\theta t}$ that is needed to compute the production term is obtained from the experimental correlations formulated as a function of freestream turbulence and local pressure gradient as follows:

$$Re_{\theta t} = [1173.51 - 589.428Tu + \frac{0.2196}{Tu^2}]F(\lambda_\theta), \tag{3.17}$$

$$Re_{\theta t} = \begin{cases} (1173.51 - 589.428Tu + \frac{0.2196}{Tu^2})F(\lambda_\theta), & Tu \leq 1.3 \\ 331.50[Tu - 0.5658]^{-0.671}F(\lambda_\theta), & Tu > 1.3 \end{cases} \tag{3.18}$$

$$F(\lambda_\theta) = \begin{cases} 1 - [-12.986\lambda_\theta - 123.66\lambda_\theta^2 - 405.689\lambda_\theta^3]e^{-[\frac{Tu}{1.5}]^{1.5}}, & \lambda_\theta \leq 0 \\ 1 + 0.275[1 - e^{[-35.0\lambda_\theta]}]e^{-[\frac{Tu}{0.5}]}, & \lambda_\theta > 0 \end{cases} \tag{3.19}$$

The pressure gradient parameter, λ_θ, is given by:

$$\lambda_\theta = \frac{\rho\theta^2}{\mu}\frac{dU}{ds} \tag{3.20}$$

where $\frac{dU}{ds}$ represents the streamwise acceleration given by:

$$\frac{dU}{ds} = \frac{u}{U}\frac{dU}{dx} + \frac{v}{U}\frac{dU}{dy} + \frac{w}{U}\frac{dU}{dz} \tag{3.21}$$

$$\frac{dU}{dx} = \frac{1}{2\sqrt{U}}\left[2u\frac{du}{dx} + 2v\frac{dv}{dx} + 2w\frac{dw}{dx}\right] \tag{3.22}$$

$$\frac{dU}{dy} = \frac{1}{2\sqrt{U}}\left[2u\frac{du}{dy} + 2v\frac{dv}{dy} + 2w\frac{dw}{dy}\right] \tag{3.23}$$

$$\frac{dU}{dz} = \frac{1}{2\sqrt{U}}\left[2u\frac{du}{dz} + 2v\frac{dv}{dz} + 2w\frac{dw}{dz}\right] \tag{3.24}$$

$$U = \sqrt{u^2 + v^2 + w^2} \tag{3.25}$$

The value of F(λ_θ) is evaluated using an iterative procedure by assuming $\lambda_\theta = 0.0$ for the first iteration. The freestream value of $\overline{Re_{\theta t}}$ is set to $Re_{\theta t\infty}$, which can be computed from the above experimental correlations under a zero pressure gradient condition by setting λ_θ to zero. At a wall boundary, a zero gradient condition is applied to $\overline{Re_{\theta t}}$. The model constants are:

$$c_{e1} = 1.0; \quad c_{a1} = 2.0; \quad c_{e2} = 50.0; \quad c_{a2} = 0.06; \quad \sigma_f = 1.0 \tag{3.26}$$

$$c_{\theta t} = 1.0; \quad \sigma_{\theta t} = 2.0 \tag{3.27}$$

A correction to the intermittency flowfield was proposed to improve the prediction of transition induced by a laminar separation bubble and is given by:

$$\gamma_{\text{sep}} = \min\left(s_1 \max\left[0, \left(\frac{Re_v}{3.235 Re_{\theta c}}\right) - 1\right] F_{\text{reattach}}, 2.0\right) F_{\theta t} \tag{3.28}$$

$$\gamma_{\text{eff}} = \max(\gamma, \gamma_{\text{sep}}) \tag{3.29}$$

where, $F_{\text{reattach}} = e^{-\left(\frac{R_T}{20}\right)^4}$, and $s_1 = 2.0$.

3.2 Formulation of the $\gamma - Re_\theta -$ SA Transition Model

The $\gamma - Re_\theta -$ SA model retains the primary features of the original model by solving two scalar transport equations, and using the local vorticity Reynolds number criterion and experimental correlations for transition momentum thickness, to predict transition onset. However, the following changes have been made to the original model:

1. New correlations for $Re_{\theta t}$ based on a combination of vorticity Reynolds number criterion, experimental data, and laminar flow simulations

2. Constant freestream turbulence intensity in the flowfield

3. Modified production and destruction terms in the intermittency equation

4. Omission of the separation-induced transition modification

5. Destruction term in the baseline S-A turbulence model not scaled by intermittency

Reasons for these modifications are presented in the following discussion. All zero-pressure gradient flat plate simulations in this work used a Cartesian computational domain with boundary conditions as shown in Fig. 3.1. The Cartesian mesh has 545 points in the streamwise direction and 245 points in the wall-normal direction, with 449 points from the leading-edge of the flat plate to the outflow boundary. The leading-edge of the flat plate is located at X = 0 in Fig. 3.1.

3.2.1 Modified Experimental Correlations for $Re_{\theta t}$

The $\gamma - Re_\theta$ model uses experimental correlations for $Re_{\theta t}$, combined with the vorticity Reynolds number criterion, to predict transition onset via the F_{onset1} function (Eq. 3.7). The original transition model uses correlations similar to those of Abu-Ghannam and Shaw (Eq. 3.30), but with improved sensitivity to low freestream turbulence levels for natural transition prediction.

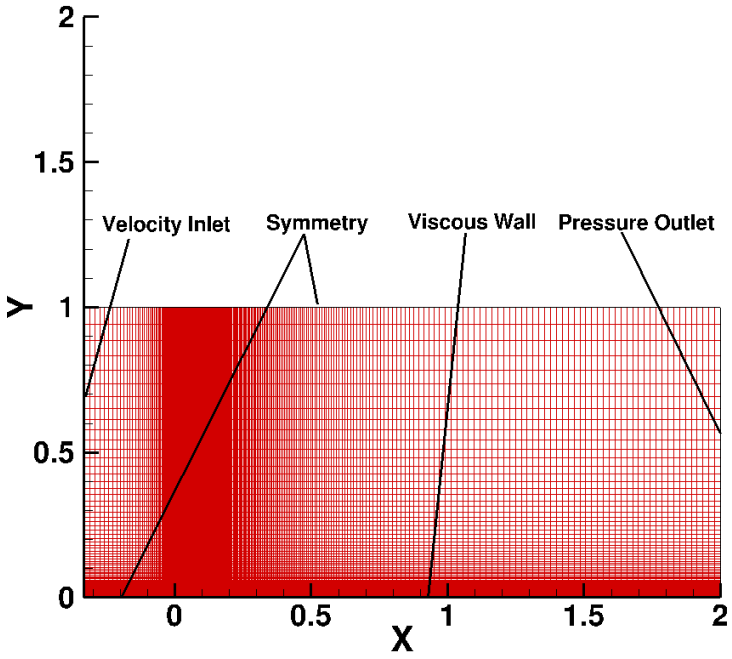

Figure 3.1: Cartesian mesh and boundary conditions used for zero-pressure gradient flat plate simulations

Abu-Ghannam and Shaw correlations (AGS) [1]

$$Re_{\theta t} = 163.0 + \exp\left\{F(\lambda_\theta) - \frac{F(\lambda_\theta)}{6.91} Tu\right\} \tag{3.30}$$

$$F(\lambda_\theta) = \begin{cases} 6.91 + 12.75\lambda_\theta + 63.64(\lambda_\theta)^2, & \lambda_\theta \leq 0 \\ 6.91 + 2.48\lambda_\theta - 12.27(\lambda_\theta)^2, & \lambda_\theta > 0 \end{cases} \tag{3.31}$$

Original $\gamma - Re_\theta$ model correlations (Langtry) [6]

$$Re_{\theta t} = \begin{cases} \left(1173.51 - 589.428\, Tu + \frac{0.2196}{Tu^2}\right) F(\lambda_\theta), & Tu \leq 1.3 \\ 331.50\,[Tu - 0.5658]^{-0.671}\, F(\lambda_\theta), & Tu > 1.3 \end{cases} \tag{3.32}$$

$$F(\lambda_\theta) = \begin{cases} 1 - [-12.986\lambda_\theta - 123.66\lambda_\theta^2 - 405.689\lambda_\theta^3]\, e^{-\left[\frac{Tu}{1.5}\right]^{1.5}}, & \lambda_\theta \leq 0 \\ 1 + 0.275\left[1 - e^{[-35.0\lambda_\theta]}\right] e^{-\left[\frac{Tu}{0.5}\right]}, & \lambda_\theta > 0 \end{cases} \tag{3.33}$$

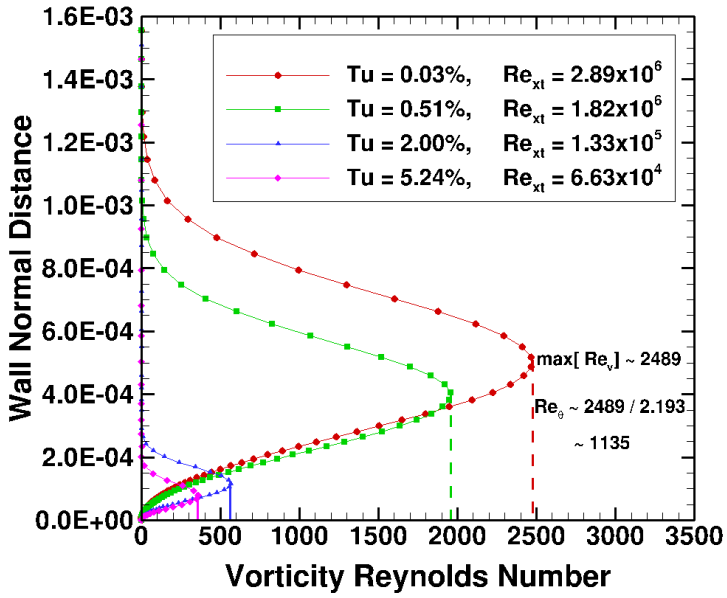

Figure 3.2: Evaluation of new correlations between $\mathrm{Re}_{\theta t}$ and Tu based on T3-series flat plate data and Vorticity Reynolds number criterion

In this work, a new set of correlations between $\mathrm{Re}_{\theta t}$ and Tu is developed to ensure consistency between the T3-series zero-pressure gradient flat plate experimental data and the vorticity Reynolds number criterion. The T3-series data provides transition Reynolds number based on plate length (Re_{xt}) at four discrete values of Tu. The objective is to numerically evaluate $\mathrm{Re}_{\theta t}$ values that satisfy the vorticity Reynolds number criterion at each of the four Tu levels. For this purpose, a laminar flow simulation of a flat plate boundary layer at zero-pressure gradient was carried out, and the maximum vorticity Reynolds number was recorded at the four streamwise stations corresponding to the four Re_{xt} values of the T3-series data. Numerical values of $\mathrm{Re}_{\theta t}$ are then computed for each freestream turbulence level using the vorticity Reynolds number criterion as show in Eq. 3.34. This process is

T3 Case	Tu%	$\mathrm{Re}_{\theta t,\ \mathrm{new}}$
–	0.01	1800.0
S-K	0.03	1135.0
T3AM	0.51	894.0
–	1.33	392.0
T3A	2.00	252.0
T3B	5.25	165.0
–	6.5	100.0

Table 3.1: Piecewise linear correlations between $\mathrm{Re}_{\theta t}$ and Tu

demonstrated in Fig. 3.2.

$$Re_{\theta t,\ \mathrm{new}} = \frac{\max\left[Re_{v,\mathrm{CFD-Laminar}}\right]}{2.193} \tag{3.34}$$

The resulting correlations are implemented in a piecewise linear form of the values listed in Table 3.1 and compared against the correlations of Abu Ghannam and Shaw (Eq. 3.30), and Langtry and Menter(Eq. **??**) in Fig. 3.3. Intermediate Tu values are added in order to achieve correlations similar to those of AGS and Langtry. The effect of pressure gradient on $\mathrm{Re}_{\theta t}$ is provided by multiplying the piecewise linear correlations with the $\mathrm{F}(\lambda_\theta)$ equations that are unchanged from the original model (Eq. 3.33).

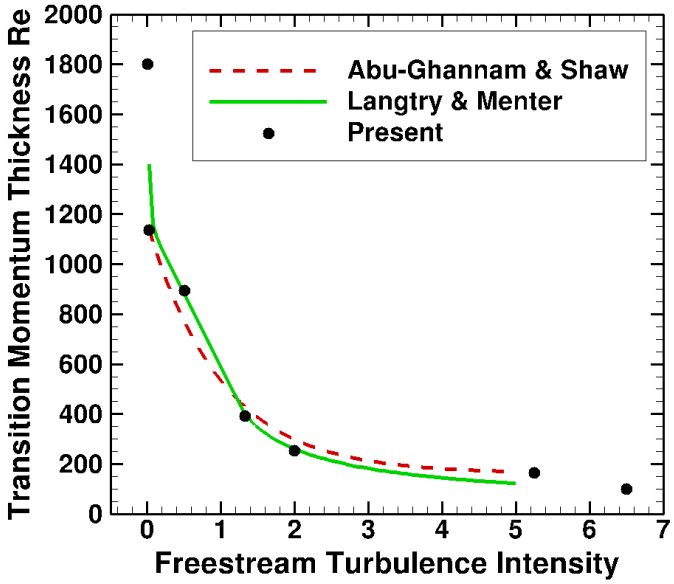

Figure 3.3: Comparison of present transition onset correlations with previous correlations

3.2.2 Intermittency Production and Destruction

The main advantage of the original $\gamma - Re_\theta$ model is its fully-local formulation using the vorticity Reynolds number criterion (Eq. 3.7). However, the shape of the Re_v profile at a given streamwise location is such that it goes to zero at the wall and at the edge of the boundary layer. Therefore, the transition onset criterion is not satisfied in these two regions downstream of the transition onset location. In the original model, the intermittency production term is activated locally at grid points where the onset criterion is satisfied, whereas the destruction term is not deactivated based on the same criterion. Rather, the destruction term is designed to gradually decay as the local Eddy viscosity value increases post-transition onset. Therefore, in

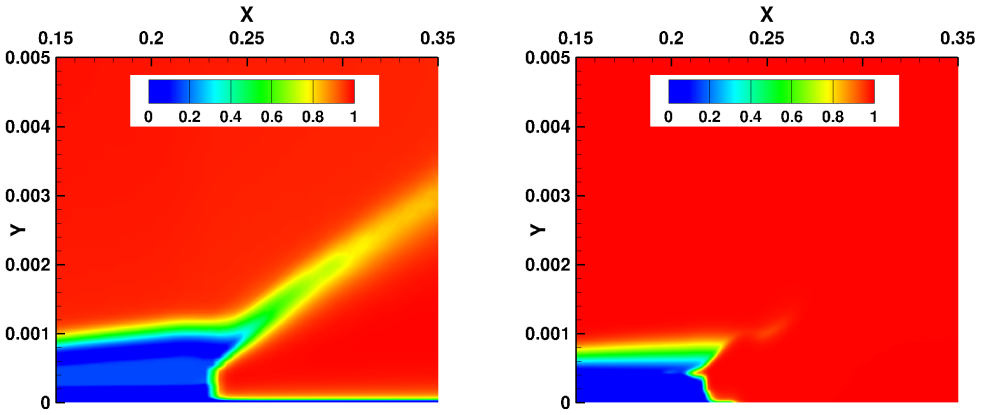

(a) Original source terms (b) Modified source terms

Figure 3.4: Flat plate intermittency contours – improved intermittency recovery in turbulent boundary layer

the two regions where the transition onset criterion fails, the production term is never activated, and intermittency may not fully recover, despite some amount of diffusion from the middle portion of the boundary layer and the freestream. This phenomenon is demonstrated in Fig. 3.4(a), where the intermittency adjacent to the wall on a flat plate stays close to zero even after transition onset. In addition, intermittency recovery at the edge of the boundary layer is not complete. This behavior is inherent to any fully-local formulation based on mean flow quantities since instabilities do not develop uniformly along the height of a transitional boundary layer. To remedy this, the intermittency production and destruction terms are modified so that they are turned on and off using the same criterion. Figure 3.4(b) shows a fully recovered intermittency flowfield downstream of the transition onset location obtained using the modified source terms. The redefined source terms are given in Eqs. 3.36–3.37.

$$P_\gamma = \rho\, F_{\text{onset}}\, G_{\text{onset}} \max\left[\frac{\Omega}{F_{\text{length}}}, \frac{1.0}{F_{\text{length, min}}}\right] \tag{3.35}$$

$$\text{If } \gamma > 1.0,\ P_\gamma = (\gamma - 1.0)P_\gamma \tag{3.36}$$

$$D_\gamma = \gamma\rho\Omega\,(1.0 - G_{\text{onset}}) \tag{3.37}$$

$$F_{\text{onset}} = \max\left(F_{\text{onset2}} - F_{\text{onset3}}, 0\right) \tag{3.38}$$

$$F_{\text{onset1}} = \frac{Re_v}{2.193.Re_{\theta c}} \tag{3.39}$$

$$F_{\text{onset2}} = \min\left(\max\left(F_{\text{onset1}}, F_{\text{onset1}}^4\right), 4.0\right) \tag{3.40}$$

$$F_{\text{onset3}} = \max\left(2 - (0.25R_T)^3, 0\right) \tag{3.41}$$

$$Re_v = \frac{\rho d^2 S}{\mu}, \quad R_T = \frac{\mu_t}{\mu} \tag{3.42}$$

Numerical correlations for critical Reynolds number and intermittency production strength are given below:

$$Re_{\theta c} = \alpha\ \overline{Re_{\theta t}}, \quad \alpha = 0.62 \tag{3.43}$$

$$F_{\text{length}} = 40.0, \quad F_{\text{length, min}} = 2.5 \tag{3.44}$$

$\mathrm{G_{onset}}$ is set to one if $\max(\mathrm{F_{onset1}}) > 1.0$ at a given streamwise station, else $\mathrm{G_{onset}}$ is zero. The purpose of $\mathrm{G_{onset}}$ is to turn on the intermittency production term when the Re_v criterion is satisfied anywhere along the height of the boundary layer at a given streamwise station, and simultaneously disable the destruction term completely. In addition, dependency of the destruction term on Eddy viscosity is avoided to prevent sensitivity of transition onset to the freestream Eddy viscosity value specified in the S-A model. The modified destruction term displays good relaminarization properties due to its direct dependence on transition onset criterion. $\mathrm{G_{onset}}$ can be evaluated

by a summation of F_{onset} along a grid line in the wall-normal direction. This aspect of the modified destruction term makes the new model non-local in the wall normal direction. The evaluation of this term does not pose any difficulty in structured meshes, but may not be suitable for unstructured meshes, unless the boundary layer region is resolved using a patched structured mesh. The new formulation of the intermittency transport equation make the $\gamma - Re_\theta -$ SA transition model independent of the choice of the turbulence model.

3.3 Model Calibration and Verification

The transport equation for $\overline{Re_{\theta t}}$ was not altered from its original form in the new model. The calibration process primarily involved tuning the source terms of the intermittency transport equation to match transition onset locations from the T3-series zero-pressure gradient flat plate experiments. The sequence of model calibration and verification steps are listed below:

1. The $\overline{Re_{\theta t}}$ equation is solved for flow past a flat plate and an airfoil to verify that the resulting streamwise $\overline{Re_{\theta t}}$ profile at the boundary layer edge remains constant for a zero-pressure gradient flat plate, increases in the presence of a favorable pressure gradient and decreases in the presence of an adverse pressure gradient on the airfoil. Implementation of the boundary layer detection function, $F_{\theta t}$, is also verified by ensuring that its value remains one inside the boundary layer and zero outside. Lagged convection and diffusion of the freestream $\overline{Re_{\theta t}}$ into the boundary layer in the presence of varying pressure

gradients is confirmed.

2. The intermittency transport equation is solved without source terms to verify that the convection and the diffusion terms, along with the boundary conditions are implemented correctly. In this case, the resulting intermittency distribution should be uniformly 1.0 across the flowfield.

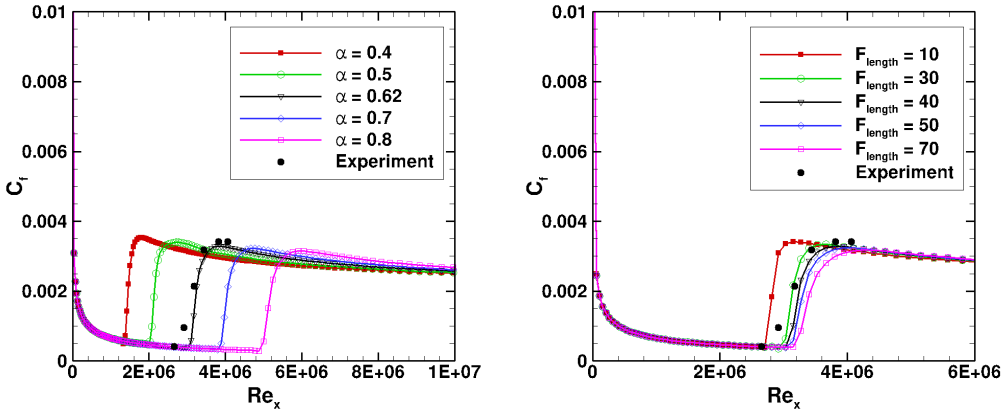

(a) Variation of α in $Re_{\theta c}$ correlation (b) Variation of F_{length}

Figure 3.5: Transition model sensitivity to critical Reynolds number and intermittency production term strength

3. Intermittency transport equation is solved with convection, diffusion, and destruction terms to ensure that the strength of the destruction term is sufficient to maintain a laminar boundary layer up to infinite Reynolds number in the absence of a production term. This is the calibration process for the destruction term, which is expected to reduce the freestream intermittency value of one to zero in the presence of shear, when the transition onset criterion is not satisfied.

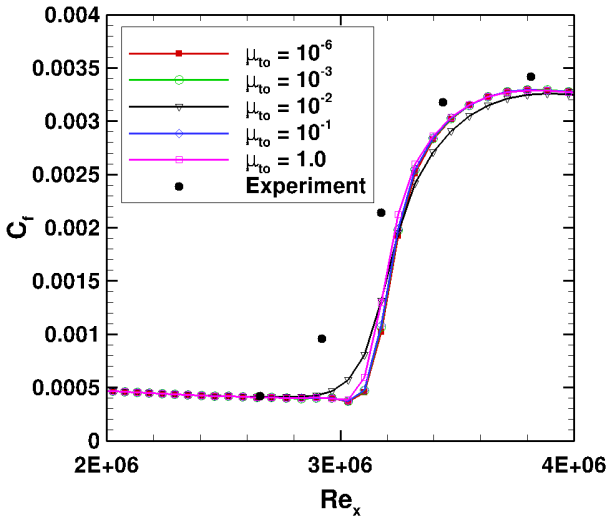

Figure 3.6: Transition model sensitivity to variation in freestream Eddy viscosity

4. Next, the complete form of the two-equation $\gamma - Re_\theta -$ SA model is solved for the zero-pressure gradient T3-series flat plate cases [80, 81] to calibrate the following two parameters – (1) Critical Reynolds number correlation controlling transition onset location ($\mathrm{Re}_{\theta c}$ in Eq. 3.43) and (2) Strength of intermittency production term controlling transition extent ($\mathrm{F}_{\mathrm{length}}$ in Eq. 3.44) – by matching computed skin friction profiles with those obtained from experiments. Figure 3.5 shows the model sensitivity to changes in these two parameters. Decreasing $\mathrm{Re}_{\theta c}$ advances the transition onset location, whereas increasing $\mathrm{F}_{\mathrm{length}}$ lengthens the transition zone. $\mathrm{F}_{\mathrm{length}}$ has a secondary effect on transition onset location. Since the Spalart-Allmaras turbulence model is designed to remain insensitive to moderate values of freestream Eddy viscosity, it is desirable to have similar insensitivity in the modified transition model. This is ensured by avoiding the use of Eddy viscosity in the intermittency de-

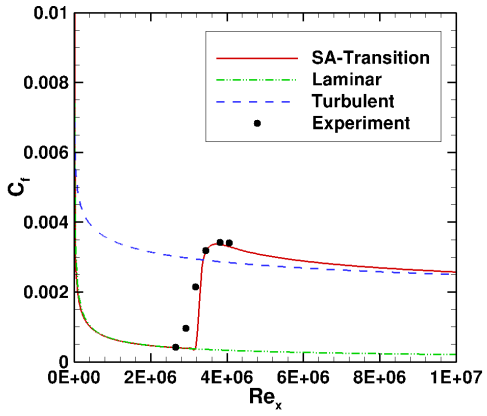

(a) S-K, Tu = 0.03% [79]

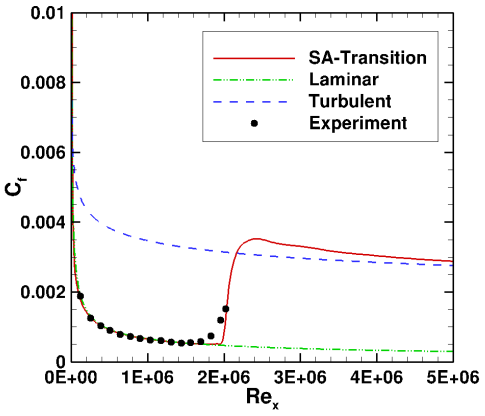

(b) T3AM, Tu = 0.51% [80]

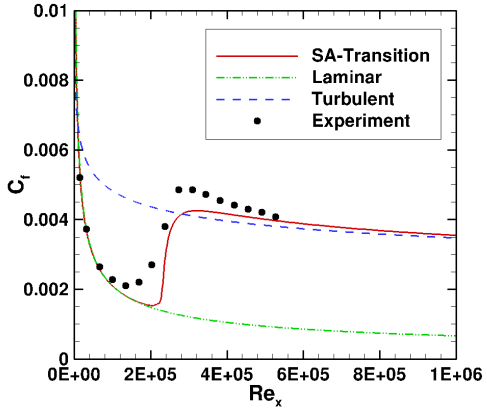

(c) T3A, Tu = 2.00% [80]

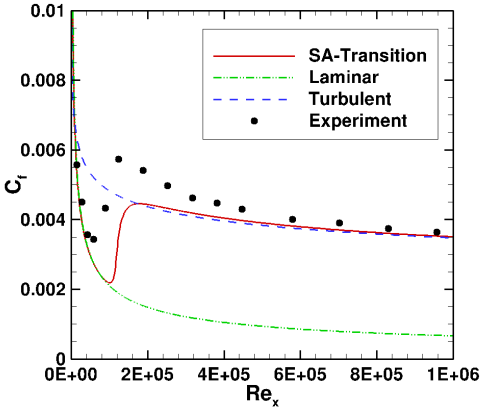

(d) T3B, Tu = 5.25% [80]

Figure 3.7: Skin friction prediction on a flat plate at zero pressure gradient using $\gamma - Re_\theta -$ SA transition model

struction term that is present in the original model. Figure 3.6 demonstrates that the predicted transition onset location and extent are largely unaffected by variations in the freestream Eddy viscosity value.

Figure 3.7 compares the computed values of skin friction with experimental data for flow past a zero-pressure gradient flat plate at four discrete values of

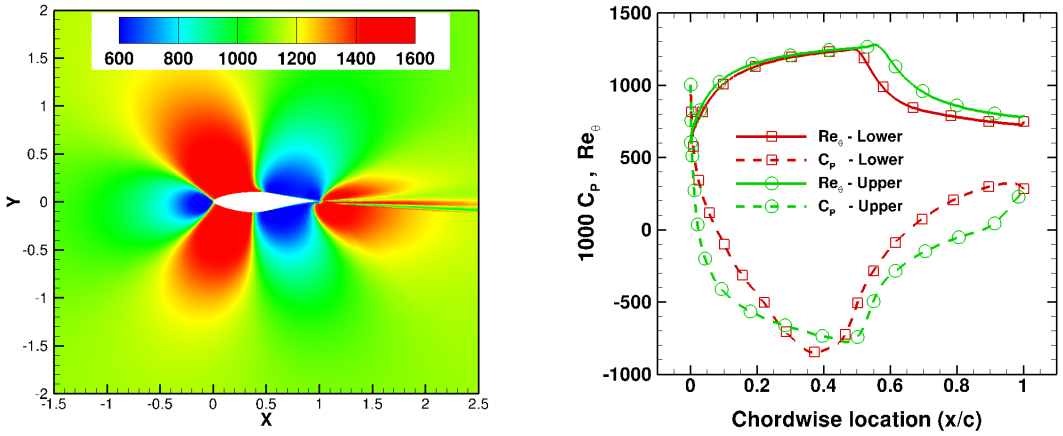

(a) Transition momentum thickness Reynolds number, $\overline{Re_{\theta t}}$

(b) Chordwise $\overline{Re_{\theta t}}$ profiles on upper and lower surfaces

Figure 3.8: Solution of $\overline{Re_{\theta t}}$ transport equation for flow past an S809 airfoil section at 0^o AoA

Tu. Transition onset is indicated by a sharp increase in the skin friction value. The skin friction profile follows the laminar path until the point of transition onset and reaches the fully turbulent profile downstream of the transition zone. Agreement between the computed and the experimental profiles is good for all four cases. While the transition prediction is slightly delayed for the higher Tu cases (T3A and T3B), such Tu values are not expected to occur in external aerodynamic applications. The modified transition model is intended for use at relatively low freestream turbulence levels (< 1 %) encountered in external flow applications.

5. Next, the behavior of the calibrated $\gamma - Re_\theta -$SA transition model is analyzed through simulations of flow past an S809 airfoil at a Reynolds number of two

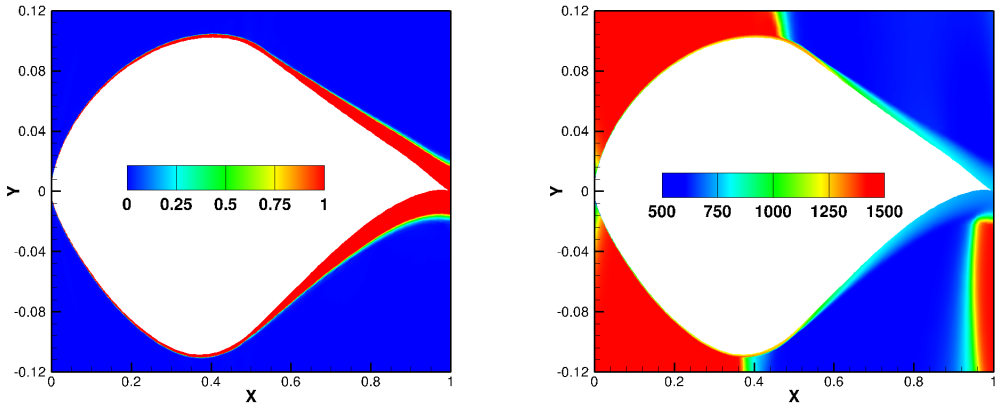

(a) Boundary layer detection function, $F_{\theta t}$ (b) Convection and diffusion of $\overline{Re_{\theta t}}$ into boundary layer

Figure 3.9: Near-wall solution of $\overline{Re_{\theta t}}$ for flow past an S809 airfoil section at 0^o AoA (not to scale)

million, a Mach number of 0.1, and at 0° angle of attack. The freestream turbulence intensity is set to 0.03%. The S809 airfoil is designed to delay the adverse pressure gradient and the boundary layer experiences a separation-induced transition on both the upper and the lower surfaces around 50% of chord at low angles of attack.

Figure 3.8(a) shows contours of $\overline{Re_{\theta t}}$ obtained from the converged solution of the $\overline{Re_{\theta t}}$ transport equation in the flowfield around the airfoil. Surface values of $\overline{Re_{\theta t}}$ and pressure coefficient are plotted in Fig. 3.8(b). The variation in $\overline{Re_{\theta t}}$ is consistent with regions of favorable and adverse pressure gradients along the fore and aft portions of the airfoil. $\overline{Re_{\theta t}}$ increases from its farfield value in the presence of adverse pressure gradients and vice versa. An interesting observation is that the sensitivity of $\overline{Re_{\theta t}}$ to adverse pressure gradients is

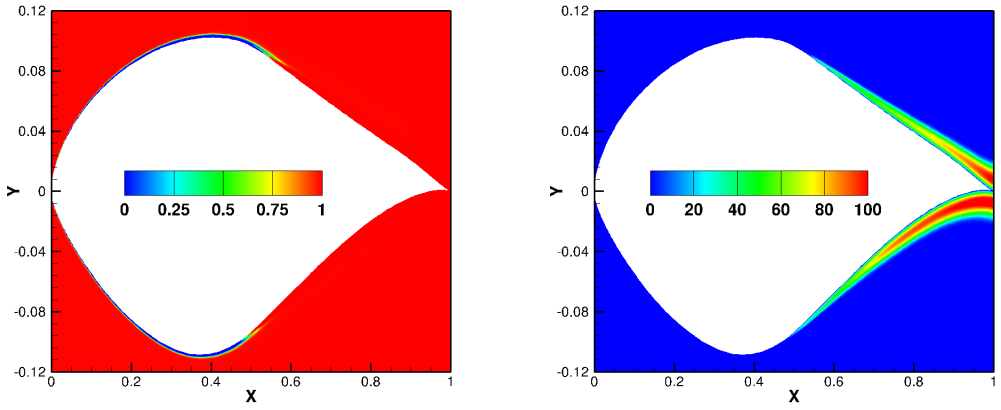

(a) Intermittency (0 = laminar, 1 = turbulent)

(b) Eddy viscosity

Figure 3.10: Production of Eddy viscosity downstream of transition onset location for flow past an S809 airfoil section at 0^o AoA (not to scale)

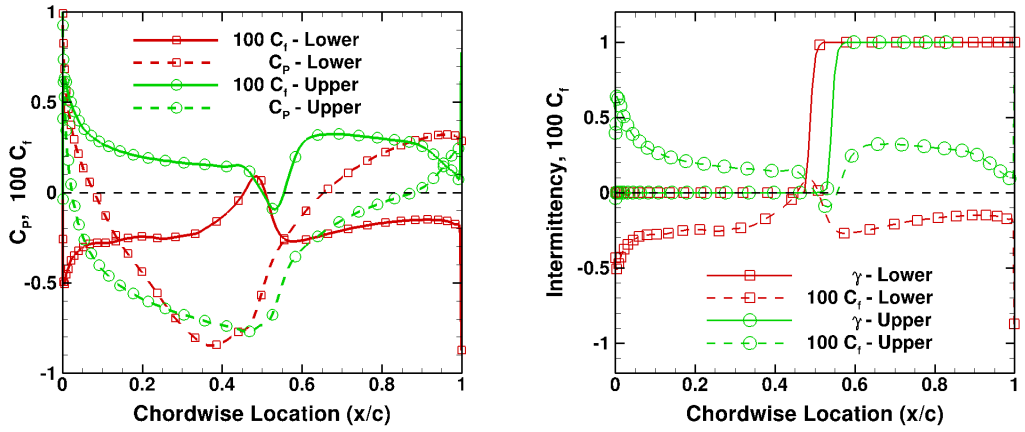

(a) Surface pressure and skin friction coefficients

(b) Surface intermittency distribution

Figure 3.11: Surface pressure, skin friction, and intermittency profiles for flow past an S809 airfoil section at 0^o AoA

greater than its sensitivity to favorable pressure gradients. This is consistent with the experimental correlations for $Re_{\theta t}$ under non-zero pressure gradients.

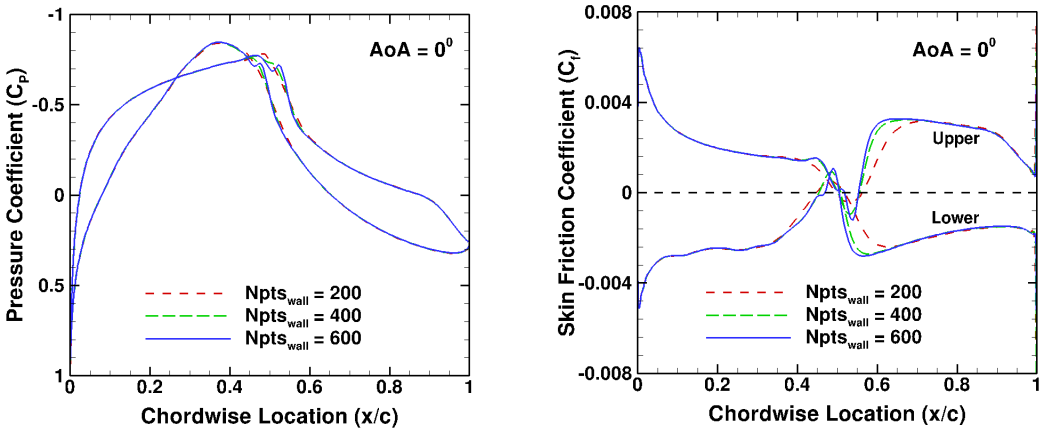

(a) Surface pressure coefficient

(b) Skin friction coefficient

Figure 3.12: Grid convergence study for flow past an S809 airfoil section at 0^o AoA

Figure 3.9(a) shows a contour plot of the boundary layer detection function, $F_{\theta t}$, that is designed to have a value of one inside the boundary layer and zero outside. Figure 3.9(b) shows convection and diffusion of $\overline{Re_{\theta t}}$ into the boundary layer due to turning off the production term using the F_θ function. This figure also demonstrates the desired lag in propagation of freestream value of $\overline{Re_{\theta t}}$ into the boundary layer to account for history effects of pressure gradients on transition onset.

Intermittency and Eddy viscosity contours in Fig. 3.10 confirm that the production of Eddy viscosity occurs only after intermittency starts to grow towards one in the boundary layer. Surface pressure and skin friction coefficient profiles are plotted in Fig. 3.11(a). Separation-induced transition onset is observed where the skin friction profiles on both the upper and the lower surfaces change their sign. Complete recovery of intermittency after transition

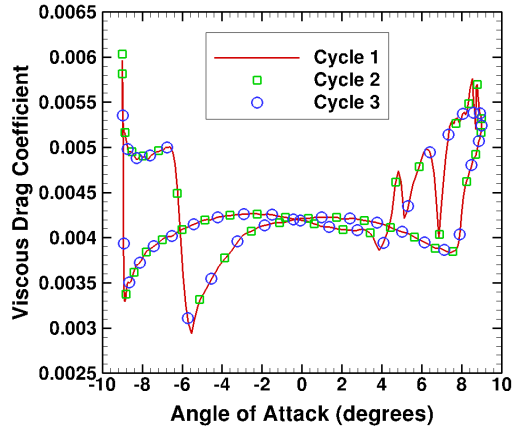

(a) Viscous drag coefficient

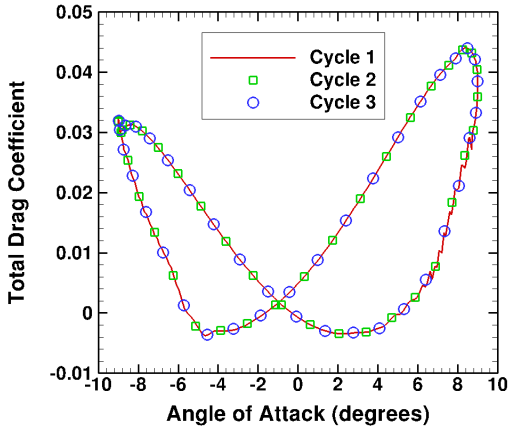

(b) Total drag coefficient

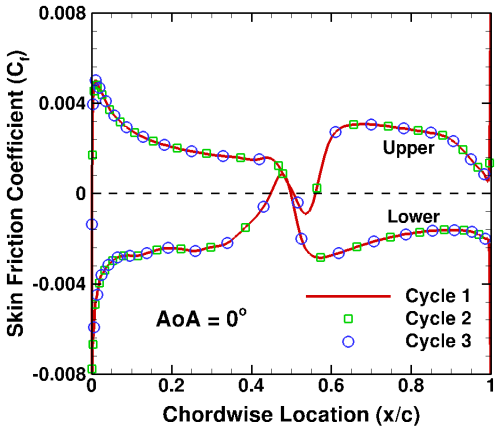

(c) Skin friction at 0^o AoA

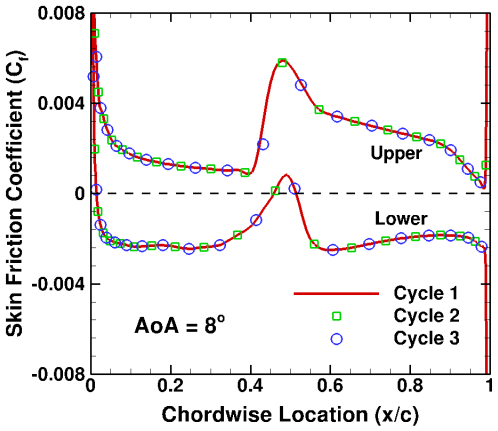

(d) Skin friction at 8^o AoA

Figure 3.13: Demonstration of hysteresis-free and relaminarization properties of $\gamma - Re_\theta -$ SA transition model by simulating a sinusoidally pitching S809 airfoil section

onset is seen in Fig. 3.11(b), demonstrating the effectiveness of the modified intermittency production and destruction terms.

A grid sensitivity study is performed at three wrap-around grid resolutions of 200, 400, and 600 points on the airfoil surface to assess model sensitivity

to streamwise grid spacing. The resulting pressure and skin friction profiles are compared in Fig. 3.12. With 200 points on the surface, transition onset location is delayed and transition extent is longer. Profiles obtained with 400 and 600 grid points show only minor differences, thereby demonstrating the good grid sensitivity behavior of the transition model. Lift coefficient values for 200, 400, and 600 grid points are 0.168, 0.166, and 0.165 respectively, and the corresponding drag coefficient values are 0.00591, 0.00601, and 0.00605. Based on this study, transition model simulations may require 400 grid points in the wrap-around direction of the airfoil when using a third-order accurate spatial derivative scheme.

Finally, the model is tested for hysteresis effects to check for dependence of transition prediction on the initial solution, and to demonstrate relaminarization capability. In the ideal case, for a given set of freestream conditions, the predicted transition onset location should be independent of whether the flowfield is initialized with a laminar or turbulent solution, or with freestream conditions. To demonstrate the new model's lack of any hysteresis effects and ability to predict relaminarization, simulation of a sinusoidally pitching S809 airfoil is carried out for multiple cycles. The sinusoidal motion is defined by a mean angle of attack of 0^o, amplitude of 5^o, and a reduced frequency of 0.1. Time histories of skin friction profiles, viscous drag, and total drag are monitored for three full cycles. Viscous and total drag coefficients plotted in Fig. 3.13(a),(b) show repeatability for three cycles. This is further verified by

the skin friction profiles at 0^o and 8^o angles of attack during upstroke, plotted for the three successive cycles in Fig. 3.13(c),(d). Movement of the transition onset location in both the upstream and the downstream directions indicates that the boundary layer is able to relaminarize with negligible hysteresis effects.

3.4 Final Form of $\gamma - Re_\theta -$ SA Transition Model

The final form of the $\gamma - Re_\theta -$ SA transition model and its coupling with the one-equation Spalart-Allmaras turbulence model is presented in this section. The transport equation for the intermittency factor, γ, is given by:

$$\frac{D(\rho\gamma)}{Dt} = P_\gamma - D_\gamma + \frac{\partial}{\partial x_j}\left[(\mu + \mu_t)\frac{\partial \gamma}{\partial x_j}\right] \tag{3.45}$$

$$P_\gamma = \rho\, F_{\text{onset}}\, G_{\text{onset}}\, \max\left[\frac{\Omega}{F_{\text{length}}}, \frac{1.0}{F_{\text{length, min}}}\right] \tag{3.46}$$

$$\text{If } \gamma > 1.0,\ P_\gamma = (\gamma - 1.0)P_\gamma \tag{3.47}$$

$$D_\gamma = \rho\, \Omega\, \gamma\, (1.0 - G_{\text{onset}}) \tag{3.48}$$

$$F_{\text{onset}} = \max\left(F_{\text{onset2}} - F_{\text{onset3}}, 0\right) \tag{3.49}$$

$$F_{\text{onset1}} = \frac{Re_v}{2.193.Re_{\theta c}} \tag{3.50}$$

$$F_{\text{onset2}} = \min\left(\max\left(F_{\text{onset1}}, F_{\text{onset1}}^4\right), 4.0\right) \tag{3.51}$$

$$F_{\text{onset3}} = \max\left(2 - (0.25R_T)^3, 0\right) \tag{3.52}$$

$$Re_v = \frac{\rho d^2 S}{\mu}, \quad R_T = \frac{\mu_t}{\mu} \tag{3.53}$$

The numerical correlations for critical Reynolds number and intermittency production strength are given below:

$$Re_{\theta c} = \alpha\ \overline{Re_{\theta t}}, \quad \alpha = 0.62 \tag{3.54}$$

$$F_{\text{length}} = 40.0, \quad F_{\text{length, min}} = 2.5 \tag{3.55}$$

The transport equation for transition momentum thickness Reynolds number, $\overline{Re_{\theta t}}$, isgiven below:

$$\frac{D(\rho\overline{Re_{\theta t}})}{Dt} = P_{\theta t} + \frac{\partial}{\partial x_j}\left[2.0(\mu + \mu_t)\frac{\partial\overline{Re_{\theta t}}}{\partial x_j}\right] \tag{3.56}$$

The source term for $\overline{Re_{\theta t}}$ is defined as:

$$P_{\theta t} = 0.03\frac{\rho}{t}(Re_{\theta t} - \overline{Re_{\theta t}})(1.0 - F_{\theta t}), \tag{3.57}$$

$$F_{\theta t} = \min\left(e^{-\left(\frac{d}{\delta}\right)^4}, 1.0\right) \tag{3.58}$$

$$\theta_{\text{BL}} = \frac{\overline{Re_{\theta t}}\mu}{\rho U}; \quad \delta_{\text{BL}} = 7.5\theta_{\text{BL}}; \quad \delta = \frac{50\Omega d}{U}.\delta_{\text{BL}} \tag{3.59}$$

$Re_{\theta t}$ values outside the boundary layer are evaluated using the piecewise linear correlations from Table 3.1 multiplied by the F(λ_θ) equations to account for freestream turbulence and streamwise pressure gradient effects:

$$F(\lambda_\theta) = \begin{cases} 1 - [-12.986\lambda_\theta - 123.66\lambda_\theta^2 - 405.689\lambda_\theta^3]e^{-[\frac{Tu}{1.5}]^{1.5}}, & \lambda_\theta \leq 0 \\ 1 + 0.275[1 - e^{[-35.0\lambda_\theta]}]e^{-[\frac{Tu}{0.5}]}, & \lambda_\theta > 0 \end{cases} \tag{3.60}$$

The pressure gradient parameter, λ_θ, is given by:

$$\lambda_\theta = \frac{\rho\theta^2}{\mu}\frac{dU}{ds} \tag{3.61}$$

where $\frac{dU}{ds}$ represents the streamwise acceleration given by:

$$\frac{dU}{ds} = \frac{u}{U}\frac{dU}{dx} + \frac{v}{U}\frac{dU}{dy} + \frac{w}{U}\frac{dU}{dz} \tag{3.62}$$

$$\frac{dU}{dx} = \frac{1}{2\sqrt{U}}\left[2u\frac{du}{dx} + 2v\frac{dv}{dx} + 2w\frac{dw}{dx}\right] \tag{3.63}$$

$$\frac{dU}{dy} = \frac{1}{2\sqrt{U}}\left[2u\frac{du}{dy} + 2v\frac{dv}{dy} + 2w\frac{dw}{dy}\right] \tag{3.64}$$

$$\frac{dU}{dz} = \frac{1}{2\sqrt{U}}\left[2u\frac{du}{dz} + 2v\frac{dv}{dz} + 2w\frac{dw}{dz}\right] \tag{3.65}$$

$$U = \sqrt{u^2 + v^2 + w^2} \tag{3.66}$$

The value of F(λ_θ) is evaluated using an iterative procedure by assuming $\lambda_\theta = 0.0$ for the first iteration. The freestream value of $\overline{Re_{\theta t}}$ is set to $Re_{\theta t\infty}$, which can be computed from the above experimental correlations under a zero pressure gradient condition by setting λ_θ to zero.

For both the transport equations, a zero gradient boundary condition is applied at a solid wall boundary. The freestream value of intermittency is set to one. At a farfield boundary, depending on the flow direction, either the freestream value or an extrapolated value from the interior is specified for the transport equations.

The solution of the intermittency transport equation is used to control the production term of eddy viscosity in S-A model as follows:

$$\frac{D\tilde{\nu}}{Dt} = \gamma P_\nu - D_\nu + \frac{1}{\sigma}\left[\nabla.((\nu + \tilde{\nu})\nabla\tilde{\nu}) + c_{b2}(\nabla\tilde{\nu})^2\right] \tag{3.67}$$

$$P_\nu = c_{b1}\tilde{\Omega}\tilde{\nu} \quad \text{and} \quad D_\nu = c_{w1}f_w[\frac{\tilde{\nu}}{d}]^2 \tag{3.68}$$

$\tilde{\Omega}$ is a function of the vorticity magnitude, Ω, and is defined as:

$$\tilde{\Omega} = \max\left(\Omega + \frac{\tilde{\nu}}{\kappa^2 d^2}f_{v2}, 0.3\Omega\right), \quad f_{v2} = 1 - \frac{\chi}{1 + \chi f_{v1}} \tag{3.69}$$

The wall damping function, f_w, is defined as:

$$f_w = g\left[\frac{1+c_{w3}^6}{g^6+c_{w3}^6}\right]^{\frac{1}{6}}, \quad g = r + c_{w2}(r^6 - r), \quad r = \frac{\tilde{\nu}}{\tilde{\Omega}\kappa^2 d^2} \tag{3.70}$$

The S-A model constants are given by: $c_{b1} = 0.1355, \sigma = 2/3, c_{b2} = 0.622, \kappa = 0.41, c_{w1} = c_{b1}/\kappa^2 + (1+c_{b2})/\sigma, c_{w2} = 0.3, c_{w3} = 2.0, c_{v1} = 7.1$.

The primary transport variable, $\tilde{\nu}$, is set to 0.1 at an inflow boundary, extrapolated from the interior at an outflow boundary, and is set to zero at a smooth solid wall boundary. The present implementation of the S-A model uses the rotational correction [82], which reduces the production of turbulence in regions where vorticity exceeds strain rate, such as in vortex core regions, where pure rotation should not produce turbulence. In this version of the S-A model, the magnitude of vorticity, Ω, used to calculate $\tilde{\Omega}$ is replaced with $\Omega + 2.\min(0, S - \Omega)$ in Eq. B.4, which is then used to compute the production term of eddy viscosity. Numerical discretization of the transition and turbulence model equations closely follows the procedure described in the original SA model formulation [35].

3.5 Computational Cost

The $\gamma - Re_\theta -$SA model solves two additional scalar transport equations using a similar discretization approach to that of the one-equation SA model. The additional computational expense of including the transition model is therefore approximately twice that of solving the SA model.

3.6 Summary

This chapter detailed the formulation, calibration, and verification of the correlation-based $\gamma - Re_\theta -$ SA transition model. Two additional transport equations were solved to obtain an intermittency flow field in the computational domain. New correlations for transition onset were developed based on a combination of experimental data and the vorticity Reynolds number criterion. While the new model retained the primary features of the original model, modifications were made to the source terms of the intermittency transport equation to improve near-wall consistency of the model. The transition model was coupled with the Spalart-Allmaras turbulence model by multiplying the intermittency factor with the eddy viscosity production term of the SA model. This enabled turbulence production to be activated only when intermittency starts to increase towards unity. Relaminarization and hysteresis behavior of the new model were studied using a 2-D pitching airfoil simulation. The next chapter describes the numerical methodology used in this work to simulate unsteady, compressible, turbulent flows using the Reynolds-Averaged Navier-Stokes equations.

4 Numerical Methodology

This chapter details the numerical methodology employed to verify and validate the newly developed transition model. All simulations were performed using the *Overset Transonic Unsteady Rotor Navier-Stokes* (OverTURNS) flow solver [83]. In OverTURNS, a system of partial differential equations governing unsteady, compressible fluid flow is numerically solved in an Eulerian framework. The final form of the governing equations is obtained through the following sequence of transformations applied to their three-dimensional Cartesian form: (1) Non-dimensionalization, (2) Reynolds-averaging, and (3) Curvilinear co-ordinate transformation. These transformed equations are numerically discretized on a computational domain in both space and time to obtain a system of coupled algebraic equations, which are then solved to obtain the flow field solution.

4.1 Governing Equations

The three-dimensional, unsteady, Navier-Stokes equations describe the behavior of fluid flow under the continuum hypothesis. In this work, they are used to represent compressible, non-reacting, idea gas flow across the boundary of a closed

domain known as a *control volume*. They ensure universal laws of conservation of mass, momentum, and energy in the control volume. The Cartesian system of equations in their strong conservation form is given by Eq. 4.1

$$\frac{\partial Q}{\partial t} + \frac{\partial F_i}{\partial x} + \frac{\partial G_i}{\partial y} + \frac{\partial H_i}{\partial z} = \frac{\partial F_v}{\partial x} + \frac{\partial G_v}{\partial y} + \frac{\partial H_v}{\partial z} + S \tag{4.1}$$

where Q is the vector of conserved variables, F_i, G_i, and H_i are the inviscid flux vectors, and F_v, G_v, and H_v are the viscous flux vectors. S represents the vector of body forces and/or accounts for a change in reference frame. The vector of conserved variables, Q, is given by Eq. 4.2:

$$Q = \begin{Bmatrix} \rho \\ \rho u \\ \rho v \\ \rho w \\ E \end{Bmatrix} \tag{4.2}$$

where, ρ is the fluid density, and (u, v, w) are components of the fluid velocity along the Cartesian coordinate system (x, y, z). E is the total energy per unit volume given by:

$$E = \rho \left[e + \frac{1}{2} \left(u^2 + v^2 + w^2 \right) \right] \tag{4.3}$$

where, e is the internal energy per unit mass. The vector of primitive variables is given by (ρ, u, v, w, p).

The inviscid and viscous flux vectors are given by Eqs. 4.4–4.9:

$$F_i = \begin{Bmatrix} \rho u \\ \rho uu + p \\ \rho uv \\ \rho uw \\ (E+p)u \end{Bmatrix} \tag{4.4}$$

$$G_i = \begin{Bmatrix} \rho v \\ \rho vu \\ \rho vv + p \\ \rho vw \\ (E+p)v \end{Bmatrix} \tag{4.5}$$

$$H_i = \begin{Bmatrix} \rho w \\ \rho wu \\ \rho wv \\ \rho ww + p \\ (E+p)w \end{Bmatrix} \tag{4.6}$$

$$F_v = \begin{Bmatrix} 0 \\ \tau_{xx} \\ \tau_{yx} \\ \tau_{zx} \\ u\tau_{xx} + v\tau_{yx} + w\tau_{zx} - q_x \end{Bmatrix} \tag{4.7}$$

$$G_v = \begin{Bmatrix} 0 \\ \tau_{xy} \\ \tau_{yy} \\ \tau_{zy} \\ u\tau_{xy} + v\tau_{yy} + w\tau_{zy} - q_y \end{Bmatrix} \tag{4.8}$$

$$H_v = \begin{Bmatrix} 0 \\ \tau_{xz} \\ \tau_{yz} \\ \tau_{zz} \\ u\tau_{xz} + v\tau_{yz} + w\tau_{zz} - q_z \end{Bmatrix} \tag{4.9}$$

where, q_x, q_y, and q_z are heat conduction terms expressed as a function of temperature (T) and coefficient of thermal conductivity (k) as follows:

$$q_j = k\frac{\partial T}{\partial x_j} \quad (j = x, y, z) \tag{4.10}$$

The viscous stress tensor for Newtonian fluids, τ_{ij}, formulated using Stokes' hypothesis [84] is given by:

$$\tau_{ij} = \mu\left[\left(\frac{\partial u_i}{\partial x_j} + \frac{\partial u_i}{\partial x_j}\right) - \frac{2}{3}\frac{\partial u_k}{\partial x_k}\delta_{ij}\right], \quad \delta_{\mathrm{ij}} = 1 \text{ if i} = \text{j};\ \delta_{\mathrm{ij}} = 0 \text{ if i} \neq \text{j} \tag{4.11}$$

The coefficient of molecular viscosity is given by Sutherland's formula in Eq. 4.12:

$$\mu = C_1\frac{T^{\frac{3}{2}}}{T + C_2} \tag{4.12}$$

where, $\mathrm{C}_1 = 1.4 \times 10^{-6}$ kg/(ms$\sqrt{K}$) and $\mathrm{C}_2 = 110.4$ K for air at standard temperature and pressure. To close the system of equations, the *equation of state* for ideal

gases is used:

$$p = \rho RT \tag{4.13}$$

where, R is the gas constant. Since all the flows studied in this work involve air at standard temperature and pressure, the calorically perfect gas assumption is valid. A calorically perfect gas is an ideal gas with constant specific heats. Specific heat at constant volume (c_v) and specific heat at constant pressure (c_p) are given by:

$$c_v = \frac{R}{\gamma - 1}; \qquad c_p = \frac{\gamma R}{\gamma - 1} \tag{4.14}$$

The following relations between thermodynamic quantities are applicable to calorically perfect gases:

$$e = c_v T \tag{4.15}$$

$$p = (\gamma - 1)\, \rho e \tag{4.16}$$

$$e = c_v T \tag{4.17}$$

The total energy per unit volume, E, can now be re-written in terms of pressure, p, and velocity components as follows:

$$E = \frac{p}{\gamma - 1} + \frac{1}{2}\rho \left(u^2 + v^2 + w^2\right) \tag{4.18}$$

In the above equations, the value of the ratio of specific heats (γ) is 1.4 for air at standard temperature and pressure.

4.2 Rotating Reference Frame

When simulating problems with moving bodies, the computational grid is usually translated and rotated based on the path of the solid surface. In such cases,

the governing equations are solved in an inertial frame of reference. This method increases computational time since it requires the calculation of grid-related quantities (such as metrics, surface normals, etc.), and to perform domain connectivity related operations for overset meshes at each timestep. The additional computational expense cannot be avoided if the motion of the body is not well-defined mathematically, or if there are multiple bodies which cannot be treated under the same reference frame due to different rotation or translation rates. However, for simulations of hovering single rotors or multiple rotors operating at a constant rotation rate, it is possible to solve the governing equations in a reference frame that is rotating with the rotor blades. This avoids the need to recalculate grid-related quantities and to evaluate domain connectivity information at each timestep. To solve the equations in a non-inertial reference frame, the three velocity components (u, v, w) in the convective flux vectors of the governing equations (Eq. 4.4–4.6) are replaced by $(u - u_g, v - v_g, w - w_g)$, where $\mathrm{U}_g = (u_g, v_g, w_g) = \Omega \times r$ is the vector of grid velocities due to rotation, and $\Omega = (\Omega_x, \Omega_y, \Omega_z)$ is the angular velocity vector. For a rotor system rotating about the z-axis, $\Omega_x = \Omega_y = 0$, and therefore $\mathrm{U}_g = (-\Omega_z y, \Omega_z x, 0)$. In addition, Coriolis acceleration terms must be included as

a source term vector, S, on the right-hand side of Eq. 4.1 as shown below:

$$S = \begin{Bmatrix} 0 \\ \rho v \Omega_z \\ -\rho u \Omega_z \\ 0 \\ 0 \end{Bmatrix} \tag{4.19}$$

4.3 Non-dimensional Form of Equations

The governing equations are often solved in their non-dimensional form. There are two advantages of doing this: (1) parameters such as Mach number and Reynolds number can be varied independently, (2) all flow variables are normalized to fall in the vicinity of (0,1), thereby reducing numerical inaccuracies that may occur due to mathematical operations between largely different values. All independent and dependent variables are non-dimensionalized using a set of reference variables indicated by the * superscript in the equations given below:

$$x^* = \frac{x}{L}, \qquad x^* = \frac{x}{L}, \qquad z^* = \frac{z}{L}, \qquad t^* = \frac{t}{L/a_\infty} \tag{4.20}$$

$$u^* = \frac{u}{a_\infty}, \qquad v^* = \frac{v}{a_\infty}, \qquad w^* = \frac{w}{a_\infty}, \qquad \mu^* = \frac{\mu}{a_\infty}, \tag{4.21}$$

$$\rho^* = \frac{\rho}{\rho_\infty}, \qquad p^* = \frac{p}{\rho_\infty {a^2}_\infty}, \qquad T^* = \frac{T}{T_\infty} \tag{4.22}$$

For problems involving airfoil sections, the chord length of the airfoil is chosen as the reference length, L. Substituting the above relations into the governing equations in Eq. 4.1 gives a new set of equations in terms of the non-dimensional variables. The non-dimensional equations are identical in form to the dimensional equations

except for the viscous stress tensor and thermal conduction terms. Modified viscous stress tensor and heat conduction terms are given below:

$$\tau_{ij} = \frac{\mu M_\infty}{Re_\infty}\mu\left[\left(\frac{\partial u_i}{\partial x_j} + \frac{\partial u_i}{\partial x_j}\right) - \frac{2}{3}\frac{\partial u_k}{\partial x_k}\delta_{ij}\right] \tag{4.23}$$

$$q_j = -\frac{\mu M_\infty}{Re_\infty Pr\,(\gamma - 1)}\frac{\partial T}{\partial x_j} \tag{4.24}$$

All independent and dependent variables in the above two equations are non-dimensional, and the superscript * representation is not used. The new non-dimensional parameters that are formed as a result of non-dimensionalization are given below:

$$\text{Reynolds number :} \qquad Re_\infty = \frac{\rho_\infty V_\infty L}{\mu_\infty} \tag{4.25}$$

$$\text{Mach number :} \qquad M_\infty = \frac{V_\infty L}{a_\infty} \tag{4.26}$$

$$\text{Prandtl number :} \qquad Pr = \frac{\mu c_p}{k} \tag{4.27}$$

For air at standard temperature and pressure, the Prandtl number, $Pr = 0.72$. V_∞ is the freestream velocity magnitude given by $\sqrt{u_\infty^2 + v_\infty^2 + w_\infty^2}$.

4.4 Reynolds-Averaged Navier-Stokes Equations

Since the current work attempts to simulate boundary layer transition from a laminar to a turbulent state, the governing equations must be solved in a form that is suitable for turbulent flows. Direct Numerical Simulation (DNS) is one approach to resolve all the spatial and temporal scales present in a turbulent flow field. However, it is well established that DNS simulations are prohibitively expensive in terms of computational hardware and run times for flow problems at

relatively high Reynolds numbers. The Reynolds-Averaged Navier-Stokes (RANS) equations augmented with turbulence models present an affordable alternative to DNS simulations. In the RANS approach, dependent variables in the baseline governing equations (4.1) are decomposed into their mean and fluctuating components and the resulting equations are averaged over a period of time. The RANS approach has made routine simulations of complex industrial CFD simulations possible, and is used in this work.

In the Reynolds-averaging procedure, the mean or time-averaged quantity $\overline{f}$ is defined as:

$$\overline{f} = \frac{1}{\Delta t} \int_{t_o}^{t_o+\Delta t} f \; dt \tag{4.28}$$

The time-period Δt must be large compared to the period of turbulent fluctuations, but small compared to the time scales of mean flow variation in unsteady flows. By definition, the time-average of a fluctuating quantity is zero:

$$\overline{f'} = \frac{1}{\Delta t} \int_{t_o}^{t_o+\Delta t} f' \; dt = 0 \tag{4.29}$$

The following relations hold for sum and product of any two fluctuating quantities:

$$\overline{\overline{f} g'} = 0 \qquad \overline{\overline{f} g} = \overline{f}\,\overline{g} \qquad \overline{f+g} = \overline{f} + \overline{g} \tag{4.30}$$

The most important identity is that the time-average of the product of two fluctuating quantities is not zero:

$$\overline{f'f'} \neq 0 \quad \text{and} \quad \overline{f'g'} \neq 0 \tag{4.31}$$

In the Reynolds decomposition approach, dependent variables in the N-S equa-

tions are written as a sum of their mean and fluctuating components as shown below:

$$u = \overline{u} + u' \qquad v = \overline{v} + v' \qquad w = \overline{w} + w' \qquad \rho = \overline{\rho} + \rho' \qquad p = \overline{p} + p' \qquad T = \overline{T} + T' \tag{4.32}$$

The turbulence field is said to be isotropic when $u' = v' = w'$. Turbulent kinetic energy (k) is defined as follows:

$$k = \frac{1}{2}\left[\overline{(u_1')^2} + \overline{(v_1')^2} + \overline{(w_1')^2}\right] \tag{4.33}$$

Turbulence intensity or turbulence level (Tu) is defined as the ratio of the root-mean-square of turbulent velocity fluctuations (U') and the mean velocity magnitude (U):

$$Tu = \frac{U'}{U} \tag{4.34}$$

$$U' = \sqrt{\frac{1}{3}\left[(u')^2 + (v')^2 + (w')^2\right]} \quad \text{and} \quad U = \sqrt{(\overline{u})^2 + (\overline{v})^2 + (\overline{w})^2} \tag{4.35}$$

The freestream turbulence intensity value is typically stated as a percentage value by multiplying Tu with 100. It is a very useful quantity that is often measured in experiments and specified in numerical simulations of turbulent flows. The typical value of $Tu\%$ in cruise flight is less than 0.1% and in turbomachinery flows is between 2% and 6%.

Substitution of the Reynolds-decomposed dependent variables in Eq. 4.32 into the instantaneous, unsteady N-S equations in Eq. 4.1, followed by time-averaging of the equations gives rise to a new set of governing equations. These are known as the Reynolds-Averaged Navier-Stokes equations. They are almost identical in form to the unsteady N-S equations, with the addition of new terms that are functions of the turbulent fluctuating quantities. These additional terms behave as an apparent

stress tensor due to the transport of momentum by turbulent fluctuations. Hence they are commonly known as the Reynolds Stress Tensor (τ_{ij}), given by:

$$(\overline{\tau_{ij}})_{turb} = -\rho\overline{u_i' u_j'} \tag{4.36}$$

Closure to the RANS equations requires representation of the Reynolds stress tensor (τ_{ij}) in terms of the mean flow quantities. The area of research concerned with finding closure to the RANS equations is known as Turbulence Modeling and the specific methods of closure are called Turbulence Models. In this work, the one-equation Spalart-Allmaras turbulence model [35] is used to provide closure to the unsteady RANS equations. Details of turbulence modeling are be discussed later in section 4.9.3 of this chapter.

4.5 Curvilinear Coordinate Transformation

Although the Cartesian form of the N-S equations are applicable to any computational grid topology, it is sometimes necessary and convenient to rewrite them in a generalized, body-conforming coordinate system when using structured grids. Due to the definition of numerical spatial derivative stencils based on uniform grid spacing, they are not suitable for grids with non-uniform spacing and rapid stretching. A Curvilinear coordinate transformation maps the governing equations from a non-uniform spaced Cartesian domain (x,y,z) onto a computational domain (ξ, η, ζ) with equal grid spacing, as shown in Fig. 4.1. This is achieved by applying the chain-rule of differentiation on the Cartesian set of equations:

$$\frac{\partial \tilde{Q}}{\partial t} + \frac{\partial \tilde{F}}{\partial \xi} + \frac{\partial \tilde{G}}{\partial \eta} + \frac{\partial \tilde{H}}{\partial \zeta} = \tilde{S} \tag{4.37}$$

where,

$$
\begin{aligned}
\tilde{Q} &= \frac{1}{J}Q \\
\tilde{E} &= \frac{1}{J}\left[\xi_t Q + \xi_x(F_i - F_v) + \xi_y(G_i - G_v) + \xi_z(H_i - H_v)\right] \\
\tilde{F} &= \frac{1}{J}\left[\eta_t Q + \eta_x(F_i - F_v) + \eta_y(G_i - G_v) + \eta_z(H_i - H_v)\right] \\
\tilde{G} &= \frac{1}{J}\left[\zeta_t Q + \zeta_x(F_i - F_v) + \zeta_y(G_i - G_v) + \zeta_z(H_i - H_v)\right] \\
\tilde{S} &= \frac{1}{J}S
\end{aligned}
\tag{4.38}
$$

J is the Jacobian of the coordinate transformation, defined by the determinant of the 3×3 matrix $\dfrac{\partial(\xi,\eta,\zeta)}{\partial(x,y,z)}$.

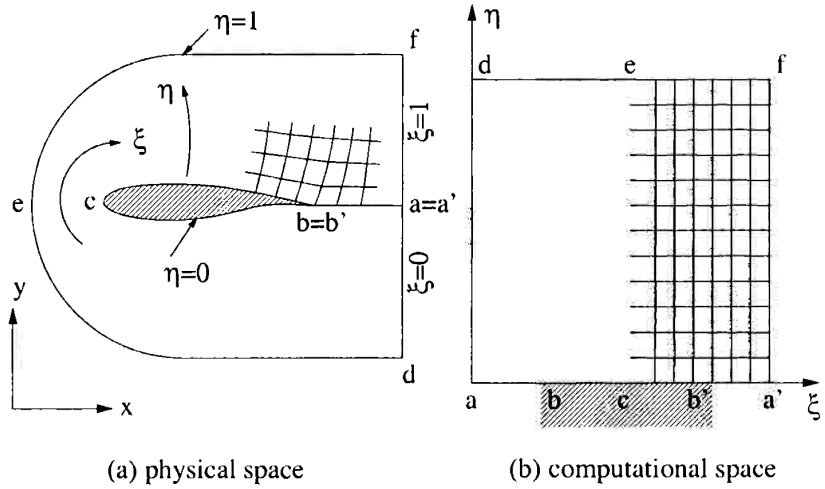

Figure 4.1: Curvilinear mapping of physical space onto computational space (reproduced from [85])

4.6 Mesh Topology

In this thesis, RANS simulations are performed for external turbulent flows past lifting surfaces such as 2-D airfoil sections, and 3-D fixed wings and rotating blades. A hyperbolic technique is used to create structured, body-fitted C-topology

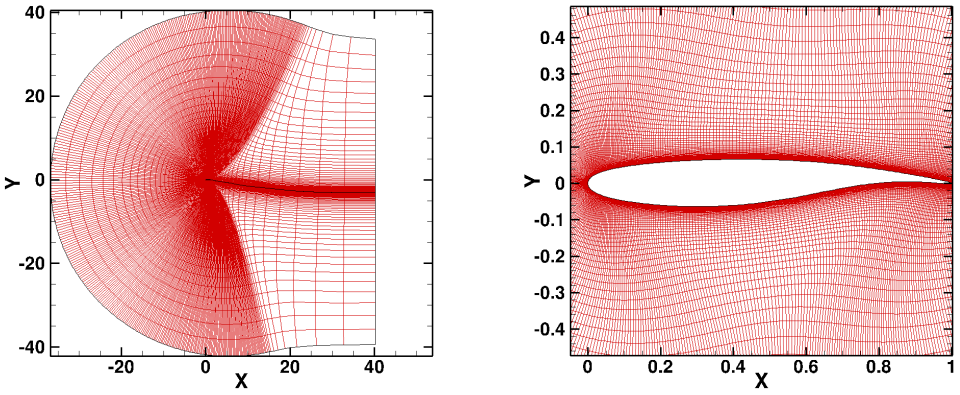

(a) Farfield boundary at 40 chord lengths from airfoil

(b) Close-up of C-mesh

Figure 4.2: Structured, C-topology, 2-D mesh around an airfoil section

meshes around 2-D airfoil sections as shown in Fig. 4.2. A typical C-topology mesh contains one physical boundary (solid wall) and two numerical boundaries (wake-cut and farfield). Numerical treatment of these boundaries is discussed in section 4.9.7 of this chapter. For 3-D rotor blades, several C-mesh sections are stacked in the spanwise direction. Near the blade root and tip regions, the C-meshes sections are rotated about the chordwise axis such that the upper and the lower surface planes collapse into a single plane as shown in Fig. 4.3. This is known as a C-O topology. The main benefit of using a C-O topology mesh for finite wings and blades is that it can provide sufficient resolution to capture root and tip vortices in a computationally efficient manner, while providing sufficient RANS grid resolution to resolve the boundary layer of the root and tip caps. In 3-D rotor simulations, the blade mesh is embedded into a cylindrical background mesh as shown in Fig. 4.4. The purpose of using a background mesh is to capture the root and tip vortices of

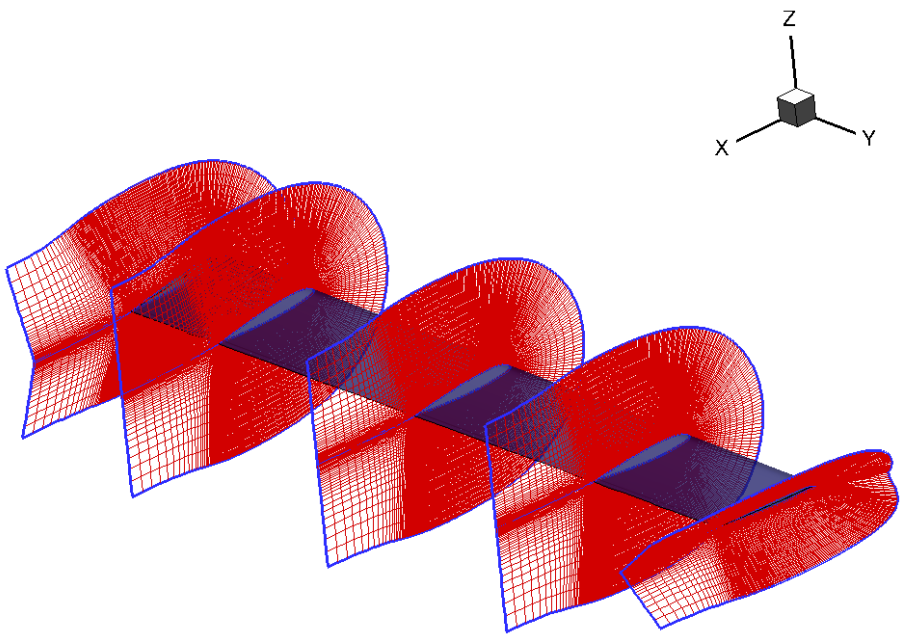

(a) Stacked C-mesh sections along blade span collapsing towards root and tip

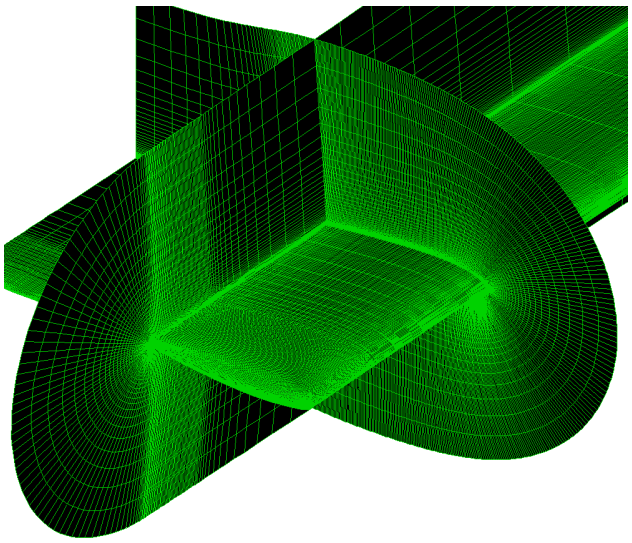

(b) Mesh clustering near blade tip

Figure 4.3: Structured, C-O topology, 3-D mesh on a rotor blade

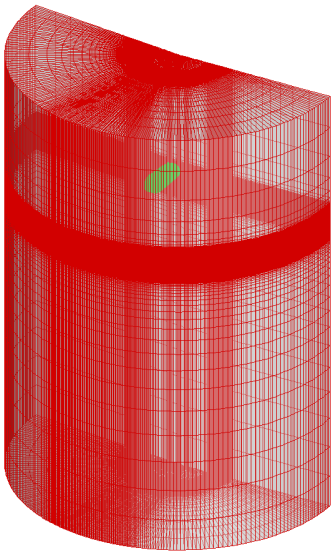

(a) Isometric view

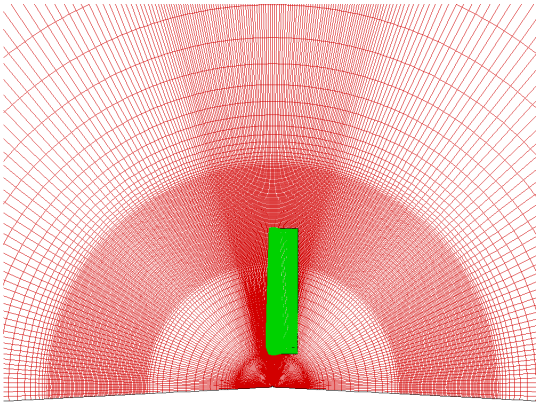

(b) Top view

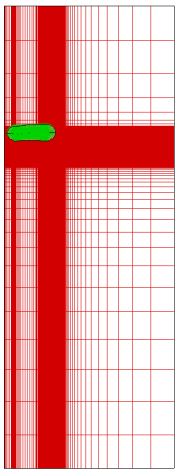

(c) Azimuthal view

Figure 4.4: Overset mesh system for rotor blades. Green – C-O topology blade mesh, Red – Cylindrical background mesh for wake capture

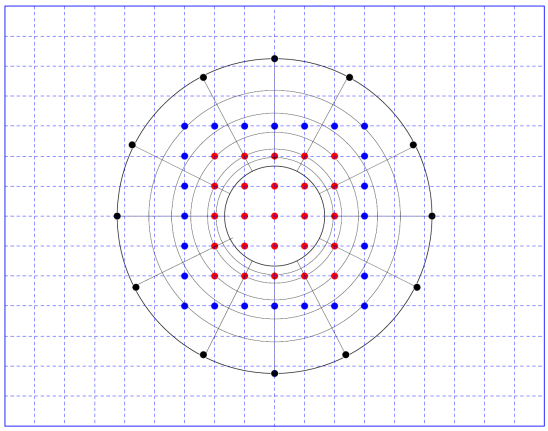

Figure 4.5: Schematic of Chimera hole-cutting technique. Red circles: Hole points, Blue circles: Hole fringe points, Black circles: Chimera boundary points. (reproduced from [86])

the rotor wake system. Such overlapping mesh systems are knows as Chimera or Overset meshes. Specific details of mesh sizes and placement will be provided when discussing simulation details and results for each test case in Chapters 5 and 6.

4.7 Overset Mesh Methodology

Overset or Chimera meshes are a set of independent computational domains on which the governing equations are solved. They are considered as an alternative to unstructured meshes for complex geometries and adaptive mesh refinement techniques. Overset meshes are often used in scenarios where using a single mesh is either not feasible or is computationally expensive. Some examples where overset meshes are advantageous include multi-element airfoils and single and multi-rotor flow environments that include a wake system. An Overset methodology typically

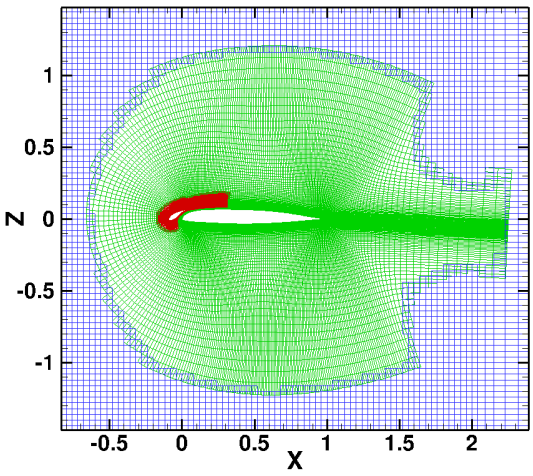

(a) Hole-cutting for wind tunnel mesh

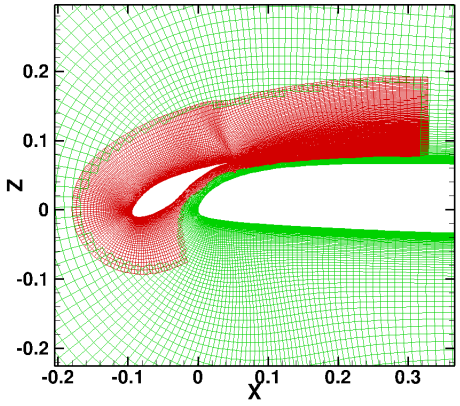

(b) Hole-cutting for multi-element airfoil

Figure 4.6: Hole-cutting for a multi-element airfoil in a background wind-tunnel mesh. Red: Leading-edge slat mesh, Green: Main element, Blue: Wind tunnel mesh

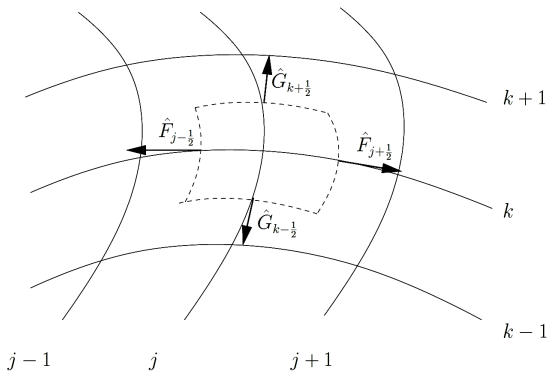

Figure 4.7: Schematic of a computational cell on a structured mesh. (reproduced from [86])

involves three major steps: (1) hole cutting, (2) identification of hole fringe and chimera boundary points, and (3) finding donor cells and interpolation weights.

The hole cutting step involves defining *hole* regions that lie inside solid walls and identifying the grid points of all the meshes that lie inside these hole regions. These hole points are excluded from being a part of the flow solution. Once the hole points are identified on each mesh, a list of hole fringe points are marked to receive information from other meshes. This step ensures that the grid points adjacent to a hole region have a numerical boundary condition. It also serves as a means to propagate information across the overlapping meshes. The final step involves identifying donor cells for the hole fringe points on each mesh. These donor cells are chosen from the other meshes using a search algorithm and ensure that the donor cells have similar cell volumes to the hole fringe points that receive flow information. For each hole fringe point, information from donor cells is transferred as a weighted sum based on linear interpolation. Grids points on the body mesh that

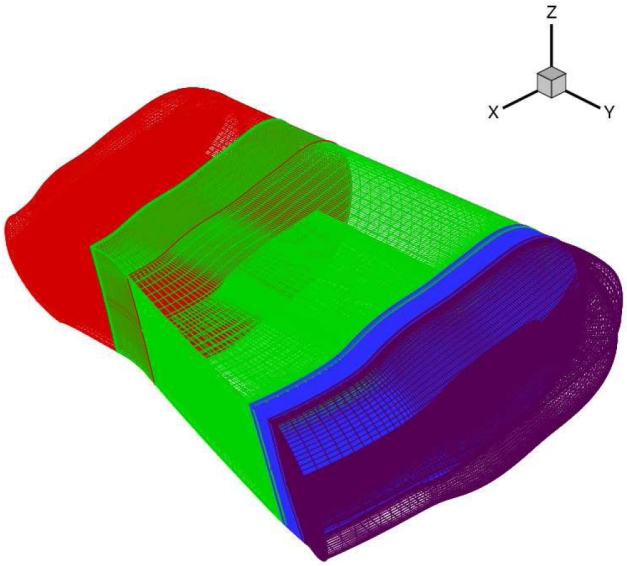

Figure 4.8: Spanwise domain decomposition of a C-O topology rotor blade mesh. Each color represents a sub-domain that is solved on a separate processor.

require information from other meshes are called Chimera points. Figure 4.5 shows a schematic of the procedure described for the Chimera hole-cutting technique. A detailed discussion on the exact overset mesh algorithm, known as Implicit Hole Cutting (IHC), and its numerical implementation in the OverTURNS flow solver is available is [86, 87]. Figure 4.6 shows an application of the Implicit Hole Cutting technique to a multi-element airfoil embedded in a background wind tunnel mesh.

4.8 Parallelization

The OverTURNS code is written using the FORTRAN 77/90 programming language in a modular fashion. The code is parallelized using the Message Passing Interface (MPI) library. It is capable of running on multiple processors simulta-

neously to solve a problem using the domain decomposition approach. In this approach, the computational domain is divided into several similarly sized blocks and solved as sub-problems. Each processor is assigned the job of solving the governing equations on a unique mesh block. At the end of each time step, the exchange of relevant data between blocks sharing a common interface is handled by the MPI implementation. Figure 4.8 shows a C-O topology blade mesh split into multiple blocks along the blade span. In wall-bounded flow domains such as rotor blade meshes, domain decomposition is done only in the spanwise direction since splitting in the wall-normal direction may affect solution convergence and accuracy, due to the presence of strong gradients in the boundary layer.

4.9 Numerical Algorithms in OverTURNS

This section describes the various numerical algorithms for spatial and temporal discretization of the governing equations, turbulence modeling, numerical boundary conditions, and convergence acceleration techniques available in the OverTURNS flow solver. The Curvilinear form of the RANS equations are solved using a cell-averaged finite-volume technique. The control volume is a computational cell defined around each grid point on a structured mesh. This cell is created by joining the mid-points of the edges of the mesh, as shown in Fig. 4.7. Inviscid and viscous fluxes are evaluated at the interfaces of this computational cell, and integrated over all faces of a cell to obtain the time rate of change of the conserved quantities at

each timestep. The resulting semi-discrete form of Eq. 4.37 is given below:

$$\frac{\partial \tilde{Q}}{\partial t} = -\frac{\tilde{F}_{j+\frac{1}{2}} - \tilde{F}_{j-\frac{1}{2}}}{\Delta\xi} - \frac{\tilde{G}_{k+\frac{1}{2}} - \tilde{G}_{k-\frac{1}{2}}}{\Delta\eta} - \frac{\tilde{F}_{l+\frac{1}{2}} - \tilde{H}_{l-\frac{1}{2}}}{\Delta\zeta} + \tilde{S}_{j,k,l} \tag{4.39}$$

where, (j,k,l) are the indices corresponding to the grid points in (ξ, η, ζ) directions respectively and $(j \pm \frac{1}{2}, l \pm \frac{1}{2}, l \pm \frac{1}{2})$ define the interfaces of the computational cell. Spatial discretization techniques used to evaluate the invscid and viscous flux contributions at each cell face are described in the following two sections.

4.9.1 Inviscid Fluxes

Evaluation of inviscid fluxes (Eq. 4.4–4.6) in OverTURNS involves two steps: (1) reconstruction of the primitive variables at cell faces, and (2) evaluation of the fluxes at cell faces using reconstructed primitive variables. Reconstruction schemes for systems with hyperbolic properties are often based on some form of upwinding, through inclusion of explicit or implicit dissipation terms. This ensures that the numerical scheme respects the direction of wave propagation and uses information only from the upstream direction. In this work, the third-order Monotone Upstream-Centered Scheme for Conservation Laws (MUSCL) [88] is used for the reconstruction of left and right states, $(\mathrm{q}^L_{i+\frac{1}{2}}, \mathrm{q}^R_{i-\frac{1}{2}})$ at each cell face as a function of the cell-averaged values $(\overline{q}_{i-1}, \overline{q}_i, \overline{q}_{i+1})$:

$$q^L_{i+\frac{1}{2}} = \overline{q} + \phi_i \left[\frac{1}{3}(\overline{q}_{i+1} - \overline{q_i}) + \frac{1}{6}(\overline{q}_i - \overline{q_{i-1}})\right] \tag{4.40}$$

$$q^R_{i-\frac{1}{2}} = \overline{q} - \phi_i \left[\frac{1}{3}(\overline{q}_{i+1} - \overline{q_i}) + \frac{1}{6}(\overline{q}_i - \overline{q_{i-1}})\right] \tag{4.41}$$

where, ϕ is Koren's differentiable limiter [89] given by:

$$\phi_i = \frac{3\Delta\overline{q_i}\nabla\overline{q_i} + \epsilon}{2(\Delta\overline{q_i} - \nabla\overline{q_i})^2 + 3\Delta\overline{q_i}\nabla\overline{q_i} + \epsilon} \tag{4.42}$$

ϵ is a small number used to prevent division by zero, and Δ and ∇ are forward and backward difference operators defined by $\Delta\overline{q}_i = (\overline{q}_{i+1} - \overline{q}_i)$ and $\nabla\overline{q}_i = (\overline{q}_i - \overline{q}_{i-1})$ The reconstructed left and right states are used to compute inviscid fluxes at each cell face using Roe's flux difference splitting scheme with an entropy fix [90], as shown below:

$$F(q^L, q^R) = \frac{F(q^L) + F(q^R)}{2} - |\tilde{A}(q^L, q^R)|\frac{q^R - q^L}{2} \tag{4.43}$$

where, F_L and F_R are the left and right state fluxes, and $\tilde{A}$ is the Roe-averaged Jacobian matrix. The second term on the right-hand side of the above equation represents numerical dissipation. Harten's entropy correction to Eigenvalues of the flux Jacobian is given by [91]:

$$|\lambda| = \begin{cases} |\lambda|, & \text{if } |\lambda| > \delta \\ \dfrac{\lambda^2 + \delta^2}{2\delta}, & \text{if } |\lambda| \leq \delta \end{cases} \tag{4.44}$$

where, $\delta = \max\left[0, (\overline{\lambda}_{i+1/2} - \lambda_i), (\overline{\lambda}_{i+1} - \lambda_{i+1/2})\right]$. The overbar on λ indicates Roe-averaged Eigenvalues.

4.9.2 Viscous Fluxes

Viscous fluxes (Eq. 4.7–4.9) in the Curvilinear form of governing equations contain derviative terms of the form:

$$\frac{\partial}{\partial\xi}\left(\alpha\frac{\partial\beta}{\partial\eta}\right) \tag{4.45}$$

They are evaluated using a second order central differencing scheme as shown below:

$$\frac{1}{\Delta\xi}\left(\left[\alpha_{j+\frac{1}{2},k}\frac{\beta_{j+\frac{1}{2},k+1}-\beta_{j+\frac{1}{2},k}}{\Delta\eta}\right]-\left[\alpha_{j-\frac{1}{2},k}\frac{\beta_{j-\frac{1}{2},k}-\beta_{j-\frac{1}{2},k-1}}{\Delta\eta}\right]\right) \tag{4.46}$$

where, $\delta_{j+\frac{1}{2},k}=\dfrac{\delta_{j,k}+\delta_{j+1,k}}{2}$ and $\delta=(\alpha,\beta)$.

4.9.3 Turbulence Modeling

One approach to turbulence closure of the RANS equations is to solve six additional transport equations, one for each of the stress tensor components, along with an equation for the energy dissipation rate. These models are categorized as Reynolds Stress Models (RSM) [92, 93]. Although Reynolds stress models adopt the most physically realistic approach to turbulence modeling, they are expensive and suffer from issues of robustness and convergence. A more common approach to turbulence modeling is based on the use of the Boussinesq eddy viscosity hypothesis, which relates the Reynolds stress tensor to the mean strain rate as follows:

$$(\overline{\tau_{ij}})_{\text{turb}}=-\overline{\rho}\overline{u_i'u_j'}=\frac{2}{3}\overline{\rho}k\delta_{ij}-\mu_t\left[\left(\frac{\partial\overline{u_i}}{\partial x_j}+\frac{\partial\overline{u_i}}{\partial x_j}\right)-\frac{2}{3}\frac{\partial\overline{u_k}}{\partial x_k}\delta_{ij}\right] \tag{4.47}$$

where, k is the turbulent kinetic energy (Eq. 4.33), and μ_t is a scalar value known as the turbulent or eddy viscosity. With this assumption, the final form of the total viscous stress tensor in the RANS equations becomes:

$$(\tau_{ij})_{\text{total}}=\frac{2}{3}\overline{\rho}k\delta_{ij}-(\mu+\mu_t)\left[\left(\frac{\partial\overline{u_i}}{\partial x_j}+\frac{\partial\overline{u_i}}{\partial x_j}\right)-\frac{2}{3}\frac{\partial\overline{u_k}}{\partial x_k}\delta_{ij}\right] \tag{4.48}$$

The turbulent kinetic energy term on the right-hand side is typically absorbed into the pressure term of the inviscid fluxes (Eq. 4.4–4.6). This approach assumes

isotropic turbulence, which causes it to perform poorly for flows with significant turbulence anisotropy, such as decelerating boundary layers. Turbulence modeling research in the past few decades has produced hundreds of models to evaluate turbulent kinetic energy and eddy viscosity in the flow field as a function of mean flow quantities. These models range from zero-equation algebraic expressions such as the Baldwin-Lomax model [94] to the four-equation $\nu^2 - f$ model [95]. Most of the turbulence models are calibrated to match theoretical solutions and experimental data for canonical flows such as boundary layers and free shear layers. Therefore, a significant level of empiricism is present in turbulence modeling. Two of the most widely used models in aerospace applications are the one-equation Spalart-Allmaras (SA) model [35] and the two-equation k-ω SST model [34], along with their variations. They are based on solving additional transport equations to compute eddy viscosity and turbulent kinetic energy, and are known for their accuracy and numerical robustness for many internal and external flow problems. These two models along with the algebraic Baldwin-Lomax model are available in the current RANS flow solver. Details of the k-ω SST model and the SA model are presented in Chapter 3. In this work, all turbulence model equations are discretized using a first order upwind scheme for the convection terms and a second order central scheme for the diffusion terms. The Diagonally Dominant Alternating Direction Implicit (DDADI) approximate factorization method [96] is then used to solve the algebraic system of equations.

4.9.4 Time Integration

After the inviscid and viscous fluxes on the right hand side of Eq. 4.39 are evaluated, the semi-discrete equation is integrated using a second-order accurate backwards in time method (also knowns as BDF2). Backwards-in-time methods are known as implicit time marching methods. They are more suited for boundary layer flows due to their superior stability and convergence characteristics compared to explicit time integration methods. In implicit methods, fluxes and source terms on the right-hand side of the semi-discrete equation are evaluated at the new time level, $n+1$. The resulting non-linear equation obtained using the BDF2 method is shown below:

$$\frac{\partial \tilde{Q}^{n+1}}{\partial t} = -\frac{\tilde{F}^{n+1}_{j+\frac{1}{2}} - \tilde{F}^{n+1}_{j-\frac{1}{2}}}{\Delta\xi} - \frac{\tilde{G}^{n+1}_{k+\frac{1}{2}} - \tilde{G}^{n+1}_{k-\frac{1}{2}}}{\Delta\eta} - \frac{\tilde{F}^{n+1}_{l+\frac{1}{2}} - \tilde{H}^{n+1}_{l-\frac{1}{2}}}{\Delta\zeta} + \tilde{S}^{n+1}_{j,k,l} \tag{4.49}$$

where,

$$\frac{\partial \tilde{Q}^{n+1}}{\partial t} = \frac{3\tilde{Q}^{n+1} - 4\tilde{Q}^{n} + \tilde{Q}^{n-1}}{2\Delta t} \tag{4.50}$$

The above non-linear equation is linearized in time using a Taylor series expansion about $\tilde{Q}^n$ as follows:

$$\tilde{F}^{n+1} = \tilde{F}^{n} + \tilde{A}\Delta\tilde{Q} + O(\Delta t^2) \tag{4.51}$$

$$\tilde{G}^{n+1} = \tilde{G}^{n} + \tilde{B}\Delta\tilde{Q} + O(\Delta t^2) \tag{4.52}$$

$$\tilde{H}^{n+1} = \tilde{G}^{n} + \tilde{C}\Delta\tilde{Q} + O(\Delta t^2) \tag{4.53}$$

where, $\Delta\tilde{Q} = \tilde{Q}^{n+1} - \tilde{Q}^{n}$ is the solution update, and A, B, C are the flux Jacobians given by $\frac{\partial\tilde{F}}{\partial\tilde{Q}}$, $\frac{\partial\tilde{G}}{\partial\tilde{Q}}$, and $\frac{\partial\tilde{H}}{\partial\tilde{Q}}$ respectively. The source term, S is also linearized in

a similar manner. Since the linearization operator is second-order accurate, it will not further degrade the time-accuracy of the BDF2 scheme. The linearized form of Eq. 4.49 in terms of the solution update, $\Delta\tilde{Q}$, is given by:

$$[I + \Delta t(\delta_\xi \tilde{A}^n + \delta_\eta \tilde{B}^n + \delta_\zeta \tilde{C}^n)]\Delta\tilde{Q} = -\Delta t[\delta_\xi \tilde{F}^n + \delta_\eta \tilde{G}^n + \delta_\zeta \tilde{H}^n] \tag{4.54}$$

The right-hand side of the above equation represents the physics of the flow field, and the left-hand side represents the numerics responsible for stability and convergence of the solution.

The above system of equations produces a banded matrix of algebraic equations that is solved using an approximate factorization method. In this work, the Lower-Upper Symmetric Gauss-Seidel (LUSGS) method [97] is used to invert the system of equations. In the LUSGS algorithm, the left-hand side of the equations is factorized by grouping terms into a lower diagonal (L), an upper diagonal (U), and a main diagonal (D) as follows:

$$[L + D + U]\Delta\tilde{Q}^n \approx [D + L]D^{-1}[D + U]\Delta\tilde{Q}^n = -\Delta t[RHS]^n \tag{4.55}$$

where,

$$L = \Delta t(-\tilde{A}^+_{j-1,k,l} - \tilde{B}^+_{j,k-1,l} - \tilde{C}^+_{j,k,l-1}) \tag{4.56}$$

$$U = \Delta t(\tilde{A}^-_{j+1,k,l} + \tilde{B}^-_{j,k+1,l} + \tilde{C}^-_{j,k,l+1}) \tag{4.57}$$

$$D = I + \Delta t(\tilde{A}^+_{j,k,l} - \tilde{A}^-_{j,k,l} + \tilde{B}^+_{j,k,l} - \tilde{B}^-_{j,k,l} + \tilde{C}^+_{j,k,l} - \tilde{C}^-_{j,k,l}) \tag{4.58}$$

This two-factor system is solved to obtain the solution update ($\Delta\tilde{Q}$) using a two-step procedure as shown below:

$$[D + L]\Delta\overline{\overline{Q}} = -\Delta t[RHS]^n \tag{4.59}$$

$$[D+U]\Delta\tilde{Q} = D\Delta\overline{\overline{Q}} \tag{4.60}$$

Since L, D, and U are block matrices of size 5×5 for the 3-D N-S equations and 4×4 for the 2-D N-S equations, inverting the above two equations is computationally expensive. In OverTURNS, the main diagonal (D) is reduced to a scalar value using the spectral radius approximation for the flux Jacobian matrices (A, B, C) as follows:

$$\tilde{A}^{+} = \frac{1}{2}(\tilde{A} + \sigma_{\xi}), \qquad \tilde{A}^{-} = \frac{1}{2}(\tilde{A} - \sigma_{\xi}) \tag{4.61}$$

$$\sigma_{\xi} = |U_{\xi}| + c + \frac{2\mu(\xi_x^2 + \xi_y^2 + \xi_z^2)}{\rho} \tag{4.62}$$

where, U_{ξ} is the contravariant velocity in the ξ-direction (and similarly for B and C).

To eliminate errors due to approximate factorization, a dual-time stepping method with Newton-like sub-iterations is used in time-accurate simulations to compute the transient solution [98]. The governing equations are discretized in pseudo-time using a backwards Euler time marching method as follows:

$$\frac{\tilde{Q}^{p+1} - \tilde{Q}^{p}}{\Delta\tau} + \frac{3\tilde{Q}^{p+1} - 4\tilde{Q}^{n} + \tilde{Q}^{n-1}}{2\Delta t} = -\frac{\tilde{F}^{p+1}_{j+\frac{1}{2}} - \tilde{F}^{p+1}_{j-\frac{1}{2}}}{\Delta\xi} - \frac{\tilde{G}^{p+1}_{k+\frac{1}{2}} - \tilde{G}^{p+1}_{k-\frac{1}{2}}}{\Delta\eta} - \frac{\tilde{F}^{p+1}_{l+\frac{1}{2}} - \tilde{H}^{p+1}_{l-\frac{1}{2}}}{\Delta\zeta} + \tilde{S}^{p+1}_{j,k,l} \tag{4.63}$$

At each time level n, p number of sub-iterations are performed to advance the solution to the new time level, $n+1$. $\tilde{Q}^{p}$ at the first sub-iteration (p = 1) is set to $\tilde{Q}^{n}$. Each sub-iteration involves the evaluation of the right-hand side fluxes and the source terms, followed by the inversion of the algebraic system of equations using the approximate factorization method. The dual time-stepping process is essentially equivalent to solving a steady state problem at solution time $t+\Delta t$ with the solution

at time Δt as the initial condition.

4.9.5 Convergence Acceleration for Low-Speed Flows

The methodology presented above is designed to numerically solve the compressible N-S equations in subsonic and transonic flow regimes. However, when it is applied to low-Mach number flows (essentially incompressible flows), convergence significantly slows down due to the large ratio between the acoustic wave speed and the convective wave speed of the Euler equations. In addition, at low Mach numbers, dissipation terms in the Roe flux difference splitting scheme (Eq. 4.43) do not scale down, causing excessive dissipation and increasing the solution error. To alleviate convergence and accuracy issues when simulating incompressible flows, the current approach uses Turkel's preconditioning technique [99]. A very thorough verification and validation study of the low-Mach preconditioning technique implementation in OverTURNS is presented [86]. In this work, the low-Mach preconditioning algorithm was used to simulate the wind turbine rotor flow discussed in Chapter 6.

4.9.6 Initial Conditions

The unsteady Navier-Stokes equations represent an Initial Boundary Value Problem (IBVP), which means that the evolution of the solution in time is influenced by the initial conditions and boundary conditions specified in the computational domain. This section describes the manner in which the initial conditions are specified. To perform the time integration of the Navier-Stokes equations, an

initial flow field consisting of the primitive variables (ρ, u, v, w, p) must be specified at each grid point. In this work, two types of problems are solved: (1) steady-state, and (2) transient (or time-accurate). For steady state simulations, initial conditions do not affect the converged solution. However, a good choice of initial conditions can improve the convergence behavior of a steady-state simulation. In simulations of external aerodynamic flows, the entire flow field is typically initialized with the freestream values. Since the non-dimensionalized N-S equations are used in this work, initial values of (u, v, w) are deduced from freestream Mach number components along the Cartesian coordinate directions. For the current choice of reference quantities, it can be shown that freestream density (ρ_∞) is unity and freestream pressure (p_∞) is $\frac{1}{\gamma}$, where $\gamma = 1.4$ is the ratio of specific heats for air at standard temperature and pressure.

4.9.7 Boundary Conditions

This section presents the numerical treatment of the physical and artificial boundaries that were part of the current simulations. Examples of physical boundary conditions are the specification of primitive variables on a solid wall boundary through a no-slip condition or an adiabatic/isothermal requirement. Artificial boundaries such as an inlet or outlet are created due to the truncation of the computational domain to a finite size. Numerical boundary conditions such as a wake-cut in a C-topology mesh or axisymmetry/periodicity are a consequence of either the grid topology or the nature of the flow problem. In this section, the discussion of

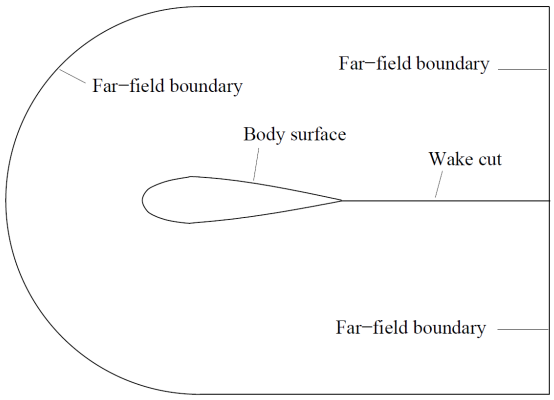

Figure 4.9: Boundary conditions on a structured C-topology mesh (reproduced from [86])

boundary conditions is limited to those arising in external flow problems simulated on a structured mesh.

As mentioned in the mesh topology section (Sec. 4.6), a structured, 2-D, C-topology mesh is for airfoil geometries. The three boundary conditions specified on a C-mesh are shown in Fig. 4.9.

Wall Boundary

At a viscous solid wall, the no-slip and no-penetration conditions are enforced. All velocity components are set to zero for grid points on a stationary wall boundary. For moving walls, the velocity components are set to based on the surface motion. Density is extrapolated from the interior of the domain. Pressure on wall boundary is obtained either by extrapolation or by solving the normal momentum equation [91].

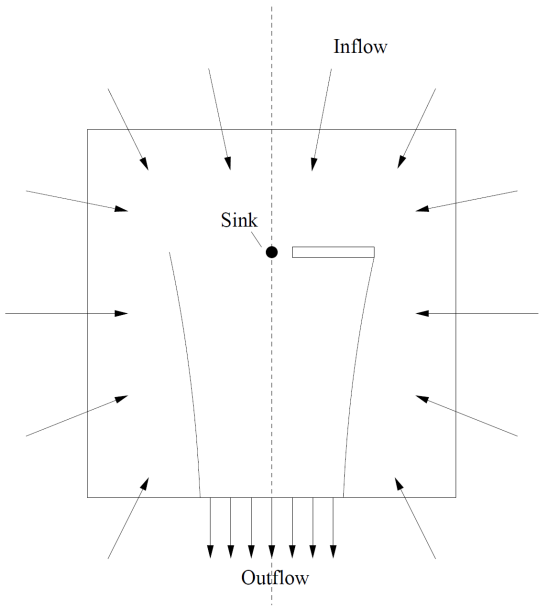

Figure 4.10: Schematic of point-sink boundary condition for downstream boundary of rotor wake mesh (reproduced from [86])

Wake-cut Boundary

A key component of a C-topology mesh is its wake-cut adjacent to the solid wall boundary. It consists of two identical grid lines overlapping in the same physical space. Since the wake-cut is an artifact of the topology, continuity of flow must be ensured across this "boundary". In OverTURNS, this is achieved by an explicit averaging of the solution on grid points from either side of the wake-cut and setting the two overlapping grid lines to the averaged solution. A wake-cut boundary also appears in a C-O topology blade mesh, on the collapsed planes at root and tip.

Far-field Boundary

In external flow simulations, the computational domain is truncated to a finite size, thus creating an artificial boundary. Specification of such a boundary condition must ensure that no spurious information propagates across the boundary: (1) waves that are going out of the domain must be allowed to pass through without any spurious reflections back into the domain, (2) only physical disturbances must be propagated into the domain from the exterior. In this work, non-reflecting boundary conditions based on one-dimensional Riemann invariants are used at far-field boundaries [91]. These boundary conditions are strictly designed to allow small disturbances to pass through the far-field boundary in the absence of strong mean flow gradients approaching the boundary. Therefore, meshes for external flow problems are typically generated with the far-field boundary located at large distances from regions of flow activity, such as flow past a solid body. Mesh stretching is also employed towards the far-field boundary to numerically dissipate strong flow gradients.

In the case of rotor simulations carried out in this thesis, a background mesh is used to capture the rotor blade root and tip vortices. To reduce computational cost, the far-field boundaries of the background mesh are placed at a distance of 5 times the rotor radius from the blades. This distance may not be sufficient to apply boundary conditions based on Riemann invariants. Instead, a point-sink boundary condition [83] is used in OverTURNS to allow the rotor wake to pass through the downstream boundary without reflections. A schematic of this approach

is shown in Fig. 4.10. Momentum theory analysis of rotor flow shows that the rotor wake contracts asymptotically in the far-field to an area that is equal to half of the rotor disk area. The corresponding downwash velocity at this location is approximately equal to $2\sqrt{C_T/2}$, where C_T is the rotor thrust coefficient. The key idea of this approach is to assume that the rotor is a point sink that induces flow into the computational domain from all boundaries except the downstream far-field boundary, labeled as "Outflow" in the schematic. To satisfy global mass conservation, an exit velocity is specified at the outflow boundary, whose magnitude is given by:

$$V_{\text{induced}} = \frac{1}{4}\sqrt{\frac{C_T}{2}}\left[\frac{R^2}{x^2+y^2+z^2}\right] \tag{4.64}$$

Riemann invariants are then used to compute all the primitive variables at this boundary.

Periodic Boundary

In all rotor simulations under axial flow conditions, flow is assumed to be periodic in the azimuthal direction. The size of the period in azimuthal space is dependent on the number of blades in the rotor. For example, the flow is periodic every 90° for a 4-bladed rotor. More generally, for an N-bladed rotor, the azimuthal period is $\frac{2\pi}{N}$ degrees. Therefore, in this work, only one period of a rotor flow field is simulated for a given rotor configuration. This is done by simulating only one rotor blade, enclosed in a background mesh that spans one period in the azimuthal direction. Periodic boundary conditions are applied at the ends of the background

mesh in this direction.

4.10 Summary

Details of the governing equations and their numerical solution methodology in the OverTURNS flow solver were summarized in this chapter. Techniques specific to three-dimensional rotor simulations were presented. Discussion also included advanced algorithms such as Implicit Hole Cutting and low-Mach preconditioning that were used in this work. In the next chapter, results will be presented for several two-dimensional airfoil simulations using the new transition model implemented in the OVERTURNS flow solver.

5 Two-dimensional Airfoil Simulations

This chapter demonstrates the ability of the $\gamma - Re_\theta -$ SA model to predict streamwise transition due to freestream turbulence and pressure gradient effects over a wide range of flow conditions and geometries taken from a diverse set of experimental sources. Reynolds number of these test cases varies from 10^5 to 50×10^6. Two-dimensional simulations of steady, subsonic flow past several single and multi-element airfoil sections are performed using the baseline S-A model and the $\gamma - Re_\theta -$SA model. CFD predictions are compared with available experimental data for quantities such as lift, drag, skin friction coefficient, and transition onset locations. Table 5.1 gives the freestream Mach Number, Reynolds number, turbulence intensity, and angles of attack for each test case.

5.1 Computational Grids

Structured, body-fitted, C-topology grids are used for airfoils in all the test cases presented in this chapter. In the wrap-around direction of the C-mesh, 400 grid points are used on the airfoil surface. This grid resolution was determined to be sufficient to capture small regions of laminar-separation bubbles seen in transi-

Airfoil	Mach Number	Reynolds Number ($\times 10^6$)	Tu (%)	Angle of Attack
Aerospatiale–A	0.15	2.1	0.05	13.3°
VA-2	0.2	2.0	0.5	-0.5°, 3.5°, 7.5°, 11.5°
S809	0.1	2.0	0.05	0° to stall
Epper 387	0.1	0.2, 0.35, 0.5	0.03	0° to stall
NACA 64_2(A)015	0.27	5.0 – 50.0	0.03	0.0°, 1.0°
MD 30P–30N	0.2	9.0	0.05	8.1°
SC2110 w/ Slat	0.28	4.1	0.5	0° to stall

Table 5.1: Two-dimensional airfoil test cases

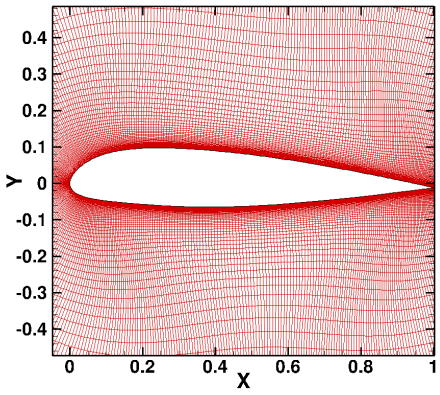

(a) Aerospatiale-A

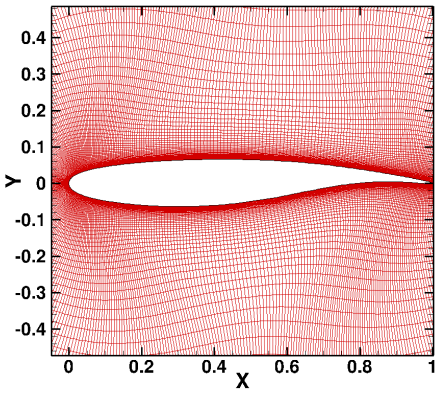

(b) VA-2

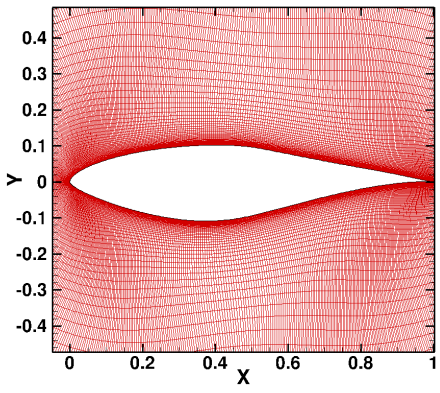

(c) S809

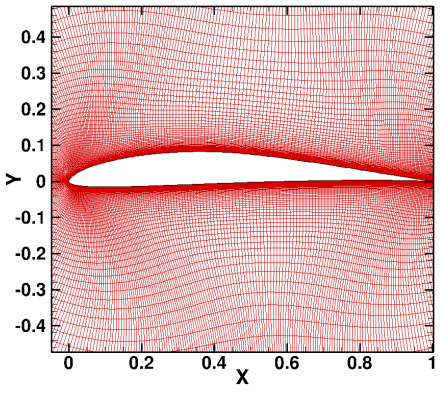

(d) E387

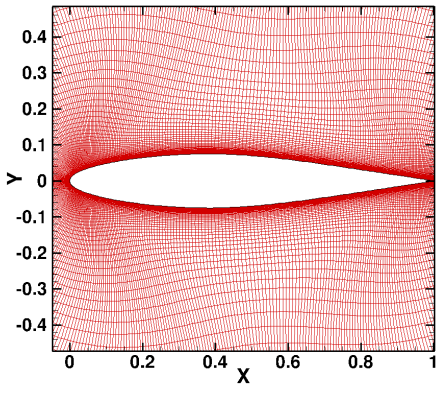

(e) NACA 64_2A015

Figure 5.1: Computational meshes for single-element airfoil simulations

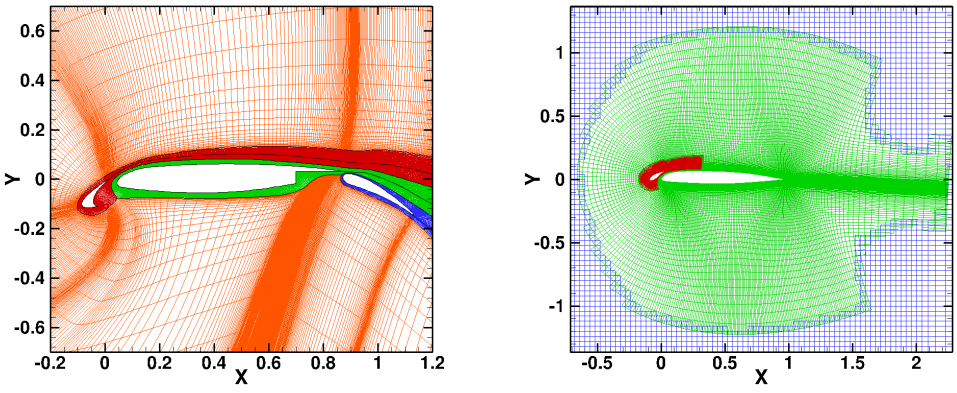

(a) MD 30P–30N – Block-structured mesh system

(b) SC2110 w/ LE slat – Overset mesh system

Figure 5.2: Computational meshes used for multi-element airfoil simulations

tional boundary layers, while ensuring a grid-converged solution. In the wall normal direction, the wall grid spacing is chosen such that a y^+ value of less than 1 is maintained based on the Reynolds number for each test case. For airfoil simulations in freestream, the outer boundary of the C-mesh is placed 40 chords away from the airfoil surface to avoid any spurious wave reflections. Computational grids for all the test cases simulated in this chapter are shown in Figs. 5.1 and 5.2. In the case of the SC2110 airfoil with a leading-edge slat, experimental data was not corrected for wind tunnel wall effects. Therefore, for this case, an overset mesh system consisting of a C-mesh around the airfoil and a rectangular background mesh for the wind tunnel is used as shown in Fig. 5.2(b). Data transfer between the airfoil mesh and the wind tunnel mesh is handled using the improved Implicit Hole Cutting (IHC) methodology described in the numerical methodology chapter. A Cartesian mesh is used to model the wind tunnel walls in the background of the airfoil mesh,

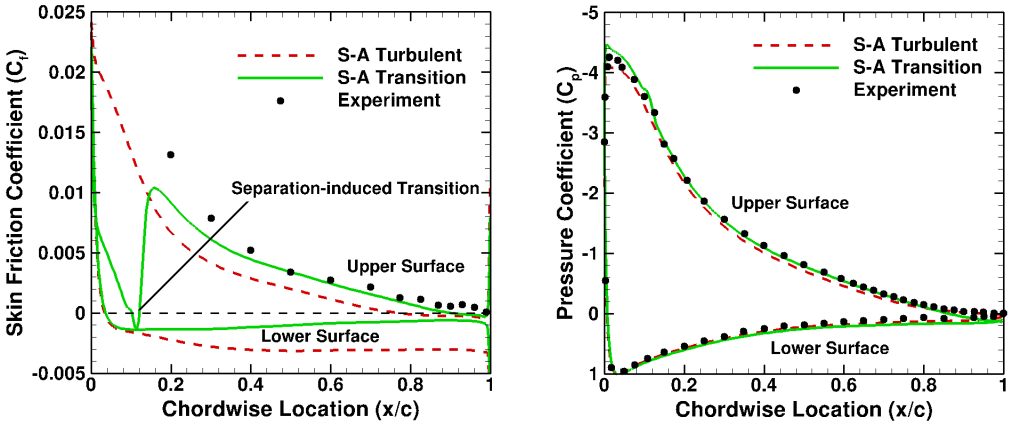

(a) Skin Friction Coefficient (b) Surface Pressure Coefficient

Figure 5.3: Pressure and skin friction profiles for Aerospatiale-A airfoil (Experiment [100])

with sufficient clustering around the airfoil in both the streamwise and the normal directions. The height of the wind tunnel mesh is determined from experimental sources. Upstream and downstream boundaries of the wind tunnel mesh are placed at approximately 20 chords away from the airfoil.

5.2 Aerospatiale–A Airfoil

The Aerospatiale–A airfoil experiment [100] conducted in the low-turbulence ONERA F1 wind tunnel has been used as a benchmark case for transition models in several CFD studies [6, 77, 101]. Experiments [100] reveal that at 13.1° angle of attack, the suction side boundary layer undergoes free transition at 12% of chord through the formation of a laminar separation bubble with turbulent reattachment. Skin friction profiles plotted in Fig. 5.3(a) show that the $\gamma - Re_\theta -$ SA transition

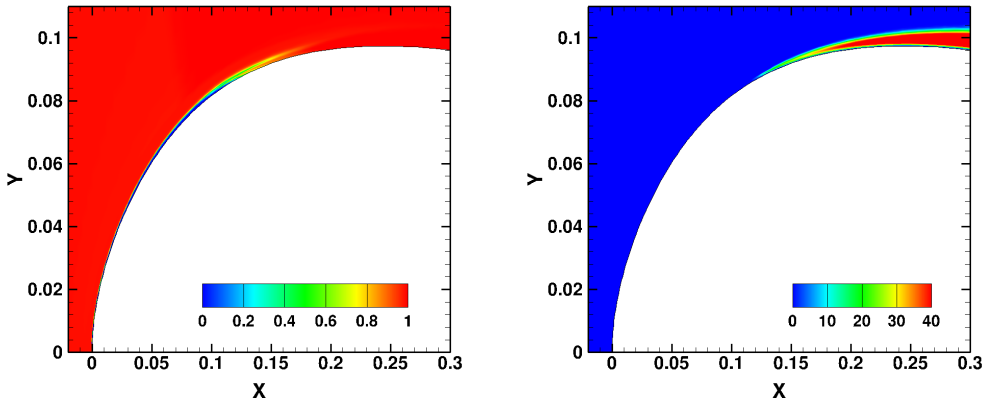

(a) Intermittency

(b) Eddy viscosity – S-A Transition

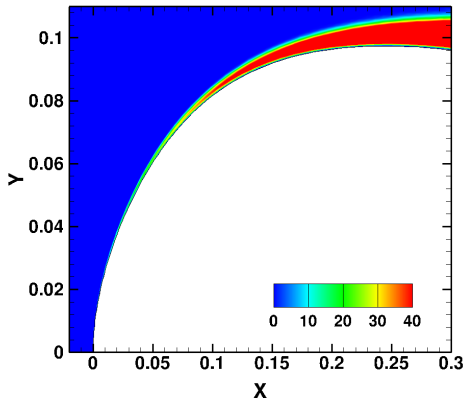

(c) Eddy viscosity – S-A Turbulent

Figure 5.4: Intermittency and Eddy viscosity production for Aerospatiale-A airfoil (not to scale)

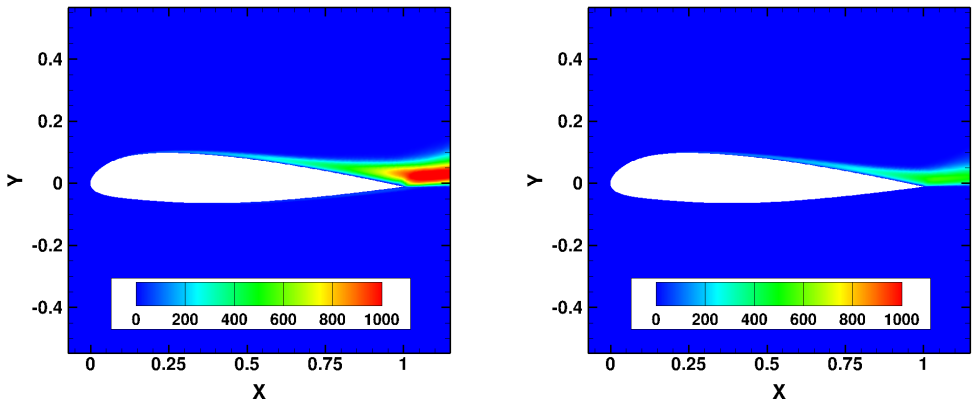

(a) S-A Turbulent

(b) S-A Transition

Figure 5.5: Eddy viscosity contours for flow past Aerospatiale-A airfoil

model is able to capture this separation-induced transition, indicated by the negative value of skin friction followed by a sharp increase. The baseline S-A model is unable to capture this phenomenon, indicated by the fully turbulent skin friction profile with no sudden jump on both sides of the airfoil. The transition model also predicts a completely laminar boundary layer on the pressure side of the airfoil. The predicted surface pressure coefficient distribution plotted in Fig. 5.3(b) shows the presence of a laminar separation bubble around 12% of the chord, indicated by a small region of constant pressure. Figure 5.4(a) intermittency production in the boundary layer starting near 12% of the chord. The corresponding Eddy viscosity contours in Fig. 5.4(b) verify that the production of turbulence begins only after the intermittency starts to increase beyond a certain value, unlike in the case without the transition model, where turbulence production starts immediately downstream of the stagnation point (Fig. 5.4(c)). Compared to the fully turbulent S-A model, the $\gamma - Re_\theta -$ SA model significantly reduces the overall turbulence production on

the entire airfoil, as seen in Fig. 5.5. Furthermore, although the skin friction values downstream of transition are slightly less than that predicted by the fully turbulent S-A model (Fig. 5.3(a)), the thickness of the boundary layer downstream of the transition onset location is much smaller than that for the fully turbulent flow (Figs. 5.4, 5.5). Experimentally measured values of lift and drag coefficients are 1.56 and 0.0208 respectively. As expected, the fully turbulent S-A model predicted these values to be 1.52 and 0.0287 with a 38% over-prediction of drag. The lift and the drag coefficient values predicted by including the transition model are 1.60 and 0.0186. The 10% under-prediction of drag with the transition model can be attributed partially to the under-prediction of skin-friction value between 20% and 40% of the airfoil chord on the upper surface. However, these predictions agree well with previous CFD simulations of this test case [6, 77].

5.3 VA-2 Supercritical Airfoil

Flow past the VA-2 supercritical airfoil section [102] provides for an interesting test case, since its upper surface has very little curvature and almost simulates a zero-pressure gradient flat plate at an angle of attack of -0.5°. Therefore, at -0.5° AoA, upper surface transition onset location is determined primarily by freestream turbulence intensity and Reynolds number effects, with negligible influence of pressure gradients. Simulations are carried out at $\mathrm{Re} = 2\times10^6$ and four angles of attack: -0.5, 3.5, 7.5 and 11.5 degrees. Computed skin friction profiles for AoA variations with and without the transition model are compared with experimental data in Fig.

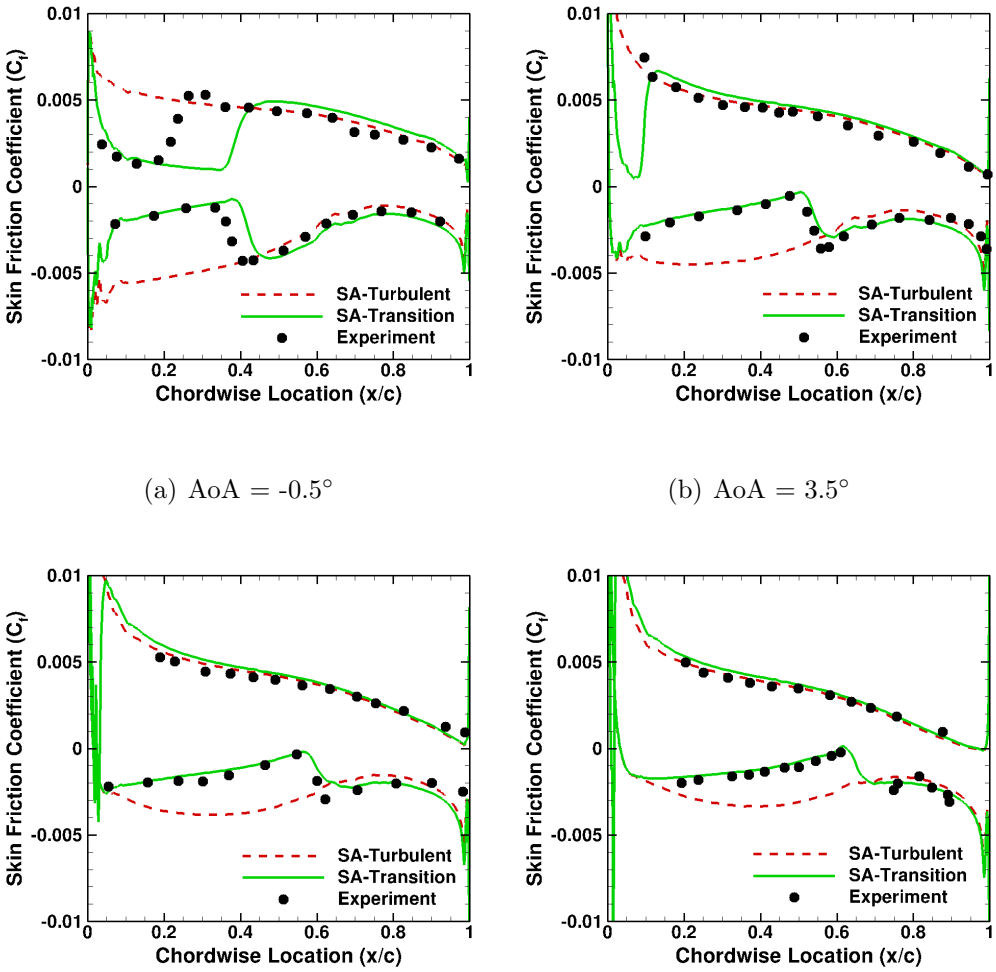

(a) AoA = -0.5°

(b) AoA = 3.5°

(c) AoA = 7.5°

(d) AoA = 11.5°

Figure 5.6: Skin friction profiles for VA-2 supercritical airfoil (Experiment [102])

5.6. The transition model is able to consistently capture the onset location and extent of transition with reasonable accuracy, whereas the baseline S-A model predicts a fully turbulent boundary layer on both the upper and the lower surfaces. As the angle of attack increases, transition onset location moves upstream on the upper surface and downstream on the lower surface. At -0.5° AoA, the delay in the computed transition onset location compared to experiment is attributed to the

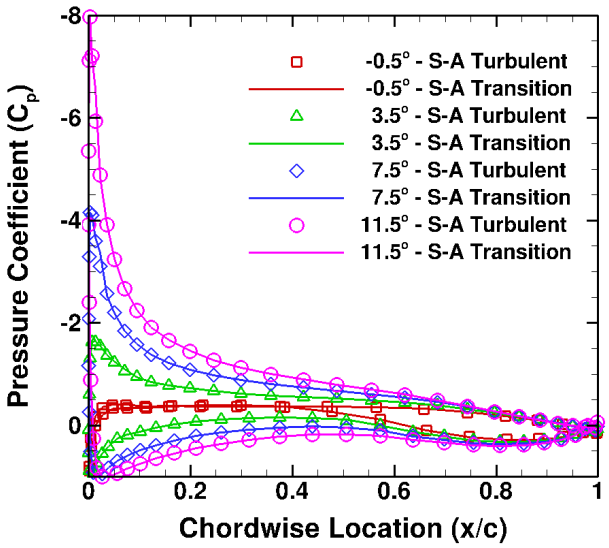

Figure 5.7: Presurre coefficient profiles for VA-2 supercritical airfoil

model calibration as a function of freestream turbulence intensity. Surface pressure distribution profiles plotted in Fig. 5.7 do not show visible differences between fully turbulent and transitional simulations. The lift and the drag coefficient values tabulated in Table 5.2 show that the lift predicted by the transition model is lower by 5% as compared to the fully turbulent prediction at 0° AoA, and less than 0.5% lower at higher AoA. More importantly, drag coefficients predicted by the transition model are lower than the fully turbulent predictions by 31%, 18%, 10.5%, and 8.0% in increasing order of AoA. This trend is consistent with the movement of the transition location further upstream and the increasing contribution of pressure drag as the angle of attack increases. Experimental lift and drag values are not available for this case.

AoA	C_l SA-Turb	C_l SA-Trans	C_d SA-Turb	C_d SA-Trans
-0.5°	0.173	0.184	0.00997	0.00689
3.5°	0.609	0.612	0.0114	0.00937
7.5°	1.031	1.038	0.0151	0.0135
11.5°	1.419	1.433	0.0225	0.0207

Table 5.2: Lift and drag coefficient predictions for VA-2 supercritical airfoil

5.4 S809 Airfoil

The S809 airfoil section is a 21% thick, laminar-flow profile designed specifically for horizontal-axis wind turbine applications. It is the primary section used on the NREL Phase VI model wind turbine rotor blade [103]. Experimental data for the lift, drag, and transition onset locations are available for this airfoil section [104]. This test case is widely used for assessing performance of transition models since the boundary layer remains laminar up to 50% of the chord on both the upper and the lower surfaces at lower angles of attack. Computationally predicted static lift and drag coefficients from 0° to 20° angles of attack are compared to the experimental data in Fig. 5.8. A closer look at the data from lower AoA values in Fig.5.8(c) reveals that the baseline S-A model significantly over-predicts the drag due to the fully turbulent treatment of the boundary layer. The transition model predictions of drag at lower AoA values are in good agreement with experimental data. At higher AoA, both the baseline S-A model and the $\gamma - Re_\theta -$ SA model over-predict lift and stall

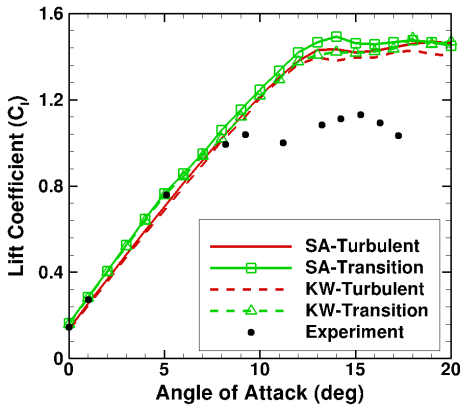

(a) Lift coefficient

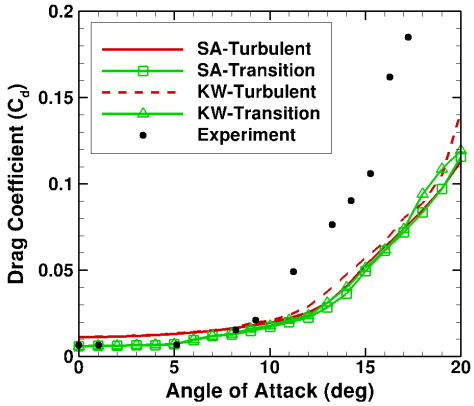

(b) Drag coefficient

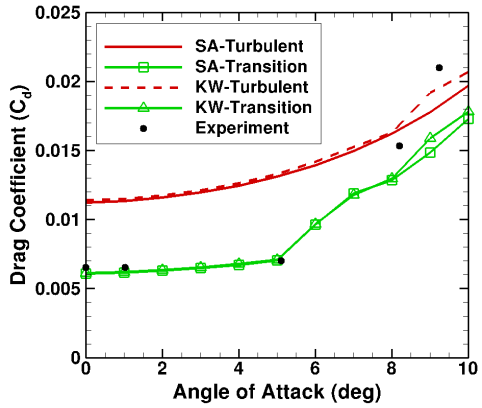

(c) Drag at lower AoA

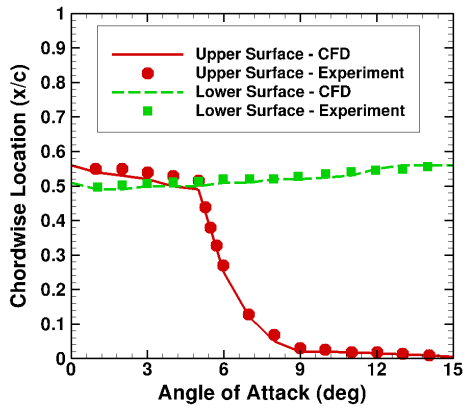

(d) Transition onset locations

Figure 5.8: Transition Model predictions for S809 airfoil section (Experiment [104])

onset compared to experimental data. The corresponding drag values are under-predicted. This is attributed to the inability of 2-D RANS simulations to predict the unsteady, three-dimensional nature of the trailing-edge flow separation zone on the suction side of the airfoil beginning around 9° AoA. Figure 5.9 shows separated flow streamlines colored by velocity magnitude at 14° and 20° AoA. Three-dimensional, well-resolved, hybrid RANS-LES methods are likely to improve lift and drag at these angles. Computed transition onset locations shown in Fig. 5.8(d) compare

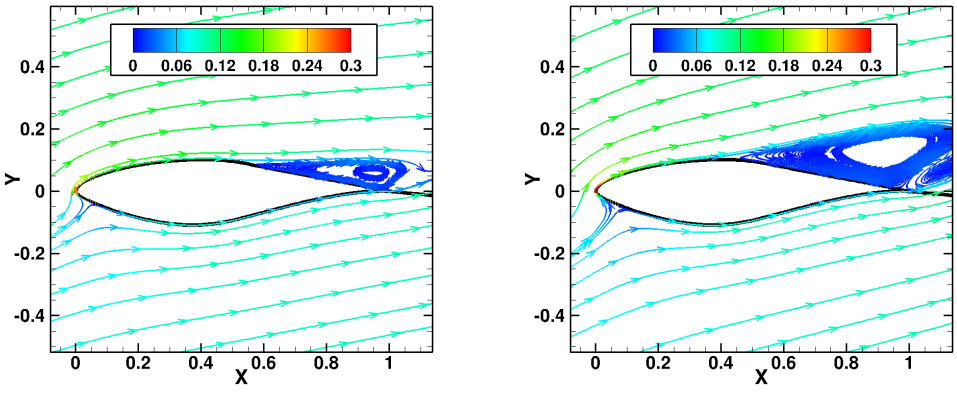

(a) AoA = 14° (b) AoA = 20°

Figure 5.9: Streamlines colored by velocity magnitude showing separation at high AoA on S809 airfoil section

very well with experimental values. Due to an increasing adverse pressure gradient with increasing angle of attack, the transition onset location on the upper surface moves from 56% of chord to the stagnation point. This process is very gradual until 5° AoA, followed by a sharp upstream movement of the transition point towards the leading-edge until 9° AoA, beyond which it remains close to the stagnation point. On the lower surface, due to an increasing favorable pressure gradient with increasing angle of attack, the transition point moves slowly downstream from 50% to 60% of the chord. The shape of the lower surface of the S809 airfoil causes an abrupt adverse pressure gradient at 50% chord. Therefore, the favorable pressure gradients at high angles of attack are unable to stabilize the boundary layer or delay transition onset. Surface pressure distributions are plotted at 1°, 9°, 14°, and 20° AoA in Fig. 5.10. At 1° AoA, the transition model shows a visible improvement in the pressure distribution compared to the fully turbulent profile. Skin friction

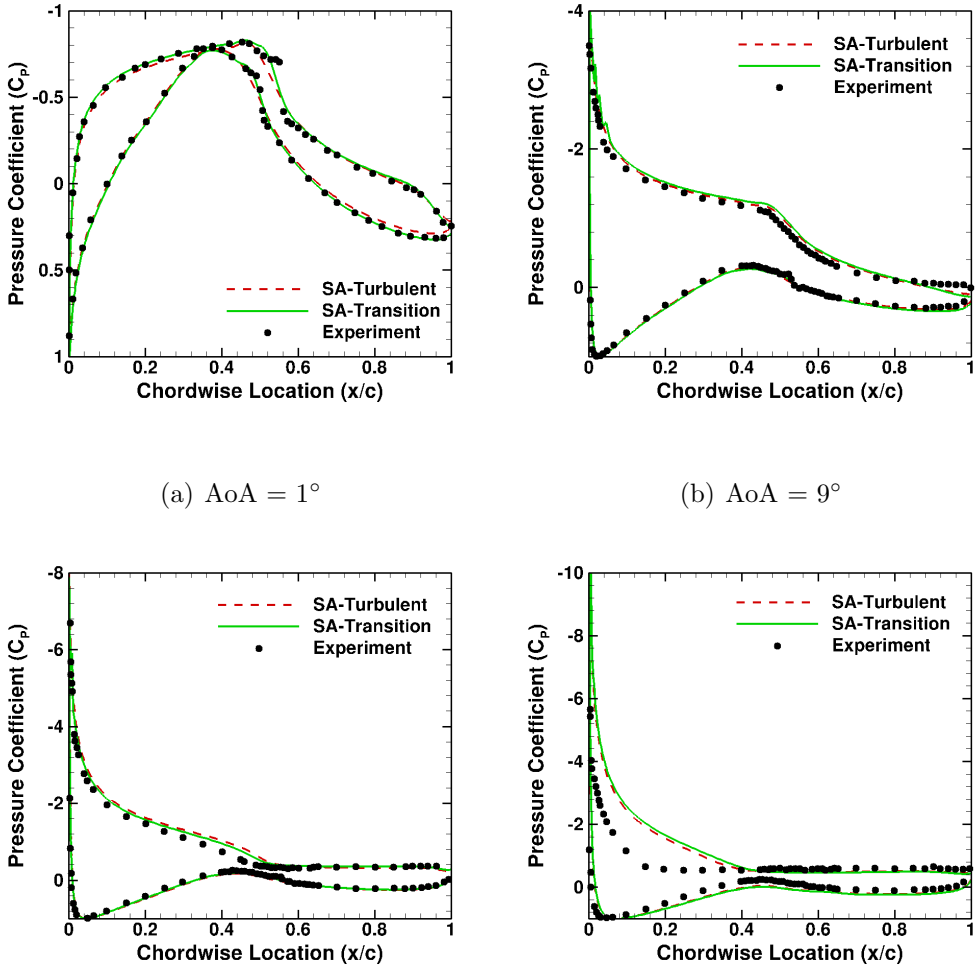

(a) AoA = 1°

(b) AoA = 9°

(c) AoA = 14°

(d) AoA = 20°

Figure 5.10: Comparison of pressure profiles for S809 airfoil section (Experiment [104])

profiles at these four angles of attack are plotted in Fig. 5.11. Transition occurs through a laminar separation bubble at 1° AoA on the upper surface, verified by the change in the sign of the skin friction value around 50% of chord. For this airfoil, separation-induced transition occurs on the lower surface at all angles of attack.

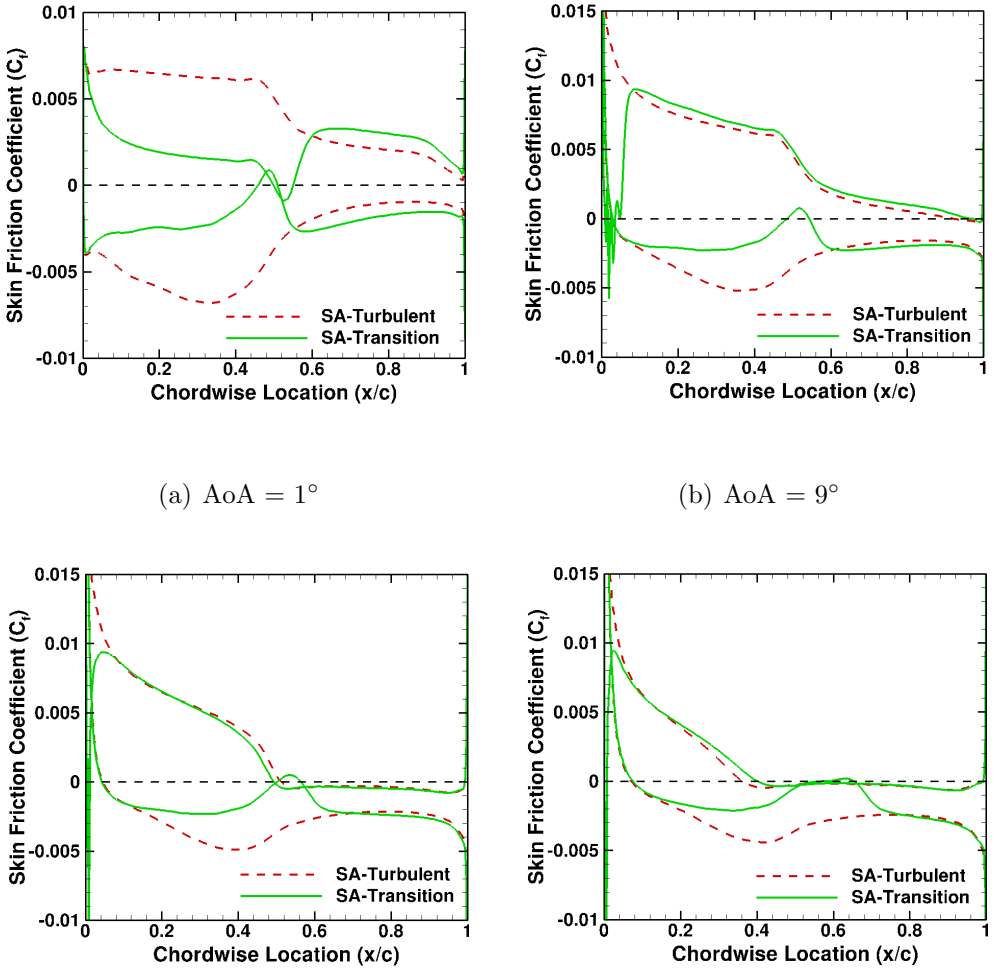

(a) AoA = 1°

(b) AoA = 9°

(c) AoA = 14°

(d) AoA = 20°

Figure 5.11: Comparison of skin friction profiles for S809 airfoil section

5.5 Eppler 387 Airfoil

Boundary layers on low Reynolds number airfoils are distinguished by transition to turbulence via formation of a separation bubble that begins with laminar separation and ends with turbulent reattachment at a downstream location. Laminar separation bubbles contribute to the increased pressure drag on airfoils. Under a U.S. Department of Energy initiative at the National Renewable Energy Laboratory

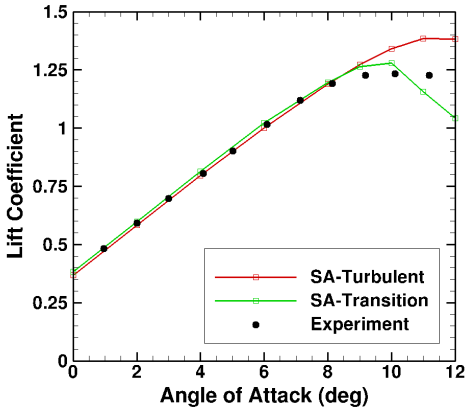

(a) Lift, Re = 200,000

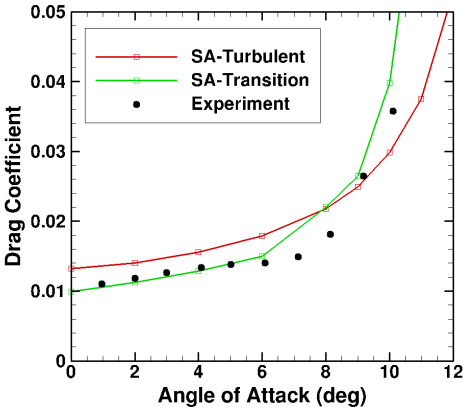

(b) Drag, Re = 200,000

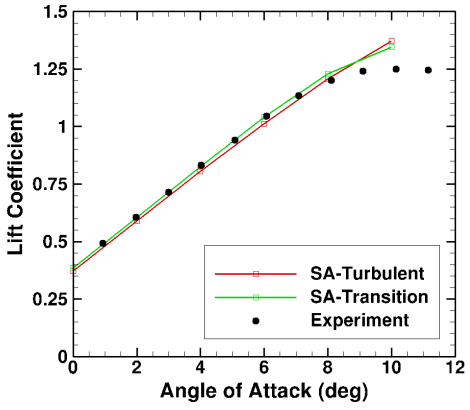

(c) Lift, Re = 350,000

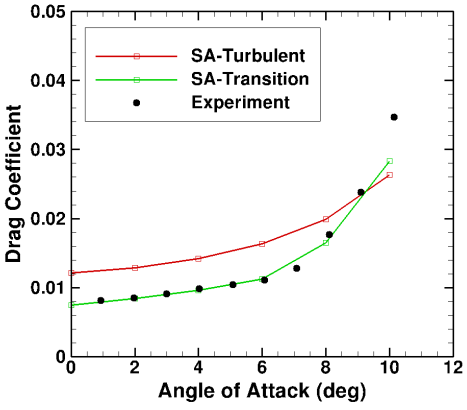

(d) Drag, Re = 350,000

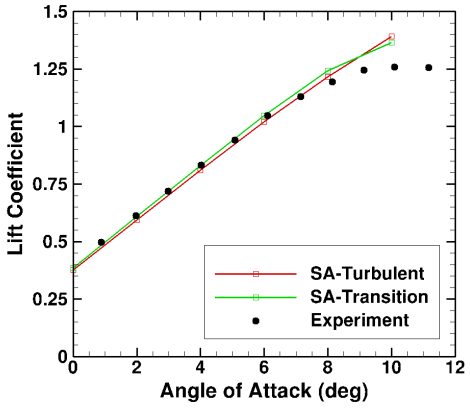

(e) Lift, Re = 500,000

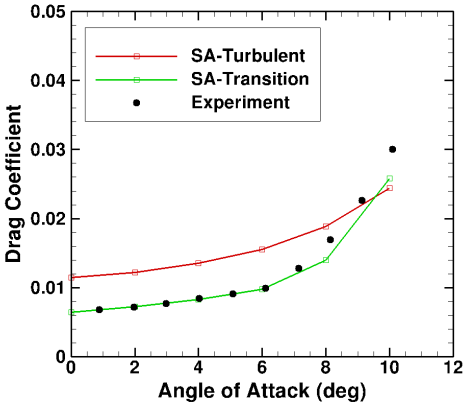

(f) Drag, Re = 500,000

Figure 5.12: Lift and drag variation for E387 airfoil section (Experiment [105])

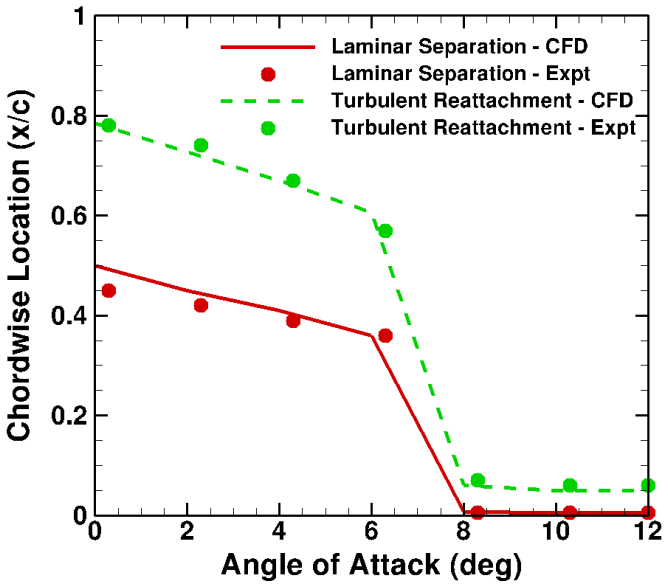

(a) Re = 200,000

Figure 5.13: Laminar separation and turbulent reattachment predictions for E387 airfoil section (Experiment [105])

(NREL), wind tunnel tests were conducted to characterize six airfoils at Reynolds numbers under 500,000 for use on small wind turbines [105]. One of the six airfoils, the Eppler 387, is simulated in this work to validate the experimental data at three discrete Reynolds numbers: 200k, 350k, and 500k. These cases pose a strong test for the reliability and robustness of the $\gamma - Re_\theta -$ SA model for low Reynolds numbers flows. The variation of lift and drag coefficients with angle of attack are plotted against experimental data at all three Reynolds numbers in Fig. 5.12. The baseline S-A model slightly under-predicts lift at lower angles for Re = 350k and 500k. The transition model lift predictions agree well with experiments in the linear range of AoA at all Reynolds numbers 5.12(a, c, e). The primary merit of transition

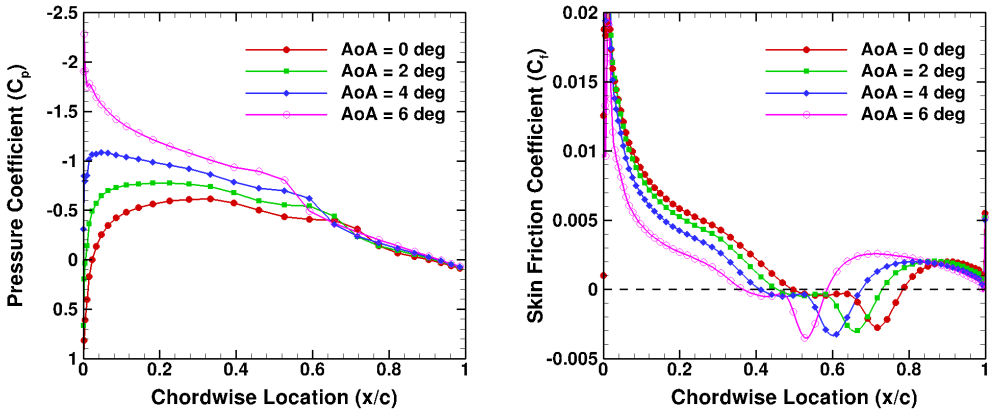

(a) Upper surface C_p, Re = 200,000 (b) Upper surface C_f, Re = 200,000

Figure 5.14: Pressure and skin friction profiles on S809 airfoil section showing presence of laminar separation bubbles

modeling is demonstrated via drag coefficient data in Figs. 5.12(b, d, f). At each of the Reynolds numbers, the baseline S-A model consistently over-predicts drag, whereas the transition model predictions agree very well with experimental data prior to separation and stall onset.

Computed laminar separation and turbulent reattachment locations for Re = 200k are plotted in Fig. 5.13. This figure verifies the model capability to predict transition onset and extent with sufficient accuracy at low Reynolds numbers. Two trends are observed in the plot for transition onset locations: (1) The laminar separation and turbulent reattachment points move upstream with increasing angle of attack, (2) The length of the separation bubble decreases with increasing angle of attack. This plot also shows that laminar separation bubbles can span close to 40% of the airfoil chord at low Reynolds numbers and low angles of attack, thereby significantly contributing to the pressure drag. Figure 5.14 shows the upper

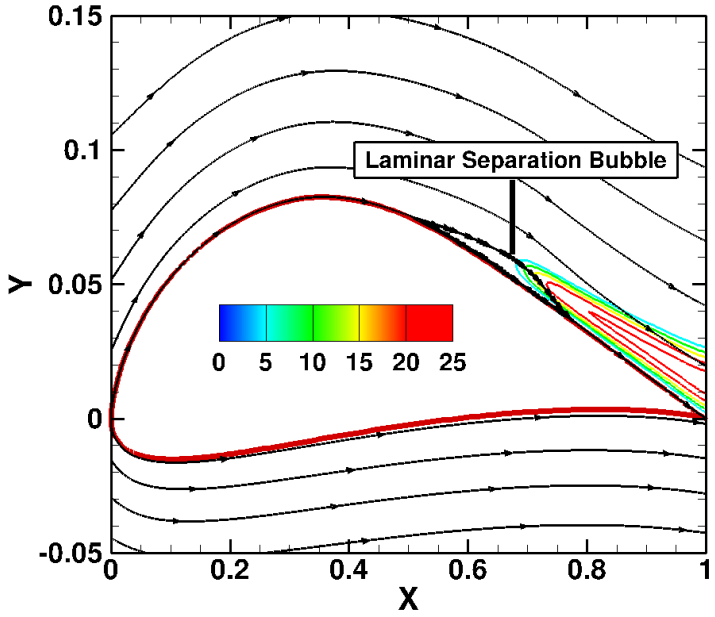

(a) Streamlines and Eddy viscosity contour lines

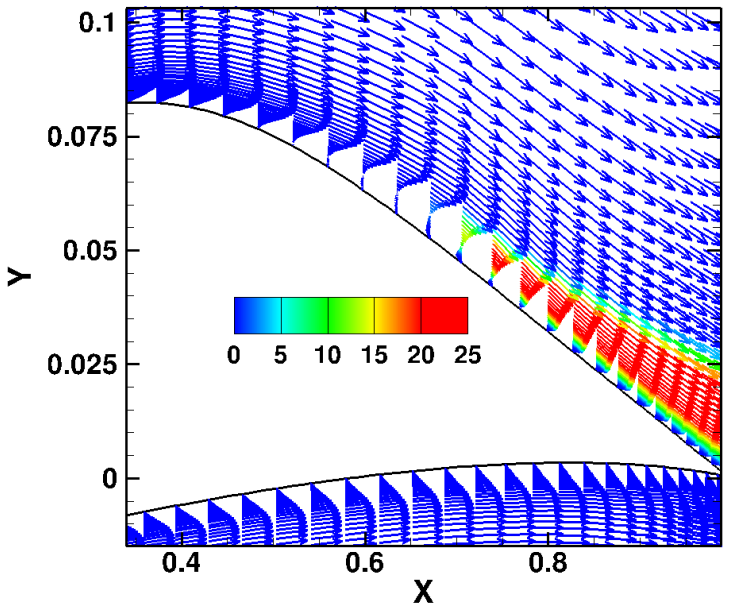

(b) Velocity vectors colored by Eddy viscosity magnitude

Figure 5.15: Visualization of laminar separation bubble for E387 airfoil at AoA = 0° and Re = 200,000

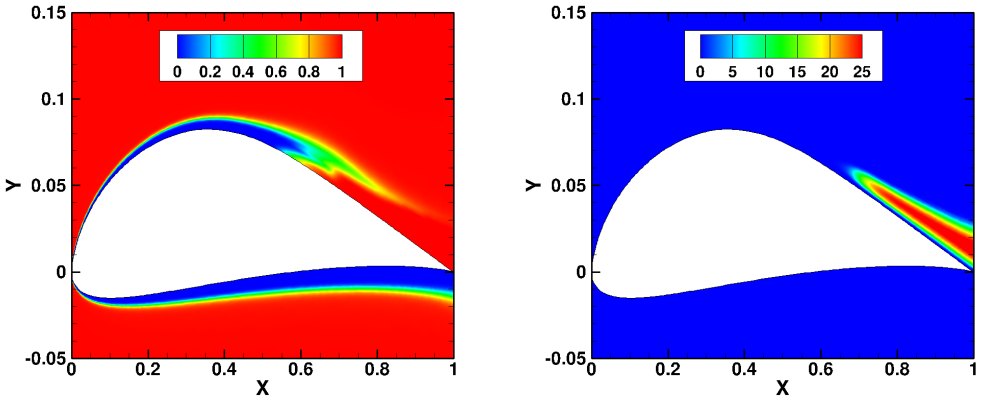

(a) Intermittency (b) Eddy viscosity

Figure 5.16: Transition onset and Eddy viscosity production for E387 airfoil at AoA = 0° and Re = 200,000

surface pressure coefficent and skin friction profiles at Re = 200k and AoA = 0, 2, 4, and 6 degrees. All pressure coefficient profiles in Fig. 5.14 exhibit a region of near-constant value over the extent of the laminar separation bubble. The upper surface skin friction profiles in Fig. 5.14 confirm the presence of a laminar separation bubble that is shortening and moving upstream with increasing angle of attack. Recall that the skin friction profile switches its sign inside the bubble due to flow reversal. Streamlines and velocity vectors plotted in Fig. 5.15 visualize the extent of the laminar separation bubble at Re = 200k and AoA = 0 degrees. Figure 5.16 shows intermittency and Eddy viscosity contours at the same flow condition.

5.6 NACA 64_2(A)015 Airfoil

This test case assesses transition model performance for very high Reynolds number flows between 10 and 50 million. Experiments were conducted on a NACA

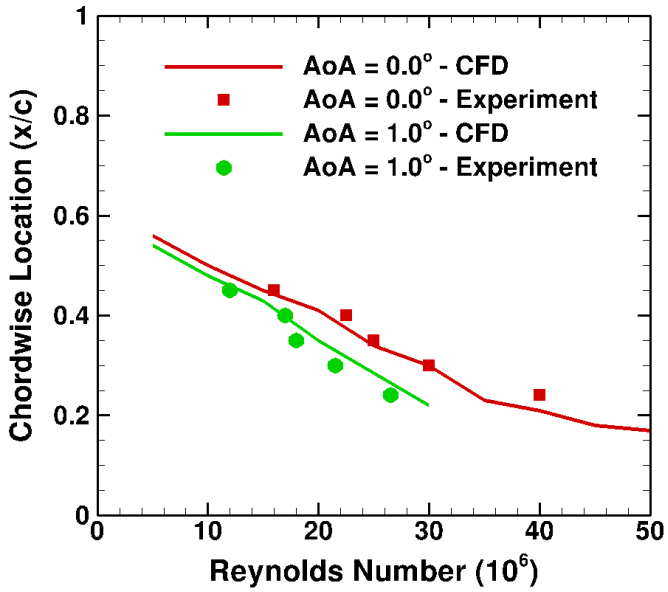

Figure 5.17: High Reynolds number transition onset location predictions for NACA 64_2(A)015 airfoil section (Experiment [106])

64_2(A)015 airfoil section in the NASA Langley Low-Turbulence Pressure Tunnel and the NASA Ames 12-foot pressure tunnel at low speeds for Reynolds numbers ranging from 10 to 40 million [106]. The primary goal of these experiments was to study boundary layer instability via the crossflow mechanism on an untapered wing at various sweep angles and angles of attack. Prior CFD studies [107] validated these experiments using the e^N method. For the present work, simulations were performed on a 2-D cross-section of the wing to compare with experimental data for the unswept wing case. The transition onset locations on the suction side plotted for 0 and 1 degree angle of attack 5.17 show good agreement with experimental measurements for the entire range of Reynolds numbers.

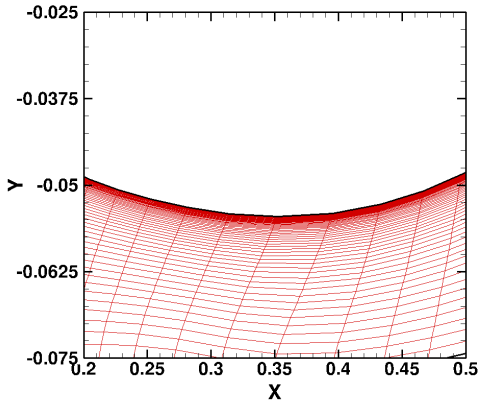

(a) Non-orthogonal grid lines on main element lower surface

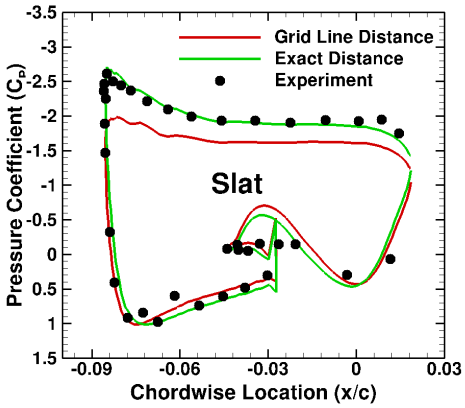

(b) Leading-edge slat

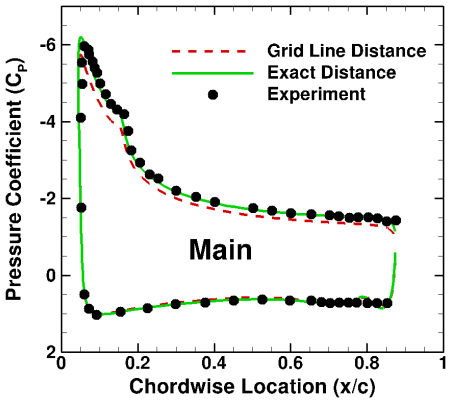

(c) Main element

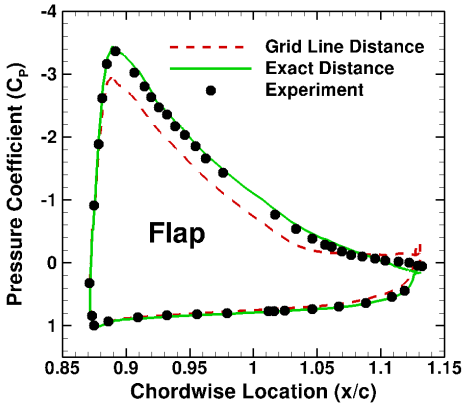

(d) Trailing-ege flap

Figure 5.18: Pressure coefficient prediction on MD 30P–30N airfoil configuration - Effect of wall distance function evaluation (Experiment [108])

5.7 MD 30P–30N Multi-element Airfoil

Multi-element airfoil (MEA) configurations with a leading-edge slat and/or a trailing edge flap are commonly used in fixed-wing aircraft in order to increase maximum lift and delay the onset of stall in low speed flights during take-off and landing.

The McDonnell Douglas 30P-30N multi-element configuration, with a leading-edge slat and a trailing-edge flap, is a classic test case to assess CFD code performance in high-lift conditions [108]. Experiments were conducted in the Langley Low Turbulence Pressure Tunnel and the transition onset locations were recorded on upper and lower surfaces of all three elements [109]. From a transition model perspective, this test case presents a strong challenge due to the influence of the upstream element's wake on the downstream element's transition onset location. A structured multi-block grid, provided by Rumsey [108] is used to simulate this test case. In this particular mesh, wall-normal grid lines are non-orthogonal to the wall tangential direction, as seen on the lower surface of the main airfoil element in Fig. 5.18(a). Since the S-A model uses nearest wall distance in its source terms, evaluating the distance function along the computational non-orthogonal grid lines, such as in the present case, will lead to an inaccurate solution. Therefore, exact nearest wall distance from each grid point was computed and used in this simulation.

Surface pressure coefficient profiles computed using the transition model are compared with experimental data in Figs. 5.18(b), (c) and (d). The pressure distribution obtained using the grid line distance function shows large discrepancies from the experimental data, whereas the exact wall distance computation shows excellent agreement for all three airfoil elements.

Figure 5.19 shows the intermittency flow field obtained using the transition model for each of the three elements. In these contour plots, turbulence production is active in regions of red (intermittency = 1), and is inactive in regions of blue (intermittency = 0). Transition onset locations from both the experiments and the

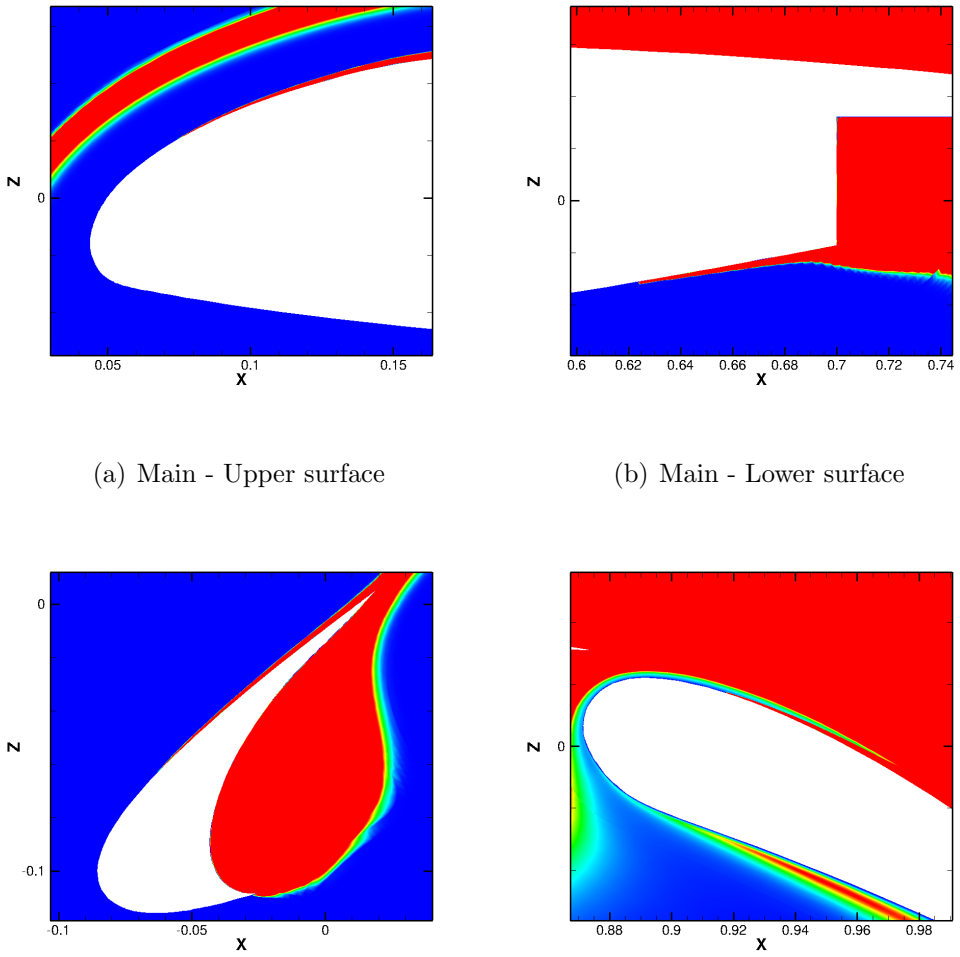

(a) Main - Upper surface

(b) Main - Lower surface

(c) Slat - Upper surface

(d) Flap - Upper surface

Figure 5.19: Intermittency contours showing transition onset on MD 30P-30N multi-element airfoil configuration: Blue - Laminar, Red - Turbulent (Experiment [108])

present simulations, along with the discrepancy between experiment and computations, are summarized in Table 5.3. The discrepancy between the computed and experimental transition onset locations is greater when the nearest wall distance value is computed along grid lines than when the exact wall distance is used. The reason for this is that the vorticity Reynolds number definition ($Re_v = \frac{\rho d^2 S}{\mu}$) used

Airfoil	Experiment [109]	CFD grid-line distance (% error)	CFD exact distance (% error)
Main upper	0.068	0.060 (3.4%)	0.074 (1.9%)
Main lower	0.526	0.22 (34.8%)	0.62 (11%)
Slat upper	-0.057	-0.068 (1.2%)	-0.062 (0.6%)
Flap upper	0.931	0.89 (4.6%)	0.92 (1.2%)

Table 5.3: Transition onset locations (x/c_{main}) for MD–30P–30N multi-element airfoil configuration (error reported as a % of main element chord length, c_{main})

to evaluate the transition onset criterion is a function of the nearest wall distance value (d) at each grid point. Therefore, the error is especially large on the lower surface of the main element where the wall-normal grid lines are the most skewed as seen in Fig. 5.18(a). Overall, the $\gamma - Re_\theta -$ SA model performance in predicting transition onset locations is satisfactory for this multi-element airfoil configuration.

5.8 SC2110 w/ Leading-edge Slat

Recently, multi-element airfoil configurations have been investigated by Lorber [110], to alleviate the onset of dynamic stall in rotorcraft applications. Due to

lower chord Reynolds numbers on lift-enhancement devices such as slats and flaps, a significant portion of their boundary layer can remain laminar, resulting in lower turbulence levels in their wake flow. The amount of turbulence in the wake of a leading-edge slat strongly influences transition to turbulence of the boundary layer on the main element. Therefore, it is important to accurately model the transitional nature of the boundary layer on the upstream elements for good overall force and moment predictions. Steady flow simulation results for flow past a high-lift

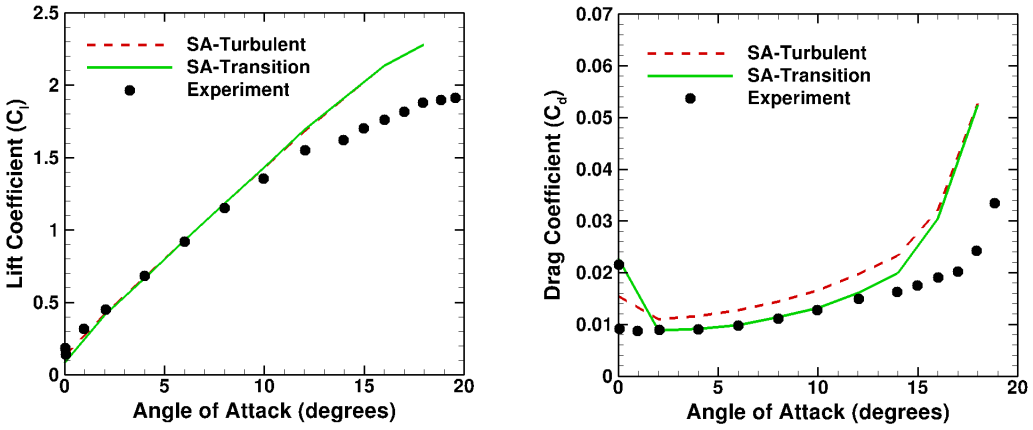

(a) Lift Coefficient (b) Drag Coefficient

Figure 5.20: Lift and drag predictions for SC2110 w/ Slat multi-element airfoil (Experiment [110])

leading-edge slat configuration (referred to as S-6 in [110]) are presented here. Since experimental measurements were not corrected for wind tunnel blockage effects, tunnel walls are modeled in this test case using a rectangular, Cartesian background mesh. Height of the wind tunnel is four times the main element chord length. In the wrap-around direction, the main element and the slat have 400 and 200 grid points respectively. Variation of the lift and the drag coefficients with angle of

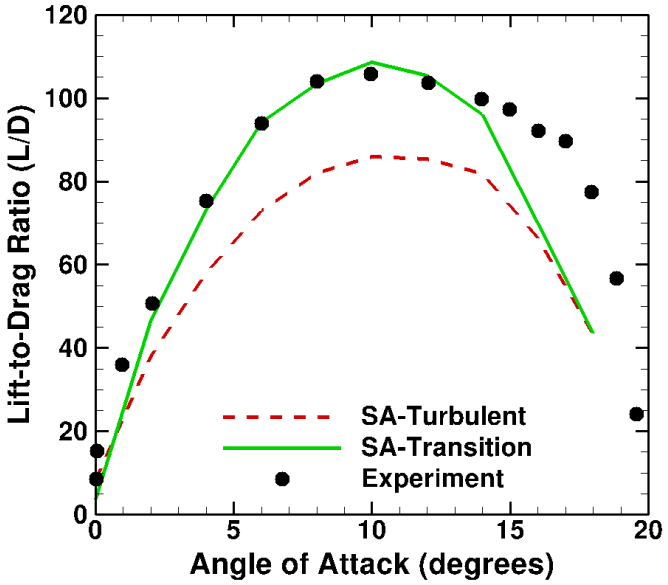

Figure 5.21: Lift-to-Drag ratio for SC2110 w/ Slat multi-element airfoil (Experiment [110])

attack, obtained with and without using the transition model, are plotted against experimental data in Fig. 5.20. While the lift predictions at lower angles of attack are acceptable even without the transition model, the baseline S-A model fails to predict the drag within acceptable error, due to the presence of significant lengths of laminar flow on both the main element and the slat. As seen earlier in the S809 airfoil case, 2-D RANS simulations at higher angles of attack over-predict maximum lift and predict a delayed stall onset for this airfoil configuration. The benefit of using a transition model is readily seen by plotting the lift-to-drag ratio (L/D) variation with angle of attack in Fig. 5.21. L/D values obtained with the transition model are in excellent agreement with experimental data up to 10° AoA, which is the point of maximum L/D. Surface pressure and skin friction coefficient profiles at

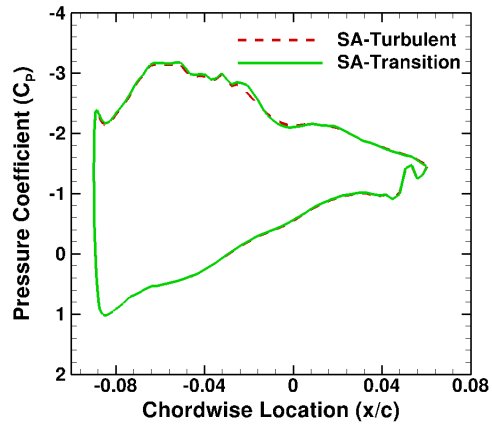

(a) Leading-edge slat

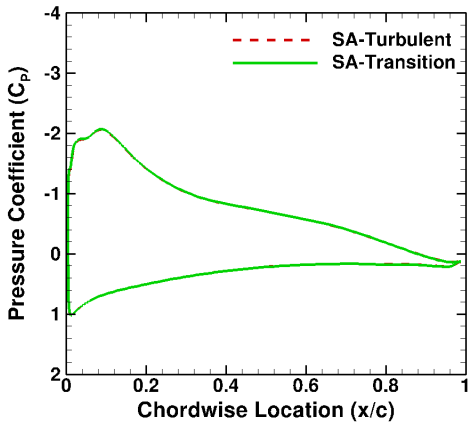

(b) Main element

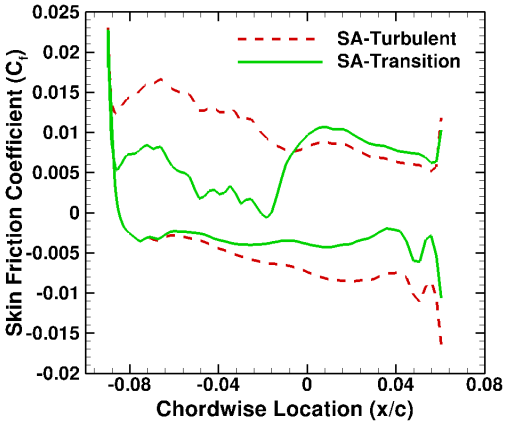

(c) Leading-edge slat

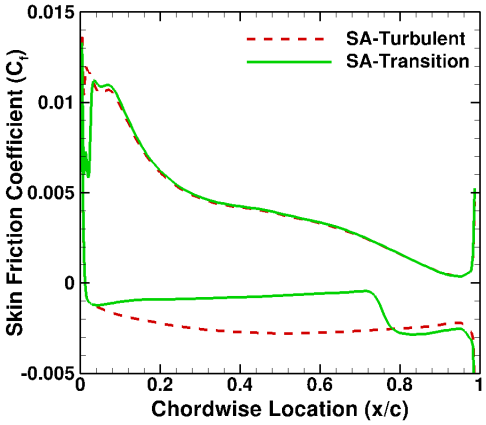

(d) Main element

Figure 5.22: Comparison of surface pressure and skin friction profiles for SC2110 w/ Slat multi-element airfoil

$[L/D]_{\max}$ are plotted in Fig. 5.22. Pressure profiles are not significantly different between the transitional and turbulent solutions, which is reflected in their similar lift coefficient values. However, the skin friction distribution of the transitional case confirms the presence of laminar regions on both the main element and the slat, thereby predicting lower drag. The boundary layer on the slat remains laminar up

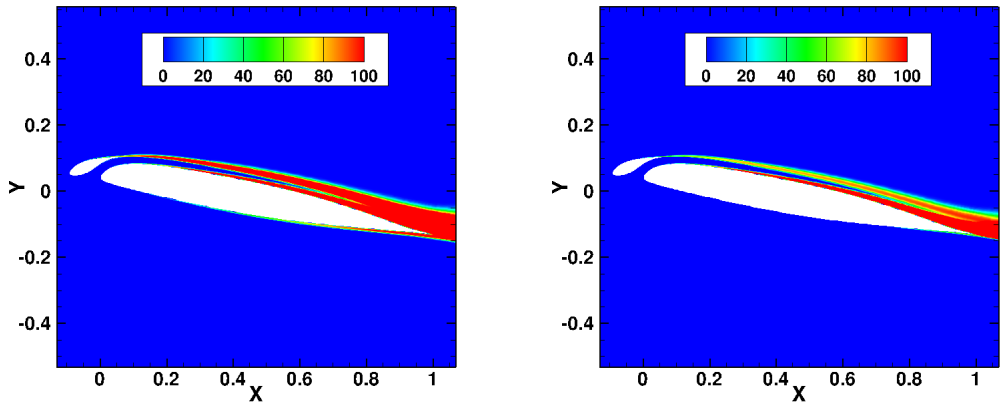

(a) S-A Turbulent

(b) S-A Transition

Figure 5.23: Comparison of Eddy viscosity contours for SC2110 w/ Slat multi-element airfoil

to half of its chord length on the upper surface and all along the lower surface. The main element boundary layer also remains laminar up to 75% of the chord on its lower surface. The eddy viscosity contours in Fig. 5.23 show reduced production of turbulence in the wake of the slat and on the main element due to the transition prediction.

5.9 Summary

In this chapter, several two-dimensional airfoils were simulated with the $\gamma - Re_\theta -$SA transition model and predictions were compared with multiple experimental data sets over a wide range of Reynolds numbers (10^5 to 5×10^6). The baseline SA model consistently over-predicted the drag at lower angles of attack where laminar boundary layers extend over larger portions of the airfoil. Encouraging results were

obtained with the transition model, for prediction of transition onset locations, lift, and drag coefficients. At low Reynolds numbers (<500,000), the transition model was able to capture the location and extent of the relatively long laminar separation bubbles with good accuracy. The capability of the model to predict transition on multi-element airfoils was also demonstrated. The next chapter will present results from three-dimensional rotor simulations.

6 Three-dimensional Rotor Simulations

The $\gamma - Re_\theta -$ SA model is calibrated for the effects of freestream turbulence and non-zero pressure gradients on transition onset location, which are applicable to both two-dimensional and three-dimensional boundary layers. However, it does not account for crossflow instability effects that are dominant in the presence of yawed flow past aerodynamic surfaces. Applications with prominent crossflow transition onset include swept wings, airframes, and rotating blades in yawed flow. Therefore, in order to assess the performance of the model for practical applications within its validity regime, rotating blade simulations are performed under purely axial flow conditions. This ensures predominantly two-dimensional flow on the airfoil sections, except in the vicinity of blade root and tip, where three-dimensional effects are present due to vortices and rotor wake contraction. In this chapter, simulation results for the following three rotating blade configurations are presented: (1) BO 105 helicopter rotor in hover, (2) UH60-A helicopter rotor in hover, and (3) NREL Phase VI model wind turbine rotor at zero yaw wind angle (similar to rotorcraft in axial descent flight). These simulations were carried out with the following two objectives: (1) to quantify the effects of including the transition model on rotor thrust and torque predictions in hover, and (2) to capture the extent of laminar flow

regions on the rotor blades under various conditions. Definitions of rotor solidity (σ), thrust coefficient (C_T), torque coefficient (C_Q), and Figure of Merit (FM) for rotating blades in axial flight are given in Eqs. 6.2–6.4.

$$\sigma = \frac{N_b c R}{\pi R^2} \tag{6.1}$$

$$C_T = \frac{T}{\rho \pi R^2 {V^2}_{tip}} \tag{6.2}$$

$$C_Q = \frac{T}{\rho \pi R^3 {V^2}_{tip}} \tag{6.3}$$

$$FM = \frac{\frac{{C_T}^{3/2}}{\sqrt{2}}}{C_Q} \tag{6.4}$$

where, N_b is the number of blades, c is the blade chord, R is the blade radius, V_{tip} is the blade tip speed. In this work, rotor blades are treated as structurally rigid, and aeroelastic effects are neglected. Since the objective is to compare predictions from two different numerical models for the same structural shape of the blade, rigid rotor simulations are not entirely inappropriate, especially in hover and descent flight conditions.

6.1 Computational Grids

A prominent feature of rotating blades in axial flow is the presence of a wake system, consisting of root and tip vortices, above or beneath the rotor plane. Vortices closer to the rotor plane have a strong effect on the effective angle of attack seen by airfoil sections, by inducing flow in the axial direction. Failing to capture rotor wake in such scenarios can lead to incorrect flowfield predictions. In CFD simulations, rotor wake effects are typically included either through a low-fidelity prescribed wake

model or by solving the Navier-Stokes equations on a large enough computational domain that envelopes the near-field vortices. In this work, the rotor blade uses a structured, C-O topology mesh and is embedded in a cylindrical background mesh to capture the rotor wake. Information transfer among the components of this overset mesh system is handled using the Implicit Hole Cutting method (IHC) described in Chapter 4. Since both the BO 105 and UH-60A rotors are 4-bladed, only one quarter of the domain in the azimuthal direction (90^o) is simulated in hover, using axisymmetric boundary conditions. For the 3-bladed NREL Phase VI wind turbine rotor, a 120^o cylindrical background mesh was used. Extents of the background cylindrical meshes for all cases are as follows: 0.03R to 4.0R in the radial direction, 3.0R above the rotor plane and 5.0R below the rotor plane. Grid clustering with a uniform grid spacing of 0.05 times the blade chord is used in all background meshes in order to capture the root and the tip vortices with reasonable resolution. Grid dimensions for the blade and background meshes for each case are provided in their respective sections.

6.2 Rotorcraft Flows

RANS simulations of the flow past helicopter rotor blades is challenging due to the rapidly varying aerodynamic environment, ranging from low-speed transitional and reverse flow regions, to high-speed shock-induced stall regions. Although significant progress has been made in time-accurate RANS computations of the rotor flow environment, there is much scope for improvement in the underlying numerical

models that govern the various viscous flow phenomena. The present work focuses on simulating the laminar-to-turbulent transition phenomenon on rotor blades in hover to improve power prediction. Unlike on fixed wings, the local Reynolds number on rotating blades increases linearly in the radially outward direction, resulting in fairly low Reynolds numbers on the inboard airfoil sections. Experimental studies have shown that the boundary layer on a rotor blade can have large regions of laminar flow in both hover and forward flight conditions. Tanner and Yaggy [111] conducted wind tunnel tests on the UH-1B tail rotor and main rotor to determine laminar-turbulent transition locations, flow direction inside the boundary layer, and the formation and effects of the blade tip vortex. It was found that the boundary layer remains laminar on the lower surface of the blades – up to 50% of chord on the tail rotor and 25% of chord on the main rotor. Experiments conducted by Velkoff [112] on a model rotor blade with the NACA 0015 airfoil section indicated the presence of a laminar separation bubble that induced transition. Location of the standing bubble was near the pressure peak on the suction side of the airfoil section and moved closer to the leading edge with an increase in the angle of attack. Transition onset location trends were comparable to that of [111]. McCroskey [113] measured laminar separation and transition onset locations, as well as the surface streamline directions on rotor blades under non-rotating and rotating configurations. Fixed-wing tests with varying yaw angles were also conducted. Results indicated that the transition onset location moved closer to the leading edge with increasing yaw angle. For the rotating configurations, centrifugal effects did not significantly impact the boundary layer development. An interesting test case in this study is a

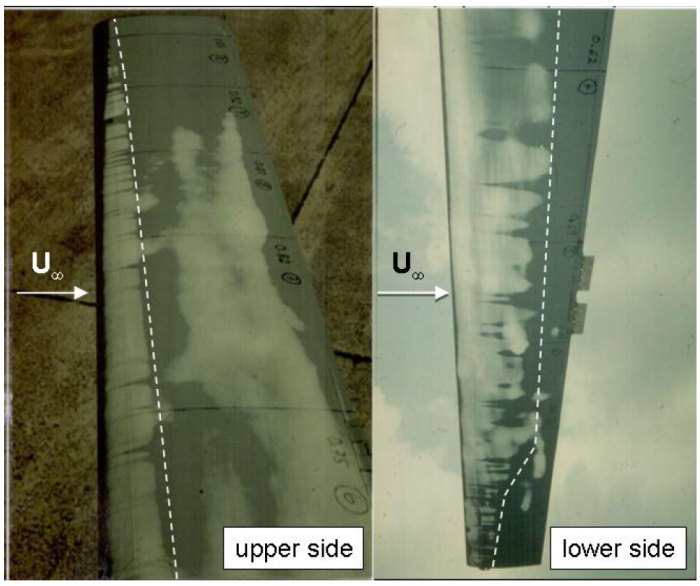

Figure 6.1: Visualization of transitional boundary layer on BO 105 rotor blades using Acenaphthene coating: Light regions – Laminar, Dark regions – Turbulent (figure reprocued from [114], Experiment [115])

2-bladed rotor configuration with the blades set at an offset. This facilitates yawed flow and three-dimensional boundary layer effects on rotating blades in hover without the complications of the unsteady aerodynamics such as BVI that are present in forward flight. Beaumier and Houdeville [116] predicted laminar-turbulent transition on the 7A rotor in forward flight conditions (advance ratio - $\mu = 0.3, 0.45$) using a boundary layer code that is capable of predicting various modes of transition. It was reported that the computed results agreed well with experiments conducted on the 7A rotors in the ONERA/S1MA wind tunnel. At $\mu = 0.3$ ($C_T/\sigma = 0.0625$), close to 25% of the upper surface of the blade was found to be laminar between 30 to 240 degrees azimuth. At $\mu = 0.45$ ($C_T/\sigma = 0.075$), the upper surface laminar zone increased on the advancing side and almost completely disappeared on the re-

treating side. Their calculations also indicated that the contribution to total power from skin friction alone is 29% at $\mu = 0.3$ and 13% at $\mu = 0.45$. At the higher advance ratio, most of the total power comes from wave drag due to transonic conditions on the advancing rotor blade. Recent work of Heister [114] used an integral boundary layer method combined with various empirical transition onset criteria to predict transition on the BO105 rotor in hover and the 7AD rotor in forward flight at $\mu = 0.33$. Computed transition onset locations agreed well with the experimental measurements of Rohardt [115]. In addition, rotor power predictions from the fully turbulent simulations were compared to those from the laminar-turbulent transitional simulations. Rotor power from transitional boundary layer simulations is reported to be $2\% - 5\%$ less than that from the fully turbulent simulations.

6.2.1 BO 105 Rigid Rotor

A full-scale, 4-bladed BO 105 rotor is simulated in hover with and without the transition model. The rotor blade has a rectangular planform, a linear twist rate of -8°, an aspect ratio of 16.58, and uses the NACA23012-mod airfoil section. In hover, the tip Mach number is 0.64 and the tip Reynolds number is 4.03×10^6. The blade is set to a collective pitch angle of 6.7° and a precone angle of 2.5°. In the corresponding flight test [115] that is simulated in this case, the laminar and the turbulent regions were visualized on one of the rotor blades using Acenaphthene coating, as seen in Fig. 6.1. Lighter regions represent laminar boundary layer and darker regions represent turbulent boundary layer. Flow visualization indicates that transition on the upper

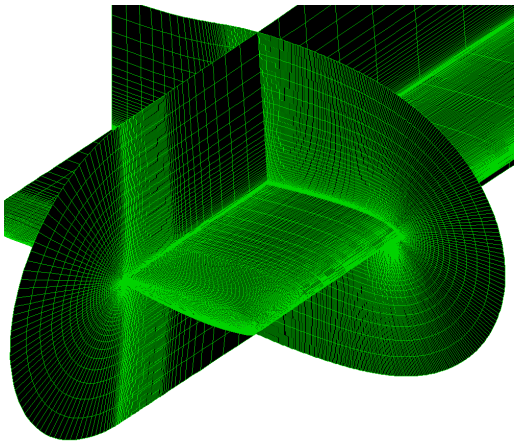

(a) C-O topology blade mesh

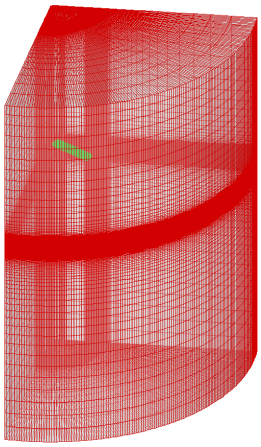

(b) Cylindrical wake mesh

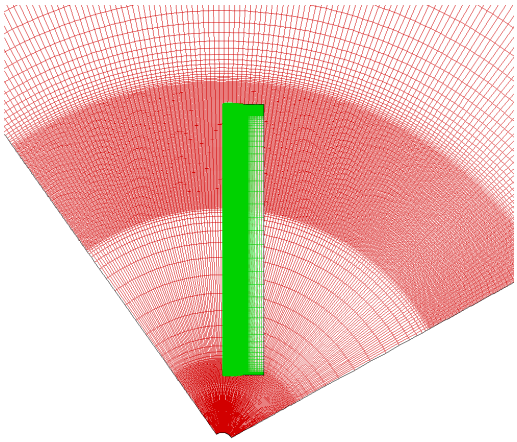

(c) Top-view of overset mesh system

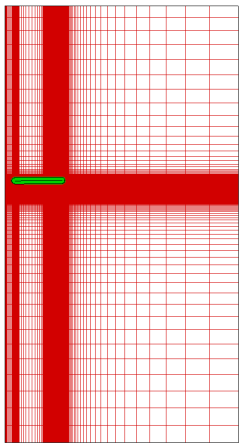

(d) Side-view of overset mesh system

Figure 6.2: Overset mesh system used for BO 105 rotor blade simulations: Green – blade mesh, Red – background mesh for wake capture

surface occurs around 22% of the chord. On the lower surface, the transition onset location gradually moves upstream in the radially outward direction. For comparison with the current simulations, the experimental data was digitized from [114], which appears to have been extracted from the dotted white line on the blades in Fig. 6.1. However, it is evident that the extracted lower surface transition line is slightly downstream of the actual transition location as indicated by the darker regions on

the blade.

The Overset mesh system used for the BO 105 rotor blade simulations is shown in Fig. 6.2. The cylindrical background mesh used for wake capture has 140×208×220 points in the azimuthal, radial, and axial directions respectively. Three levels of wrap-around grid resolution were used on the blade surface: 200, 300, and 400 points. In the spanwise and the normal directions of the blade mesh, 151 and 75 grid points were used respectively. The computed transition onset locations along the blade span for the three grid sizes are compared with those from the experiment in Fig. 6.3. A grid resolution beyond 200 points in the wrap-around direction on the blade surface had negligible effect on the transition onset locations. Excellent agreement is seen between the experimental and the computed onset locations on the upper surface. On the lower surface, the transition model predicts an earlier onset as compared to the extracted transition line from the flow visualization. Transition on the upper surface occurs primarily due to adverse pressure gradient effects. On the lower surface, the transition onset location moves upstream radially outward in an almost linear fashion indicating that it is driven by the increasing local Reynolds number.

Intermittency contours on the upper and the lower surfaces of the rotor blade are shown in Figure 6.4. An intermittency value is zero in blue regions and one in red regions, representing laminar and turbulent boundary layers respectively. Spanwise-vorticity contours, which represent skin friction on the blade upper and lower surfaces, are shown in Fig. 6.5. Lines of abrupt increase in spanwise-vorticity are identified to mark the beginning of the turbulent boundary layer. Figure 6.6

Parameter	S-A	$\gamma - Re_\theta - \text{SA}$	Change (%)
C_T	0.00490	0.00495	0.82%
C_Q	0.000370	0.000355	-4.05%

Table 6.1: Effect of transition model on performance predictions for BO 105 rotor

shows the chordwise distribution of the spanwise-vorticity profiles on the upper and lower surfaces at six spanwise stations. An abrupt increase in the vorticity is clearly seen in this plot, further verifying the trend of transition onset variation along the blade span. On the upper surface, the vorticity profiles in the inboard sections are nearly zero at the transition onset location, which is representative of separation-induced transition.

Rotor thrust and power predictions are tabulated in Table 6.1. Compared to fully turbulent computations, the transition model prediction of rotor thrust is 1% higher, and the rotor power is 4.5% lower. These values are similar to the predictions of Heister [114]. Figure 6.7(a) visualizes blade tip vortices using iso-surfaces of vorticity magnitude, and Fig. 6.7(b) shows rotor the wake contraction in one azimuthal plane as well as the first six blade passages of the tip vortex.

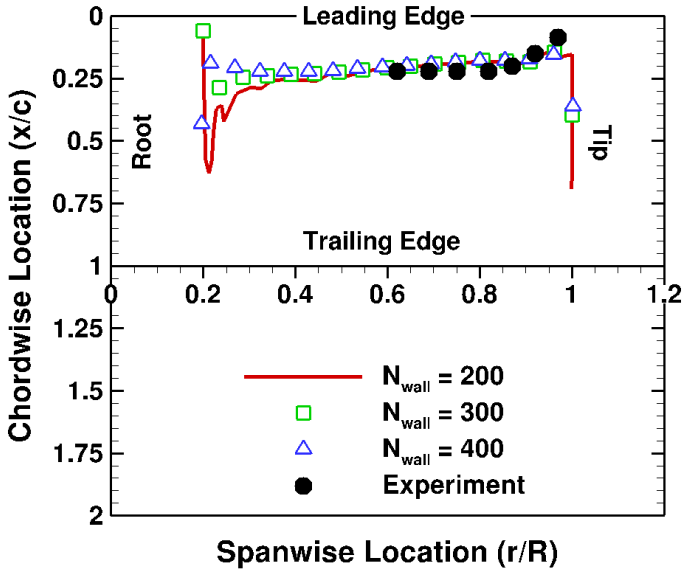

(a) Upper surface

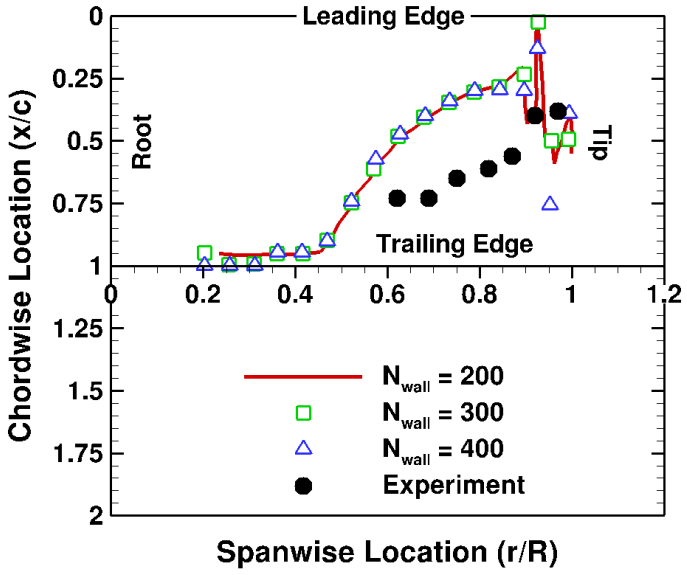

(b) Lower surface

Figure 6.3: Transition onset prediction on BO 105 rigid rotor with three wrap-around grid resolutions. N_{wall} – number of grid points on blade surface in wrap-around direction (Experiment [115])

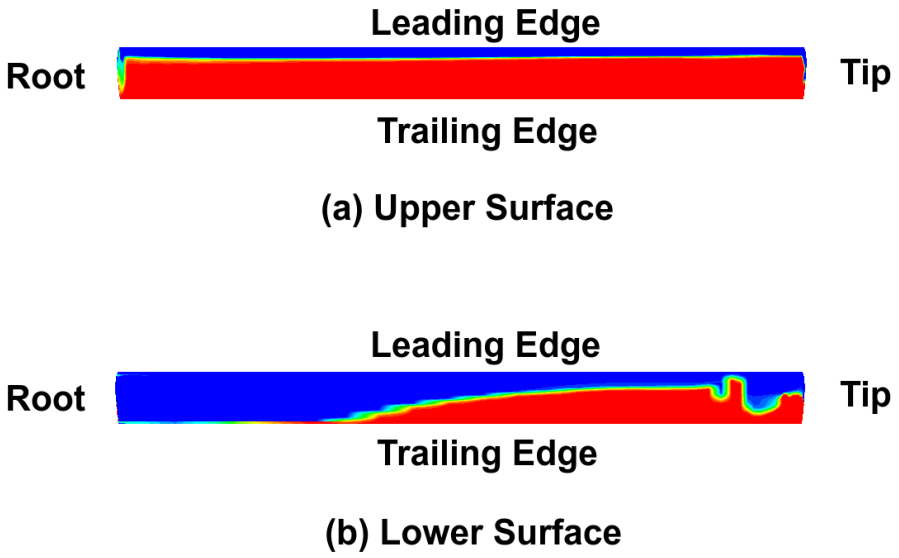

Figure 6.4: Intermittency contours on BO 105 rotor blade surface: Blue – laminar, Red – turbulent.

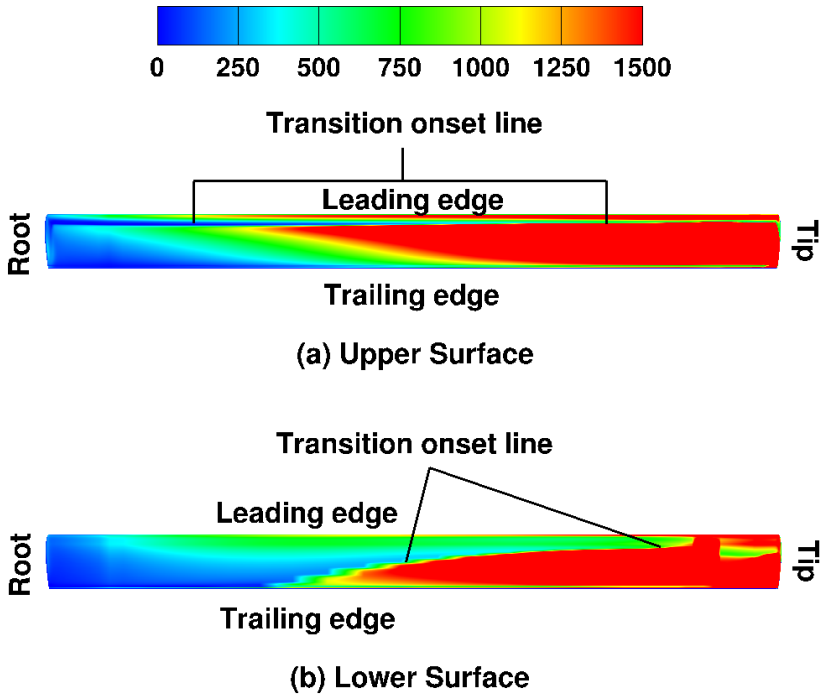

Figure 6.5: Spanwise vorticity contours on BO 105 rotor blade surface

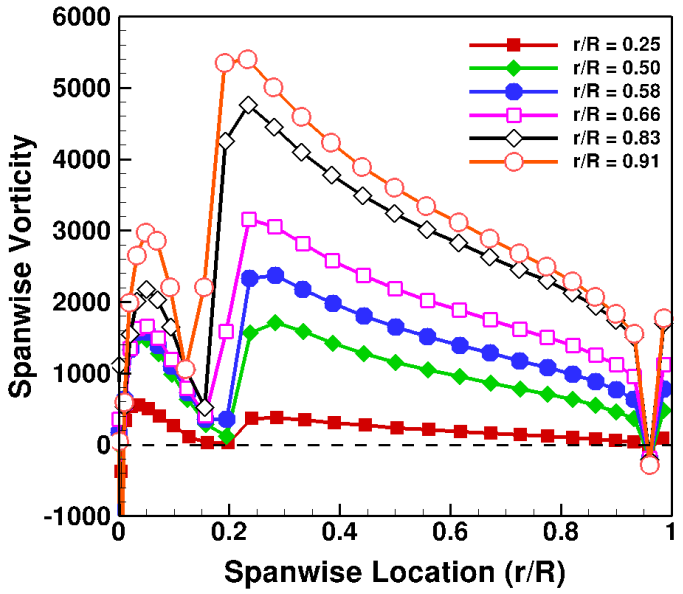

(a) Upper surface

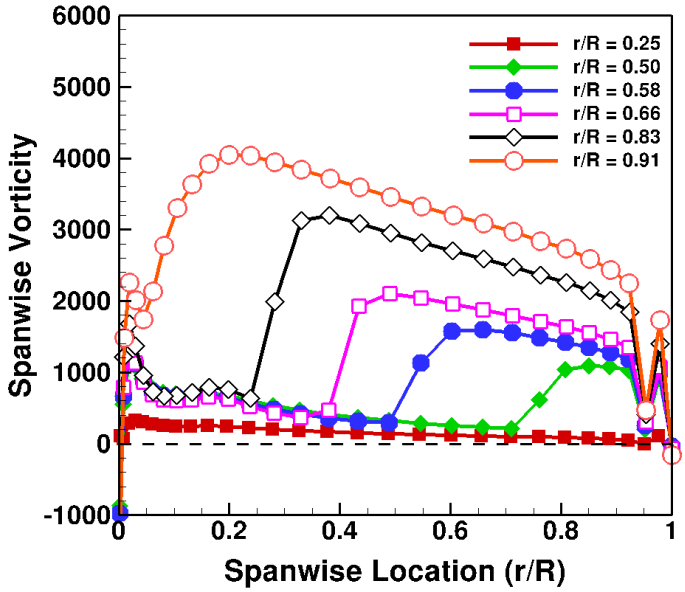

(b) Lower surface

Figure 6.6: Chordwise distribution of spanwise-vorticity profiles at six spanwise stations on the BO 105 rotor blade – sudden jump in vorticity indicates transition to turbulence

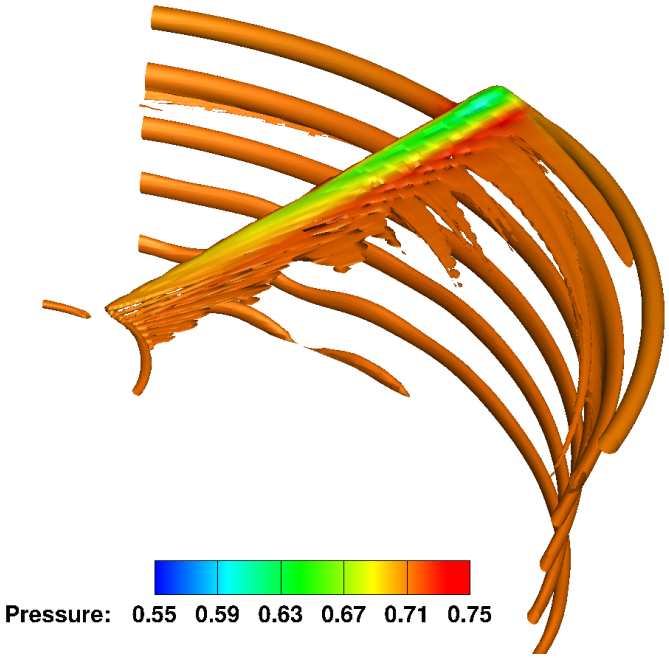

(a) Iso-surface of vorticity magnitude colored by non-dimensional pressure

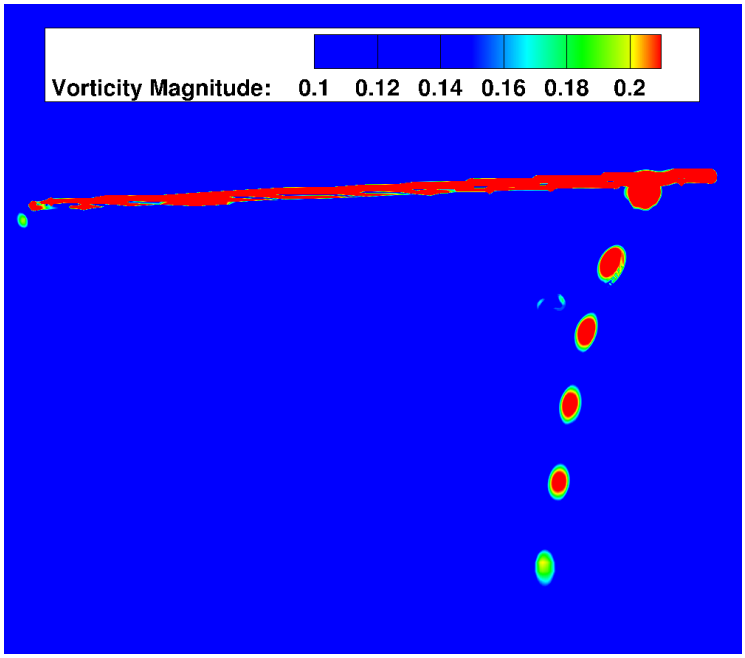

(b) Vorticity magnitude in the blade azimuthal plane

Figure 6.7: Tip-vortex and wake visualization for BO 105 rotor blade

6.2.2 UH60-A Rigid Rotor

The 4-bladed UH60-A rigid rotor is simulated with and without the transition model for collective pitch angles ranging from 0° to 15°. The rotor blade has a rectangular planform with a swept tip. It has a unique non-linear twist distribution, with a maximum twist of -13.3° at 92% of blade span, and has an aspect ratio of 15.3. The blade consists of two airfoil sections: SC1094R8 between 50% and 90% of span, and SC1095 outside of this region. In hover, the tip Mach number is 0.65 and the tip Reynolds number is 7.4×10^6. The blade planform shape and the overset mesh system used for this case are shown in Fig. 6.8. The rotor blade mesh has 200 grid points on its surface in the wraparound direction, 151 points in the spanwise direction, and 75 points in the wall-normal direction. The cylindrical background mesh used for wake capture has $140\times188\times220$ points in the azimuthal, radial, and axial directions respectively.

Figure 6.9 shows intermittency contours on the upper and the lower surfaces of the rotor blade at various collective pitch angles. Blue regions indicate a laminar boundary layer and red regions indicate a turbulent boundary layer. Variation of the predicted transition onset locations with collective pitch angles is plotted for both the upper and the lower surfaces of the rotor blade in Fig. 6.10. Spanwise variation of the transition onset locations at every collective angle is very similar to that the BO 105 rotor case. The upper surface boundary layer transitions between 10% to 20% of chord, and the lower surface boundary layer transitions in a linear fashion in the radially outward direction. With increasing collective pitch angle, the transition

point gradually moves upstream on the upper surface, and downstream on the lower surface. This is consistent with the effects of pressure gradient on transition onset location, as observed in the 2-D simulations. Downstream movement of transition onset near the blade root and tip can be attributed to the induced downwash caused by the root and tip vortices, thereby reducing the effective angle of attack. Since the boundary layer is more three-dimensional in these regions, including crossflow effects is likely to provide more realistic transition predictions.

Variation of the rotor thrust and torque with the collective pitch angle, obtained with and without the transition model, are plotted in Fig. 6.11. Both the thrust and the torque increase with increasing collective angle. Variation of rotor thrust with torque is plotted in Fig. 6.12(a). The percentage change in thrust and torque coefficients due to the inclusion of the transition model are plotted in Fig. 6.12(b). The SA-transition model predicts higher thrust values than those from the SA-turbulent model by less than 2%. Whereas, torque values obtained with SA-transition model are consistently lower than those obtained with the SA-turbulent model for all collective angles. The discrepancy is around 8% at 0° collective, and decreases to approximately 2% at 15° collective. Figure 6.13 shows the increased figure of merit due to the lower torque and higher thrust predicted by the transition model. Rotor wake visualization at 10° collective pitch angle is shown in Fig. 6.14 by plotting the iso-surfaces of vorticity magnitude. The tip vortex roll-up process is visualized in Fig. 6.15. A secondary vortex is also observed in this figure.

(a) Blade planform

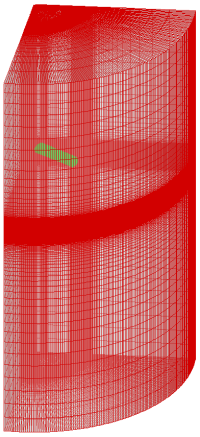

(b) Cylindrical wake mesh

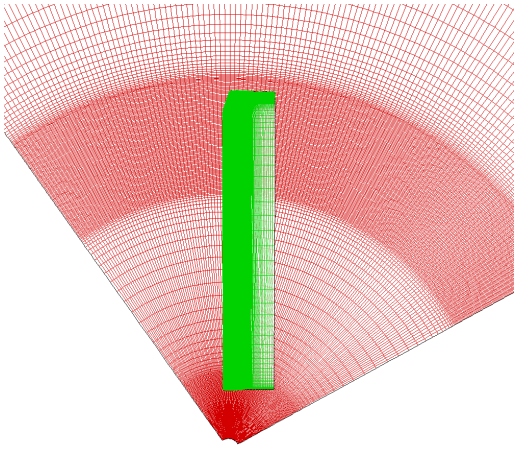

(c) Top-view of overset mesh system

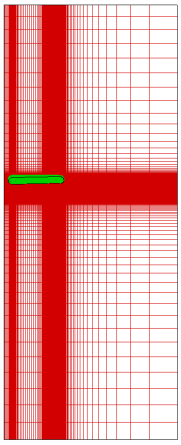

(d) Side-view of overset mesh system

Figure 6.8: Overset mesh system used for UH60-A rotor blade simulations: Green – blade mesh, Red – background mesh for wake capture

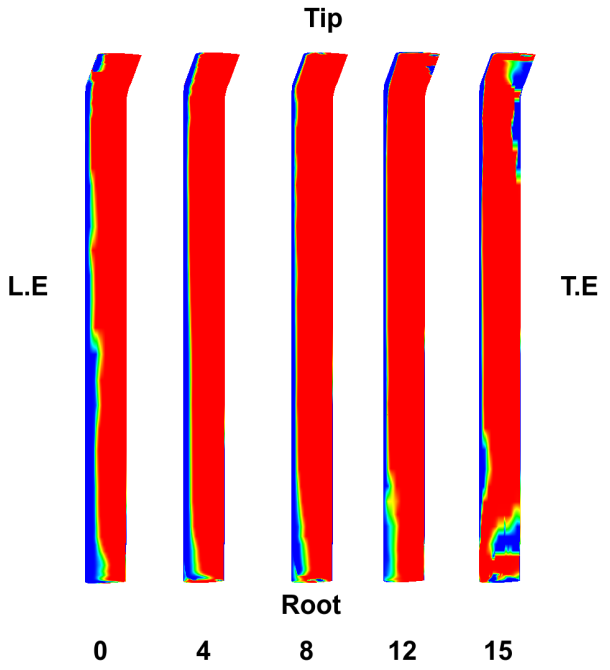

(a) Upper surface

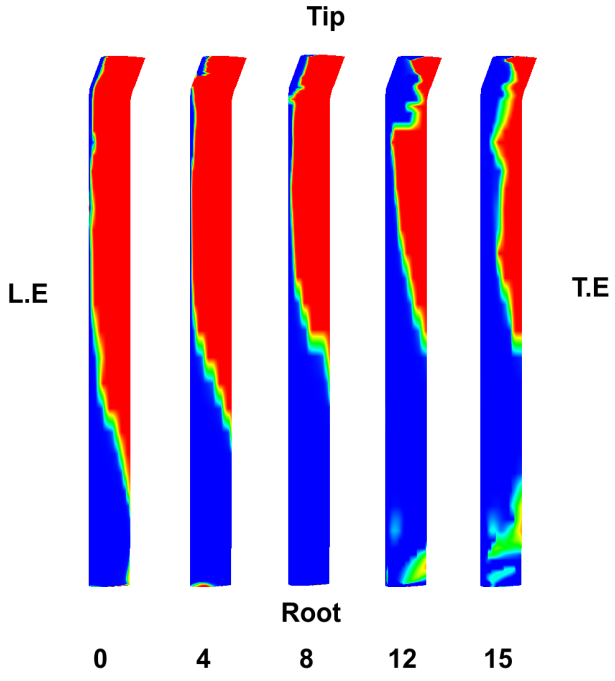

(b) Lower surface

Figure 6.9: Blade surface intermittency contours on UH60A rotor at collective pitch angles (in degrees): 0, 4, 8, 12, 15. Blue: Laminar, Red: Turbulent

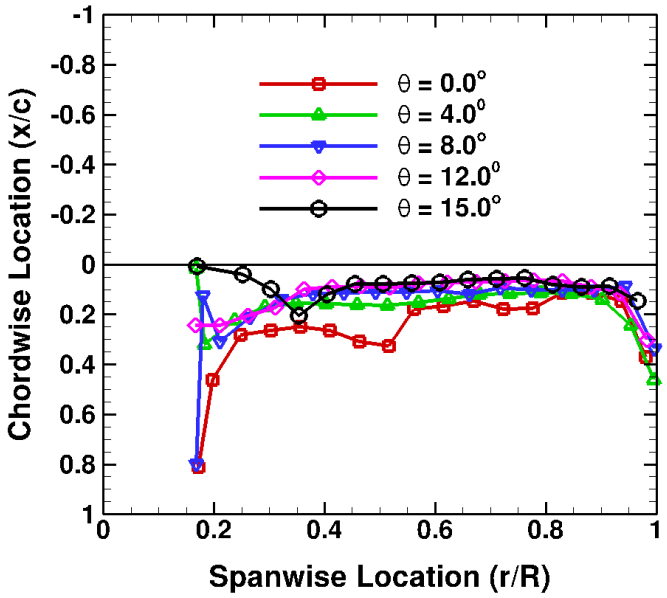

(a) Upper surface

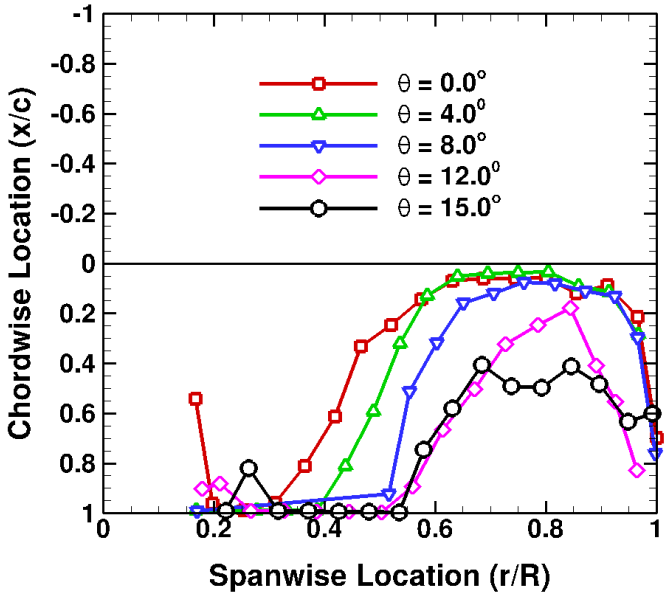

(b) Lower surface

Figure 6.10: Variation of transition onset location with collective pitch angle on UH60-A rigid rotor

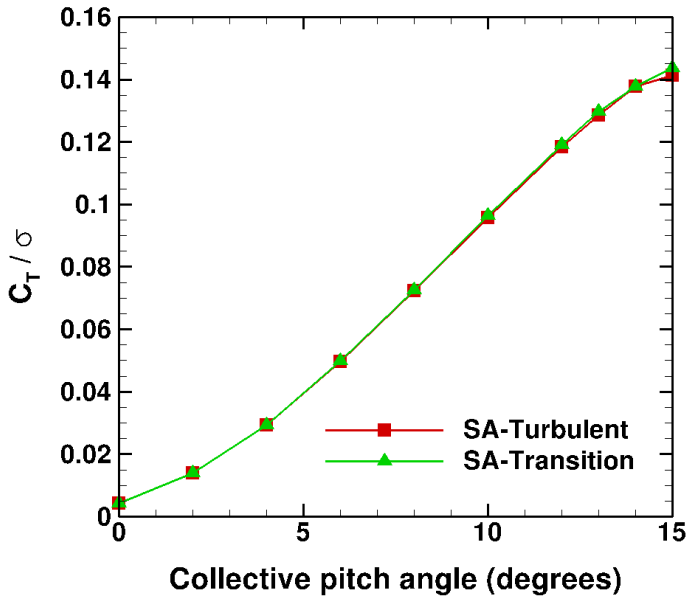

(a) Thrust Vs Collective

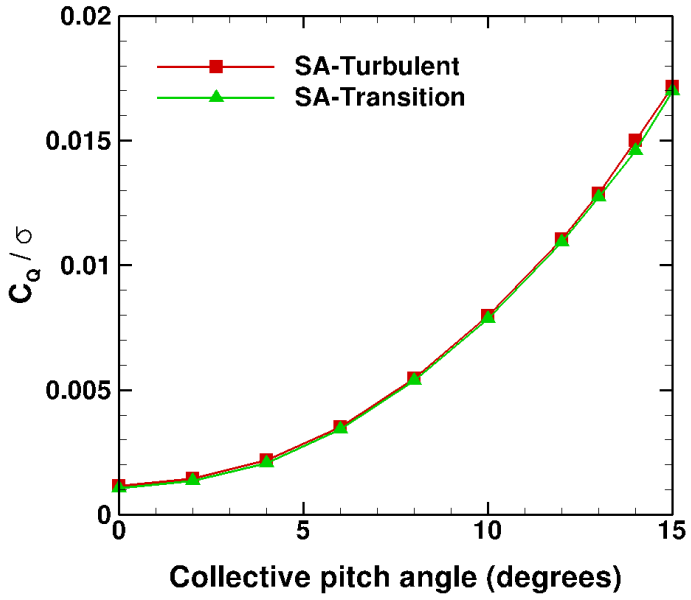

(b) Torque Vs Collective

Figure 6.11: Effect of transition model on rotor thrust and torque for UH60-A rigid rotor

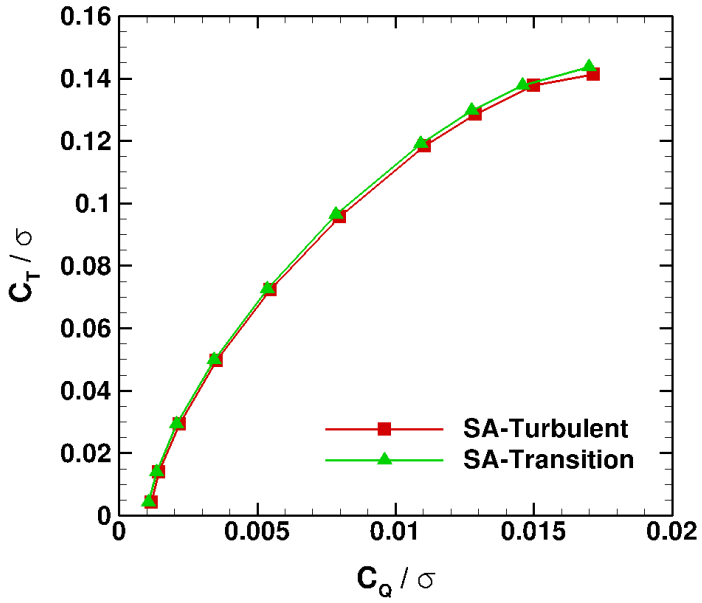

(a) Thrust Vs Power

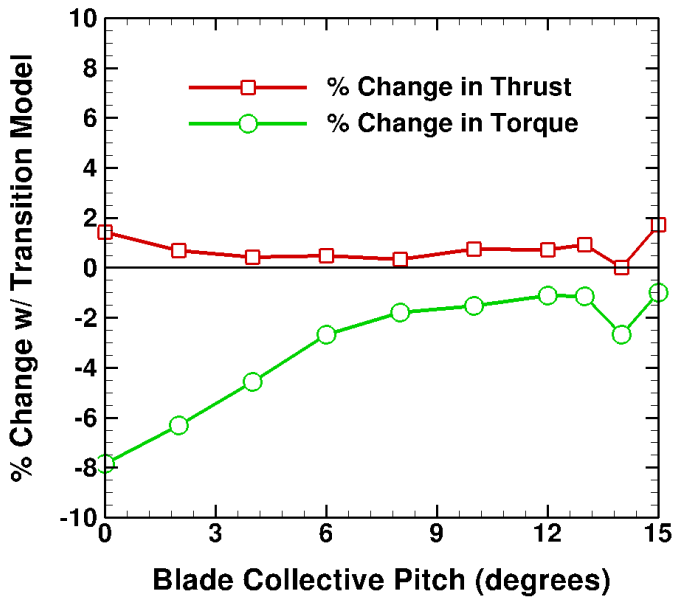

(b) % change in thrust and torque

Figure 6.12: Effect of transition model on rotor thrust and torque for UH60-A rigid rotor (positive % change represents increase from fully turbulent value, and vice versa)

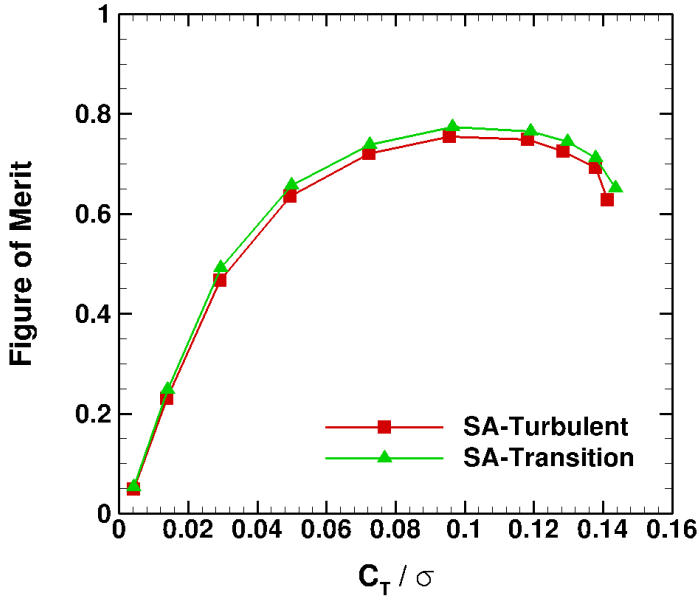

(a) FM Vs Disk loading

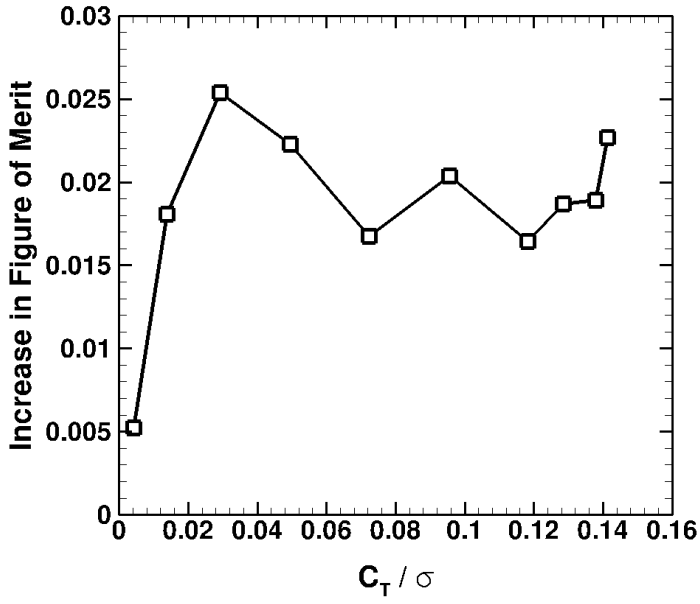

(b) Increase in FM with Transition Model

Figure 6.13: Effect of transition model on rotor figure of merit for UH60-A rigid rotor

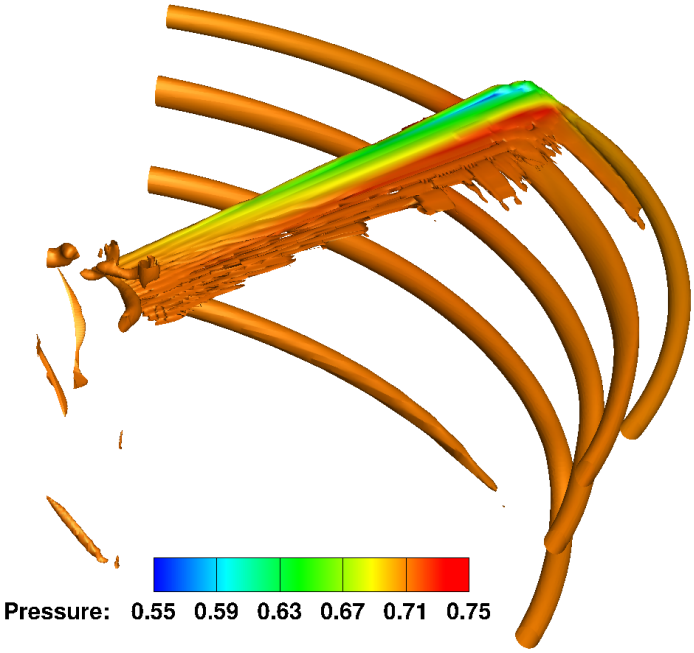

(a) Iso-surface of vorticity magnitude colored by non-dimensional pressure

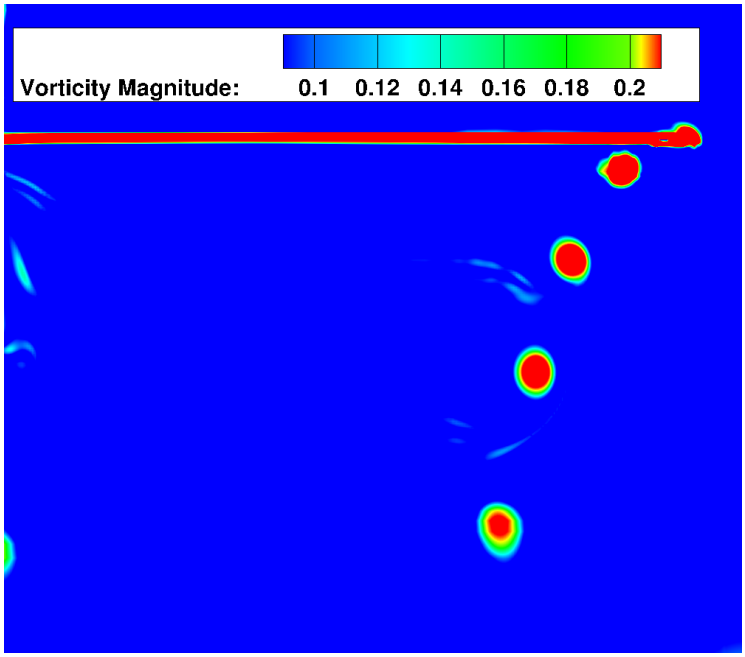

(b) Vorticity magnitude in the blade azimuthal plane

Figure 6.14: Tip-vortex and wake visualization on UH60-A rotor blade at 10° collective pitch angle

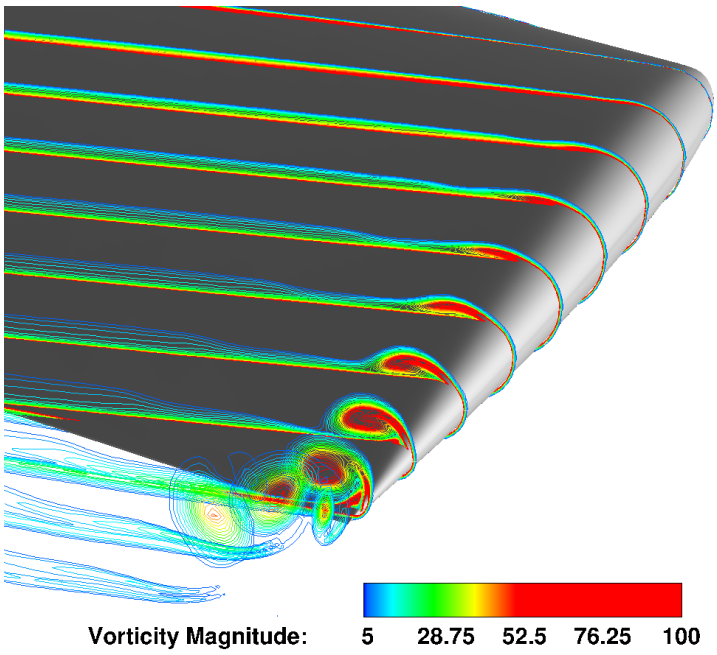

Figure 6.15: Tip-vortex roll-up for UH60-A rotor blade at 10° collective pitch angle

6.3 Wind Turbine Flows

Sustainable wind energy technology has the potential to offset the ever-increasing demand for fossil fuel-based energy resources and alleviate the associated adverse impact on the environment. Many ongoing research efforts are focused on maximizing the efficiency of wind power generation through innovative rotor blade designs. The ongoing work at Sandia National Laboratories [117] towards the development of a 100-meter all-glass rotor blade for offshore wind farms is one such example. With the introduction of new composite materials and large rotor diameters in such designs, accurate aeroelastic analysis [117] becomes particularly important in predicting the aerodynamic and structural loads. This can provide valuable data to optimize rotor blade design for increased performance and fatigue life.

Wind turbine blades extract energy from wind to generate torque. Thus the aerodynamic environment of isolated wind turbine blades is very similar to that of rotorcraft blades when the helicopter is in descent flight beyond a certain descent rate. Although compressibility effects are not a major concern in wind turbines, both pitch regulated and stall regulated turbine blades experience dynamic stall due to their operation at very high effective angles of attack. In smaller wind turbines with rated power of less than 100kW, the boundary layer can remain laminar on large portions of the blades. In addition, due to the lower rotational speeds of wind turbines compared to rotorcraft, most of the blade span operates at essentially incompressible flow conditions. Transition, dynamic stall, and low-speed flow form a challenging aerodynamic environment for traditional CFD codes that solve the

compressible RANS equations using conventional turbulence models. The purpose of the present simulations is to assess the performance of the transition model and the OverTURNS solver for the NREL Phase VI model rotor configuration at various wind speeds.

6.3.1 Previous CFD Studies of NREL Phase VI Rotor

The Phase VI rotor experiments were conducted by the US National Renewable Energy Laboratory (NREL) as part of the *Unsteady Aerodynamics Experiment* (UAE). These experiments were carried out in NASA-Ames wind tunnels [103]. The Phase VI rotor is a 2-bladed configuration with a rotational speed of 72 RPM and a blade radius of 5.03 meters. The 21% thick S809 airfoil section is used on the rotor blades. Experiments were conducted for a range of wind speeds, pitch angles, and yaw angles.

The NREL Phase VI rotor is one of the most widely investigated configurations in CFD simulations due to the availability of detailed experimental data for validation. Most of the CFD studies simulated wind speeds between 7 m/s and 20 m/s. At zero pitch and yaw angles, flow separation occurs on the upper surface of the blade at wind speeds of 10 m/s and higher. Several CFD studies have reported unsatisfactory predictions for the 10 m/s test case due to the difficulty in capturing incipient separation on the blades. RANS simulations of Duque [118] using a coupled aerodynamics-structural dynamics methodology (OVERFLOW-D2 and CAMRAD II) demonstrated good agreement with experimental data for power and

spanwise loading in both axial and yawed flow conditions. The boundary layer was treated as fully turbulent and used the Baldwin-Barth turbulence model. This work also included comprehensive analysis using the aeroelastic code CAMRAD II [119], with various stall delay models and dynamic stall models. The comprehensive analysis produced satisfactory predictions for attached flow conditions, but at higher wind speeds, the method failed to capture stalled rotor flow properly, which was attributed to the airfoil characteristics database and the stall models used. Sorensen and Michelsen [120] used the incompressible ELLIPSYS3D solver along with the two-equation k-ω SST turbulence model. Their study showed sensitivity of predictions to the choice of turbulence model when incipient separation is present at a wind speed of 10 m/s.

Le Pape and Lecanu [121,122] used the compressible ELSA flow solver and the k-ω SST turbulence model. Their studies showed improved predictions for the 10 m/s wind speed case with the use of a low-Mach number preconditioning technique. Xu and Sankar [123] used a hybrid inviscid-viscous methodology along with the S-A turbulence model, the Baldwin-Lomax turbulence model, and the Eppler transition model. Although the predictions at 7 m/s and 20 m/s were close to the experimental data, the 10 m/s solution again showed discrepancy similar to the other CFD studies. More recently, Gomez and Steijl [124] simulated the Phase VI rotor using an unsteady RANS solver and the k-ω SST turbulence model. They studied the effect of wind tunnels walls and the tower. Inclusion of the tower showed a reduction of rotor thrust and generated torque due to blade/tower interaction. Recent $\gamma - Re_\theta$ transition model simulations of the Phase VI rotor by Langtry [125] and

Aranake [126] showed some benefit of predicting the laminar-separation bubble at higher wind speeds to trigger earlier separation than a fully turbulent simulation.

6.3.2 NREL Phase VI Rotor Simulations

In this work, the NREL Phase VI rotor blades were simulated at 0° pitch and yaw angles. The following seven wind speed values were simulated with and without the transition model: 3.5, 7, 10, 15, 20 and 25 m/s. The rotor overset mesh system used for these simulations is shown in Fig. 6.16. Since this is a 2-bladed rotor, the wake mesh extends from 0° to 180° with periodicity in the azimuthal direction. Dimensions of the C-O mesh for the rotor blade used are 257 x 51 x 51 points in the wraparound, spanwise, and normal directions respectively. Dimensions of the cylindrical background mesh are 201 x 133 x 164 points in the azimuthal, radial, and axial directions respectively. Since the tip Mach number for these simulations is approximately 0.11, a low-speed incompressible flow environment is present in the computational domain. Therefore, the low-Mach preconditioner algorithm in the OverTURNS flow solver was used in these computations to improve convergence and accuracy of the solution.

Thrust and torque predictions obtained from fully turbulent and transitional flow simulations are compared to experimental data in Tables 6.2 and 6.3, as well as plotted in Fig. 6.17. Since the effective angle of attack increases with increasing wind speed, the rotor thrust also increases. Thrust predictions with and without transition model are in reasonable agreement with experimental data at all wind

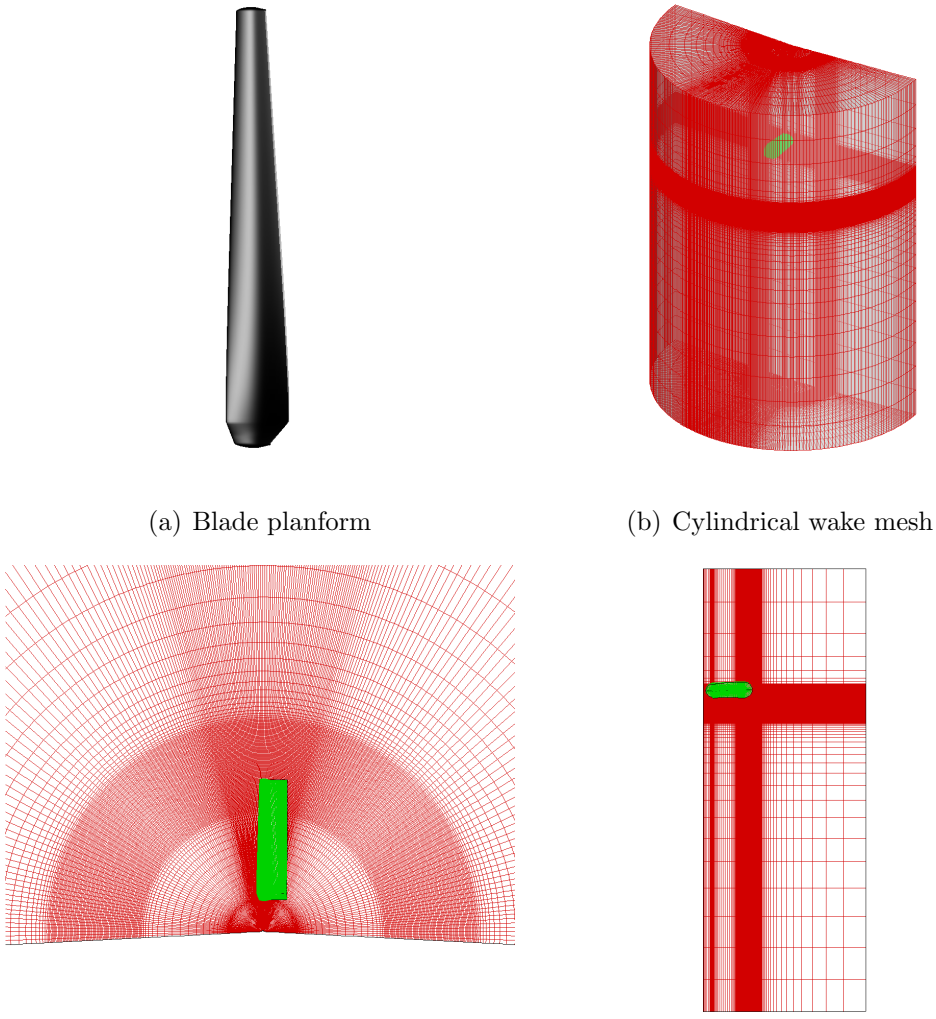

(a) Blade planform

(b) Cylindrical wake mesh

(c) Top-view of overset mesh system

(d) Side-view of overset mesh system

Figure 6.16: Overset mesh system used for NREL Phase VI rotor blade simulations: Green – blade mesh, Red – background mesh for wake capture

speeds. The transition model does not have a significant impact on thrust predictions as thrust is dominated by the pressure distribution rather than skin friction under these flow conditions. Maximum discrepancy in thrust values between the SA-turbulent and the SA-transition simulations is 6% at the lowest wind speed (3.5 m/s). CFD predictions of shaft torque also agree well with experimental data at wind speeds of 15 m/s and higher.

Wind Speed (m/s)	S-A	$\gamma - Re_\theta -$ SA	Experiment [103]
3.5	282.0	299.0	–
5.0	648.0	672.0	–
7.0	1181.0	1223.0	1154.0
10.0	1784.0	1696.0	1675.0
15.0	2584.0	2528.0	2283.0
20.0	3705.0	3758.0	3005.0
25.0	4850.0	4654.0	3889.0

Table 6.2: Comparison of thrust predictions for NREL Phase VI rotor (thrust in Newtons)

At wind speeds of 3.5 m/s, 5 m/s, and 7 m/s, torque values obtained with the transition model are greater than their fully turbulent values by 70.0%, 12.5%, and 7.2% respectively. These three cases correspond to generated power of 0.3 kW, 2 kW, and 5.8 kW based on the fully turbulent simulation values for this rotor. It is evident that for smaller wind turbines that operate at relatively low rated power ($<$ 5 kW), fully turbulent simulations are likely to under-predict power. Since the transition model captures the laminar portions of the blade boundary layer, the viscous drag is lower and consequently, the predicted torque is higher.

At a wind speed of 10 m/s, the torque is over-predicted by the baseline SA model and under-predicted by the $\gamma - Re_\theta -$ SA model as compared to the experi-

Wind Speed (m/s)	S-A	$\gamma - Re_\theta - \text{SA}$	Experiment [103]
3.5	40.0	68.0	–
5.0	270.0	304.0	–
7.0	778.0	834.0	805.0
10.0	1542.0	1100.0	1340.0
15.0	1108.0	756.0	1177.0
20.0	1039.0	1191.0	1110.0
25.0	1461.0	1493.0	1485.0

Table 6.3: Comparison of shaft torque predictions for NREL Phase VI rotor (torque in Newton-meter)

mental value. At the higher wind speeds (15, 20, 25 m/s), the transition model has less impact on both thrust and torque due to the massively separated flow present over a large region of the blade. Unsteady RANS simulations with the SA model in such flow regimes are not reliable, and may require the use of hybrid RANS-LES methods to resolve the flow structures in the separated regions. Detailed analysis of the flow field, including spanwise thrust/torque distributions, blade surface streamlines, eddy viscosity contours, surface pressure, and surface intermittency contours provide further insight into the performance predictions discussed above.

Spanwise thrust and torque distribution profiles at wind speeds of 3.5, 5, 7, 10, and 15 m/s are plotted in Figs. 6.18–6.20. The curves in these figures correspond to

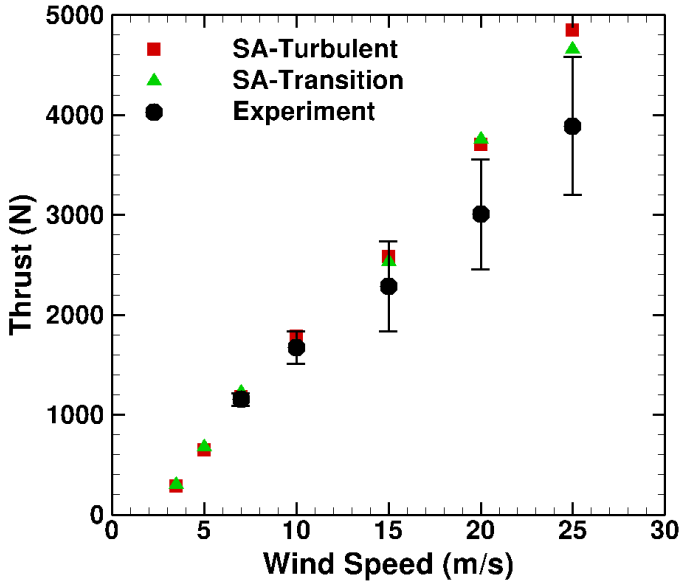

(a) Thrust

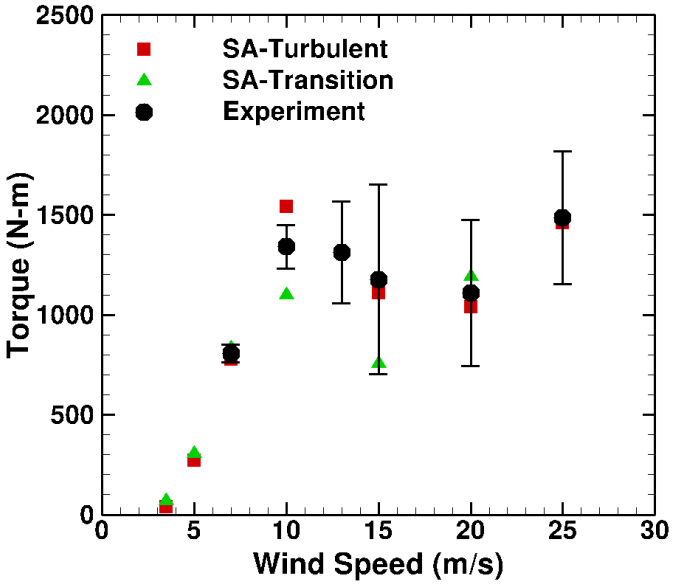

(b) Torque

Figure 6.17: NREL Phase VI rotor thrust and torque predictions with $\gamma - Re_\theta -$ SA transition model (Experiment from [103])

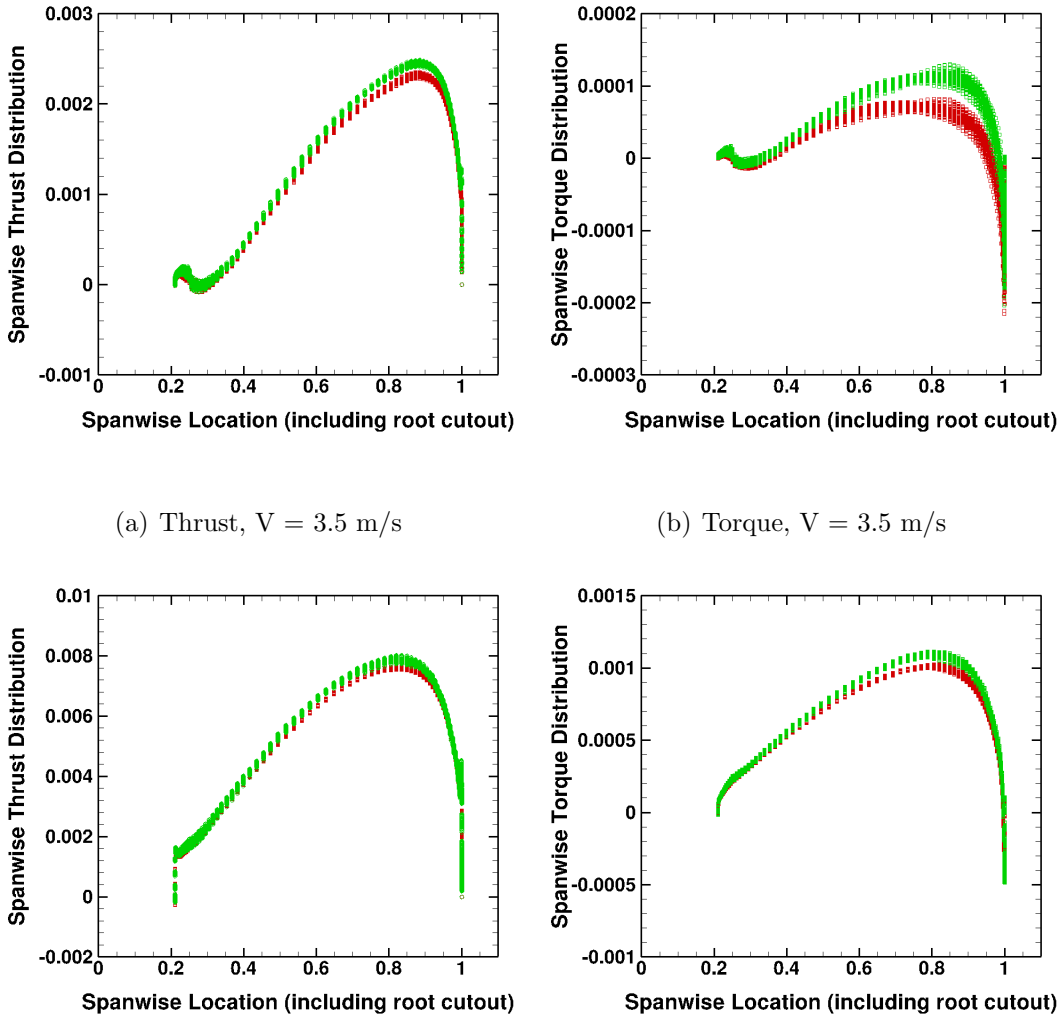

(a) Thrust, V = 3.5 m/s

(b) Torque, V = 3.5 m/s

(c) Thrust, V = 5.0 m/s

(d) Torque, V = 5.0 m/s

Figure 6.18: NREL Phase VI rotor spanwise thrust and torque distribution profiles at wind speeds of 3.5 m/s and 5.0 m/s. Data is plotted for one rotor revolution. Red: SA–Turbulent, Green: SA–Transition

the variation of the spanwise profiles over one complete rotor revolution. At 3.5, 5, and 7 m/s, the SA-transition model predictions of thrust and torque distributions outboard of 40% rotor radius are greater than those from the SA-turbulent model. At 10 m/s, the decrease in thrust and torque profiles outboard of 50% of span

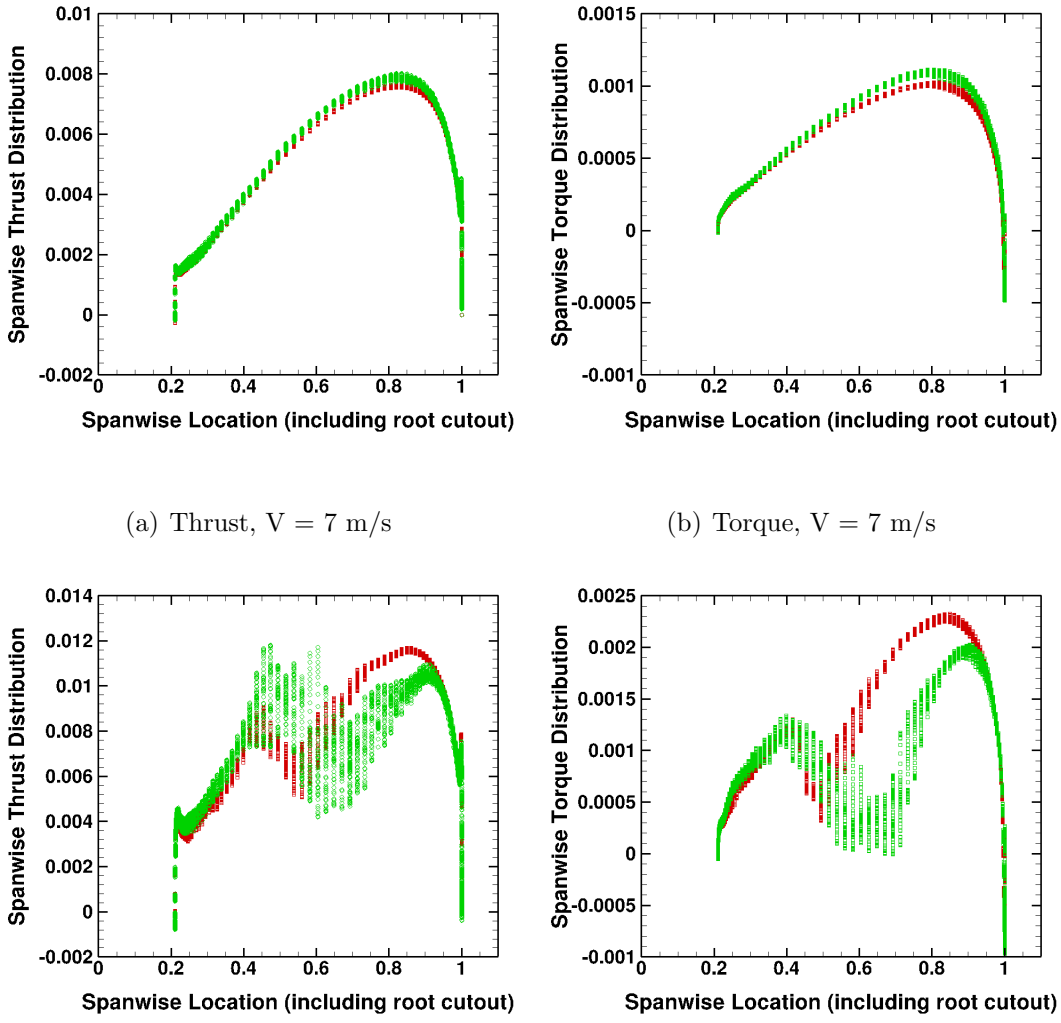

(a) Thrust, V = 7 m/s

(b) Torque, V = 7 m/s

(c) Thrust, V = 10 m/s

(d) Torque, V = 10 m/s

Figure 6.19: NREL Phase VI rotor spanwise thrust and torque distribution profiles at wind speeds of 7 m/s and 10 m/s. Data is plotted for one rotor revolution. Red: SA–Turbulent, Green: SA–Transition

indicates flow separation. The SA-transition model predicts a larger separation region compared to those from the SA-turbulent model at this wind speed. The amount of unsteadiness in the spanwise profiles increases due to separation. At 15 m/s, the SA-transition model predicts separation on most of the blade surface,

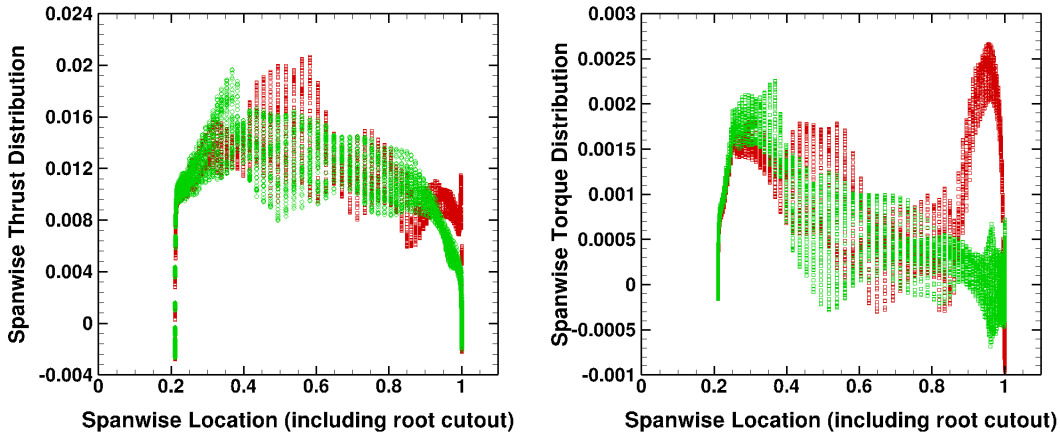

(a) Thrust, V = 15 m/s

(b) Torque, V = 15 m/s

Figure 6.20: NREL Phase VI rotor spanwise thrust and torque distribution profiles at a wind speed of 15 m/s. Data is plotted for one rotor revolution. Red: SA–Turbulent, Green: SA–Transition

whereas the SA-turbulent model indicates an attached boundary layer closer to the tip region.

Instantaneous chordwise surface pressure coefficient profiles obtained with and without the transition model are compared with experimental data for wind speeds of 7, 10, 15, 20, and 25 m/s at the following four radial stations (in term of % of rotor radius): 30, 47, 80, and 95 (see Figs. 6.21–6.25). At 7 m/s, both versions of CFD predictions are in good agreement with experimental data. Pressure profiles obtained using the transition model show a small region of relatively constant value around mid-chord, indicating the presence of a small laminar separation bubble. At 10 m/s, the SA-turbulent predictions appear to be in better agreement with measurements. However, the plotted CFD profiles correspond to instantaneous data in a highly unsteady environment. CFD predictions are within experimental uncertainty

for all the cases presented (experimental uncertainty bars are not shown) [126]. Flow separation for the 10 m/s case at 47% radial location is captured by both the turbulent and the transitional flow simulations (Fig. 6.22(b)). For the 15 m/s case at the 95% radial station shown in Fig. 6.23(d), the SA-turbulent pressure profile prediction is much closer to the experimental measurement compared to the SA-transition prediction. In this case, the transition model predicts a fully separated boundary layer near the blade tip, manifested in the form of a loss of suction peak on the upper surface. This observation is also supported by the spanwise thrust and torque distribution plotted at 15 m/s in Fig. 6.20. However, such a loss in lift near the blade tip is not in seen in experiments at 15 m/s. This shows that the laminar separation bubble predicted by the transition model is unstable and does not reattach, causing loss of lift and increased pressure drag. Robustness and convergence properties of the transition model for low-speed, low-Reynolds number separation-induced transition may need improvement. In addition, crossflow transition may occur near the tip due to the spanwise flow created by the tip vortex. Spanwise flow in combination with pressure gradients may accelerate the transition process and reduce separation separation in this region. Results from preliminary work performed on the prediction of crossflow transition on swept wings and rotating blades are presented in Appendix A of this thesis. At wind speeds of 20 m/s and 25 m/s, the pressure profiles obtained with both the SA-turbulent and the SA-transition models show fully separated boundary layer, and are in good agreement with experimental data.

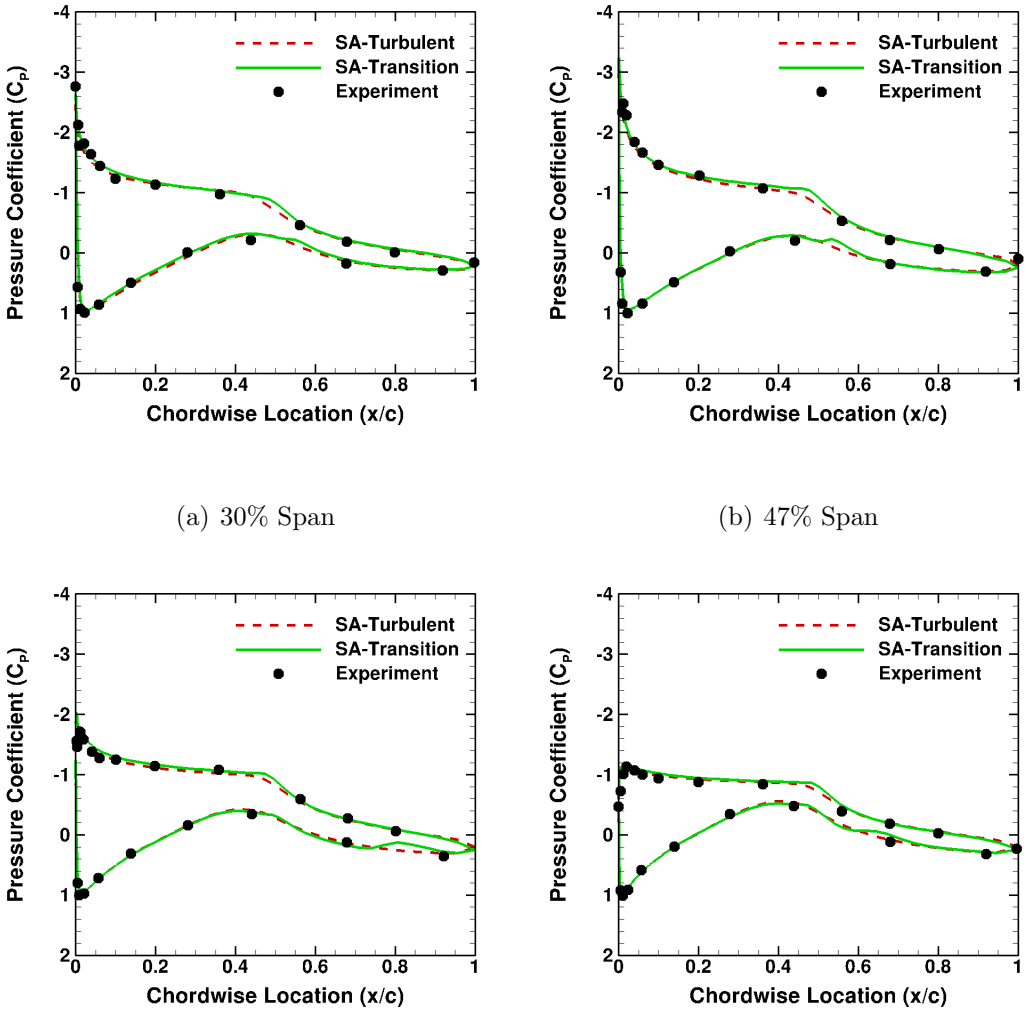

(a) 30% Span

(b) 47% Span

(c) 80% Span

(d) 95% Span

Figure 6.21: Chordwise blade surface pressure distribution profiles at four spanwise stations for wind speed of 7 m/s on the NREL Phase VI rotor blade (Experiment from [103])

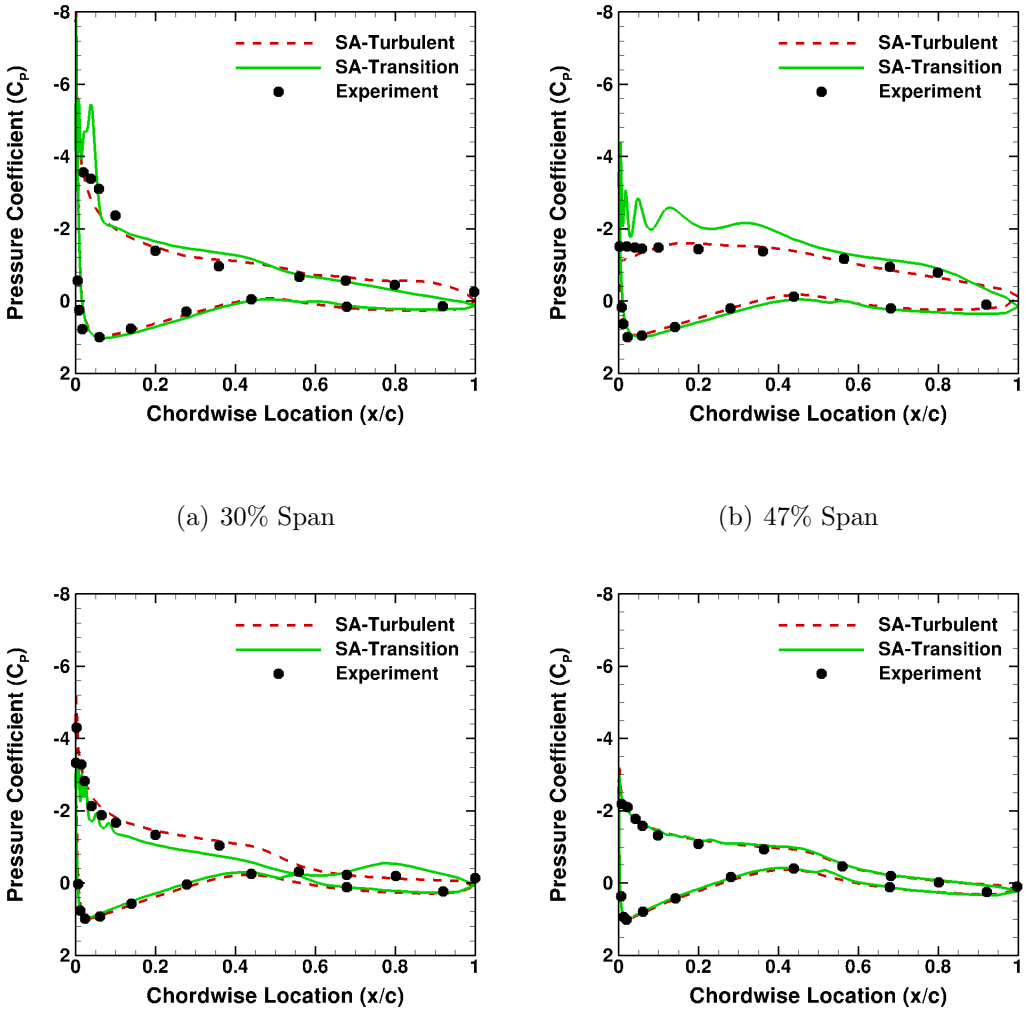

(a) 30% Span

(b) 47% Span

(c) 80% Span

(d) 95% Span

Figure 6.22: Chordwise blade surface pressure distribution profiles at four spanwise stations for wind speed of 10 m/s on the NREL Phase VI rotor blade (Experiment from [103])

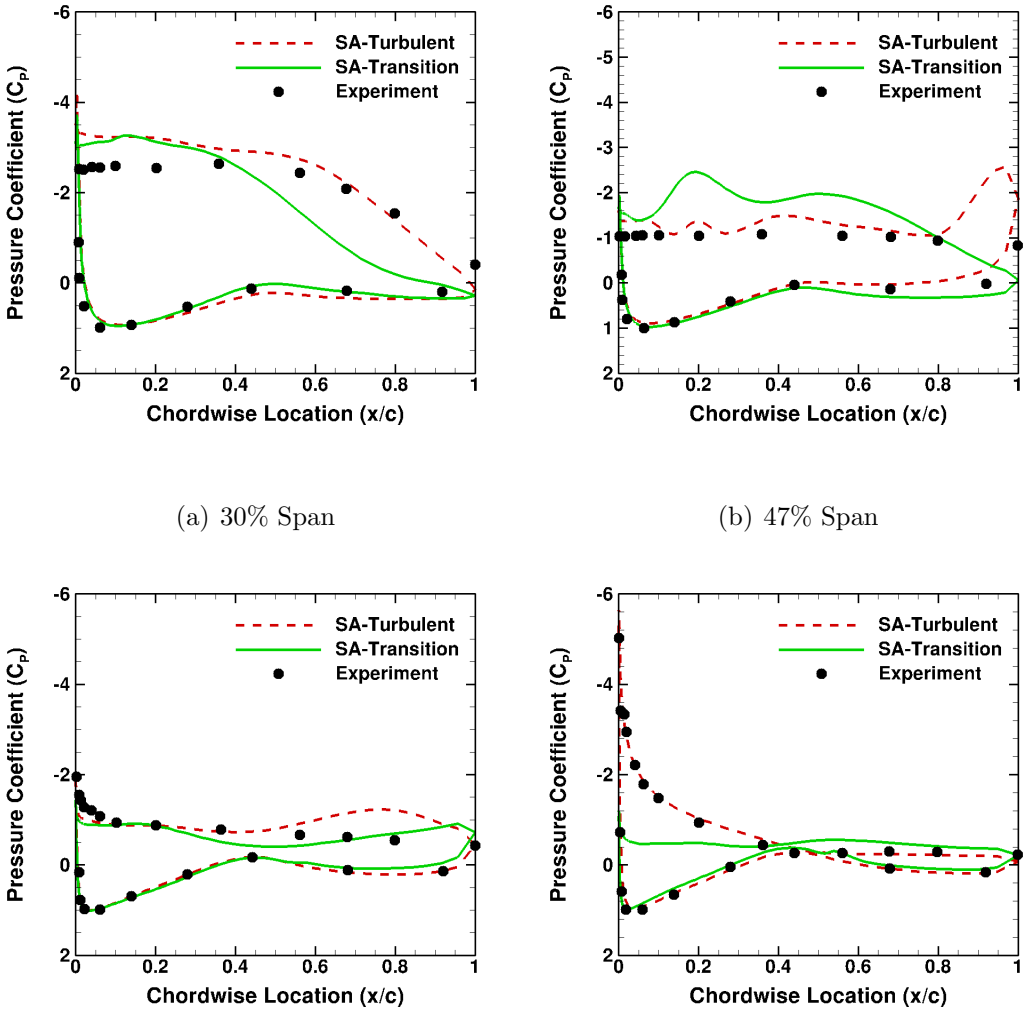

(a) 30% Span

(b) 47% Span

(c) 80% Span

(d) 95% Span

Figure 6.23: Chordwise blade surface pressure distribution profiles at four spanwise stations for wind speed of 15 m/s on the NREL Phase VI rotor blade (Experiment from [103])

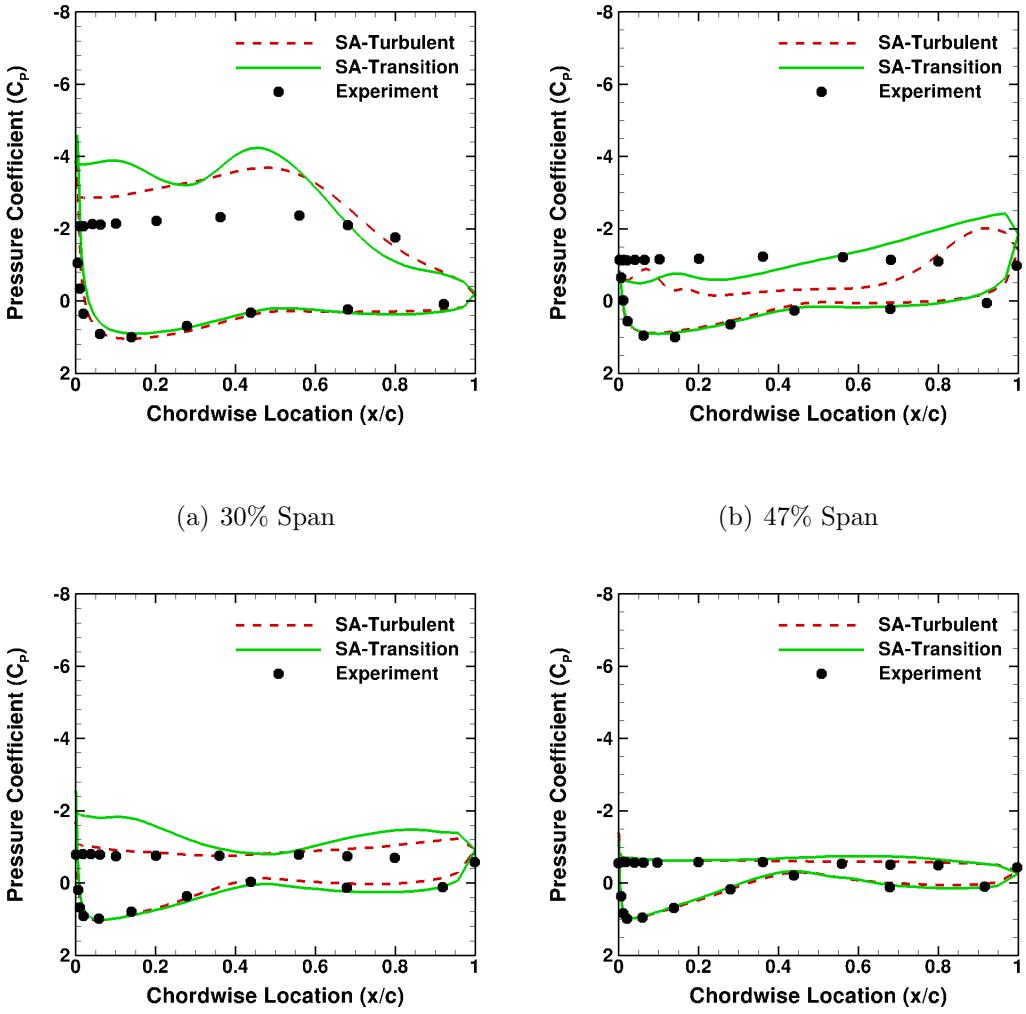

(a) 30% Span

(b) 47% Span

(c) 80% Span

(d) 95% Span

Figure 6.24: Chordwise blade surface pressure distribution profiles at four spanwise stations for wind speed of 20 m/s on the NREL Phase VI rotor blade (Experiment from [103])

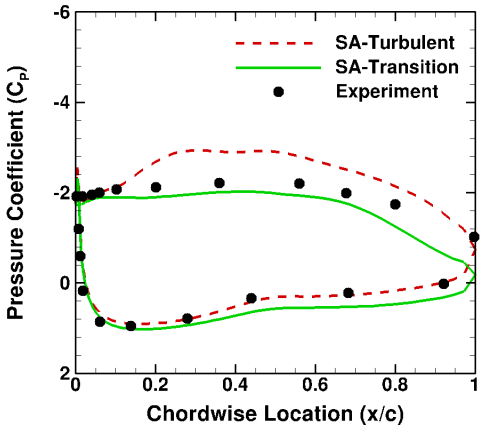

(a) 30% Span

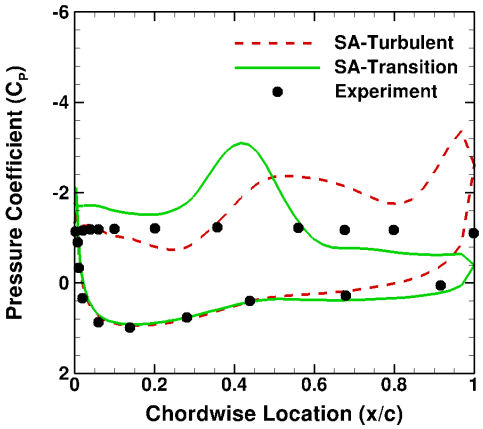

(b) 47% Span

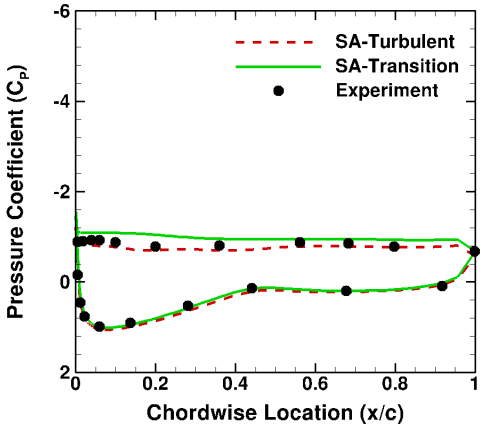

(c) 80% Span

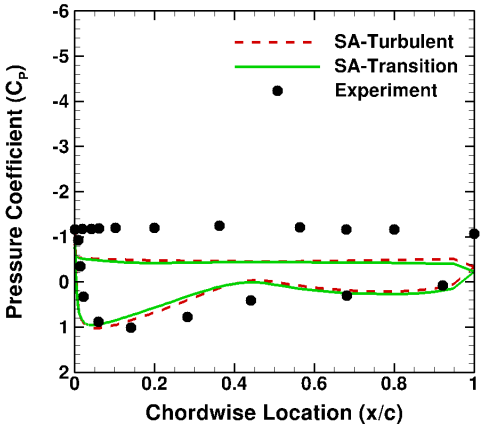

(d) 95% Span

Figure 6.25: Chordwise blade surface pressure distribution profiles at four spanwise stations for wind speed of 25 m/s on the NREL Phase VI rotor blade (Experiment from [103])

Upper and lower surface streamlines on the rotor blade are plotted for all wind speeds from 3.5 m/s to 20 m/s in Figs. 6.26–6.28. At lower wind speeds (up to 7 m/s), the inclusion of the transition model results in streamlines that clearly show the presence of a separation bubble on both the upper and the lower surfaces around the mid-chord along the entire blade span. Recall that the NREL Phase VI rotor blade is made of the S809 airfoil section. Transition onset predictions for two-dimensional flow S809 airfoil presented in Chatper 5 also showed that the onset location stays around the mid-chord on the upper surface until 6° AoA and then moves upstream abruptly, whereas it remains close to mid-chord on the lower surface between 0° and 20° AoA. The transition onset locations for the 3-D rotor cases presented here are also verified by the surface intermittency contours shown in Fig. 6.29. For wind speeds of 3.5, 5, and 7 m/s, intermittency contours confirm transition onset around the mid-chord. the Transition onset locations on the lower surface are irregular for wind speeds of 5 m/s and 7 m/s. Although the exact reason for this has not been identified, it is likely due to the inability of the boundary layer to reattach after the laminar separation point. This could be attributed to insufficient intermittency production in the laminar separation bubble. At wind speeds of 10 m/s and higher, the lower surface is entirely laminar as seen in the intermittency contour plot. Whereas, on the upper surface, transition onset location moves very close to the leading-edge. The irregular intermittency contours on the upper surface at higher wind speeds is due to flow separation, which is also visualized in the surface streamline plots shown in Figs. 6.27–6.28. For wind speeds of 15 m/s and higher, the streamlines for the SA-turbulent and SA-transition simulations indicate

complete separation on the upper surface of the blade and a fully attached boundary layer on the lower surface. Significant spanwise flow is observed in all cases with flow separation.

Streamlines at a wind speed of 10 m/s obtained with the SA-transition model show a larger separation region compared to that obtained with the SA-turbulent model. This is consistent with the spanwise distribution profiles of rotor thrust and torque for the 10 m/s case plotted in Fig. 6.19(b). Therefore, as reported in other CFD studies, the 10 m/s case appears to be a critical condition for this configuration, where incipient separation occurs. Use of transition model results in earlier boundary layer separation due to failure of the laminar-separation bubble to reattach (also known as the bursting phenomenon). Figure 6.30 shows the eddy viscosity contours at various spanwise sections for the 10 m/s case. While both the SA-turbulent and the SA-transition simulations show separation on the upper surface, the fully turbulent flow case shows separation only aft of the maximum thickness, whereas the transitional flow case indicates separation at the leading-edge of the airfoil, suggesting the occurrence of laminar bubble bursting. For this case, the SA-turbulent model over-predicts the shaft torque whereas, the SA-transition model under-predicts the torque compared to the experimental value. Although the transition model is able to trigger separation earlier than the fully turbulent SA model, its advantage is not conclusive due to the limitation of an unsteady RANS approach for separated flows.

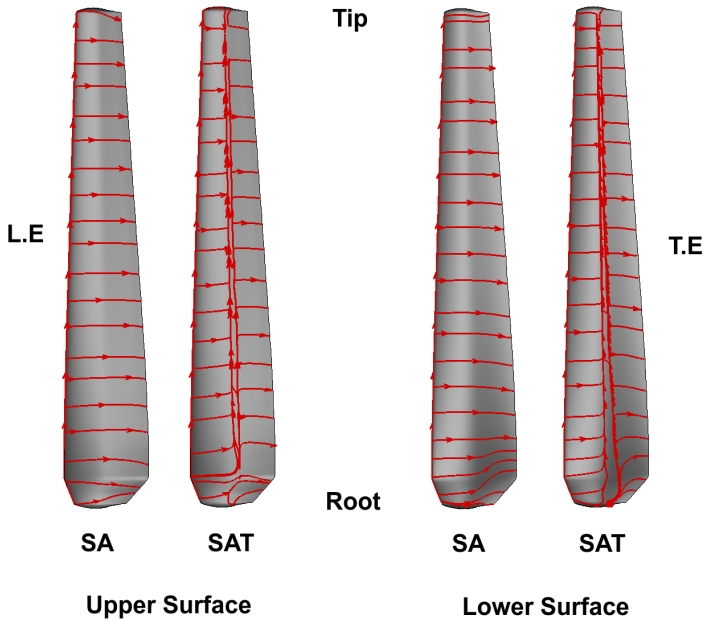

(a) V = 3.5 m/s

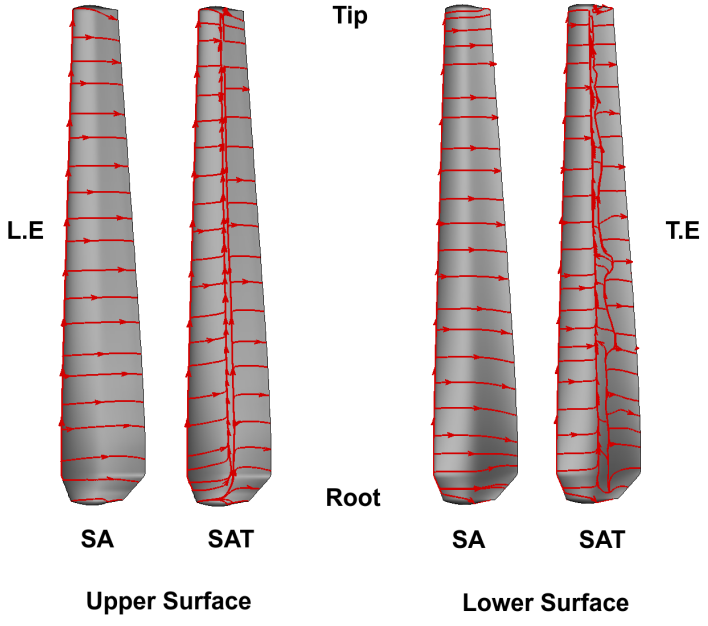

(b) V = 5 m/s

Figure 6.26: Blade surface streamlines on NREL Phase VI rotor at wind speeds of 3.5 m/s and 5 m/s. SA: SA–Turbulent, SAT: SA–Transition

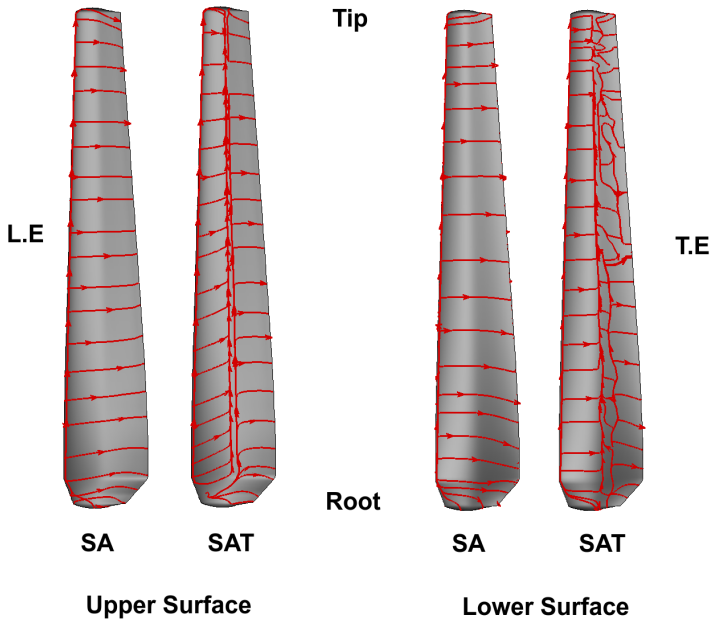

(a) V = 7 m/s

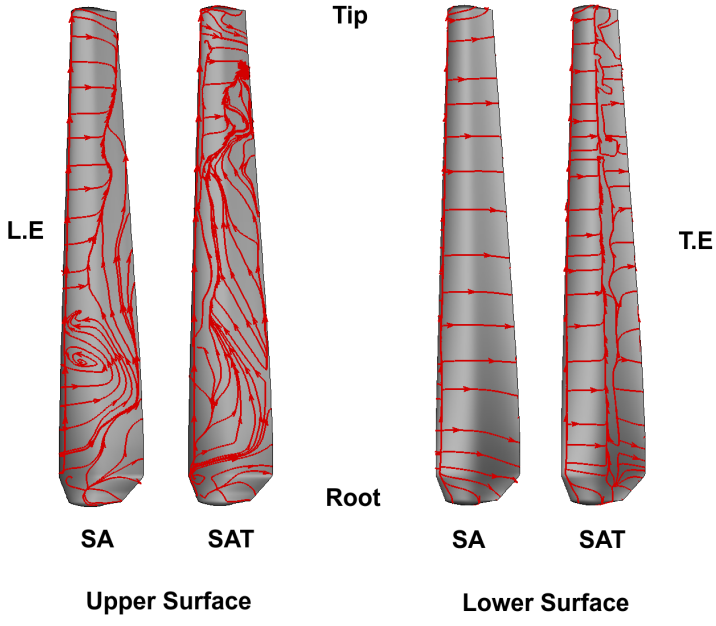

(b) V = 10 m/s

Figure 6.27: Blade surface streamlines on NREL Phase VI rotor at wind speeds of 7 m/s and 10 m/s. SA: SA–Turbulent, SAT: SA–Transition

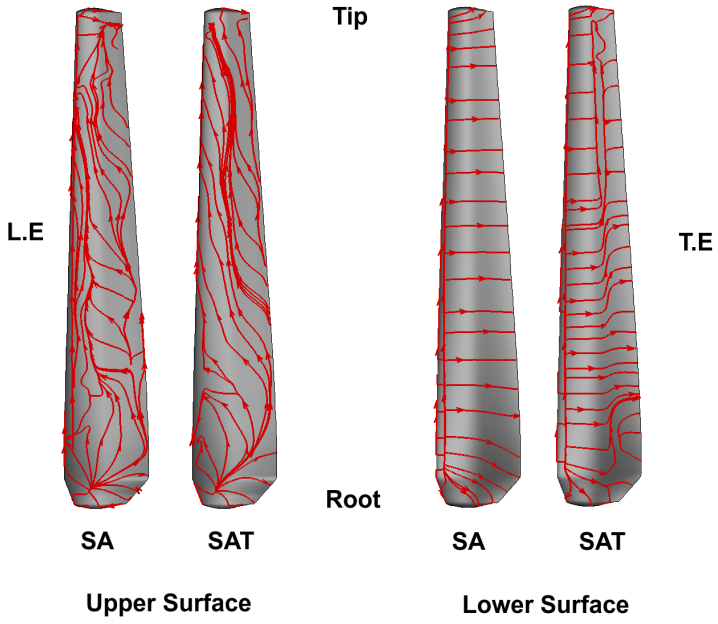

(a) V = 15 m/s

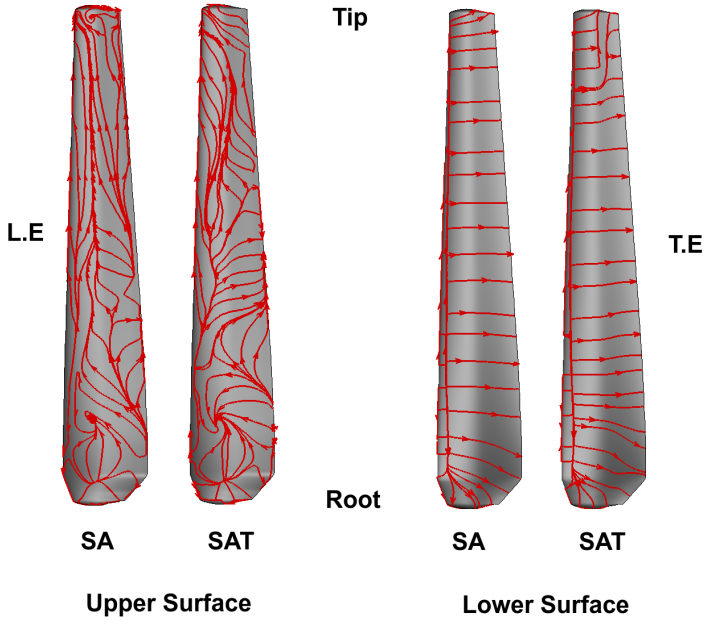

(b) V = 20 m/s

Figure 6.28: Blade surface streamlines on NREL Phase VI rotor at wind speeds of 15 m/s and 20 m/s. SA: SA–Turbulent, SAT: SA–Transition

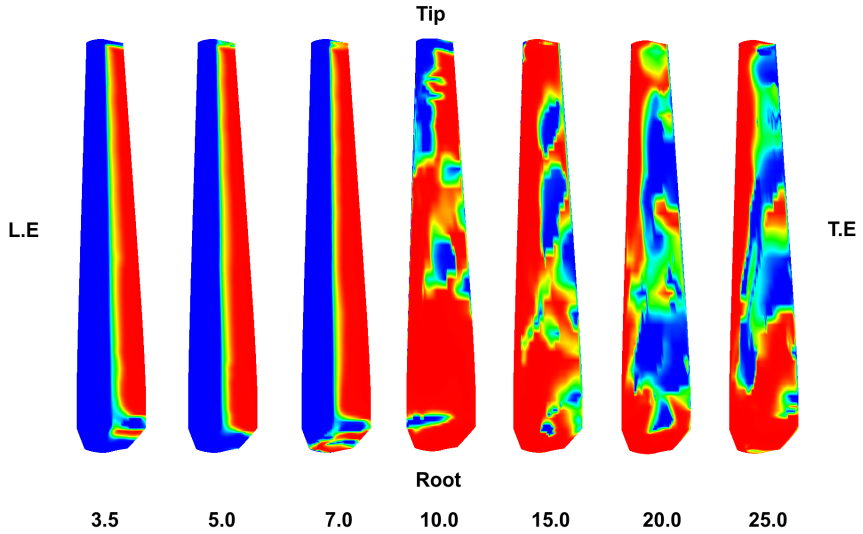

(a) Upper surface

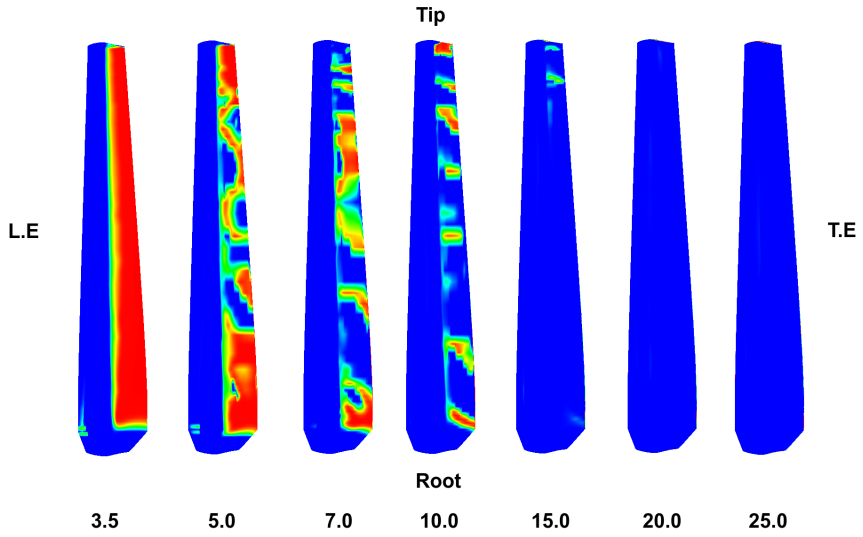

(b) Lower surface

Figure 6.29: Blade surface intermittency contours on NREL Phase VI rotor for wind speed range 3.5–25 m/s. Blue: Laminar, Red: Turbulent

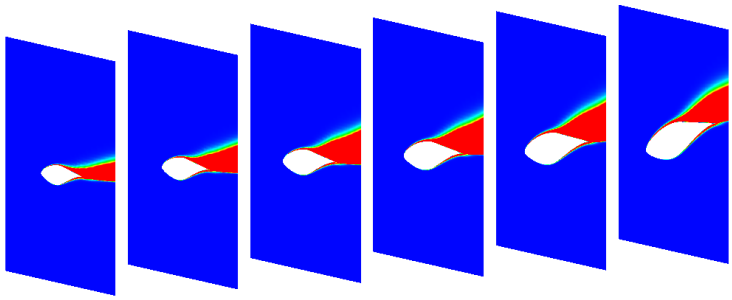

(a) SA-Turbulent

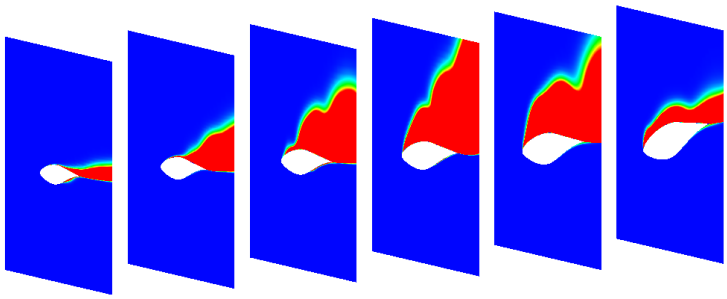

(b) SA-Transition

Figure 6.30: Spanwise variation of Eddy viscosity contours at V = 10 m/s showing increased unsteady separated flow with transition model (red indicates separated flow regions)

Figures 6.31 and 6.32 visualize the wake flow field behind the wind turbine rotor at wind speeds of 3.5, 5, 7, and 10 m/s. In Fig. 6.31, the blade tip vortices are shown using iso-surfaces of vorticity magnitude. In Fig. 6.32, tip vortex cross-sections are shown using vorticity magnitude contours on an azimuthal cross-section of the wake flow field. These two figures show that the distance between successive blade tip vortices increases with increasing wind speed as expected. In addition, the development of unsteadiness in the rotor wake is observed at a wind speed of 10 m/s.

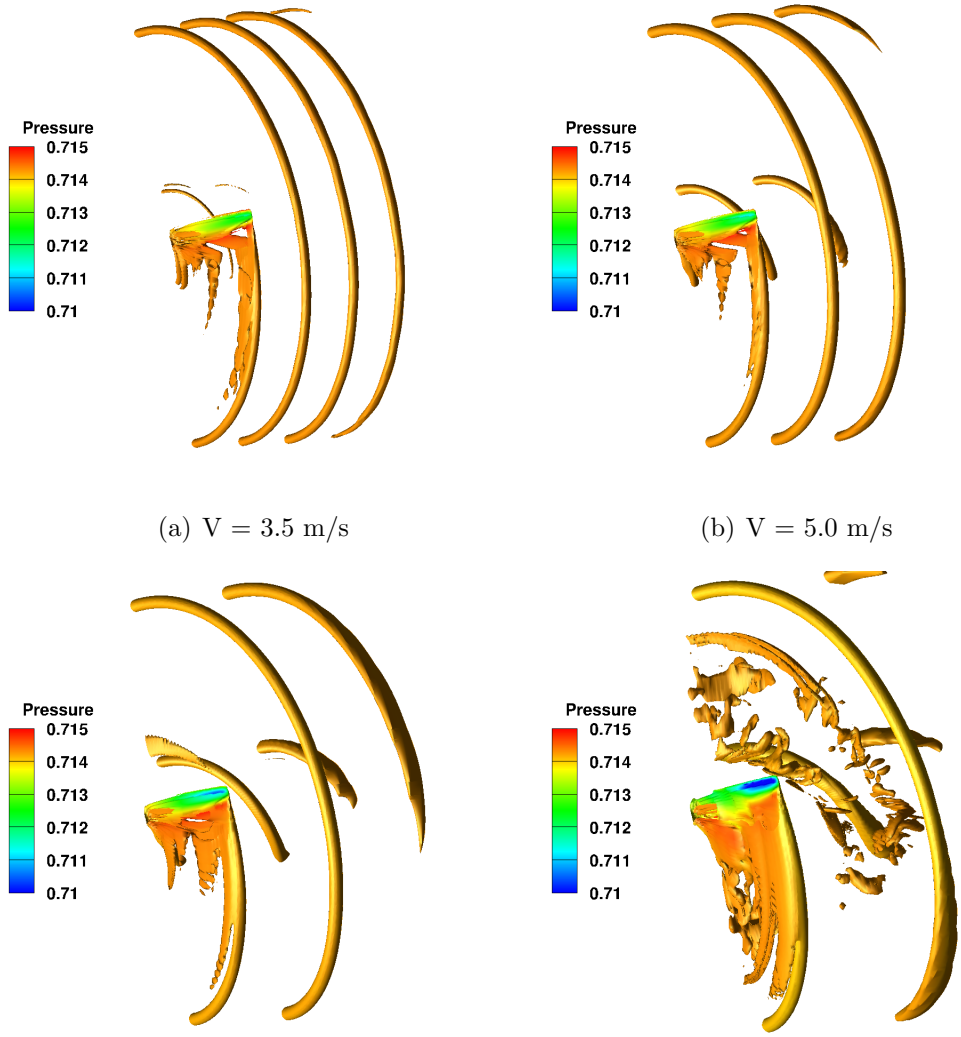

(a) V = 3.5 m/s

(b) V = 5.0 m/s

(c) V = 7.0 m/s

(d) V = 10.0 m/s

Figure 6.31: Iso-surfaces of vorticity magnitude showing tip vortices for the NREL Phase VI rotor blade

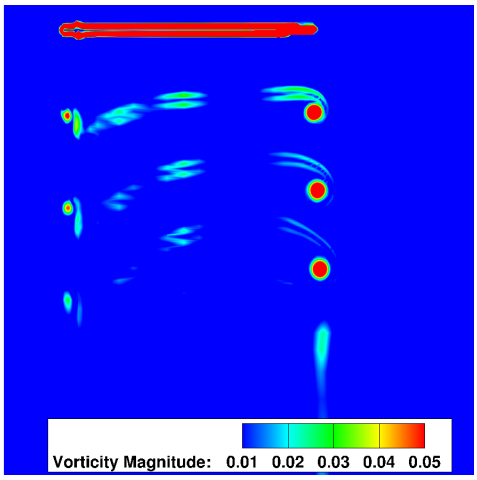

(a) V = 3.5 m/s

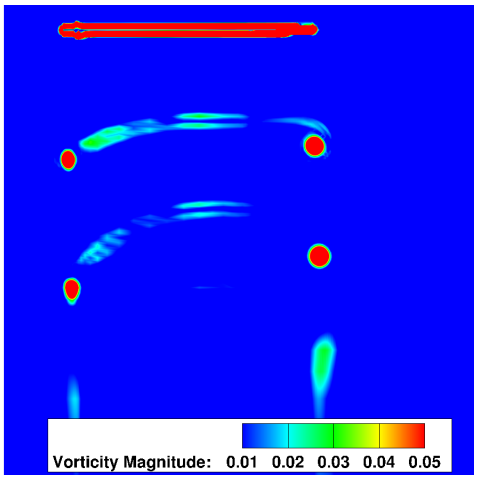

(b) V = 5.0 m/s

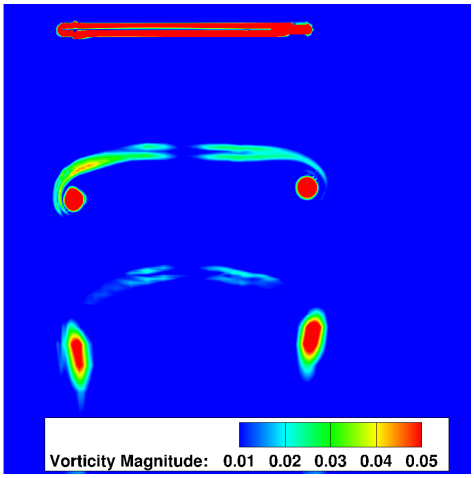

(c) V = 7.0 m/s

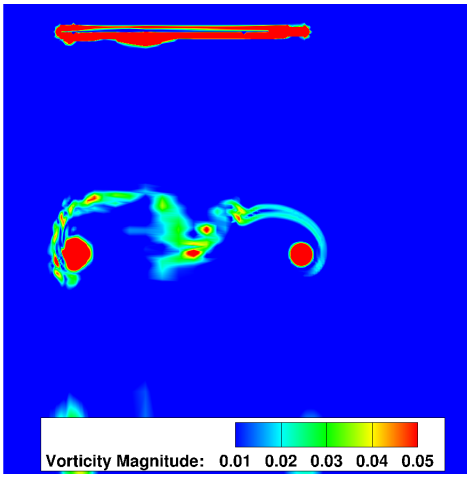

(d) V = 10.0 m/s

Figure 6.32: Vorticity magnitude contours in one azimuthal cross-section of rotor wake flow field, showing root and tip vortices for the NREL Phase VI rotor blade

6.4 Summary

This concludes the chapter on three-dimensional rotor simulations with the $\gamma - Re_\theta -$ SA transition model. Helicopter rotor simulations in hover demonstrated that the inclusion of transition effects results in increased thrust and reduced torque. Transition onset predictions for the BO 105 rotor were in reasonable agreement both qualitatively and quantitatively with the experimental data. The UH60-A rotor results showed a greater impact of transition model on performance at lower collective pitch angles. The NREL Phase VI rotor simulations showed that predicting a laminar separation bubble near the leading-edge may result in early separation at critical flow conditions leading to incipient separation. In addition, the predicted shaft torque was higher when a transitional boundary layer was predicted. Transition modeling may be necessary for accurate estimation of thrust and torque on small wind turbine rotors with lower rated power ($<$ 5 kW). Inclusion of crossflow effects may be necessary to obtain more realistic predictions in the blade root and tip regions which may have considerable spanwise flow. Appendix A presents preliminary work performed on crossflow transition prediction for swept wings and rotating blades.

7 Conclusions

This chapter summarizes the motivation for this thesis, the overall approach adopted, key results and observations, and provides recommendations for future work.

7.1 Summary

Laminar-turbulent transition and relaminarization prediction in boundary layers has been the subject of several recent research efforts, with a focus on model development as well as their application to various aerospace problems. The main motivation behind these efforts is the need to estimate drag and heat transfer on aerodynamic surfaces, which can be used to design applications with improved fuel economy or life-time. Since the use of DNS and LES for routine industrial CFD simulations is beyond current capabilities and computational resources, robust low-fidelity models are needed to predict transitional flows with reasonable accuracy. Challenges to developing low-fidelity transition models include (1) insufficient insights into complex transition mechanisms, and (2) compatibility of models with conventional CFD codes. A recent encouraging development in the area of transi-

tion modeling is the correlation-based $\gamma - Re_\theta$ model of Langtry and Menter for use with the two-equation k-ω turbulence model. The $\gamma - Re_\theta$ model can predict the onset of transition due to freestream turbulence and non-zero pressure gradients. It has been highly successful for internal and external flows in complex geometries due to its accuracy, robustness, applicability to wide range flow conditions, and compatibility with modern structured and unstructured mesh CFD codes through a fully local formulation.

The present work is a step towards extending the model to use with the one-equation Spalart-Allmaras turbulence model for external aerodynamic flows. The modified transition model, called the $\gamma - Re_\theta -$SA model, can predict transition onset at low freestream turbulence levels ($\leq 0.5\%$), which is the typical range for aircraft in flight. The following approach was adopted to develop, verify, and validate the modified transition model:

1. Implement the original transition model into the OverTURNS CFD solver: a 3-D, compressible, unsteady RANS methodology, that is well-established for studying rotorcraft flows

2. Remove explicit dependence of transition model on k and ω and make the transition model independent of the choice of the turbulence model

3. Reformulate production and destruction terms of the intermittency transport equation to improve near-wall recovery of intermittency post-transition onset

4. Remove sensitivity of the transition model to the value of the freestream eddy viscosity used in S-A turbulence model

5. Recalibrate the transition model using experimental data for transition of boundary layer on a zero-pressure gradient flat plate

6. Verify the model implementation through analysis of various flow parameters. Relaminarization and model hysteresis behavior were studied through simulation of a pitching airfoil

7. Validate the model against experimental data for several two-dimensional airfoil flows over a wide range of Reynolds numbers

The $\gamma - Re_\theta - \text{SA}$ model was then used to quantify the effect of transition prediction on the performance of rotorcraft and wind turbine rotors under axial flow conditions. The key observations from 2-D and 3-D simulations performed in this work are summarized in the next section.

7.2 Key Observations

7.2.1 Two-Dimensional Airfoil Simulations

Two-dimensional airfoil flows were simulated with and without the transition model to demonstrate capability of the model to predict transition onset and extent. Several experimental cases were identified to cover flow Reynolds numbers ranging from 10^5 to 5×10^6 and freestream turbulence levels under 0.5%. Validated data included skin friction coefficient, transition onset locations, lift coefficient, and drag coefficient. Test cases were chosen to demonstrate the effect of non-zero pressure gradients on transition onset, which is a common occurrence on lifting surfaces.

With increasing angle of attack, the transition model predicted movement of onset location towards the leading-edge on the upper surface, due to a stronger adverse pressure gradient.

1. For all cases with a non-negligible laminar extent in the boundary layer, the baseline Spalart-Allmaras model consistently over-predicted drag due to a fully turbulent treatment.

2. Excellent agreement with experimental data was obtained for transition onset locations and force coefficients using the transition model.

3. Model performance was found to be sensitive to calibration for cases with mild adverse pressure gradients, where transition onset is driven by freestream turbulence effect.

4. Separation-induced transition under strong adverse pressure gradients was well-captured in all cases. At low Reynolds numbers ($< 500{,}000$), the model was able to predict laminar separation and turbulent reattachment points with good accuracy.

5. Capability of the model to predict transition onset on multi-element airfoils was demonstrated. The SC2110 w/ leading-edge slat case showed significant improvement in lift-to-drag ratio with the inclusion of transition effects.

7.2.2 Three-dimensional Rotor Simulations

Three-dimensional simulations of helicopter and wind turbine rotors were performed with and without the transition model. The following three configurations were studied: (1) BO 105 helicopter rotor, (2) UH60-A helicopter rotor, and (3) NREL Phase VI wind turbine rotor. Since the transition model does not account for effects of yawed flow, all rotor simulations were performed under axial flow conditions, ensuring a predominantly two-dimensional flow on the rotor blades along the chordwise direction, except near the root and the tip regions. The objective of these simulations was to study the role of transition on the performance of rotors. Rotor blades were treated as structurally rigid in these simulations.

BO 105 Rotor

Experimental data for transition onset locations were available on upper and lower surfaces of a full-scale, 4-bladed BO 105 rotor in hover at a collective pitch angle of 6.7° and precone angle of 2.5°. On the upper surface, the transition onset location was around 25% of chord from leading-edge along most of the blade span. On the lower surface, the transition onset location varied along the span, with a later transition on inboard sections, due to lower local Reynolds numbers. Three simulations were performed with varying number of points (200, 300, 400) on the blade surface in the chordwise direction. Transition model did not show strong dependence of predicted onset locations on grid resolution.

1. On the upper surface, the transition onset locations predicted using the tran-

sition model agreed very well with measurements. Near the tip, the predicted transition location abruptly shifted downstream due to lower effective angle of attack, which is caused by the induced velocity of the tip vortex. However, this may not be the case if crossflow effects on transition are included.

2. On the lower surface, the transition onset location was predicted earlier compared to experimental data. This can be attributed to the sensitivity of the model for transition caused due to mild adverse pressure gradients and more dominant freestream turbulence effects seen on the inboard regions of the blade.

3. Compared to the fully turbulent predictions, the transition model prediction of the rotor thrust value increased by 0.8%, whereas, the rotor torque value decreased by 4%. The decrease in the rotor torque was primarily due to capturing the laminar boundary layer regions on the blade. Predicted figure of merit values with and without the transition model were 0.655 and 0.693 respectively. These differences in rotor performance were found to be similar to other CFD studies with transition prediction.

UH60-A Rotor

Simulations of a full-scale, 4-bladed UH60-A rotor in hover were performed for collective pitch angles between 0° and 15°. The rotor thrust and torque predictions were compared without and without the transition model, and the trends of transition onset locations were studied.

1. The transition onset location on the upper surface varied between 10% and 20% of chord over the entire range of collective pitch angles. This indicates that transition on the upper surface is dominated primarily by adverse pressure gradients.

2. On the lower surface, the transition onset location moved further downstream with increasing collective angle. This trend is also seen in the two-dimensional airfoil simulations. However, three-dimensional effects such as crossflow instability may need to be included to obtain a more realistic estimate. Spanwise variation of transition onset was driven by the local Reynolds number, similar to the BO 105 rotor case.

3. With the inclusion of transition effects, the rotor thrust increased by less than 2% at all collective angles.

4. The rotor torque was reduced with the inclusion of transition effects. The amount of reduction varied with the collective pitch angle. Torque is lower by 8% at 0° and 1.5% at 15°. This trend is consistent with the fact that the contribution of viscous drag to the total torque is higher at lower collective pitch angles. Therefore, the lower skin friction drag prediction with the inclusion of the transition model has a greater impact on rotors operating at lower power.

NREL Phase VI Rotor

The 3-bladed NREL Phase VI model rotor was simulated in axial flow for wind speeds between 3.5 m/s and 25 m/s. Due to the relatively low local Mach numbers

along the blade span, a preconditioning algorithm was used in these simulations to improve convergence and accuracy. Rotor thrust and torque distributions, as well as pressure profiles, obtained with and without the transition model, were compared with available experimental data.

1. At wind speeds of 3.5, 5, and 7 m/s, rotor thrust showed good agreement with experimental data. The difference between fully turbulent and transitional predictions of thrust were less than 5% at these wind speeds, with the transition model predicting higher thrust. The rotor shaft torque showed more sensitivity to the inclusion of transition effects at these lower wind speeds. The generated torque predicted with the transition model was lower than that predicted with the baseline turbulence model by 70%, 12.5%, and 7.2% at wind speeds of 3.5, 5, and 7 m/s respectively. This increase in torque was primarily due to the reduced drag prediction with the inclusion of the transition model. This has important implications for the analysis of small wind turbines operating at lower rated power values (< 5 kW).

2. At 10 m/s, the rotor thrust was over-predicted by the fully turbulent model, whereas the transition model showed a better agreement with the experimental value. As reported in the current literature, torque predictions at 10 m/s showed sensitivity to turbulence/transition modeling. A fully turbulent treatment over-predicted the torque value at 10 m/s, whereas, the transition model under-predicted it. Closer inspection showed that the baseline turbulence model predicted separation on the upper surface at the point of maximum

thickness, whereas, with a transition model, separation was predicted at the leading-edge, likely due to bursting of the laminar separation bubble.

3. At higher wind speeds, both simulations predicted massively separated flow on a large portion of the blade. Although both the thrust and the torque with both models are within the experimental uncertainty, unsteady RANS simulations with conventional turbulence models are operating out of their validity regime for such flows. Use of hybrid RANS-LES methods may be more appropriate in these cases.

4. Visualization of limiting streamlines on the blade upper and lower surfaces confirmed the presence of a laminar separation bubble. Streamlines also showed significant spanwise flow in cases with flow separation.

7.3 Recommendations for Future Work

The methodology and results presented in this thesis demonstrate the potential of a correlation-based approach to transition prediction in external aerodynamic flows. Successful validation of data from a varied set of experiments provides confidence in the robustness and accuracy of the new transition model coupled with the Spalart-Allmaras turbulence model. However, the current version of the model does not account for effects of crossflow, surface roughness, curvature, and many others, on the transition onset location. Since the model is based on independent empirical correlations for each transition mechanism and influencing factor, several enhancements are possible. At the same time, such an approach presents new challenges

in the context of laminar flow control and high-fidelity CFD methods such as LES. Some of the possible model requirements and enhancements are listed below.

1. Crossflow effects are dominant in yawed flow boundary layers that occur on swept wings and truly three-dimensional geometries such as airframes. Therefore, the first and the most important enhancement to the new model would be the inclusion of a well-validated crossflow transition onset correlation. Potential applications include fixed wings of transport aircraft, fuselages, and rotor blades under yawed flow conditions. Preliminary work done on crossflow transition prediction is presented in Appendix A of this thesis.

2. Surface roughness can influence the transition onset process, and is considered an important element in laminar flow control on 3-D swept wings. In addition, the transition process is accelerated on roughened wind turbine blades. Although some of the current turbulence models account for roughness, it is desirable to include its effects into the present transition model as well.

3. Wind turbine rotor simulations indicated instability of the laminar separation bubble on the lower surface of the blade, which was not seen in the hovering helicopter rotor simulations. Since wind turbine rotors operate at much lower speeds, model robustness and performance under such low-Mach number scenarios needs further investigation.

4. Most of the two-dimensional simulations presented in this work demonstrate the inability of the RANS turbulence models to predict stall onset accurately.

Future work must focus on improving stall onset prediction in both 2-D and 3-D RANS simulations. Preliminary work performed on improving sensitivity of the one-equation S-A turbulence model to strong adverse pressure gradients (APG) and therefore improving 2-D stall onset prediction is presented in Appendix B of this thesis.

5. The effect of hybrid RANS-LES methods in combination with the $\gamma - Re_\theta - \text{SA}$ transition model and the APG-corrected S-A turbulence model could be investigated, especially for scenarios where laminar-separation bubbles are present.

6. Laminar flow control methods are actively being investigated to delay transition onset. Applicability of correlation-based models need to be assessed for transition prediction in the presence of active or passive flow control techniques.

A Crossflow Transition Onset Correlation

A.1 Introduction

Current version of the $\gamma - Re_\theta$ transition model can predict natural, bypass, and separation-induced transition using empirical criteria deduced from experimental data. Since crossflow instabilities can cause earlier transition onset in 3-D boundary layers with yawed flow and favorable pressure gradients, it is essential for transition models to account for this important mechanism. This is particularly important for applications involving swept wings, rotating blades, and airframes that experience significant yawed flow due to the presence of strong pressure gradients and unpredictable nature of incoming flow direction. Preliminary attempt was made in this work to develop a new semi-local crossflow transition onset criterion for three-dimensional boundary layers on swept-wing flows. The new criterion is integrated into the $\gamma - Re_\theta -$ SA model and its predictive capability is demonstrated on a swept wing and a rotating blade configuration.

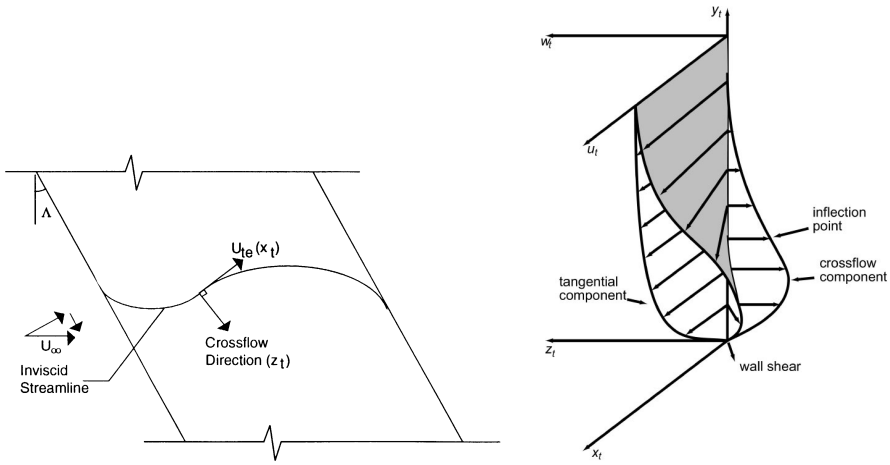

(a) Curved streamlines over a swept wing (b) Swept wing boundary layer profile

Figure A.1: Crossflow transition on swept wings [27]

A.2 Crossflow Transition Physics and Modeling

Saric and Reed [27] provide an excellent review of the stability and transition of 3-D boundary layers. Figure A.1 shows a schematic of streamlines and velocity profiles in a typical 3-D boundary layer on a swept wing [27]. The combination of sweep and pressure gradient gives rise to inviscid streamline curvature, which in turn causes a crossflow component of velocity inside the boundary layer. This crossflow velocity component can develop inflectional instabilities and accelerate transition onset in 3-D boundary layers on swept wings and rotating blades. Neglecting crossflow instability effects in 3-D simulations could lead to a delayed transition onset prediction and under-prediction of viscous drag.

Many fundamental experimental and numerical studies have been dedicated to understanding the transition phenomenon through crossflow instabilities. How-

ever, existing engineering modeling methods to predict crossflow transition suffer from geometry-dependence, non-local procedures, and reliability for a wide range of flow configurations. Typical empirical models for crossflow prediction methods use quantities like the pressure gradient parameter, streamline curvature parallel to the wall, geometric sweep angle, momentum thickness, and shape factor. The Kohama parameter [60] and the C1-criterion of Arnal [59]are two such empirical prediction methods.

Watanabe, et al. [127] integrated Kohama's crossflow criterion with the $\gamma - Re_\theta$ model to predict crossflow transition onset. The Kohama parameter is based on the analogy between the Gortler instability and the crossflow instability. In both cases, the imbalance between the viscous and inertial forces inside the boundary layer due to inviscid streamline curvature triggers transition. The Kohama parameter is given by Eq. A.1 below.

$$C_K = \frac{U_e \theta}{\nu} \sqrt{\frac{\theta}{r}} \tag{A.1}$$

The main drawback of the Kohama parameter is that its threshold value for transition onset is geometry dependent - for example, the critical value of C_K is 5 for a rotating disk, while it is 2.8 for a yawed cylinder. Kohama proposed that a fixed value of C_K could be used for a given family of airfoils. Besides, the Kohama criterion also requires numerical integration to compute the boundary layer momentum thickness, which can be inefficient and ill-defined in complex flow configurations.

A more recent work by Seyfert and Krumbein [128] extended the $\gamma - Re_\theta$

transition model to predict crossflow transition using the C1-criterion of Arnal, given by Eq. A.2.

$$Re^*_{\delta 2t} = \frac{300}{\pi}\arctan\left[\frac{0.106}{(H-2.3)^{2.05}}\right], \quad 2.3 \leq H < 2.7; \quad \text{and} \quad Re^*_{\delta 2t} = 150.0, \quad H < 2.3 \tag{A.2}$$

The C1-criterion is based on a correlation between the crossflow displacement thickness based Reynolds number and the shape factor at the transition onset location. The applicability of the C1-criterion is limited to accelerated flows in the vicinity of the leading edge of swept wings. Seyfert et al. [128] used Falkner-Skan-Cooke equations to evaluate the local shape factor as a function of the pressure gradient parameter, λ, that is already computed in the $\gamma - Re_\theta$ transition model. However, this implementation involves knowledge of the geometric sweep angle that is more suited for fixed-wings, but restricts its applicability to generic 3-D geometries.

A third empirical criterion for crossflow transition onset prediction proposed by Owen et al. [129] is given by Eq. A.3.

$$Re_{\text{crossflow}} = \frac{U_{\text{crossflow}_{\max}}\delta_{10\%}}{\nu} \tag{A.3}$$

Owen's criterion is based on a critical value for a "Crossflow Reynolds number" based on the maximum crossflow velocity and the boundary layer height where the crossflow velocity is 10% of its maximum value. Evaluation of this parameter requires searching for the maximum crossflow velocity and the specific boundary layer height, which can be computationally inefficient.

The above three methods suffer from drawbacks such as incompatibility with RANS solvers, computational inefficiency, and unsuitability to generic 3-D geometries. In the following section, we discuss the development and calibration of a new crossflow transition onset criterion based on a Modified Crossflow Reynolds Number that minimizes some of these limitations.

A.3 New Crossflow Transition Onset Criterion - Modified Crossflow Reynolds Number

In this work, two variations of the *Modified Crossflow Reynolds Number* were developed and analyzed - $\mathrm{Re}_{\mathrm{MCF}_1}$ and $\mathrm{Re}_{\mathrm{MCF}_2}$ given by Eqs. A.4 and A.5.

$$\mathrm{Re}_{\mathrm{MCF}_1} = \frac{\mathrm{U}_{\mathrm{CF}_1}\mathrm{R}}{\nu} \tag{A.4}$$

$$\mathrm{Re}_{\mathrm{MCF}_2} = \frac{\mathrm{U}_{\mathrm{CF}_2}\mathrm{R}}{\nu} \tag{A.5}$$

For the length scale, both Reynolds numbers use the inviscid streamline radius of curvature parallel to the wall, R. Procedure for numerical evaluation of R is described in detail by Watanabe et al. [127]. Although R is a non-local quantity that is evaluated near the edge of the boundary layer, in this work, the effort to compute its value is minimized by using the boundary layer detection parameter, $\mathrm{F}_{\theta\mathrm{t}}$, from the $\gamma - Re_\theta$ model framework. The value of $\mathrm{F}_{\theta\mathrm{t}}$ is 1.0 inside the boundary layer and 0.0 outside. This aspect of the new crossflow model makes it a partially non-local, yet a highly feasible approach, since the modified crossflow Reynolds numbers can be computed locally at each solution point in the computational domain. Since

the crossflow transition onset criterion is based purely on mean flow quantities, it is generic enough to be used with any existing turbulence model.

The two versions of the modified crossflow Reynolds numbers differ in their definition of the velocity scale. $\mathrm{Re}_{\mathrm{MCF}_1}$ uses the absolute value of the traditional definition of the crossflow velocity, $\mathrm{U}_{\mathrm{CF1}}$, given by Eq. A.6 whereas $\mathrm{Re}_{\mathrm{MCF}_1}$, uses a modified definition of crossflow velocity, $\mathrm{U}_{\mathrm{CF2}}$, given by Eq. A.7.

$$\mathrm{U}_{\mathrm{CF}_1} = |\mathrm{u.r}_1 + \mathrm{v.r}_2 + \mathrm{w.r}_3| \tag{A.6}$$

$$\mathrm{U}_{\mathrm{CF}_2} = |\mathrm{u.r}_1| + |\mathrm{v.r}_2| + |\mathrm{w.r}_3| \tag{A.7}$$

where, (u, v, w) are the local velocity vector components and (r_1, r_2, r_3) are unit vectors of R.

Crossflow transition onset is detected when the maximum value of the crossflow Reynolds number profile within the boundary layer at a given station exceeds a constant critical value, as shown in Eqs. A.8 and A.9.

$$\mathrm{F}_{\theta \mathrm{t}} \bullet \max\left[\mathrm{Re}_{\mathrm{MCF}_1}\right]_{\mathrm{BL}} > 0.7 \tag{A.8}$$

$$\mathrm{F}_{\theta \mathrm{t}} \bullet \max\left[\mathrm{Re}_{\mathrm{MCF}_2}\right]_{\mathrm{BL}} > 2.0 \tag{A.9}$$

Calibration of Crossflow Onset Criterion

The new crossflow model is calibrated using experimental data for transition onset locations measured by Dagenhart [130] for a range of Reynolds numbers, on an infinite swept-back wing with NLF(2)-0415 airfoil section. The experimental wing

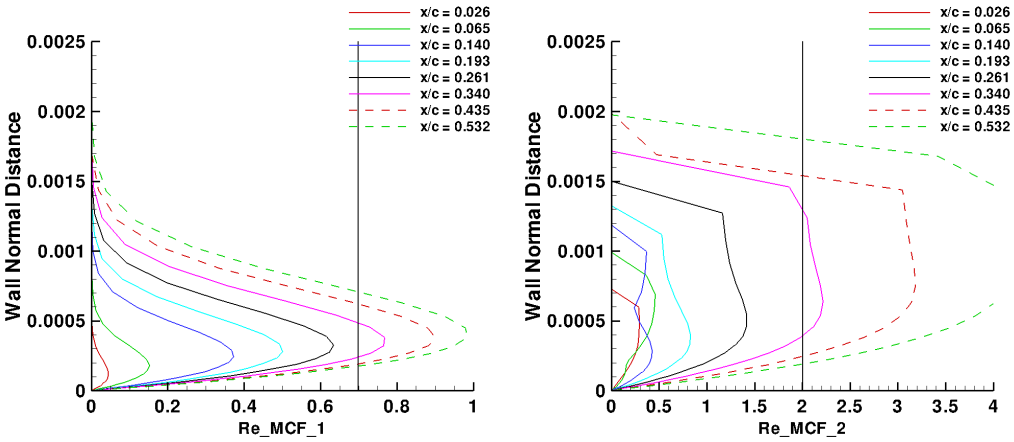

(a) $\mathrm{Re}_{\mathrm{MCF}_1}$, monotonic peaks

(b) $\mathrm{Re}_{\mathrm{MCF}_2}$, monotonic peaks

Figure A.2: Modified Crossflow Reynolds Number Profiles for Laminar Boundary Layer at Re = 3.73×10^6 on NLF(2)-0415 infinite swept-wing

sweep-back angle is 45° and the freestream angle of attack is -4°. Laminar flow simulations are performed at five different Reynolds numbers and a Mach number of 0.1. The critical values of the two criteria in Eqs. A.8 and A.9 are obtained by identifying the peak values of the computed $\mathrm{Re}_{\mathrm{MCF}_1}$ and $\mathrm{Re}_{\mathrm{MCF}_2}$ profiles at the experimental transition onset locations along the airfoil upper surface. The computed and experimental onset locations are tabulated in Table A.1. Representative profiles of $\mathrm{Re}_{\mathrm{MCF}_1}$ and $\mathrm{Re}_{\mathrm{MCF}_2}$ are plotted in Fig. A.2 along the upper surface of the airfoil section at Re = 3.73×10^6. Note the monotonically increasing peak values of the profiles with increasing chordwise location.

Stability of Crossflow Criterion Post-Transition Onset

The profiles of the first version of crossflow Reynolds number, $\mathrm{Re}_{\mathrm{MCF}_1}$, shown in Fig. A.2 are extracted from a laminar boundary layer solution. While the peak

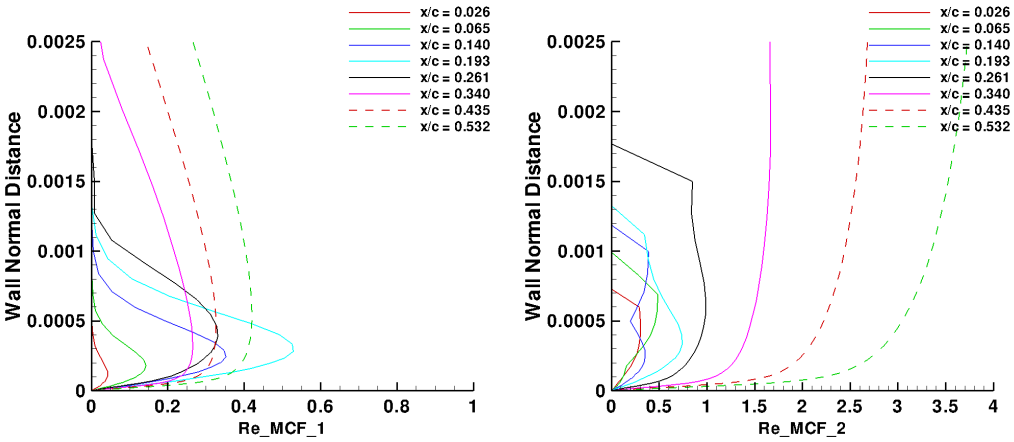

(a) $\mathrm{Re}_{\mathrm{MCF}_1}$, non-monotonic peaks (b) $\mathrm{Re}_{\mathrm{MCF}_2}$, monotonic peaks

Figure A.3: Modified Crossflow Reynolds Number Profiles for Boundary Layer Tripped at 25% of chord, Re = 3.73×10^6 on NLF(2)-0415 infinite swept-wing

values of $\mathrm{Re}_{\mathrm{MCF}_1}$ profiles increase monotonically with chordwise location in a laminar boundary layer, this is not the case in a transitional boundary layer. The $\mathrm{Re}_{\mathrm{MCF}_1}$ profiles plotted in Fig. A.3(a) for a boundary layer tripped around 25% of chord on the upper surface reveal this behavior. The peak value of the spanwise velocity component, $v.r_2$, decreases rapidly beyond transition onset location, causing the $\mathrm{Re}_{\mathrm{MCF}_1}$ to drop below the critical value required for transition onset. This leads to a loss of turbulence production immediately after transition onset and results in relaminarization. Therefore, while $\mathrm{Re}_{\mathrm{MCF}_1}$ is a reliable crossflow transition onset detection parameter and can be used for steady flow simulations, its practical applicability for unsteady flows and problems with moving walls is limited.

The second version of the crossflow Reynolds number, $\mathrm{Re}_{\mathrm{MCF}_2}$, is designed to have a monotonically increasing peak value through a transitional boundary layer, as seen in Fig. A.3(b). However, the profiles in the neighborhood of the transition

Reynolds No.	CFD	Experiment [130]
1.92×10^6	0.68	0.70 - 0.85
2.37×10^6	0.52	0.48 - 0.68
2.73×10^6	0.43	0.40 - 0.65
3.27×10^6	0.35	0.20 - 0.45
3.73×10^6	0.32	0.20 - 0.40

Table A.1: NLF(2)-0415 Infinite Swept Wing - Comparison of CFD ($\mathrm{Re}_{\mathrm{MCF}_2}$) and Experimental [130] Transition Onset Locations

onset location still experience a slight drop below the critical value, causing an oscillatory transition onset behavior within 5% of chord of the mean onset location. Ongoing work involves improving the stability of $\mathrm{Re}_{\mathrm{MCF}_2}$ criterion.

Integration of Crossflow Onset Criterion into $\gamma - Re_\theta$ Transition Model

The key idea of the $\gamma - Re_\theta - \mathrm{SA}$ transition model is to use the empirical criterion for transition onset, which states that the ratio of the vorticity Reynolds number to the momentum thickness Reynolds number reaches a threshold value in a laminar boundary layer before transition is triggered. This is given by the function $\mathrm{F}_{\mathrm{onset1}}$ in Eq. A.10:

$$\mathrm{F}_{\mathrm{onset1}} = \frac{\mathrm{Re}_{\mathrm{v}}}{2.193.\mathrm{Re}_{\theta \mathrm{c}}} > 1.0, \quad \text{for} \quad \text{transition} \quad \text{onset} \tag{A.10}$$

In this work, the $\mathrm{F}_{\mathrm{onset1}}$ criterion is modified to include the new crossflow Reynolds

number correlation as shown in Eq. A.11.

$$\mathrm{F_{onset1}} = \max\left[\frac{\mathrm{Re_v}}{2.193.\mathrm{Re_{\theta c}}}, \frac{\mathrm{F_{\theta t}Re_{MCF_2}}}{2.0}\right] \tag{A.11}$$

A.4 Preliminary Results

ONERA M-6 Wing

The effectiveness of the newly developed crossflow transition criterion is demonstrated on the ONERA M-6 swept wing test case. The flow conditions for the ONERA M6 swept wing are obtained from the experiments by Schmitt, et al. [131]: M = 0.262 and Re = 3.5×10^6, Tu_∞ = 0.2%. Figure A.4 compares the intermittency contours predicted by the $\gamma - Re_\theta -$ SA streamwise and crossflow transition models with experimental naphthalene distributions indicating laminar (blue) and turbulent (red) regions. It is evident from these contours that accounting for streamwise transition alone severely delays transition onset compared to experimental observations for all angles of attack. As expected, the transition onset locations are identical on pressure and suction sides of the wing at 0° AoA. However, at 5° and 15° AoA, the $\gamma - Re_\theta -$ SA model predicts transition onset quite close to the stagnation point on the suction side, but almost near the trailing edge on the pressure side. This trend can be explained based on the fact that transition onset on the suction side of the wing is primarily driven by the streamwise adverse pressure gradient, whereas on the pressure side transition is delayed due to a streamwise favorable pressure gradient. However, experiments indicate that the transition onset on the suction side is much

closer to the leading edge at 10° and 15° AoA which provides evidence for strong crossflow instabilities. It is evident that the inclusion of the new crossflow criterion into the $\gamma - Re_\theta -$SA transition model significantly improves the agreement between CFD and experimental observations.

Offset Rotor in Hover

Flow past the 4-bladed UH60-A rigid rotor is simulated in hover at a tip Mach number of 0.65, a tip Reynolds number of 7.4×10^6 and a 10° collective. To qualitatively study the effects of strong yawed flow on transition onset locations without the complexities of the aerodynamic environment present in forward flight (such as BVI), a special configuration of offset rotor blades is simulated in this work. This concept is borrowed from the experiments of McCroskey [113]. The ratio of the offset distance to the blade radius represents the advance ratio of the particular configuration. Figure. A.5 shows the rotor blades offset in the direction of rotation, representing a rotor blade in forward flight at an advance ratio of 0.3 and located at 0° azimuth location (similar to a swept-back wing). This "positive" offset creates a yawed flow in the outboard direction from the blade root to the blade tip. The corresponding configuration with a "negative" offset creates an inboard yawed flow and represents a rotor blade in forward flight at 180° azimuth location (similar to a swept-forward wing).

Figures A.6(a)–(c) show the intermittency contours obtained using the $\gamma - Re_\theta -$SA model for the baseline, swept-back, and swept-forward configurations of the

rotor blade respectively. For the baseline rotor with no offset, the difference between the predictions with and without crossflow transition model are mostly confined to the outboard regions on the blade lower surface. Large regions of laminar flow on both upper and lower surfaces of the blade are predicted with the transition model.

For the offset rotor configurations, the transition model without crossflow effects predicts large portions of laminar flow on the lower surface, similar to the zero offset rotor case. However, since the offset rotor experiences strong yawed flow, the crossflow transition model predicts onset location very close to the leading edge on both lower and upper surfaces of the blade. These results indicate that the nature of the boundary layer in forward flight is significantly different from that in hover depending on the azimuthal position of the rotor blade.

A.5 Summary

In this discussion, focus was drawn to the physics and modeling approaches of crossflow transition. The drawbacks of current crossflow transition prediction methods for use in the simulation of complex industrial applications were listed. A new non-dimensional parameter termed *Modified Crossflow Reynolds Number* is introduced and used to define two variations of a new empirical crossflow transition onset criterion. The new onset criterion is semi-local and is easy to calculate in traditional RANS flow solvers. It is also compatible with any turbulence model since it depends only on mean flow quantities. The new criterion was calibrated using experimental data on an infinite swept-back wing. Stability issues of the onset

criterion downstream of the transition onset location were discussed. The calibrated onset criterion was integrated into the $\gamma - Re_\theta -$ SA transition model. Transition onset predictions on the ONERA M-6 fixed wing test were significantly improved with the inclusion of crossflow effects. This test case also demonstrated that the transition onset can be significantly delayed on the pressure side of airfoil sections on 3-D wings if only streamwise transition effects are included without accounting for crossflow effects. The UH60-A offset rotor configuration case showed that yawed flow can have a major influence on crossflow transition onset on rotating blades.

Ongoing work includes further refinement, testing, and validation of the crossflow transition onset criterion. In conclusion, the current work shows that it is possible to extract meaningful parameters based on mean flow to predict complex flow phenomena such as crossflow transition in industrial applications.

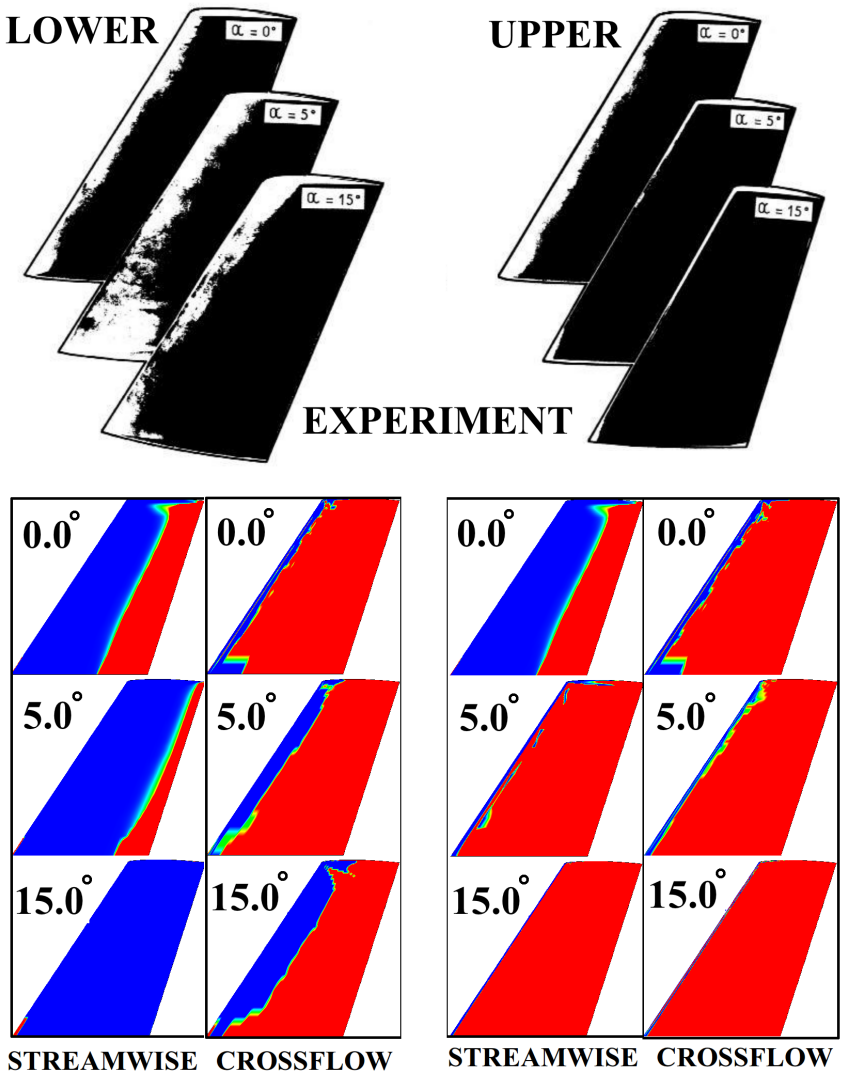

Figure A.4: Improved transition onset prediction with new crossflow transition criterion: ONERA M6 Wing

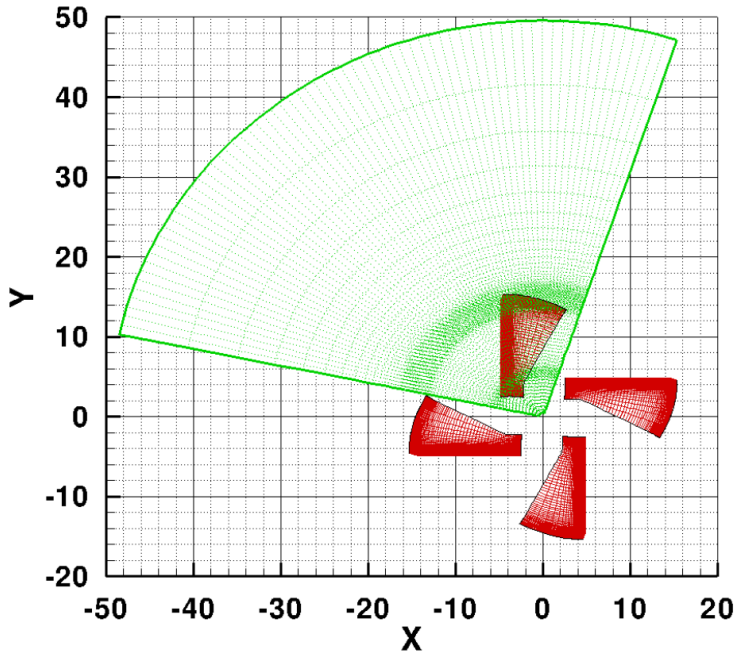

Figure A.5: UH60-A rotor system with offset blades to create outboard yawed flow (blades rotate counter-clockwise)

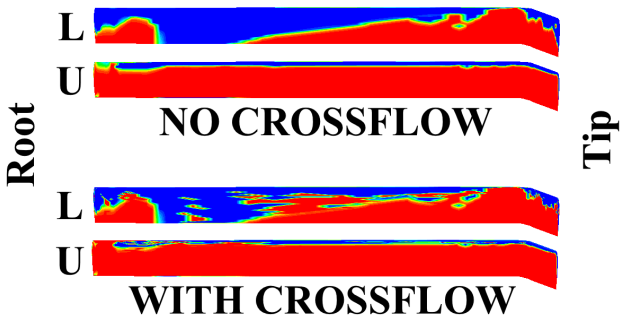

(a) Baseline rotor with no offset

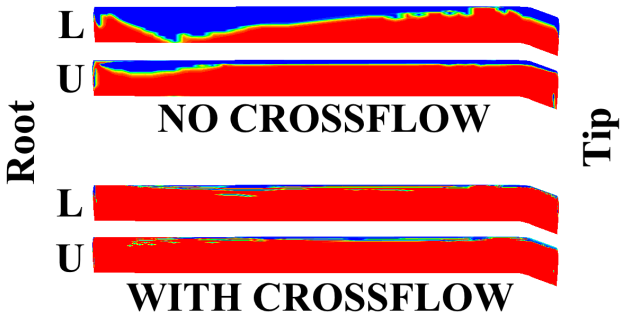

(b) Offset rotor without outboard flow

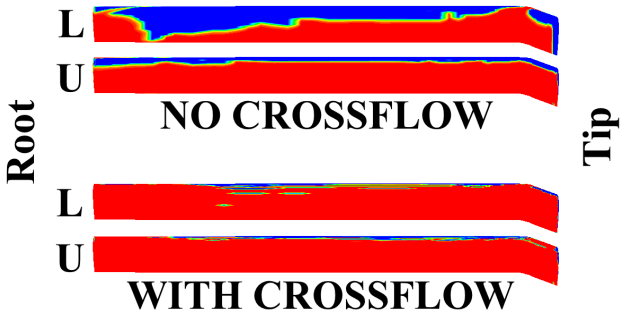

(c) Offset rotor with inboard flow

Figure A.6: Intermittency contours for UH60-A rotor in hover without offset (Blue - Laminar, Red - Turbulent, L - Lower Surface, U - Upper Surface)

B Strong Adverse Pressure Gradient Correction

B.1 Introduction

Accurate numerical prediction of static and dynamic stall onset in aerodynamic applications continues to be a challenge in the CFD community. The ability of turbulence models to accurately model the effects of strong adverse pressure gradients (APG) is crucial to the prediction of boundary layer separation in RANS simulations of wall-bounded flows. However, most one- and two-equation RANS turbulence models fail to accurately predict stall onset on airfoil sections at high angles of attack (AoA), where strong APG is encountered. Consequently, they tend to over-predict the maximum lift and stall onset angle for a given set of flow conditions. Two-dimensional airfoil simulations presented in this thesis support this observation.

Celic, et al. [132] compared the performance of 11 Eddy-viscosity based turbulence models for aerodynamic flows with adverse pressure gradients and concluded that none of the models perform satisfactorily for flow past airfoils near maximum

lift conditions. A related problem where traditional turbulence models perform poorly is that of transonic flow past airfoils with shock-induced separation. This unsatisfactory performance can be attributed to the underlying assumptions and simplifications that are part of all eddy viscosity based turbulence models. One such assumption is that equilibrium conditions exist in a boundary layer, which implies a balance between the production and dissipation of turbulent kinetic energy. This assumption allows for scaling of velocity profiles in the defect layer, and is instrumental in the formulation of many turbulence models. However, it is well known that boundary layers under strong APG are not in equilibrium and are characterized by Clauser's [133] pressure gradient parameter, given by $\frac{\delta^*}{\tau_w}\frac{dP}{dx}$. In addition, the outer layer scaling is affected under APG, whereas the viscous sublayer and log-layer are relatively unchanged. This is demonstrated in Fig. B.1 through the non-dimensional U^+ Vs y^+ profiles on a NACA 0012 airfoil at different angles of attack. With increasing angle of attack, the adverse pressure gradient in higher on the upper surface and therefore the defect layer penetrates deeper into the boundary layer. Therefore, many turbulence models that assume equilibrium conditions fail to produce satisfactory behavior for strong APG flows. Nevertheless, models with stress limiters, such as the SST version of the k-ω turbulence model [34], and Wilcox's modified k-ω [134] model, and the strain-adaptive formulation of the Spalart-Allmaras turbulence model [35, 135] are known to perform better than the other models. Although using higher fidelity turbulence modeling methods (Non-linear Eddy Viscosity models, Reynolds-Stress models, LES, etc) might produce better results, the robustness and computational cost associated with the usage of

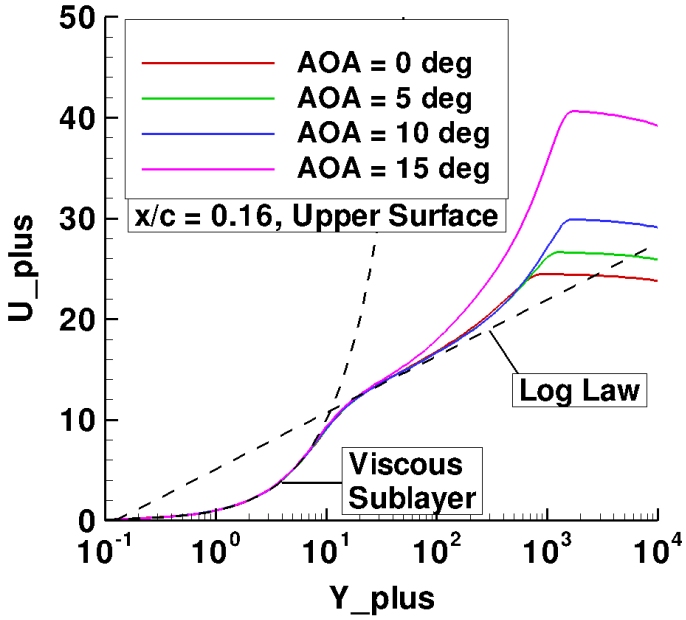

Figure B.1: Effect of adverse pressure gradient on the defect layer (NACA 0012 airfoil, Re = 6×10^6)

these methods is a major deterrent to their wider applicability for practical flows.

In this work, the effectiveness of a new empirical modification to the one-equation Spalart-Allmaras turbulence model is investigated, to improve its sensitivity to strong adverse pressure gradients, and therefore improve prediction of flow reversal and separation at high AoA and due to shocks.

B.2 Spalart-Allmaras Turbulence Model

The one-equation Spalart-Allmaras (S-A) turbulence model [35] solves for the modified Eddy viscosity, $\tilde{\nu}$, which relates to the kinematic Eddy viscosity ν_t as follows:

$$\nu_t = \tilde{\nu} f_{v1}; \quad f_{v1} = \frac{\chi^3}{\chi^3 + c_{v1}^3}; \quad \chi = \frac{\tilde{\nu}}{\nu} \tag{B.1}$$

The governing equation of the S-A model without the trip terms is given by:

$$\frac{D\tilde{\nu}}{Dt} = P_\nu - D_\nu + \frac{1}{\sigma}\left[\nabla.((\nu + \tilde{\nu})\nabla\tilde{\nu}) + c_{b2}(\nabla\tilde{\nu})^2\right] \tag{B.2}$$

where, P_ν and D_ν are the production and destruction terms of $\tilde{\nu}$, given by:

$$P_\nu = c_{b1}\tilde{\Omega}\tilde{\nu} \quad \text{and} \quad D_\nu = c_{w1} f_w [\frac{\tilde{\nu}}{d}]^2 \tag{B.3}$$

$\tilde{\Omega}$ is a function of the vorticity magnitude, Ω, and is defined as:

$$\tilde{\Omega} = \Omega + \frac{\tilde{\nu}}{\kappa^2 d^2} f_{v2}, \quad f_{v2} = 1 - \frac{\chi}{1 + \chi f_{v1}} \tag{B.4}$$

The function f_w is defined as:

$$f_w = g\left[\frac{1 + c_{w3}^6}{g^6 + c_{w3}^6}\right]^{\frac{1}{6}}, \quad g = r + c_{w2}(r^6 - r), \quad r = \frac{\tilde{\nu}}{\tilde{\Omega}\kappa^2 d^2} \tag{B.5}$$

The model constants are: $c_{b1} = 0.1355, \sigma = 2/3, c_{b2} = 0.622, \kappa = 0.41, c_{w1} = c_{b1}/\kappa^2 + (1 + c_{b2})/\sigma, c_{w2} = 0.622, c_{w3} = 2.0, c_{v1} = 7.1$. The current implementation of the S-A turbulence model uses the rotational correction [82] which reduces the production of turbulence in regions where vorticity exceeds strain rate, such as in vortex core regions, where pure rotation should not produce turbulence. In this version of the S-A model, the magnitude of vorticity, Ω, used to calculate $\tilde{\Omega}$ is replaced with $\Omega + 2.\min(0, S - \Omega)$ in Eq. B.4, which is then used to compute the production term.

Strain-Adaptive Formulation of S-A Model

The strain-adaptive formulation [135] extends the applicability of the S-A model to non-equilibrium flow conditions by modifying the model coefficient c_{b1}, which is a constant in the original model. In the SALSA formulation, c_{b1} is replaced by c'_{b1}, which varies as a function of the local strain rate magnitude. This modification affects the production term of the S-A model through c'_{b1} and destruction term of the S-A model through c_{w1} as shown below:

$$\mathrm{c'_{b1}} = 0.1355\sqrt{\Gamma}, \quad \Gamma = \min\left[1.25, \max(\gamma, 0.75)\right] \tag{B.6}$$

$$\gamma = \max(\alpha_1, \alpha_2), \quad \alpha_1 = \left[\frac{1.01\tilde{\nu}_\mathrm{t}}{\kappa^2 \mathrm{d}^2 \mathrm{S}}\right]^{0.65}, \quad \alpha_2 = \max\left[0, 1 - \tanh\left(\frac{\chi}{68}\right)\right]^{0.65} \tag{B.7}$$

$$\mathrm{c_{w1}} = \frac{\mathrm{c'_{b1}}}{\kappa^2} + \frac{1 + \mathrm{c_{b2}}}{\sigma} \tag{B.8}$$

B.3 APG Modification to S-A Model

While the S-A model performs quite well for attached boundary layers under moderate APG, it suffers from poor sensitivity to strong APG. Before proposing any modification to a well-established turbulence model, it is important to understand its construction and limitations. The S-A model was formulated based on dimensional analysis and empiricism, and does not use explicit velocity and length scale equations as in the case of the two-equation turbulence models. It was calibrated to produce an accurate log layer in a zero pressure gradient boundary layer by assuming equilibrium among the production, diffusion, and destruction terms. The near-wall and the

defect layer profiles were calibrated using damping functions. The primary effects of strong APG are felt in the defect layer of a turbulent boundary layer, whereas the viscous sublayer and log layer are unaffected. The formulation of S-A model allows for modification of the defect layer behavior through the damping function f_w in Eq. B.5. This function controls the rate at which the turbulence destruction term decays away from the wall. It appears that the destruction term decay is faster than desired for strong APG flows, resulting in a boundary layer that is more turbulent and resilient to separation.

As a cost-efficient engineering solution to predict APG boundary layer flows, a new modification is proposed to the damping function f_w based on the experimental observations of Perry and Schofield [136]. Their experiments on APG boundary layers revealed that the ratio of the magnitudes of local turbulent shear stress to wall shear stress is a good indicator of the validity of the traditional defect law. It was observed that this ratio does not exceed 1.5 for equilibrium boundary layers. The profiles of $\delta = \dfrac{\mu_t|S_{ij}|}{1.5|\tau_w|}$ (Fig. B.2) on a zero pressure gradient flat plate up to a Reynolds number of 15 million, verify that the peak values do not exceed 1.0.

Based on this inequality, the parameter r used in the defect layer damping function f_w is modified as follows:

$$r = \frac{\tilde{\nu}}{\tilde{\Omega}\alpha^2 d^2} \tag{B.9}$$

where,

$$\alpha = \kappa - 0.15\beta, \quad \beta = \min(\max(\delta - 1, 0.0), 1.0)\tanh(\delta), \quad \delta = \frac{\mu_t|S_{ij}|}{1.5|\tau_w|} \tag{B.10}$$

The proposed APG modification increases the magnitude of the turbulence destruc-

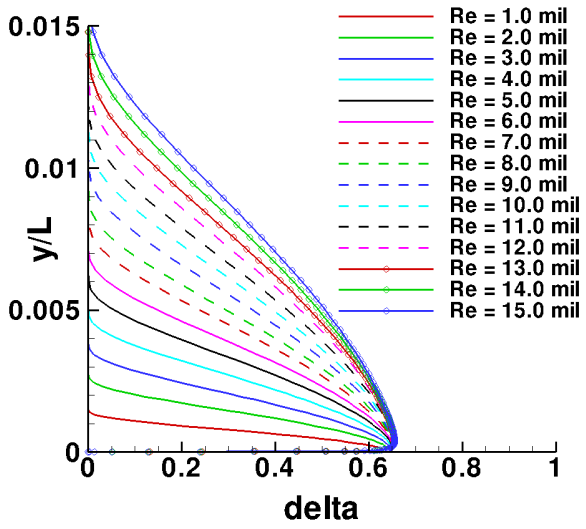

Figure B.2: δ profiles on a zero pressure gradient flat plate

tion term when the value of δ increases beyond 1.0. This is achieved by decreasing the value of the von Karman constant value κ from 0.41 to 0.15. Decreasing the value of κ in this modification is only for numerical purposes and is not indicative of the nature of the log law slope under strong APG.

The contour plot of the δ for a NACA 0012 airfoil at Re = 6×10^6 and AoA = 10° in Fig. B.3(a) shows that its value is below 1.0 in the favorable pressure gradient region on the pressure side, and greater than 1.0 in the adverse pressure gradient region on the suction side.

Preliminary results obtained with the proposed SA-APG model shows improved predictions of 2-D static stall onset (NACA 0012 airfoil) and dynamic stall onset and recovery (OA209, SC1095, NACA0012 airfoils) as will be shown in the next section. An important requirement of this modification is that it should not alter the baseline turbulence model behavior for moderate pressure gradient flows,

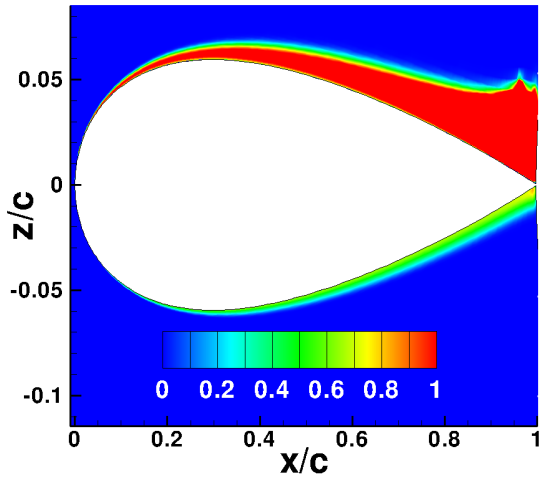

Figure B.3: δ criterion indicating strong adverse pressure gradient region on the upper surface of NACA 0012 airfoil at 10° AoA, Re = 6×10^6

as will be demonstrated in the Results section. The APG modification also showed improved prediction of shock-induced separation where strong pressure gradients are present.

B.4 Preliminary Results

2-D Static Stall

Two-dimensional steady flow past a NACA 0012 airfoil section is simulated at a Reynolds number of 6×10^6 and a Mach number of 0.15. The number of grid points in the wrap-around and normal directions of the C-topology computational mesh are 897 and 257 respectively, with 511 points on the airfoil surface. Lift and drag predictions from the 2-D simulations are plotted in Fig. B.4(a) and (b). The APG-modification and the SALSA formulation of the S-A model show improved agreement

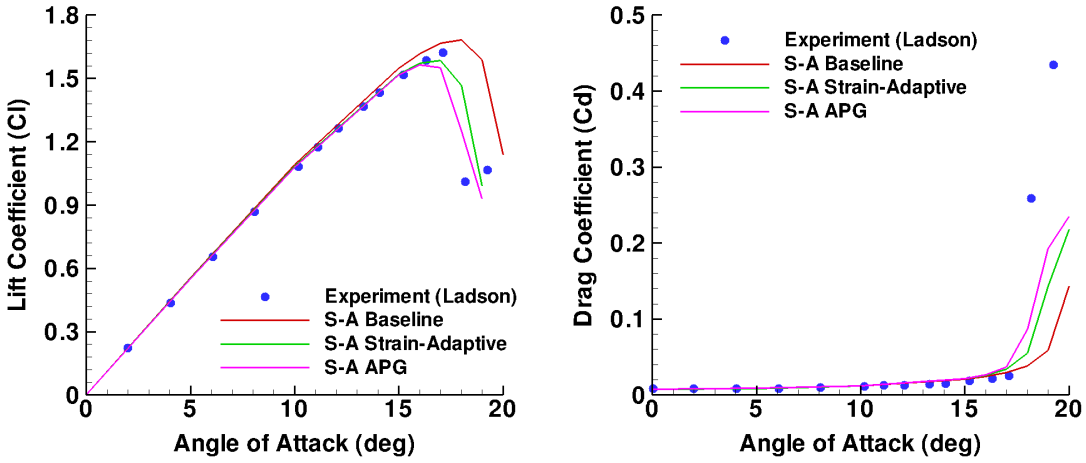

(a) Lift

(b) Drag

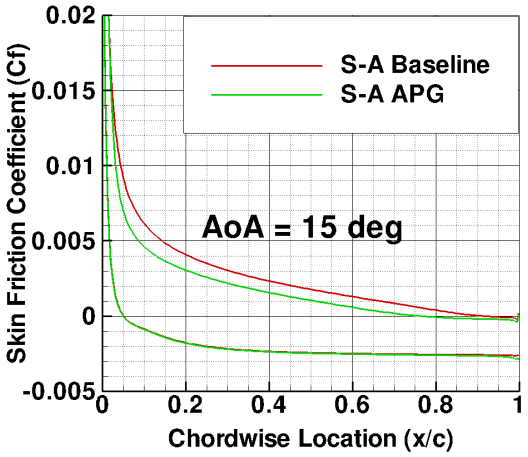

(c) Skin Friction,15 deg AoA

Figure B.4: Improved static stall prediction with SA-APG model (Expt [137]: NACA 0012 airfoil, Re = 6×10^6, M = 0.15)

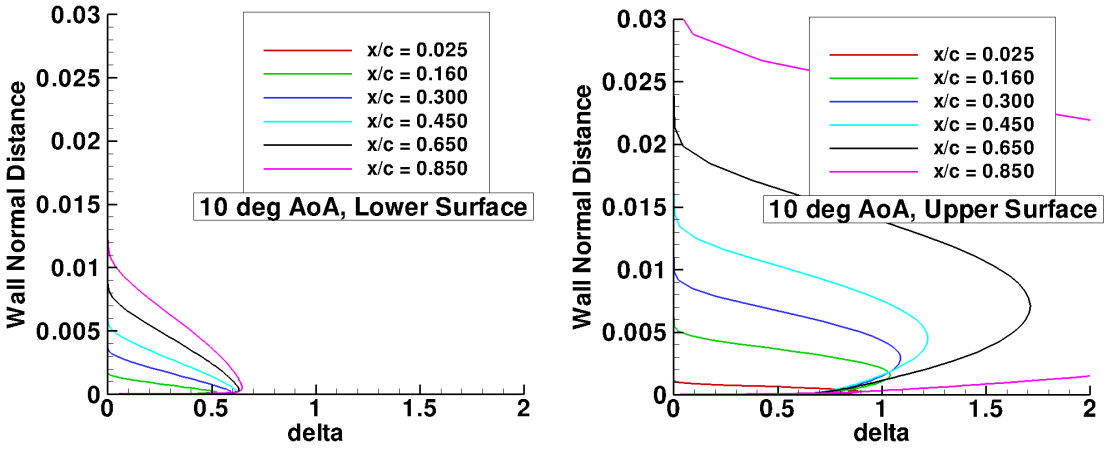

(a) Lower Surface (b) Upper Surface

Figure B.5: δ criterion indicating strong adverse pressure gradient region on the upper surface of NACA 0012 airfoil at 10° AoA, Re $= 6 \times 10^6$

with experimental data [137] at higher at AoA and do not over-predict the stall onset angle like the baseline model does. As expected, the SA-APG modification did not alter the results at lower AoA with moderate adverse pressure gradients. Figure B.4 (c) shows the reduced skin friction on the upper surface at 15° AoA, and the increased reverse flow region near the trailing edge obtained with the APG modification.

At 10° AoA, the boundary layer profiles of δ plotted in Fig. B.5 show that the peak value does not exceed 1.0 on the lower surface, which ensures that the baseline turbulence model behavior is not altered in favorable pressure gradient regions. The upper surface δ profiles exceed 1.0 beyond 15% of the chord. The corresponding upper surface mean velocity profiles at 10° AoA plotted at six chordwise stations (Figs. B.6–B.7) show increasing differences between the baseline and APG predic-

tions towards the trailing edge where the APG is stronger. The SA-APG model predicts a larger velocity defect compared to the baseline S-A model.

At 15° AoA, the δ profiles (Fig. B.8) on the upper surface exceed 1.0 almost immediately after the stagnation point, indicating a strong APG throughout the uppper surface. The lower surface profiles are consistently below 1.0 indicating a uniformly favorable APG. The corresponding mean velocity profiles on the upper surface show significant velocity defect due to the APG modification at all chordwise stations (Figs. B.9–B.10). Figures B.11–B.12 shows the reduced Eddy viscosity levels on the upper surface due to the APG modificaiton.

2-D Dynamic Stall

The next test case is flow past an sinusoidally pitching SC1095 airfoil in a wind tunnel. The flow conditions for the corresponding experimental case [138] are given in Table B.1. The C-mesh around the airfoil has 391 points in the wrap around direction and 101 points in the normal direction. The lift coefficient hysteresis plotted in Fig.B.13 shows that the baseline S-A model fails to predict the amount of lift loss, and also reattaches much sooner compared to experimental data. The APG modification shows significantly improved dynamic stall behavior thus proving that the proposed empirical criterion is applicable to unsteady flows with moving wall boundaries.

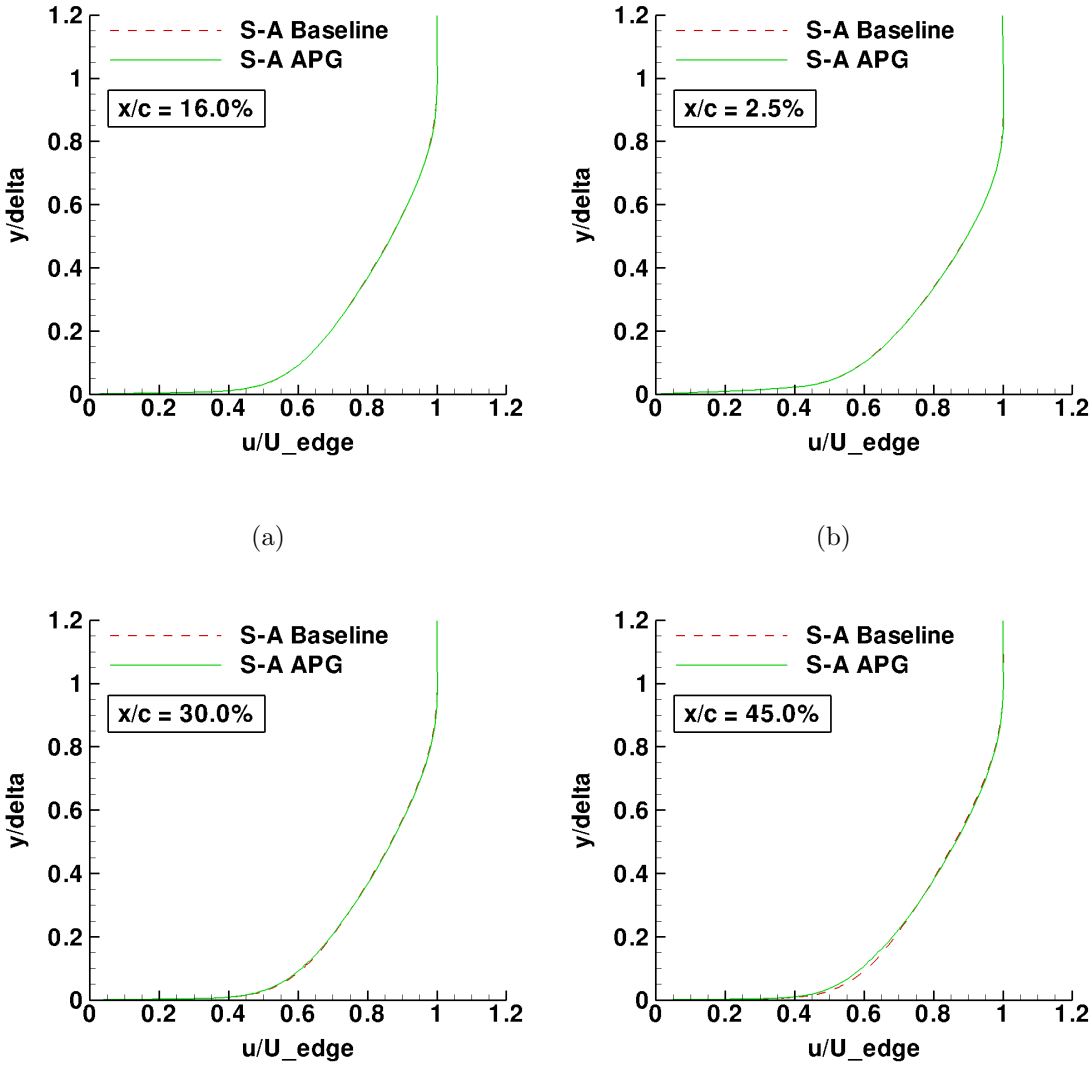

Figure B.6: Upper surface mean velocity profiles at 10° AoA on NACA 0012 airfoil, Re $= 6 \times 10^6$

Case	Airfoil	Re ($\times 10^6$)	M	k ($= \frac{\omega c}{2U_\infty}$)	α_o	α_s
a	SC1095	3.75	0.30	0.049	9.93°	4.91°

Table B.1: Flow conditions for 2-D dynamic stall test case of SC1095 airfoil (sinusoidal pitching motion - $\alpha(t) = \alpha_o + \alpha_s \sin(\omega t)$)

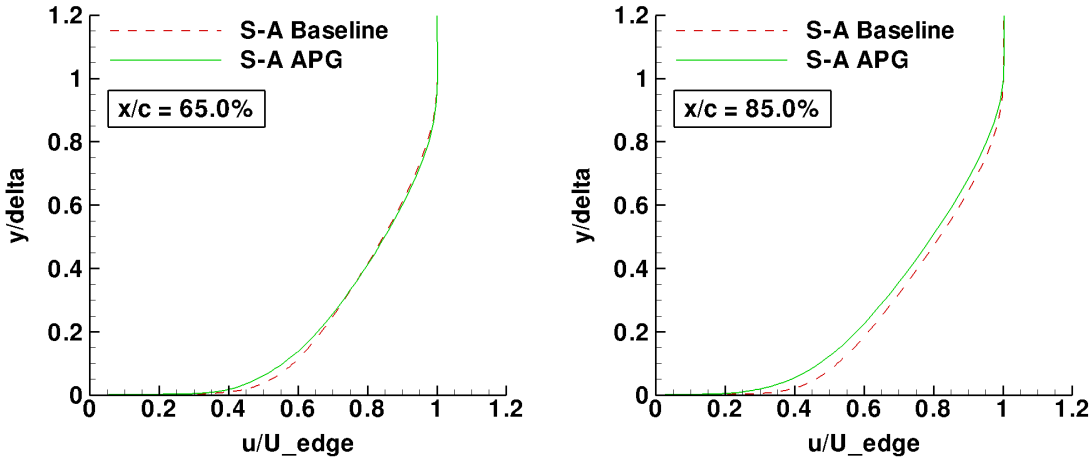

(a) (b)

Figure B.7: Upper surface mean velocity profiles at 10° AoA on NACA 0012 airfoil, Re = 6×10^6

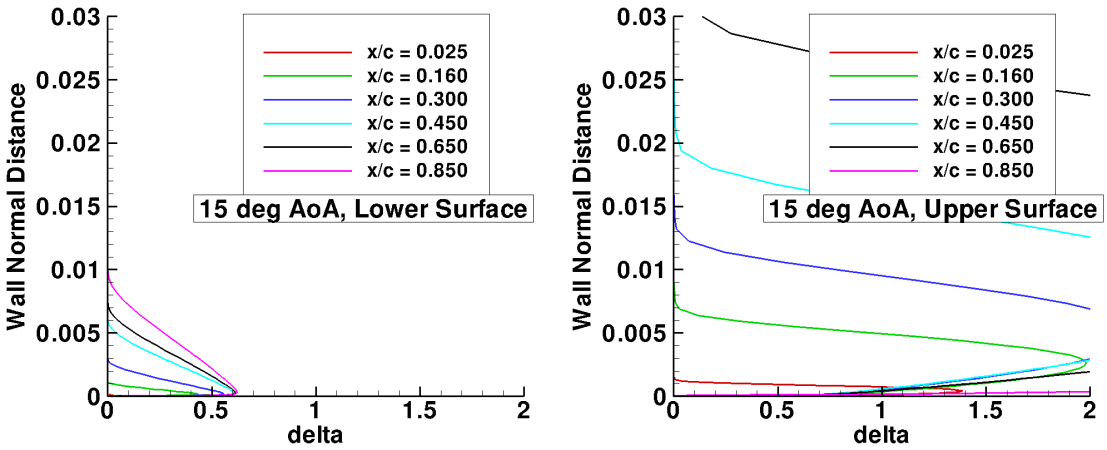

(a) Lower Surface (b) Upper Surface

Figure B.8: δ criterion indicating strong adverse pressure gradient region on the upper surface of NACA 0012 airfoil at 15° AoA, Re = 6×10^6

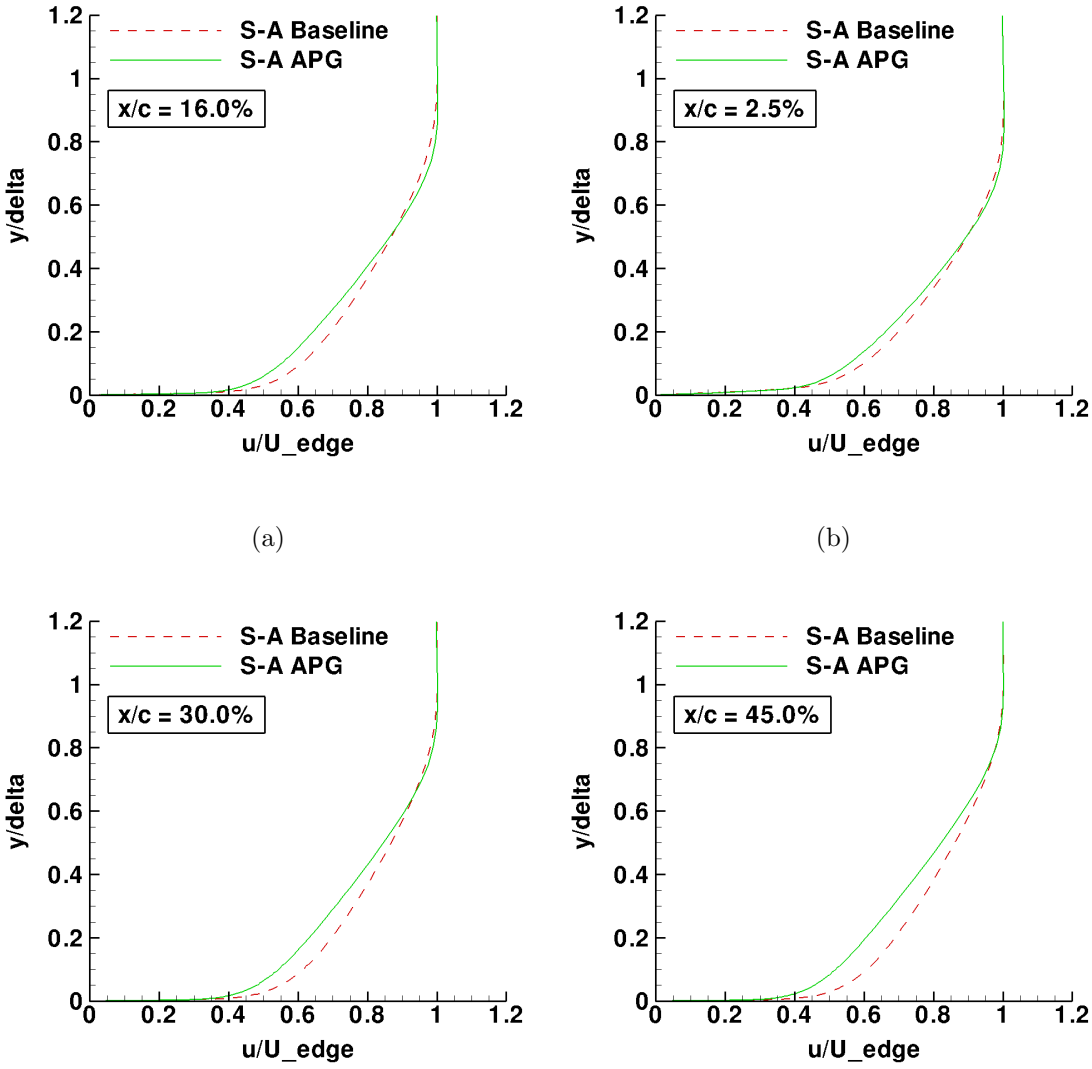

(a)

(b)

(c)

(d)

Figure B.9: Upper surface mean velocity profiles at 15° AoA on NACA 0012 airfoil, $\mathrm{Re} = 6 \times 10^6$

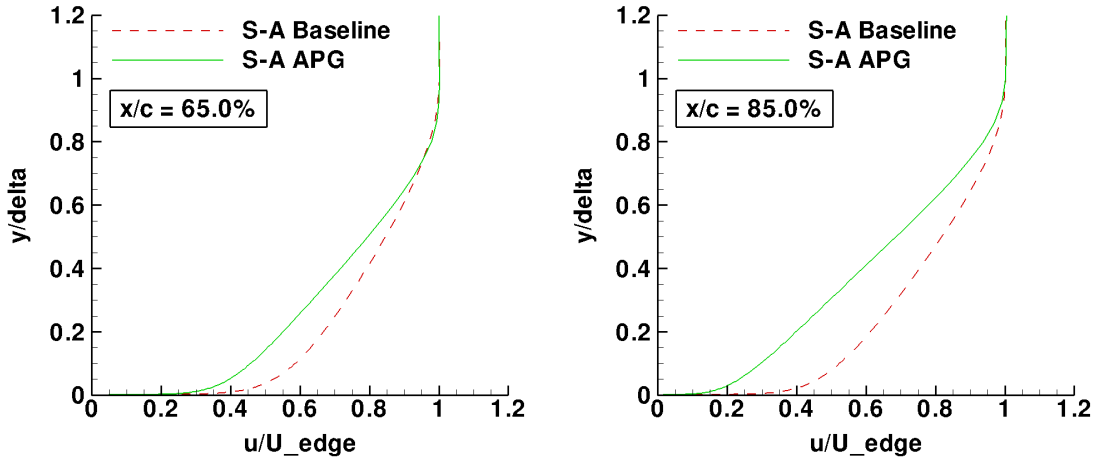

(a) (b)

Figure B.10: Upper surface mean velocity profiles at 15° AoA on NACA 0012 airfoil, $\mathrm{Re} = 6 \times 10^6$

2-D Shock-induced Separation

Finally, transonic flow past a NACA 0012 airfoil is simulated at a Reynolds number of $6{\times}10^6$, Mach number of 0.799, and an angle of attack of 2.26°. The number of grid points in the wrap-around and normal direction of the C-mesh are 897 and 257 respectively, with 511 points on the airfoil surface. Pressure coefficient plotted in Fig. B.14(a) shows significant improvement in the prediction of shock location using the APG modification and the SALSA formulation, indicated by the sharp discontinuity in the pressure coefficient profile on the upper surface. The baseline S-A model predicted shock further downstream compared to the experimental data [139]. Comparison of the Mach number contours in Fig. B.14(b) and (c) shows the upstream movement of shock and the increased shock-induced separation region with the APG modification. The computed lower surface pressure is consistently

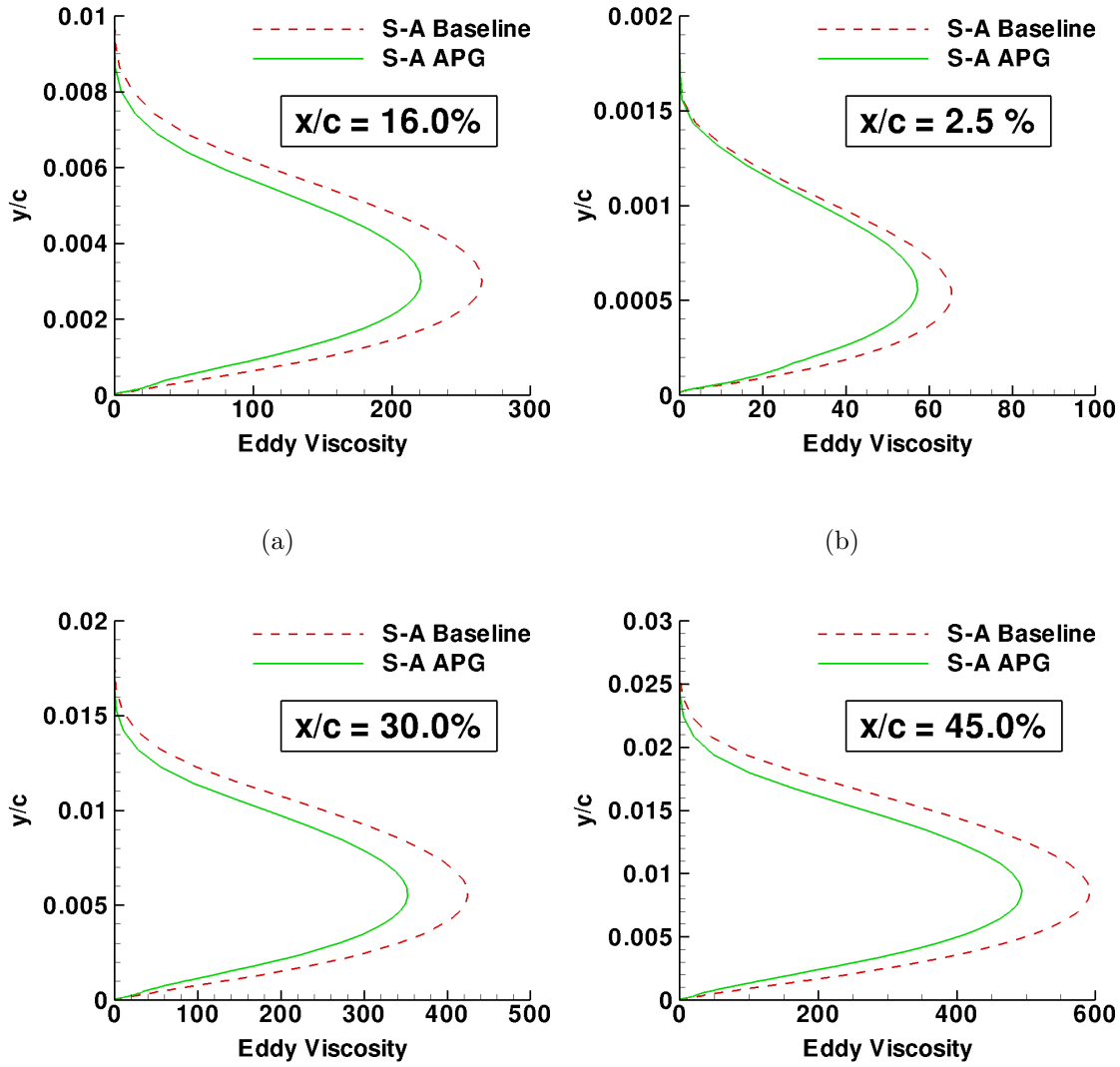

Figure B.11: Upper surface Eddy viscosity profiles at 15° AoA on NACA 0012 airfoil, Re $= 6 \times 10^6$

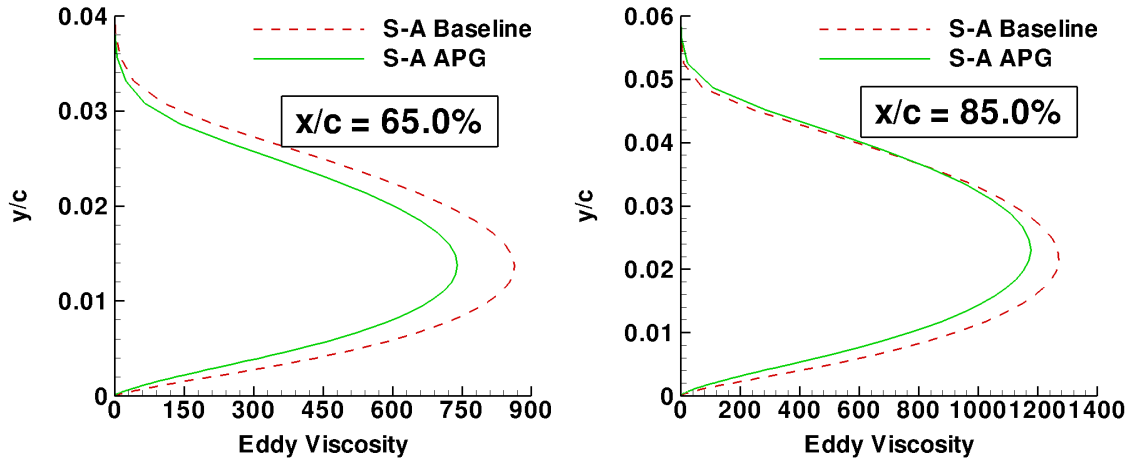

(a) (b)

Figure B.12: Upper surface Eddy viscosity profiles at 15° AoA on NACA 0012 airfoil, Re $= 6 \times 10^6$

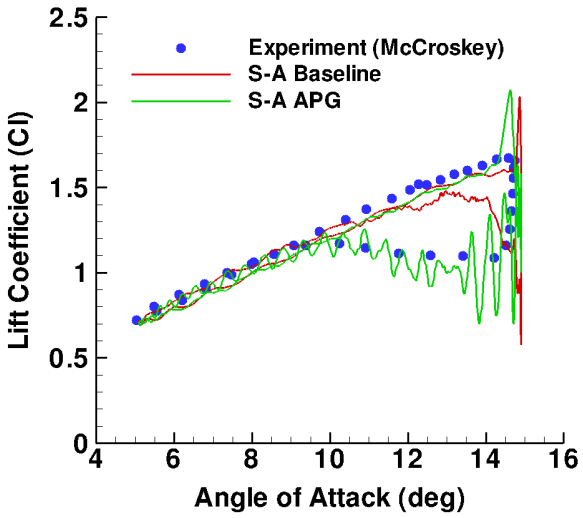

Figure B.13: Improved dynamic stall predictions with SA-APG model (Expt [138]: SC1095 airfoil)

inaccurate for all three version of the S-A model.

B.5 Summary

A new criterion for improved sensitivity to strong adverse pressure gradients, that is applicable to RANS turbulence models, is developed. The one-equation Spalart-Allmaras model is modified using this criterion. Preliminary results for 2-D static and dynamic stall, as well as shock-induced separation obtained using the SA-APG model are encouraging. The performance of the SA-APG model is comparable to the SA-SALSA formulation. On-going work includes extending the APG modification to two-equation turbulence models, and evaluating its performance for 3-D fixed wings (static and oscillating) and rotating blades.

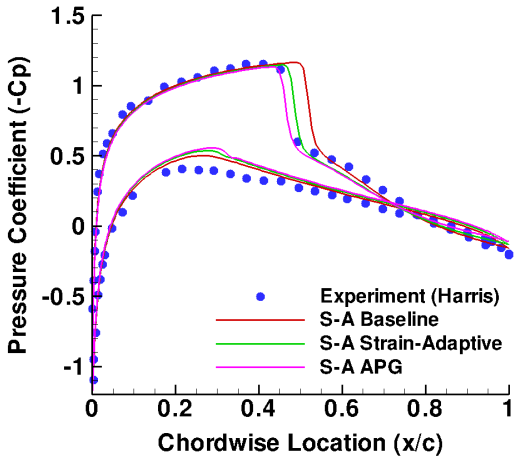

(a) Pressure Coefficient

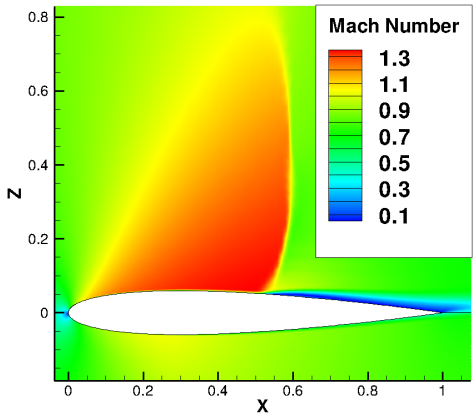

(b) Mach Number, S-A Baseline

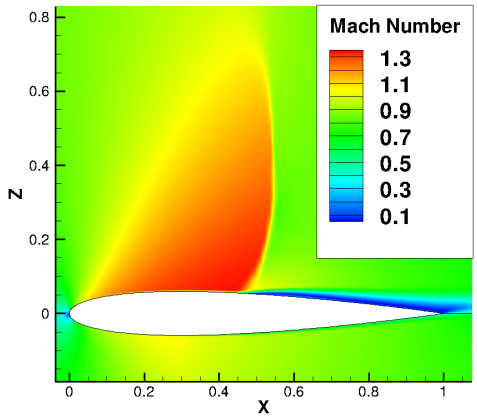

(c) Mach Number, S-A APG

Figure B.14: Improved shock location prediction with SA-APG model (NACA 0012 airfoil, Expt [139]: $\mathrm{Re} = 9 \times 10^6$, $\mathrm{M} = 0.799$, $\mathrm{AoA} = 2.26°$)

Bibliography

[1] B. J. Abu-Ghannam and R. Shaw. Natural transition of boundary layers – the effects of turbulence, pressure gradient, and flow history. *Journal of Mechanical Engineering Science*, 22(5):213–228, 1980.

[2] I. Tani. Boundary-layer transition. *Annual Review of Fluid Mechanics*, 1:169–196, 1969.

[3] E. Reshotko. Boundary-layer stability and transition. *Annual Review of Fluid Mechanics*, 8:311–349, 1976.

[4] M. V. Morkovin, D. Arnal, L. M. Mack, E. Reshotko, D. I. A. Poll, and T. Herbert. Special course on stability and transition of laminar flow. Technical Report AGARD-R-709, AGARD, von Karman Institute Rhode-Saint-Genese, Belgium., 1984.

[5] H. L. Reed, T. S. Haynes, and W. S. Saric. Computational fluid dynamics validation issues in transition modeling. *AIAA Journal*, 36(5):742–751, 1998.

[6] R. B. Langtry. *A correlation-based transition model using local variables for unstructured parallelized CFD codes*. PhD thesis, University of Stuttgart, 2006.

[7] E. Reshotko. Progress, accomplishments and issues in transition research. In *28^{th} Fluid Dynamics Conference*, number 1997-1815. AIAA, 1997.

[8] M. V. Morkovin. On the many faces of transition. In *Proceedings of the Symposium on Viscous Drag Reduction*. Plenum Press, New York, 1969.

[9] M. V. Morkovin. *Bypass-transition research: Issues and philosophy*. Kluwer Academic Publishers, 1993.

[10] E. Reshotko. Transient growth: A factor in bypass transition. *Physics of Fluids*, 13:1067–1075, 2001.

[11] W. S. Saric. Physical description of boundary-layer transition: Experimental evidence. Technical Report AGARD-R-793, AGARD, 1994.

[12] T. Herbert. Secondary instability of boundary layers. *Annual Review of Fluid Mechanics*, 20:487–526, 1988.

[13] W. S. Saric, H. L. Reed, and E. J. Kerschen. Boundary-layer receptivity to freestream disturbances. *Annual Review of Fluid Mechanics*, 34:291–319, 2002.

[14] H. W. Emmons. The laminar-turbulent transition in a boundary layer - part 1. *Journal of Aerospace Science*, 18(7):490–498, 1951.

[15] M. Mitchner. Propagation of turbulence from an instantaneous point disturbance. *Journal of the Aeronautical Sciences*, 21(5):350–351, 1954.

[16] J. W. Elder. An experimental investigation of turbulent spots and breakdown to turbulence. *Journal of Fluid Mechanics*, 9(2):235–246, 1960.

[17] S. Dhawan and R. Narasimha. Some properties of boundary layer flow during the transition from laminar to turbulent motion. *Journal of Fluid Mechanics*, 3(4):418–436, 1958.

[18] W. MF. Orr. The stability or instability of the steady motions of a liquid: Part i. In *Proceedings of the Royal Irish Academy A*, number 27: 9–68, 1907.

[19] W. MF. Orr. The stability or instability of the steady motions of a liquid: Part i. In *Proceedings of the Royal Irish Academy A*, number 27: 9–68, 1907.

[20] W. MF. Orr. Ein beitrag zur hydrodynamische erklrung der turbulenten flssigkeitsbewegungen. In *Proceedings of the 4^{th} International Congress of Mathematicians III*, number 116–124, 1908.

[21] G. B. Schubauer and H. K. Skramstad. Laminar-boundary-layer oscillations and transition on a flat plate. Technical Report 909, NACA, 1948.

[22] E. Reshotko. *Disturbances in a laminar boundary layer due to surface roughness*. North-Holland, 1984.

[23] T. Zaki and P. A. Durbin. Mode interaction and the bypass route to transition. *Journal of Fluid Mechanics*, 531:85–111, 2005.

[24] P. A. Durbin and X. Wu. Transition beneath vortical disturbances. *Journal of Fluid Mechanics*, 39:107–128, 2007.

[25] R. E. Mayle. The role of laminar-turbulent transition in gas turbine engines. *Journal of Turbomachinery*, 113:509–537, 1991.

[26] H. W. Emmons. Dreidimensionales zur stabilitatstheorie laminarer grenzschichten. *Journal of Applied Mathematics and Mechanics*, 35(9–10):362–363, 1955.

[27] W. S. Saric, H. L. Reed, and E. B. White. Stability and transition of three-dimensional boundary layers. *Annual Review of Fluid Mechanics*, 35:413–442, 2003.

[28] W. S. Saric, R. B. Carrillo, and M . S. Reibert. Nonlinear stability and transition in 3-d boundary layers. *MEccanica*, 33:469–487, 1998.

[29] W. S. Saric, R. B. Carillo, and M. S. Reibert. Leading-edge roughness as a transition control mechanism. In *36th Fluid Dynamics Conference*, number 1998-0781. AIAA, 1998.

[30] E. B. White and W. S. Saric. Application of variable leading-edge roughness for transition control on swept wings. In *38th Fluid Dynamics Conference*, number 2000-0283. AIAA, 2000.

[31] X. Zhong and X. Wang. Direct numerical simulation on the receptivity, instability, and transition of hypersonic boundary layers. *Annual Review of Fluid Mechanics*, 44:527–561, 2012.

[32] L. M. Mack. Linear stability theory and the problem of supersonic boundary layer. *AIAA Journal*, 13(3):278–289, 1975.

[33] R. B. Langtry and F. R. Menter. Correlation-based transition modeling for unstructured parallelized computational fluid dynamics codes. *AIAA Journal*, 47(12):2894–2906, 2009.

[34] F. R. Menter. Two-equation eddy-viscosity turbulence models for engineering applications. *AIAA Journal*, 32(8):1598–1605, 1994.

[35] P. R. Spalart and S. R. Allmaras. A one-equation turbulence model for aerodynamic flows. *Recherche Aerospatiale*, (1):5–21, 1994.

[36] D. Di Pasquale and A. Rona. A selective review of cfd transition models. In *39th AIAA Fluid Dynamics Conference*, number 2009-3812. AIAA, 2009.

[37] A. Sveningsson. Transition modelling – a review. Technical report, Division of Fluid Dynamics, Dept. of Applied Mechanics, Chalmers University of Technology, Goteberg, 2006.

[38] D. Arnal, G. Casalis, and R. Houdeville. Practical transition prediction methods: subsonic and transonic flows. in vki lecture series: Advances in laminar-turbulent transition modeling. Technical report, Goteberg, 2009.

[39] R. G. Jacobs and P. A. Durbin. Simulations of bypass transition. *Journal of Fluid Mechanics*, 428:185–212, 2001.

[40] X. Wu and P. Moin. Simulations of bypass transition. *Journal of Fluid Mechanics*, 630:5–41, 2009.

[41] J. Wissink and W. Rodi. Dns of separation-induced transition influenced by freestream fluctuations. In *Sixth IUTAM symposium on laminar-turbulent transition*, pages 389–394, 2006.

[42] P. Schlatter. *Large-eddy simulation of transition and turbulence in wall-bounded shear flow*. PhD thesis, ETH Zurich, 2005.

[43] V. Michelassi, J. Wissink, J. Frohlich, and W. Rodi. Large eddy simulation of flow around a turbine blade with incoming wakes. *AIAA Journal*, 41(1):2143–2156, 2003.

[44] J. Bodart and J. Larsson. Sensor-based computation of transitional flows using wall-modeled large eddy simulation. Technical report, Center for Turbulence Research, Stanford University, 2012.

[45] J. Smagorinsky. General circulation experiments with the primitive equations: 1. the basic experiment. *Monthly Weather Review*, 91:99–164, 1963.

[46] P. Schlatter, S. Stolz, and L. Kleiser. Applicability of les models for prediction of transitional flow structures. In *Sixth IUTAM symposium on laminar-turbulent transition*, pages 323–328, 2006.

[47] M. Germano, U. Piomelli, P. Moin, and W. H. Cabot. A dynamic subgrid-scale eddy viscosity model. *Physis of Fluids A*, 3(7):1760–1765, 1991.

[48] H. L. Reed, W. S. Saric, and D. Arnal. Linear stability theory applied to boundary layers. *Annual Review of Fluid Mechanics*, 28:389–428, 1996.

[49] A. M. O. Smith and N. Gamberoni. Transition, pressure gradient and stability theory. Technical Report Rep. ES 26388, Douglas Aircraft Company, Long Beach, Calif., 1956.

[50] J. L. Van Ingen. A suggested semi-empirical method for calculation of the boundary layer transition region. Technical Report Rep. VTH-74, University of Delft, Dept. of Aerospace Engineering, Delft, The Netherlands, 1956.

[51] J. L. Van Ingen. The e^n method for transition prediction. historical review of work at tu delft. In *38th AIAA Fluid Dynamics Conference and Exhibit*, number 2008-3830. AIAA, 2008.

[52] M. Drela and M. B. Giles. Viscous-inviscid analysis of transonic and low reynolds number airfoils. *AIAA Journal*, 25:1347–1355, 1987.

[53] M. Drela. Mises implementation of modified abu-ghannam/shaw transition criterion. Technical report, MIT, Dept. of Aeronautics and Astronautics, Massachusetts, 1995.

[54] A. Deperrois. Xlrf5 user manual: Analysis of foils and wings operating at low reynolds numbers. Technical report, 2003.

[55] T. Herbert. Parabolized stability equations. *Annual Review of Fluid Mechanics*, 29:245–283, 1997.

[56] A. Krumbein and G. Schrauf. Automatic transition prediction in hybrid flow solver, part 1: Methodology and sensitivities. *Journal of Aircraft*, 46(4):1176–1190, 2009.

[57] A. Krumbein and G. Schrauf. Automatic transition prediction in hybrid flow solver, part 2: Practical application. *Journal of Aircraft*, 46(4):1191–1199, 2009.

[58] D. Arnal, R. Houdeville, A. Seraudie, and O. Vermeersh. Overview of laminar-turbulent transition investigations at onera toulouse. In *41st AIAA Fluid Dynamics Conference and Exhibit*, number 2011-3074. AIAA, 2011.

[59] D. Arnal, M. Habiballah, and E. Coutols. Thorie de linstabilit laminaire et critres de transition en ncoulement bi et tridimensionnel. *Recherche Aerospatiale*, 2:125–43, 1984.

[60] Y. Kohama and S. S. Davis. A new parameter for predicting crossflow instability. *JSME International Journal, Series B: Fluids and Thermal Engineering*, 36-B:1–80, 1993.

[61] J. Dey and R. Narasimha. An integral method for calculation of 2-d transitional boundary layers. *Journal of Aircraft*, 27(10):865–859, 1990.

[62] J. R. Cho and M. K. Chung. A k–ϵ–γ equation turbulence model. *Journal of Fluid Mechanics*, 237:301–322, 1992.

[63] J. Steelant and E. Dick. Modelling of bypass transition with conditioned navier-stokes equations coupled to an intermittency transport equation. *International journal of numerical methods in fluids*, 23(3):193–220, 1996.

[64] W. P. Jones and B. E. Launder. The calculation of low reynolds number phenomena with a two-equation model of turbulence. *International Journal of Heat and Mass Transfer*, 15(2):301–314, 1973.

[65] D. C. Wilcox. Simulation of transition with a two-equation turbulence model. *AIAA Journal*, 32(2):247–255, 1994.

[66] D. Biswas and Y. Fukuyama. Calculation of transitional boundary layers with an improved low-reynolds-number version of the k-ϵ turbulence model. *ASME Journal of Turbomachinery*, 116:765–773, 1994.

[67] E. S. Warren and H. A. Hassan. Transition closure model for predicting transition onset. *Journal of Aircraft*, 35(5):769–775, 1998.

[68] D. F. Robinson and H. A. Hassan. Modeling turbulence without damping functions using k–ζ model. In *15th Applied Aerodynamics Conference*, number 97-2312. AIAA, 1997.

[69] Y. B. Suzen and P. G. Huang. Modeling of flow transition using an intermittency transport equation. *Journal of Fluids Engineering*, 122:273–284, 2000.

[70] D. K. Walters and J. H. Leylek. A new model for boundary layer transition using a single-point rans approach. *Journal of Turbomachinery*, 126(1):193–202, 2004.

[71] D. K. Walters and D. Cokljat. A three-equation eddy-viscosity model for reynolds-averaged navier-stokes simulations of transitional flow. *Journal of Fluids Engineering*, 130(121401):1–14, 2008.

[72] J. G. Coder and M. D. Maughmer. A cfd-compatible transition model using an amplification factor transport equation. In *51st AIAA Aerospace Sciences Meeting including the New Horizons Forum and Aerospace Exposition*, number 2013-0253. AIAA, 2013.

[73] E. R. Van Driest and C. B. Blumer. Boundary layer transition: Freestream turbulence and pressure gradient effects. *AIAA Journal*, 1(6):1303–1306, 1963.

[74] T. Misaka and S. Obayashi. Application of local correlation-based transition model to flow around wings. In *44th AIAA Aerospace Sciences Meeting and Exhibit*, number 2009–918. AIAA, 2006.

[75] K. Pettersson and S. Crippa. Implementation and verificaiton of a correlation based transition prediction method. In *38th Fluid Dynamics Conference and Exhibit*, number 2008–4401. AIAA, 2008.

[76] N. N. Sorensen. Cfd modeling of laminar-turbulent transition ofr airfoils and rotors using the $\gamma - re_\theta$ model. In *26th AIAA Applied Aerodynamics Conference*, number 2008–7323. AIAA, 2008.

[77] P. Malan, K. Suluksna, and E. Juntasaro. Calibrating the $\gamma - re_\theta$ transition model for commercial cfd. In *47th AIAA Aerospace Sciences Meeting Including The New Horizons Forum and Aerospace Exposition*, number 2009–1142. AIAA, 2009.

[78] K. Suluksna, P. Dechaumphai, and E. Juntasaro. Correlations for modeling transitional boundary layers under influences of freestream turbulence and pressure gradient. *International Journal of Heat and Fluid Flow*, 30:66–75, 2009.

[79] G. B. Schubauer and P. S. Klebanoff. Contribution on the mechanics of boundary layer transition. Technical Report 3489, NACA, 1955.

[80] J. Coupland. Special interest group on laminar-to-turbulent transition and retransition: T3a and t3b test cases. Technical report, ERFCOFTAC, 1990.

[81] J. Coupland. Special interest group on laminar-to-turbulent transition and retransition: T3c test cases. Technical report, ERFCOFTAC, 1990.

[82] J. Dacles-Mariani, G. G. Zilliac, J. S. Chow, , and P. Bradshaw. Numerical/experimental study of a wingtip vortex in the near field. *AIAA Journal*, 9(33):1561–1568, 1995.

[83] J. D. Baeder G. R. Srinivasan. Turns: A free-wake euler/navier-stokes numerical method for helicopter rotors. *AIAA Journal*, 31(5):959–962, 1993.

[84] F. M. White. *Viscous Fluid Flow*. McGraw-Hill, 3 edition, 2005.

[85] J. Blazek. *Computational Fluid Dynamics: Principles and Applications, Second Edition*. Elsevier Science, 2006.

[86] V. K. Lakshminarayan. *Computational investigation of micro-scale coaxial rotor aerodynamics in hover*. PhD thesis, University of Maryland College Park, 2009.

[87] Y. Lee. *On overset grids connectivity and automated vortex tracking in rotorcraft CFD*. PhD thesis, University of Maryland College Park, 2008.

[88] B. Van Leer. Towards the ultimate conservative difference scheme: V. a second-order sequel to godunov's method. *Journal of Computational Physics*, 135(2):229–248, 1997.

[89] B. Koren. Upwind schemes, multigrid and defect correction for the steady navier-stokes equations. In *Proceedings of the 11th International Conference on Numerical Methods in Fluid Dynamics*, 1988.

[90] P. Roe. Approximate riemann solvers, parameter vectors and difference schemes. *Journal of Computational Physics*, 135(2):250–258, 1997.

[91] C. Hirsch. *Numerical computation of internal and external flows, Volume–2*. Wiley Publishers, 1990.

[92] B. E. Launder, G. J. Reece, and W. Rodi. Progress in the development of a reynolds-stress turbulent closure. *Journal of Fluid Mechanics*, 68(3):537–566, 1975.

[93] P. Durbin. A reynolds stress model for near wall turbulence. *Journal of Fluid Mechanics*, 249:465–498, 1993.

[94] B. Baldwin and H. Lomax. Thin layer approximation and algebraic model for separated flows. In *16th AIAA Aerospace Sciences Meeting*, number 1978–257. AIAA, 1978.

[95] P. Durbin. Near-wall turbulence closure modeling without "damping functions". *Theoretical and Computational Fluid Dynamics*, 3:1–13, 1991.

[96] T. H. Pulliam and D. Chaussee. A diagonal form of an implicit approximate factorization algorithm. *Journal of Computational Physics*, 39(2):347–363, 1981.

[97] A. Jameson and S. Yoon. Lower-upper implicit schemes with multiple grids for euler equations. *AIAA Journal*, 25(7):1987, 929–935.

[98] T. Pulliam. Time accuracy and use of implicit methods. In *11th AIAA Computational Fluid Dynamics Conference*, number 1993–3360. AIAA, 1993.

[99] E. Turkel. Preconditioning techniques in computational fluid dynamics. *Annual Review of Fluid Mechanics*, 31:385–416, 1999.

[100] E. Chaput. Chapter iii: Application-oriented synthesis of work presented in chapter ii, notes on numerical fluid mechanics. Technical Report 58, ERF-COFTAC, Vieweg Braunschweig, Wiesbaden, 1997.

[101] W. Haase, E. Chaput, E. Elsholz, M. Leschziner, and U. R. Mueller. Ecarp – european computational aerodynamics research project: Validation of cfd codes and assessment of turbulence models; notes on numerical fluid mechanics. Technical Report 58, 1997.

[102] G. G. Mateer, D. J. Monson, and F. R. Menter. Skin-friction measurements and calculations on a lifting airfoil. *AIAA Journal*, 34(2):231–236, 1996.

[103] M. M. Hand, D. A. Simms, L. J. Fingersh, D. W. Jager, J. R. Cotrell, S. Schreck, and S. M. Lawood. Unsteady aerodynamics experiment phase vi: Wind tunnel test configurations and available data campaigns. Technical Report TP-500-29955, NREL, 2001.

[104] D. M. Somers. Design and experimental results for the s809 airfoil. Technical Report SR-440-6918, NREL, 1997.

[105] M. S. Selig and B. D. McGranahan. Wind tunnel aerodynamic tests of six airfoils for use on small wind turbines. Technical Report SR-500-34515, NREL, 2004.

[106] F. W. Boltz, G. C. Kenyon, and C. Q. Allen. Effects of sweep angle on the boundary-layer stability characteristics of an untapaered wing at low speeds. Technical Report D-338, NASA, 1960.

[107] H. W. Stock. Airfoil validation using coupled navier-stokes and e^n transition prediction methods. *Journal of Aircraft*, 39(1):51–58, 2002.

[108] C. L. Rumsey, T. B. Gatski, S. X. Ying, and A. Bertlrud. Prediction of high-lift flows using turbulent closure. *AIAA Journal*, 36(5):765–774, 1998.

[109] S. M. Klausmeyer and J. C. Lin. An experimental investigation of skin friction on a multi-element airfoil. In *12th AIAA Applied Aerodynamics Conference*, number 1994-1870. AIAA, 1994.

[110] P. F. Lorber, A. Bagai, and B. E. Wake. Design and evaluation of slatted airfoils for improved rotor performance. In *AHS International 62nd Annual Forum and Technology Display*. AHS, 2006.

[111] W. H. Tanner and P. F. Yaggy. Experimental boundary layer study on hovering rotors. *Journal of American Helicopter Society*, 11(3):22–37, 1966.

[112] H. R. Velkoff, D. A. Blaser, and K. M. Jones. Boundary-layer discontinuity on a helicopter rotor blade in hovering. *Journal of Aircraft*, 8(2):101–107, 1971.

[113] W. J. McCroskey. Measurements of boundar layer transition, separation and streamline direction on rotating blades. Technical Report NASA-TN D-6321, NASA, 1971.

[114] C. C. Heister. Laminar-turbulent transition prediction for helicopter rotors in hover and forward flight - a rans based investigation of transition mechanisms using empirical criteria. In *39th European Rotorcraft Forum 2012*. AHS, 2012.

[115] C. H. Rohardt. Flow visualization on a helicopter rotor in hover using acenaphthene. In *13th European Rotorcraft Forum*. AHS, 1987.

[116] Ph. Beaumier and R. Houdeville. 3d laminar-turbulent boundary layer calculations on helicopter rotors in forward flight: Application to drag prediction. In *21st European Rotorcraft Forum*. AHS, 1995.

[117] D. A. Corson, D. T. Griffith, T. Ashwill, and F. Shakib. Investigating aeroelastic performance of multi-megawatt wind turbine rotors using cfd. In *53rd AIAA/ASME/ASCE/AHS/ASC Structures, Structural Dynamics and Materials Conference*, number 2012–1827. AIAA, 2012.

[118] E. P. N. Duque, M. D. Burklund, and W. Johnson. Navier-stokes and comprehensive analysis performance predictions of the nrel phase vi experiment. *ASME Journal of Solar Energy Engineering*, 125(4):457–467, 2003.

[119] W. Johnson. Rotorcraft aerodynamics models for a comprehensive analysis. In *American Helicopter Society 54th Annual Forum*, 1998.

[120] N. N. Sorensen, J. A. Michelsen, and S. Schreck. Navier-stokes predictions of the nrel phase vi rotor in the nasa ames 80 ft $\times$ 120 ft wind tunnel. *Wind Energy*, 5(2–3):151–169, 2002.

[121] A. Le Pape and J. Lecanu III. Navier-stokes computations of a stall-regulated wind turbine. *Wind Energy*, 5(2–3):151–169, 2002.

[122] A. Le Pape and V. Gleize. Improved navier-stokes computations of a stall-regulated wind turbine using low mach number preconditioning. In *44th AIAA Aerospace Sciences Meeting*, number 2006–1502. AIAA, 2006.

[123] G. Xu and L. N. Sankar. Application of a viscous flow methodology to the nrel phase vi rotor. In *40th AIAA Aerospace Sciences Meeting*, number 2002–0030. AIAA, 2002.

[124] S. Gomes-Iradi, R. Steijl, and G. N. Barakos. Development and validation of a cfd technique for the aerodynamic analysis of hawt. *ASME Journal of Solar Energy Engineering*, 131(3):031009–1–031009–13, 2009.

[125] R. B. Langtry, J. Gola, and F. R. Menter. Predicting 2d airfoil and 3d wind turbine rotor performance using a transition model for general cfd codes. In *44th AIAA Sciences Meeting and Exhibit*, number 2006–395. AIAA, 2006.

[126] A. C. Aranake, V. K. Lakshminarayan, and K. Duraisamy. Assessment of transition model and cfd methodology for wind turbine flows. In *42nd AIAA Fluid Dynamics Conference and Exhibit*, number 2012–2720. AIAA, 2012.

[127] Y. Watanabe, T. Misaka, S. Obayashi, T. Arima, and Y. Yamaguchi. Application of crossflow transitio criteria to local correlation-based transition model. In *47th AIAA Aerospace Sciences Meeting*, number 2009-1145. AIAA, 2009.

[128] C. Seyfert and A. Krumbein. Correlation-based transition transport modeling for three-dimensional aerodynamic configurations. In *50th AIAA Aerospace Sciences Meeting*, number 2012-0448. AIAA, 2012.

[129] P. R. Owen and D. J. Randall. Boundary-layer transition on a swept-back wing. Technical Report TM Aero 277, RAE, 1952.

[130] J. R. Dagenhart. Crossflow stability and transition experiments in a swept-wing flow. Technical Report TM 108650, NASA, 1992.

[131] V. Schmitt, B. Monneris, G. Dorey, and C. Capelier. Etude de la couche limite tridimensionelle sur une aile en fleche. Technical Report 14/1717 AN, 1975.

[132] A. Celic and E. H. Hirschel. Comparison of eddy-viscosity turbulence models in flows with adverse pressure gradient. *AIAA Journal*, 44(10):2156–2169, 2006.

[133] F. H. Clauser. The turbulent boundary layer. *Advanced Applied Mechanics*, 4:1–54, 1956.

[134] D. C. Wilcox. Formulation of the k-ω turbulence model revisited. *AIAA Journal*, 46(11):2823–2838, 2008.

[135] T. Rung, U. Bunge, M. Schatz, and F. Thiele. Restatement of the spalart-allmaras eddy-viscosity model in strain-adaptive formulation. *AIAA Journal*, 47(7):1396–1399, 2003.

[136] A. E. Perry and W. H. Schofield. Mean velocity and shear stress distributions in turbulent boundary layers. *The Physics of Fluids*, 16(12):2068–2074, 1973.

[137] C. L. Ladson. Effects of independent variation of mach and reynolds numbers on the low-speed aerodynamic characteristics of the naca 0012 airfoil section. Technical Report TM-4074, NASA, 1988.

[138] K. W. McAlister. An experimental study of dynamic stall on advanced airfoil sections volume 2. pressure and force data. Technical Report TM-84245, NASA, 1982.

[139] D. Harris. Two-dimensional aerodynamic characteristics of the naca 0012 airfoil in the langley 8-foot transonic pressure tunnel. Technical Report TM-81927, NASA, 1981.